Reviewer comments in black, author response in blue

The major comments from my previous review were about the data used, the assumption of a constant feedback parameter and the length/prose of the paper. While the authors have tried to address all, I am not yet satisfied with the solutions and I recommend another round of major revisions. I still believe the manuscript will become a valuable piece in the discussion of climate sensitivity, as it provides a comprehensive overview of modes of internal variability.

Major comments:

1. The authors still use HadCRUT4 as if it were a global average. They justified this by citing other papers that have done the same. The Nicholls paper seems to make the same mistake as the authors. However, the other paper does not. Liang et al. (2020) use HadCRUT4, but they do take into account that it is not a global average and that there is missing data, especially around the poles. They use a mask of the CMIP output so that the spatial coverage of the datasets is the same. This takes some work to implement, so I suggest the authors choose any of the four datasets with global coverage. Instead of comparing HadCRUT4 with CW14 (f.i. in Table 1, Figure 12), the authors can compare CW14 with NOAAGlobalTemp v5. Dropping HadCRUT4 from the manuscript completely also helps making the paper shorter.

HadCRUT4 uses HadSST3 for sea surface temperatures, which further shows slower warming due to biases in ship measurements in comparison with HadSST4. As I understand it, even the incomplete (not infilled) provisional version of HadCRUT5 shows more warming than HadCRUT4. CW14 uses HadSST3 as well, potentially explaining why it warms more slowly compared to some other global averages.

> We thank the reviewer for suggesting we change our primary data set in our manuscript. We have decided to use the infilled, global version of HadCRUT5 throughout as our main data set, which was released in late 2020. Switching from HadCRUT4 to HadCRUT5 changes the quantitative details of our results in an important manner, as HadCRUT5 exhibits more warming over the past few decades than HadCRUT4. However, we still find that many of the CMIP6 GCMs warm too quickly over the past few decades compared to empirical determination of the attributable anthropogenic warming rate (AAWR), and that many of the GCMs exhibit higher values of ECS compared to our empirical determination. Upon use of the HadCRUT5 data record, we now find that 7 of the 28 CMIP6 GCMs for which we can compute AAWR and ECS lie within the minimum and maximum values of our empirical determination. This overlap is an incredibly important new result that follows from our adoption of the HadCRUT5 data record and is illustrated in New Fig. S17. We added the following text to the main manuscript on lines 854-862 to explain this new result: **We conclude this section by commenting on the relationship between ECS and AAWR in our model framework. Eight of the CMIP6 GCMs (GFDL-ESM4, GISS-E2-1-G, INM-CM5-0, INM-CM4-8, MIROC6, MIROC-ES2L, NorESM2-LM, and NorESM2-MM) exhibit values of ECS and AAWR consistent with the minimum and maximum estimates based on our EM-GC constrained by the HadCRUT5 GMST record (Table S5 and Fig. S17). An analysis of the relationship between AAWR and ECS from the CMIP6 GCMs illustrates that 78% of the variance in ECS among the 28 CMIP6 GCMs that provide both quantities is explained by AAWR (see Fig. S17). This result indicates CMIP6 GCMs that accurately simulate the rise in observed ΔT over the past few decades exhibit values of ECS that are in line with our empirically based estimate.**

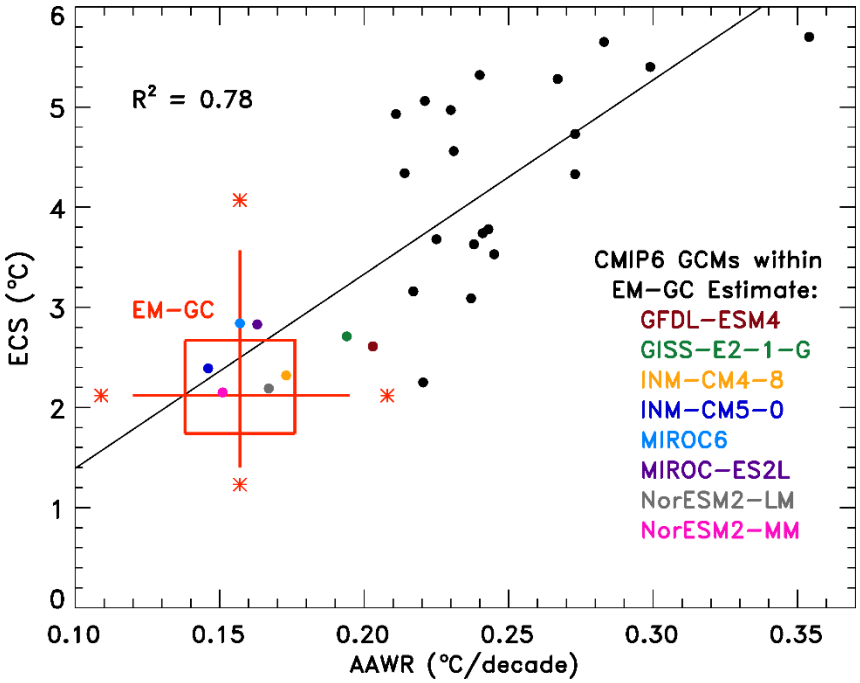

New Figure S17. Values of ECS versus AAWR for the CMIP6 multi-model ensemble. The EM-GC estimates of AAWR and ECS based on training to the HadCRUT5 GMST record are plotted as a box and whisker. The box shows the average 25th, 50th, and 75th percentiles for the five OHC records shown for HadCRUT5 in Fig. 6 and Fig. 7. The whiskers represent the average 5th and 95th percentiles. The stars denote the average minimum and maximum values of AAWR or ECS. The eight CMIP6 GCMs that obtain values of AAWR and ECS that are both within the minimum and maximum estimates provided by the EM-GC are identified on the figure. Values of AAWR explain about 78% of the variance in ECS among the CMIP6 GCMs.

Upon switching to HadCRUT5, we noticed the uncertainties for the GMST anomaly decreased dramatically compared to those provided with the HadCRUT4 record (New Figure S4c versus S4e). The difference is especially noticeable in the beginning of the temperature record. If we use the HadCRUT5 uncertainties in our current model framework, the EM-GC is not able to achieve a value less than or equal to 2 for χ^2_{ATM} or χ^2_{RECENT}. The fits between the observed and modeled GMST are visually good fits, but the values of χ^2 that are calculated never fall below 2 due to the incredibly small uncertainties of the HadCRUT5 record. We could either increase our constraint limit to admit simulations with values of χ^2 less than or equal to 4 or 8, adjust the HadCRUT5 uncertainties in some manner to be more "realistic", or use the HadCRUT4 uncertainties for the HadCRUT5 temperature record. After much internal debate and considerable analysis not shown in this reply, we decided to adopt the HadCRUT4 uncertainties for all of the GMST records. Our deep dive into the GMST records, highlighted in New Figs. S4, S5 and New Table 1, have led us to conclude the uncertainties for GMST provided by HadCRUT4 are more realistic than those provided by HadCRUT5. As explained below, the comparisons are complicated by the provision of GMST anomalies for different baselines by various data centers. Finally, our adoption of HadCRUT4 has a great benefit of allowing the uncertainty in all of the quantities found using data from various centers, such as AAWR, ECS, and the probability of achieving certain global warming limits, to now be treated in a consistent manner.

We have added the following text to the supplement beginning on line 66 to explain our use of the HadCRUT4 uncertainties for all of the GMST data records. **Figure S4 shows values of ΔT for the seven individual GMST records (GISTEMP, BEG, HadCRUT4, CW14, HadCRUT5,**

NOAAGT, and JMA) with their corresponding 1σ and 2σ uncertainties. A horizontal line at zero denotes the time period of the baseline for each record. The multi-record mean, excluding the data set that is plotted, is also shown. Since the multi-record mean and individual ΔT record are plotted on the same baseline, the data sets closely match over this time period. Panels (a), (b), (e), and (f) illustrate that the uncertainties for these GMST records are not large enough to encompass the multi-record mean over 1850-2019. The multi-record mean in panel (a) is below the GISTEMP 1σ uncertainty range between 1880 and 1900, and again between 1980 to 2019. In panel (b), the multi-record mean is above the BEG 1σ range from 1850 until 1865, 1880 to 1895, and below the 1σ uncertainty range from 2000 to 2019. The multi-record mean in panel (e) is below the HadCRUT5 1σ uncertainty range from 1990 until 2019. In panel (f), the multi-record mean is above the NOAAGT 1σ uncertainty range from 1920 until 1955. The JMA GMST record does not provide an uncertainty estimate. We therefore use the HadCRUT4 uncertainty estimate for JMA in panel (g). The multi-record mean lies at the edge of the 1σ uncertainty range from 1891 until 2000. After 2000, the multi-record mean falls above the 1σ and 2σ HadCRUT4 uncertainty range. The HadCRUT4 uncertainty time series shown in panel (c) is the only uncertainty estimate large enough to cover the spread in the various GMST records.

Figure S5 shows ΔT based on all seven GMST records and the multi-record mean relative to three baseline periods. The 1σ and 2σ uncertainties from HadCRUT4 are plotted about the multi-record mean. Panels (a) and (d) show the GMST records relative to 1891-1920, which are the first 30 years all of the data sets have in common. Between 1850-1970, all of the data sets fall within the 1σ uncertainty. After 1970, the GMST records start to deviate and some fall outside of the 1σ uncertainty and remain within the 2σ uncertainty, except for JMA which falls outside of the 2σ uncertainty. Panels (b) and (e) show the GMST records relative to the HadCRUT baseline period of 1961-1990. We see similar behavior as in panels (a) and (d), where the GMST records largely fall within the 1σ uncertainty until about 1970. Panels (c) and (f) show the GMST records forced to match HadCRUT5 from 2010-2019, which is baselined to 1961-1990. In these two panels, we see a large spread between the GMST records from the beginning of the time period until 2005.

Table S1 shows the percentage of ΔT annual values since 1940 from all seven data records that lie within the 1σ and 2σ of the multi-record mean, found using the HadCRUT4 uncertainties. Year 1940 is used to be consistent with the definition of our χ^2_{RECENT} parameter. Depending on the choice of baseline period, the number of data points within the uncertainty range varies. For a baseline of 1891-1920, 80% of the data points for all seven records are within the 1σ uncertainty and 95% of the data points are within the 2σ limit. For a baseline of 1961-1990, 88% and 93% of data points are within the 1σ and 2σ HadCRUT4 uncertainties, respectively. If the ΔT records are forced to match the average value of the HadCRUT5 data set over the last decade, 72% of the data points are within the 1σ uncertainty and 88% are within the 2σ uncertainty. This analysis shows that depending on which baseline is used, the percentage of points within the 1σ or 2σ uncertainty ranges varies. Overall, these comparisons support the utility of the HadCRUT4 uncertainty for GMST, since the 1σ and 2σ uncertainty ranges capture a percentage of points approximately correct for a pure Gaussian distribution. Therefore, we have adopted the HadCRUT4 uncertainties in GMST for all of the analyses in the main paper. The uncertainties published by other data centers tend to be smaller than the HadCRUT4 uncertainties. Since only the HadCRUT4 uncertainties span the range of values for ΔT from the seven data records in a somewhat realistic fashion, we have decided to use these uncertainties uniformly throughout the analysis.

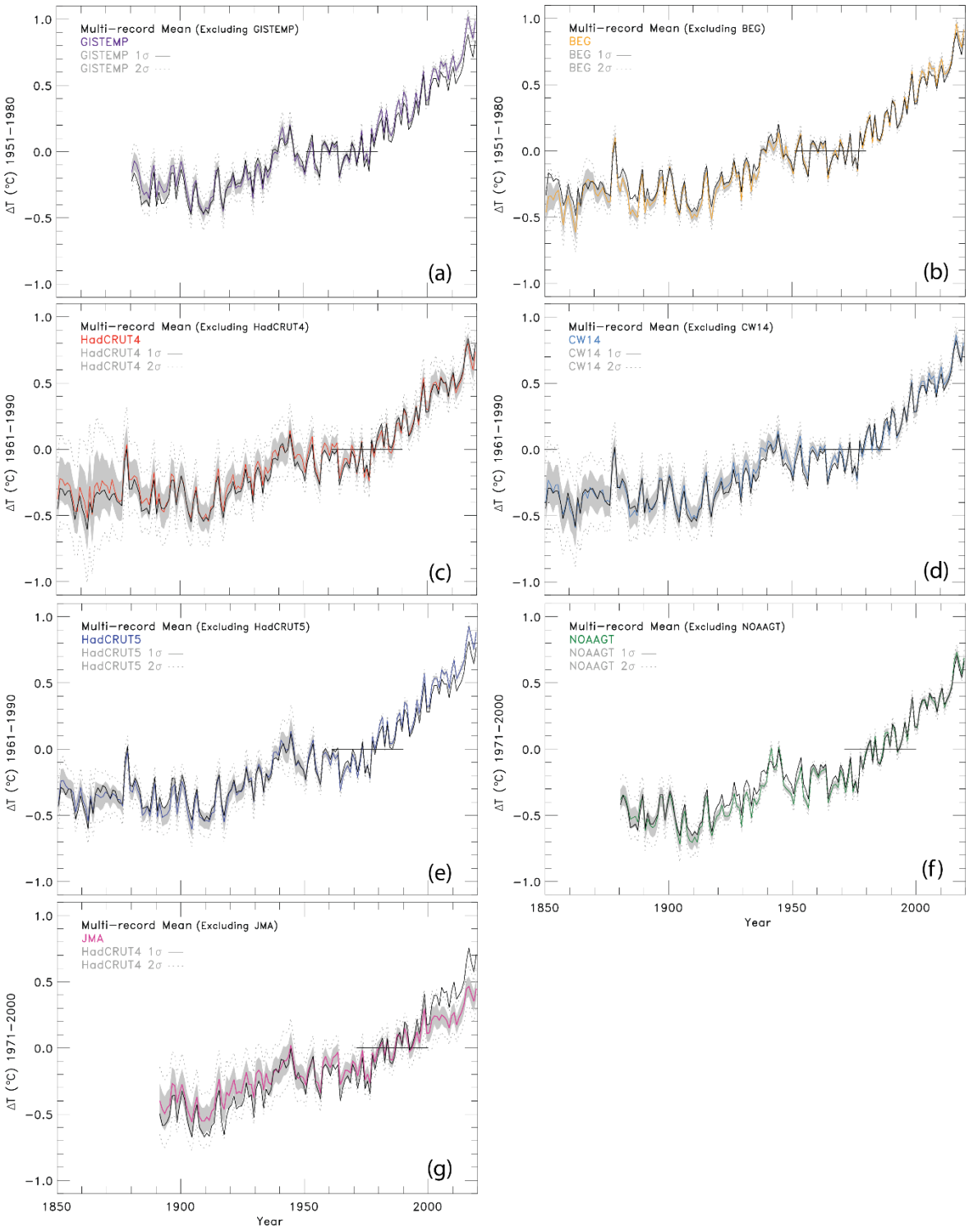

New Figure S4. Annual GMST (ΔT) anomaly for seven data records relative to their individual baseline and the multi-record mean. The multi-record mean does not include the data set that is being shown. The 1σ and 2σ uncertainties for each GMST record are shown, and the horizontal like for ΔT=0 spans the baseline used for the specific panel. (a) GISTEMP. (b) BEG. (c) HadCRUT4. (d) CW14. (e) HadCRUT5. (f) NOAAGT. (g) JMA. Since the JMA data provider does not provide an uncertainty time series, the HadCRUT4 uncertainty is used.

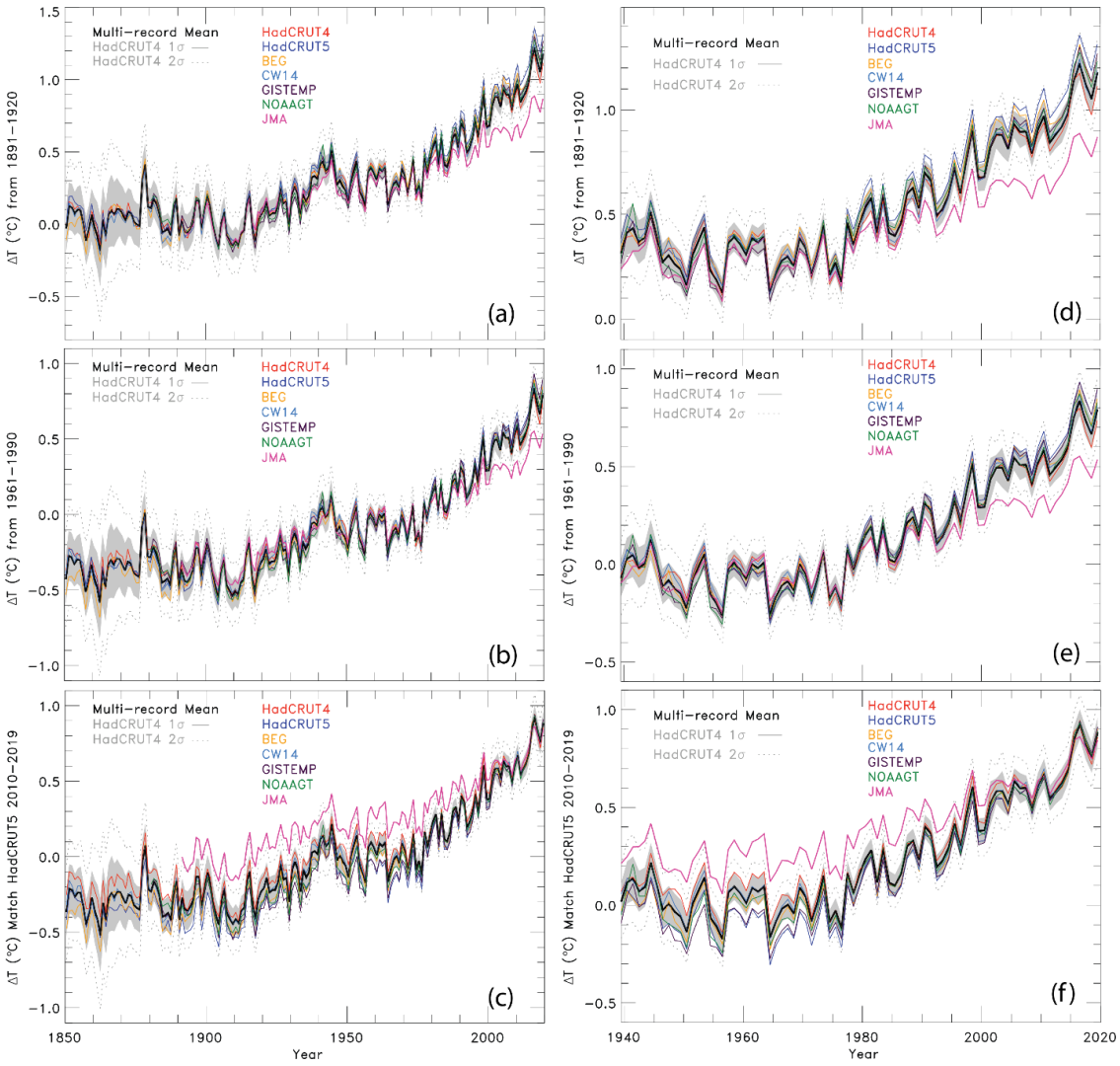

New Figure S5. Annual GMST anomaly relative to several baseline periods for seven data records. The 1σ (shaded grey) and 2σ (dotted grey) HadCRUT4 uncertainties are plotted about the multi-model record mean (black). (a) Baseline of 1891-1920 plotted from 1850-2019. (b) Same as (a) using a baseline of 1961-1990. (c) Same as (a) except all of the ΔT records are forced to match the average ΔT anomaly over 2010-2019 given by HadCRUT5 that is relative to 1961-1990. (d) – (f) Same as (a) – (c) except plotted from 1940-2019.

New Table S1. Percentage of annual values between 1940-2019 of the GMST record within the 1σ or 2σ HadCRUT4 uncertainties about the multi-record mean for each baseline period.

Baseline: 1891-1920	1σ		2σ	
	N_{WITHIN}	N_{TOTAL}	N_{WITHIN}	N_{TOTAL}
HadCRUT4	77 = 96%	80	80 = 100%	80
HadCRUT5	42 = 53%	80	80 = 100%	80
CW14	80 = 100%	80	80 = 100%	80
BEG	71 = 89%	80	80 = 100%	80
GISTEMP	73 = 91%	80	80 = 100%	80
NOAAGT	76 = 95%	80	80 = 100%	80
JMA	29 = 36%	80	54 = 68%	80
AVERAGE	**80%**		**95%**	

Baseline: 1961-1990				
HadCRUT4	80 = 100%	80	80 = 100%	80
HadCRUT5	68 = 85%	80	80 = 100%	80
CW14	80 = 100%	80	80 = 100%	80
BEG	80 = 100%	80	80 = 100%	80
GISTEMP	75 = 94%	80	80 = 100%	80
NOAAGT	80 = 100%	80	80 = 100%	80
JMA	27 = 34%	80	48 = 60%	80
AVERAGE	**88%**		**93%**	
Match 2010-2019				
HadCRUT4	68 = 86%	80	80 = 100%	80
HadCRUT5	47 = 59%	80	86 = 95%	80
CW14	78 = 98%	80	80 = 100%	80
BEG	77 = 96%	80	80 = 100%	80
GISTEMP	47 = 59%	80	79 = 99%	80
NOAAGT	73 = 91%	80	80 = 100%	80
JMA	11 = 14%	80	18 = 23%	80
AVERAGE	**72%**		**88%**	

We have included New Figs. S4, S5, and New Table S1 in the supplement to provide an explanation for why we use the HadCRUT4 uncertainties for all seven GMST data records. We added the following text on lines 270-273 of the main manuscript to direct the reader to the supplement for the explanation for using the HadCRUT4 uncertainties: **We use the uncertainty time series from HadCRUT4 for all GMST records because the HadCRUT4 uncertainty provides a realistic description of the variation in GMST among the seven records (see the supplement, Figs. S4 and S5, and Table S1 for more information).**

2. The authors have developed an application of EM-GC with blended observations, but temperature output of CMIP6 to test whether EM-GC has predictive power for future temperatures. This is not quite what I intended with my comment, but I admit I wasn't clear before. I had hoped the authors would develop a pure model-based test of predictive power. The outcome of the blended result shows that EM-CG often underestimates ECS, but the authors claim in the body of the text that it is a very good predictor.

We thank the reviewer for elaborating on their previous comment. Since our application of using the EM-GC with the CMIP6 multi-model output was not what the reviewer was referring to, we have removed this analysis from the supplement and the corresponding text from the main manuscript, which has made this revised paper shorter than the prior version.

In response to the prior review from the other reviewer, we created a model-based test of predictive power by altering the training period of the GMST to forecast future ΔT. We had, in the prior revision, included Fig. S2 of the supplement to make the point that altering the training period of our model has a small effect on our results

For this revision, we have modified Fig. S2 to show results for training of our model for various periods of time and included New Fig. S3 to address the reviewer's suggestion that we "develop a pure model-based test of predictive power". Both figures are included below, for convenience.

We project relatively similar results for end of century warming for training periods that start in 1850 and end in either 2009 or 2019. The "shape" of our model parameter space is similar for training periods ending in 1999, 2009, or 2019. The training period that ends in 1989 (Fig. S2a) yields a different "shape" of model parameter space for which good fits to the climate record can be obtained, compared to the other training periods. The different shape for this shorter training period is due to the formulation of the ocean component of our model. In training to 1989, we are only considering 35 years of the observed OHC record. We are able to calculate good fits to the OHC record over this shorter time period that diverge from the OHC record after 1989. Also, for this shorter time period, aerosol radiative forcing of climate cools in a manner that nearly mirrors the warming due to rising GHGs, resulting in a wider range of model parameters that lead to a "good fit" of the climate record, compared to model simulations constrained by data that extend closer to present-day. The highest values of ΔT_{2100} in Fig. S2a are associated with the largest values of λ_{Σ}, which in our model corresponds to excessively high values of κ that we can rule out, based on OHC data collected during 1990 to 2019.

We added New Fig. S3 and the following text on lines 41-52 of the supplement to illustrate the predictive power of the EM-GC: **Figure S3 shows the observed (HadCRUT5) and modeled ΔT anomaly from 1945-2060 for the four different training periods described above. Each panel contains three projections of future ΔT for SSP4-3.4: projection using the value of climate feedback that provides the best fit to the historical climate record for a value of AER RF_{2011} = −0.9 W m^{-2}, the lowest value of climate feedback that provides a good fit to the observed ΔT record for a value of AER RF_{2011} = −0.1 W m^{-2}, and the highest value of climate feedback that provides a good fit to the historical climate record (the associated value of AER RF_{2011} varies depending on the training period). As more years are added to the training period, the range of projection for future temperature decreases (Fig. S3a vs S3d). All of the best fit projections (solid line) and highest value of climate feedback (upper dashed line) closely follow the mid-point of the data, regardless of the training period. Given the nature of this test (i.e., predicting GMST out to 2019 for a series of trainings that stop in either 1989, 1999, or 2009), Figure S3 supports the quantitative accuracy of our approach for simulating and projecting future ΔT.**

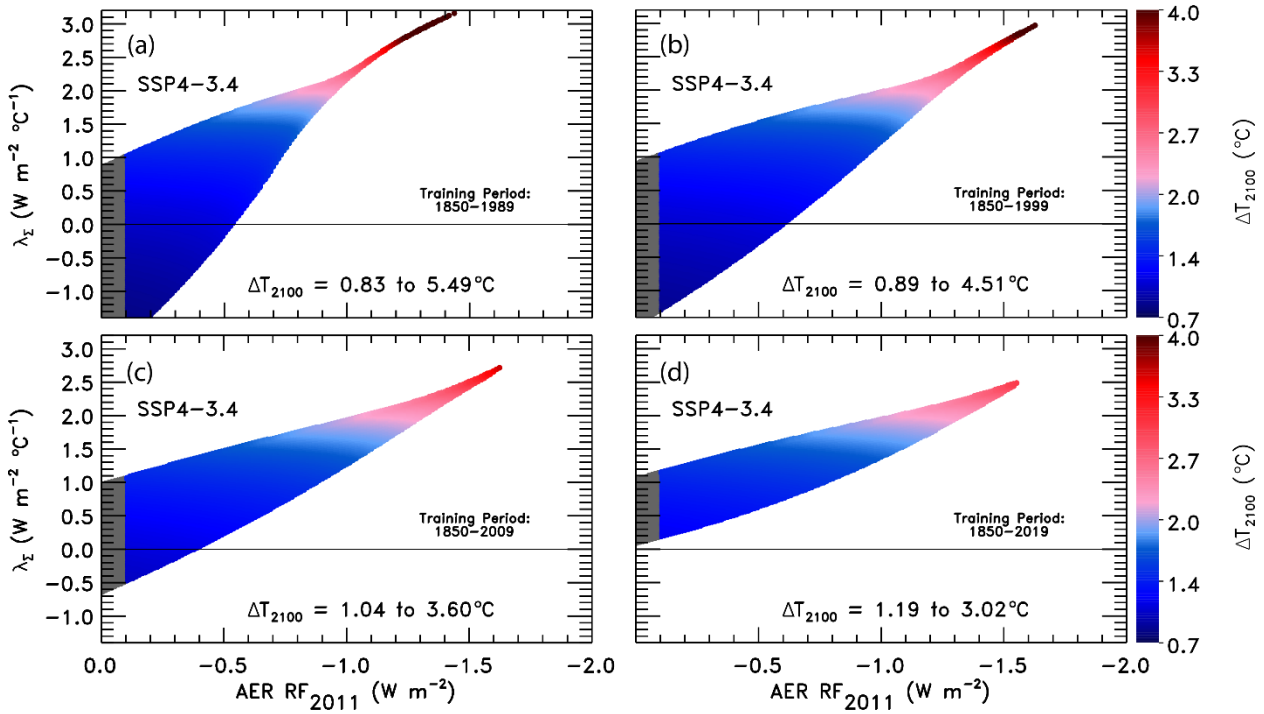

Figure S2. ΔT_{2100} as a function of climate feedback parameter and tropospheric aerosol radiative forcing in 2011 using the EM-GC trained with the HadCRUT5 ΔT record for SSP4-3.4. (a) Training period of 1850-1989. The region outside of the AER RF_{2011} range provided by IPCC 2013 is shaded (grey). Colors denote the GMST change in year 2100 relative to pre-industrial. The color bar is the same across all four panels for comparison. (b) Training period of 1850-1999. (c) Training period of 1850-2009. (d) Training period of 1850-2019, which is the normal training period used in our analysis.

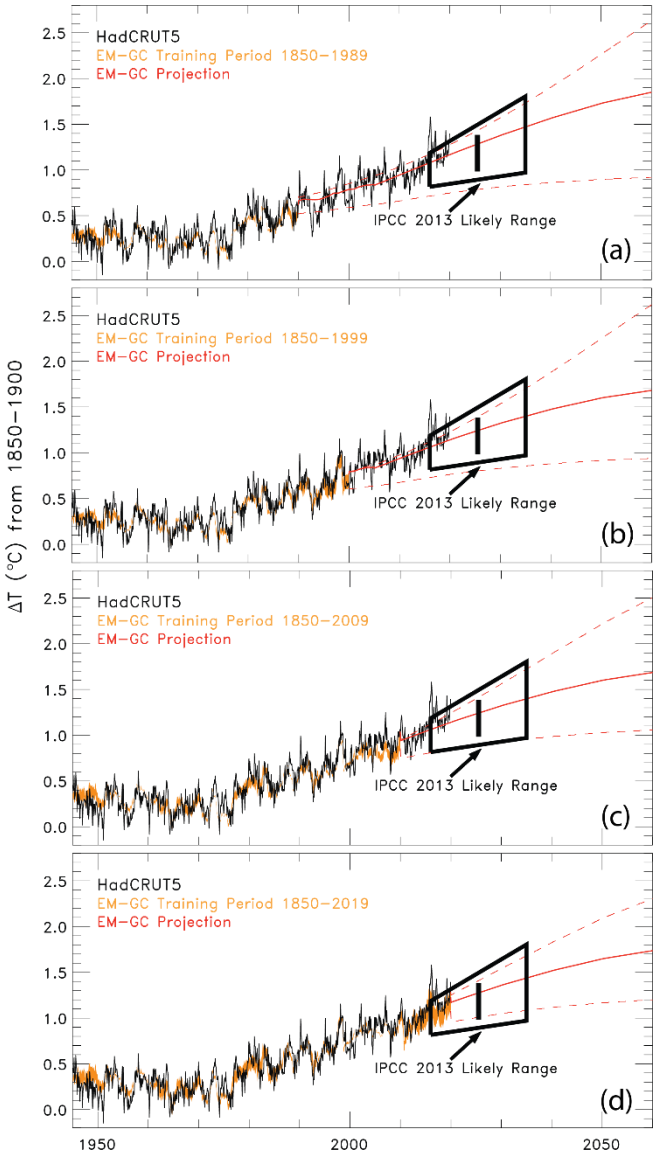

New Figure S3. Observed and modeled GMST anomaly relative to 1850-1900 from 1945-2060 for four training periods. (a) Observations from HadCRUT5 (black), the EM-GC GMST anomaly simulation for a training period of 1850-1989 (orange) of HadCRUT5, and the EM-GC projections for SSP4-3.4 out to 2060. Three EM-GC projections are shown in red: The best estimate of climate feedback for AER $RF_{2011} = -0.9$ W m^{-2}, the lowest value of climate feedback that satisfies the χ^2 constraints for AER $RF_{2011} = -0.1$ W m^{-2}, and the highest value of climate feedback that satisfies the χ^2 constraints (value of AER RF_{2011} varies depending on training period). The IPCC 2013 likely range of warming is denoted as the black trapezoid. (b) Training period of 1850-1999. (c) Training period of 1850-2009. (d) Training period of 1850-2019.

3. The authors now examine a time-varying feedback parameter, which varies with radiative forcing. They do not give justification for why they integrate a time-varying feedback like that. Global feedback is thought to change because of cloud feedbacks above a slow- changing ocean. A delay of a couple of decades between radiative forcing and the change of feedback is therefore expected. Disregarding the physics lead to a biased outcome, as the model is trying to fit the rise in the feedbacks too early, and it is only natural that would fail. Scaling with RF would mean that there is barely any feedback in the first half of the twentieth century, which is also unphysical.

Different formulations for time-varying global feedback exist for simple models, such as (Armour et al., 2013; Geoffroy et al., 2013; Goodwin, 2018). All of these formulations have in common that the feedback only changes some time after radiative forcing, with different lags. I think the Goodwin approach is most suitable for adjustment into EM-GC. Goodwin, also using a data-driven model, shows that the upper range of climate sensitivity is extremely sensitive to the time-scale. I further believe that getting an optimal global constant by fitting, and then adjusting the model to include time-varying feedbacks will tend to favour the former. Ideally, the fitting is done simultaneously.

We thank the reviewer for this suggestion on how to improve our analysis of a time-varying climate feedback. We examined the Goodwin (2018) study as suggested. In the Goodwin (2018) analysis, he separated the radiative forcing due to greenhouse gases into several terms, such as the radiative forcing due to CO_2, CH_4, and N_2O. Goodwin (2018) also partitioned the climate feedback into several terms based on the length of time it would take for the various feedbacks to respond to a change in radiative forcing.

We have applied the idea from Goodwin (2018) that there is a delay in the response of the climate feedback due to a change in radiative forcing within our model framework. In the revised paper, we now incorporate a 20-year delay between the change in radiative forcing and our new calculation of the time variant lambda time series. We chose the 20-year delay because this delay is included in Table 1 of Goodwin (2018) as an estimate of the adjustment timescale between a change in radiative forcing and the cloud-spatial SST adjustment feedback. This feedback is the longest delay between the radiative forcing and climate feedback. The other forms of climate feedback such as water and lapse rate, fast cloud feedback, and snow and sea ice albedo feedback occur with response delays of several days to several months (Goodwin, 2018).

New Figure 14 shows the change in observed and modeled GMST under four assumptions regarding λ^{-1}. First, the value of λ^{-1} is constant over time (New Figs. 14a, e). Second, the value of λ^{-1} varies by 50% between 1850-2100 (New Figs. 14b, f). The third assumption involves λ^{-1} varying over time while χ^2_{RECENT} is always less than or equal to two (New Figs 14c, g). Fourth, λ^{-1} varies over time while χ^2_{ATM} is always less than or equal to two (New Figs. 14d, h). The 20-year delay results in better fits to the observed change in GMST for a 50% increase in lambda (New Fig. 14b) than if the instantaneous response is used (New Fig. S23b). The 20-year delay allows larger variations in lambda over time that still lie below our reduced chi squared constraints (New Fig. 14c, d versus New Fig. 23 c, d). If there truly is time varying climate feedback that responds to a change in radiative forcing with a 20-year delay, then our projections of future GMST may increase up to 1.5°C above the estimates obtained assuming time invariant feedback. If climate feedback varies with a 20-year delay due to the change in radiative forcing and rises over time as suggested by some of the CMIP6 (Rugenstein et al., 2020) and CMIP5 GCMs (Marvel et al., 2018), our projections of global warming would be a few tenths of a degree warmer than our current best estimate, as indicated by the difference between the red line and black circle in 2100 for New Fig. 14b. If we changed the 20 year delay to the shorter delays used in Goodwin (2018), than our results would be between those from the instantaneous response of climate feedback to a change in RF to the 20-year delay in response of climate feedback to a change in RF.

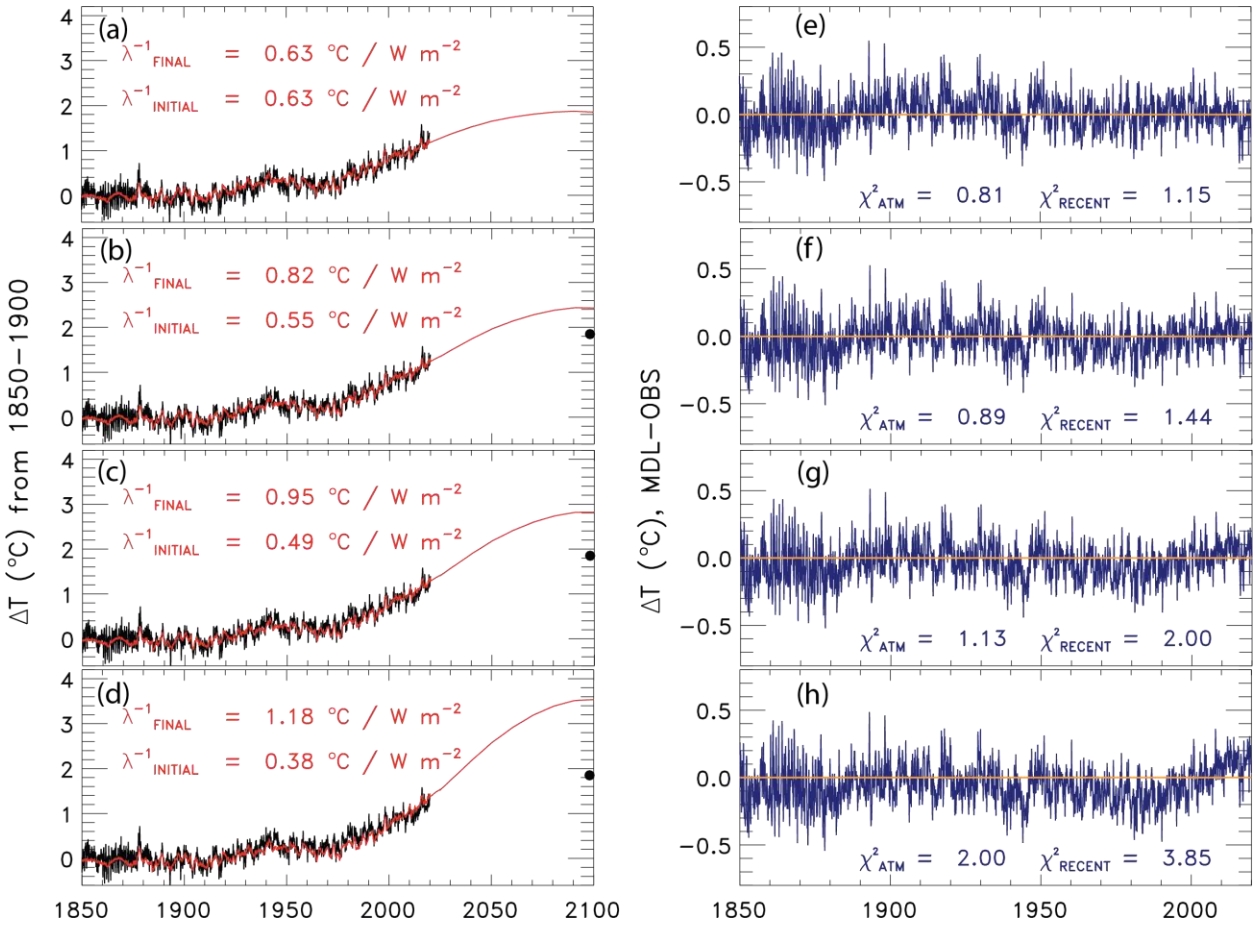

New Figure 14. Change in GMST from 1850-1900 for observations from HadCRUT5 (black) and 1850-2100 for modeled (red) using SSP4-3.4 and the residual between modeled and observations incorporating a 20 year delay between λ^{-1} and a change in RF. The black circles denote the amount of warming when λ^{-1} is time invariant. (a) Rise in GMST assuming a constant value of λ^{-1}. (b) Rise in GMST allowing λ^{-1} to increase by 50%. (c) Rise in GMST allowing λ^{-1} to vary while the value of χ^2_{RECENT} is kept below 2. (d) Rise in GMST allowing λ^{-1} to vary while the value of χ^2_{ATM} is kept below 2. (e) Residual between modeled and observed rise in GMST from 1850-2019 for constant λ^{-1}. (f) Same as (e) but for increasing λ^{-1} by 50%. (g) Same as (f) but for varying λ^{-1} while the value of χ^2_{RECENT} is kept below 2. (h) same as (g) but for varying λ^{-1} while the value of χ^2_{ATM} is kept below 2.

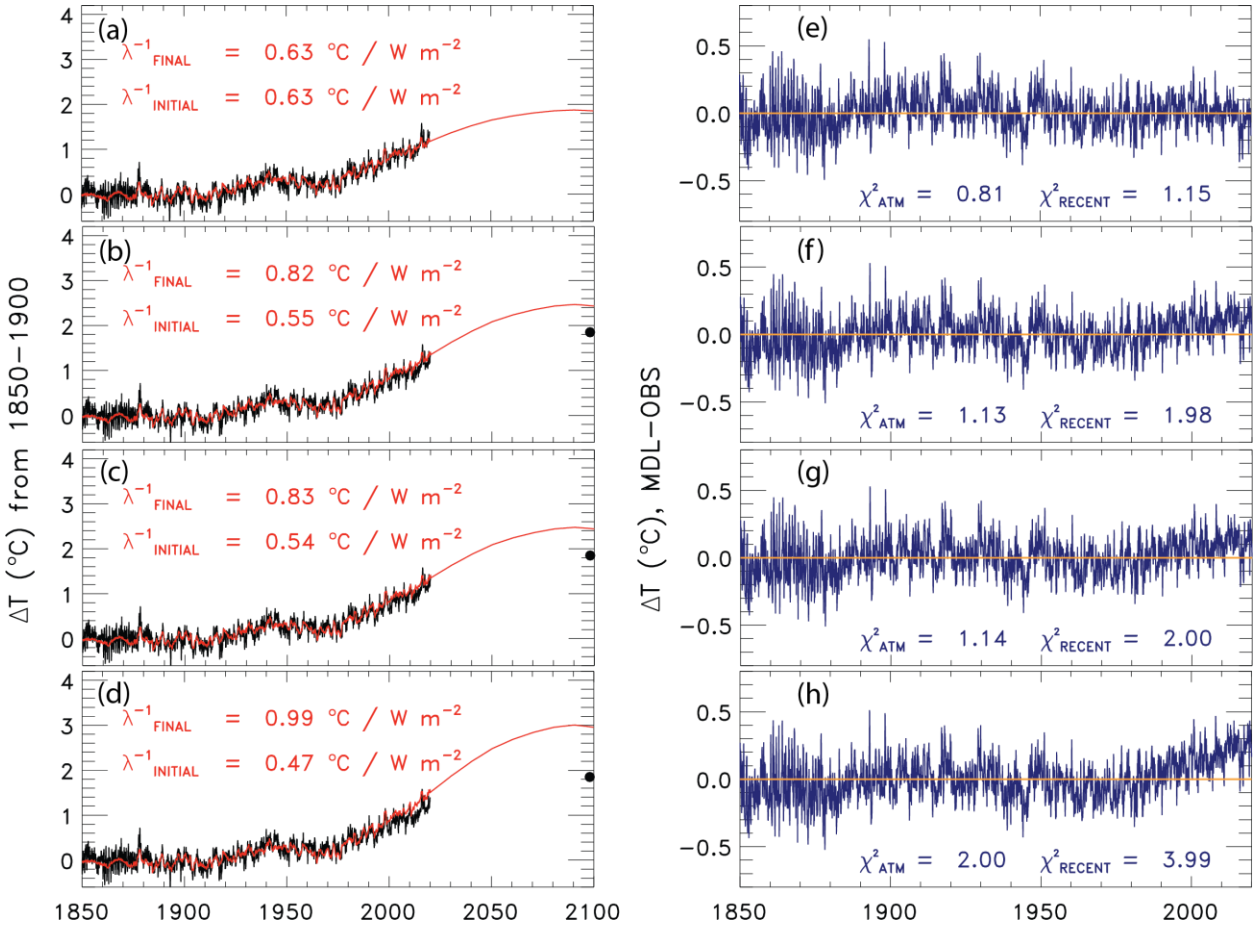

New Figure S23. Change in ΔT from 1850-2019 for observations from HadCRUT5 (black) and 1850-2100 for modeled (red) using SSP4-3.4 and the residual between modeled and observations using an instantaneous time variant λ^{-1}. (a) Rise in GMST assuming a constant value of λ^{-1}. (b) Rise in GMST allowing λ^{-1} to increase by 50%. (c) Rise in GMST allowing λ^{-1} to vary while the value of χ^2_{RECENT} is kept below 2. (d) Rise in GMST allowing λ^{-1} to vary while the value of χ^2_{ATM} is kept below 2. (e) Residual between modeled and observed rise in GMST from 1850-2019 for constant λ^{-1}. (f) Same as (e) but for increasing λ^{-1} by 50%. (g) Same as (f) but for varying λ^{-1} while the value of χ^2_{RECENT} is kept below 2. (h) same as (g)but for varying λ^{-1} while the value of χ^2_{ATM} is kept below 2.

We have updated Fig. 14 in our revised manuscript to include the 20-year delay between the change in radiative forcing and the time varying climate feedback. We added the following text starting at line 1160 to the main manuscript to explain our new method: **In all cases for time varying feedback, we also assume the value of λ^{-1} has the same shape as the SSP4-3.4 RF time series along with a lag of 20 years and that the new time series for λ^{-1} maintains an average value over the observational record identical to the constant value for λ^{-1} of 0.63 °C / W m^{-2}. We chose a lag of 20 years to represent the longest delay in response of climate feedback to a change in RF suggested by Goodwin (2018). If we use the shorter delays represented in Goodwin (2018), then our results would be between those from the instantaneous response of climate feedback to a change in RF (Fig. S23) and the 20-year delay. Finally, in the simulations described below, the value of λ^{-1} is assumed to continue to rise into the future at the same proportionality to $\Delta T_{ATM,HUMAN}$ as the prior increase.**

We included New Fig. S23 to show how our results differ if we use an instantaneous response of λ^{-1} to the change in RF.

4. I don't see how the authors determined the uncertainty around the carbon cycle. I cannot find a mention of 10% of Friedlingstein (which concluded that emission-driven simulations warm a tad more than concentration-driven simulations in CMIP5). Ten percent seems low, but this is not my expertise.

Thank you for this comment and alerting us that we need to better describe the uncertainty around the carbon cycle. The uncertainty we consider for our estimates of transient climate response to cumulative emissions (TCRE) is much larger than 10%. The largest variation in our estimates of TCRE is driven by the uncertainty in AER RF. This uncertainty is incorporated into the probability of achieving the Paris Agreement target and upper limit through the aerosol weighting method. New Figure S21 shows the rise in ΔT from pre-industrial for SSP5-8.5 versus the cumulative emissions of CO_2, in Gt C, since 1870. The colored lines denote the probability of reaching at least that temperature by the end of century. The large spread in projections of future ΔT is driven by the uncertainty in AER RF. The computed probabilities are based on the aerosol weighting method, so the uncertainty in AER RF is considered when determining the likelihood of achieving the Paris Agreement target of 1.5°C and upper limit of 2.0°C.

We also incorporate the uncertainty in how atmospheric CO_2 will respond to the prescribed carbon emissions, for the overall uncertainty of TCRE. We examined Fig. 2 and Table 3 (both included below) from Friedlingstein et al. 2014 and determined that the multi-model average of CO_2 concentrations in 2100 from emission driven runs of CMIP5 coupled carbon cycle models was 985 ppm with a standard deviation of 97 ppm, which is about 10% of the average. We used this 10% value to represent the 1σ uncertainty in the response of atmospheric CO_2 to prescribed carbon emissions, which is a component of the overall uncertainty in TCRE. We also examined Fig. 9b from Murphy et al., 2014 (below) to calculate an estimate in the uncertainty of emissions driven runs of the coupled carbon climate models from CMIP5. We also estimated an uncertainty of about 10%.

Finally, based on our desire to be sure 10% was realistic for this portion of the overall uncertainty in TCRE, we examined the very highly cited, albeit older study by Friedlingstein et al. 2006. Their Figure 1a (below) shows the rise in atmospheric CO_2 over time simulated by 11 coupled atmospheric / carbon cycle models. The mean estimate of atmospheric CO_2 in 2100 determined by reading values from the figure is 850 ppm with a 1σ sigma uncertainty of 89 ppm. Consequently, we again find a value close to 10%. Even though an uncertainty of 10% may seem low, this numerical value has been determined by three independent studies.

The 10% uncertainty is included in our determination of the carbon budgets for each probability of achieving the Paris Agreement target and upper limit. We have updated the main text of the manuscript and the supplement to better describe the uncertainties in the carbon cycle within the EM-GC framework. We have updated the following text on lines 1047-1049 of the main manuscript to better describe the uncertainties in the carbon cycle within the EM-GC framework: **The largest variation in our carbon budget estimates is driven by the uncertainty in AER RF, which is incorporated into the probability of achieving the Paris Agreement target and upper limit (see Fig. S21 and the supplement).**

We have added the following text beginning on line 277 of the supplement to further explain the uncertainties in our carbon budget estimates: **Figure S21 shows the rise in ΔT from pre-industrial for SSP5-8.5 versus the cumulative emissions of CO_2, in Gt C, since 1870. The colored lines denote the probability of reaching at least that temperature by the end of century. The large spread in projections of future ΔT is driven by the uncertainty in AER RF. The computed probabilities are based on the aerosol weighting method, so the uncertainty in AER RF is considered when determining the likelihood of achieving the Paris Agreement target of 1.5°C and upper limit of 2.0°C for the cumulative carbon emissions.**

We use the uncertainty suggested by coupled atmospheric / carbon cycle models in how atmospheric CO_2 will respond to the prescribed carbon emissions. Examination of Fig. 2 and Table 3 from Friedlingstein et al. (2014) and Fig. 9b from Murphy et al. (2014) led to our determination that the uncertainty in estimates of atmospheric CO_2 from emissions driven runs of CMIP5 coupled atmospheric / carbon cycle models is about 10% (1σ). We include this 10% uncertainty in our determination of the carbon budgets for each probability of achieving the Paris Agreement target and upper limit shown in Table 2.

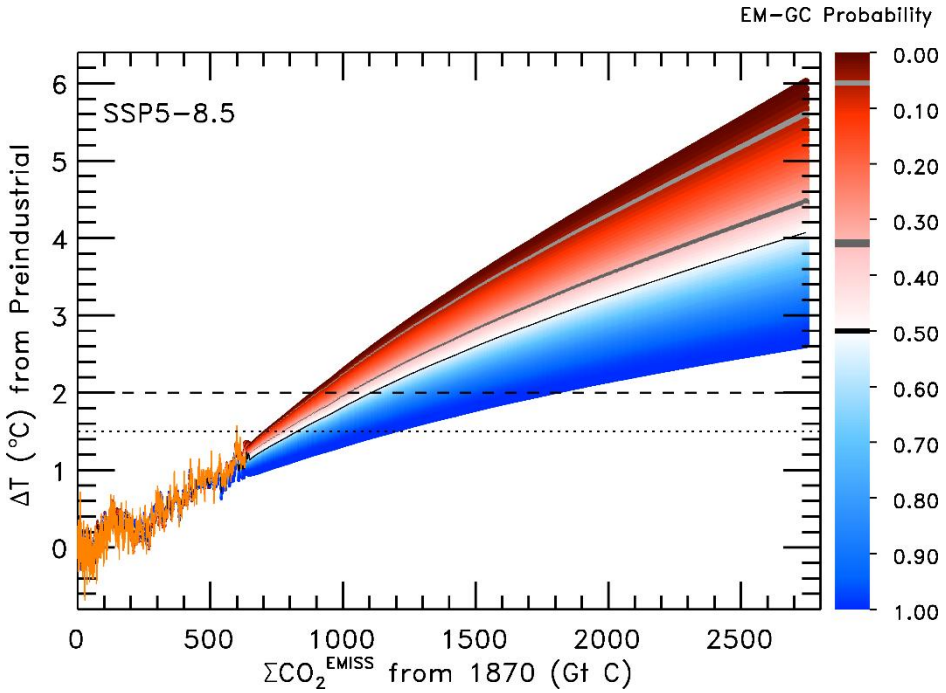

New Figure S21. Transient climate response to cumulative CO_2 emissions for SSP5-8.5 using the EM-GC. Simulations of the rise in ΔT versus cumulative CO_2 emissions in units of Gt C. The orange line is observations of ΔT from HadCRUT5 plotted against cumulative carbon emissions from the Global Carbon Budget project (Friedlingstein et al., 2019). The dotted and dashed lines denote the Paris Agreement target and upper limit, respectively. The EM-GC projections represent the probability that the future value of ΔT will rise to the indicated level, considering only acceptable fits to the climate record. The probabilities were determined using the aerosol weighting method. The light grey, dark grey, and black curves denote the 95, 66, and 50% probabilities of either the Paris target (intersection of dotted horizontal lines) or upper limit (intersection of dashed lines with curves) being achieved.

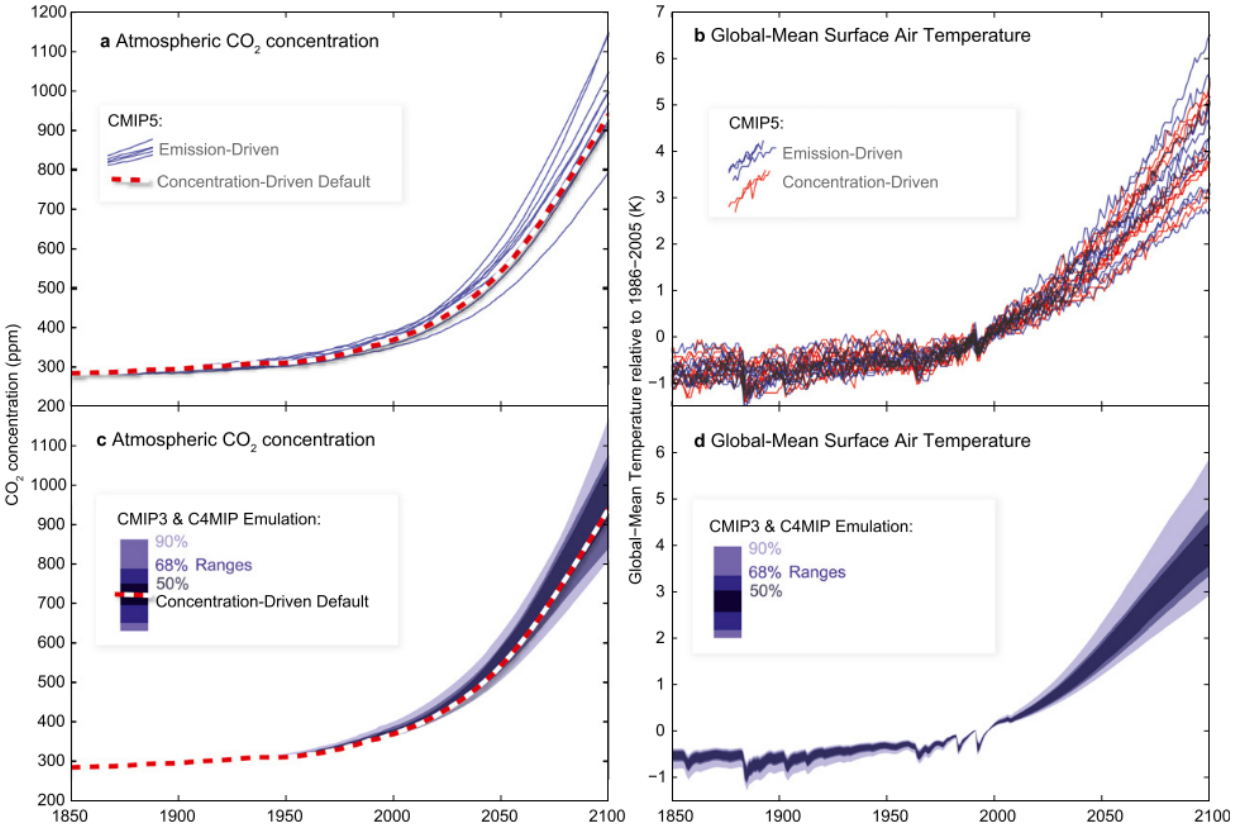

FIG. 2. Range of (a) simulated atmospheric CO_2 (ppm) and (b) global surface temperature change (K) from the 11 ESMs E-driven (blue lines) and C-driven (red lines) simulations. Also shown is the full range of (c) simulated atmospheric CO_2 (ppm) and (d) global surface temperature change (K) simulated by MAGICC6 when emulating all 19 CMIP3 climate models and 10 C^{4}MIP climate–carbon cycle models. The red-line curve in (a) and (c) is the baseline estimate from MAGICC6.

TABLE 3. Twenty-first-century atmospheric CO_2 (2100), global surface warming (2081–99 relative to 1986–2005), cumulative land and ocean uptake (1850–2100) for the E-driven simulations and global surface warming (2081–99 relative to 1986–2005) for the C-driven simulations (where atmospheric CO_2 reaches 941 ppm by 2100). Also shown are the multimodel mean and range (1σ) as well as the same quantities simulated by MAGICC6 in its reference setting.

	E-driven CO_2 (ppm)	E-driven delta T (°C)	E-driven cumulative land C uptake (PgC)	E-driven cumulative ocean C uptake (PgC)	C-driven delta T (°C)
CanESM2	1048	5.0	161	455	4.5
GFDL-ESM2G	997	2.9	167	550	2.8
HadGEM2-ES	998	4.3	352	543	4.7
IPSL-CM5A-LR	926	4.5	300	555	4.5
MIROC-ESM	1149	5.6	−165	544	4.7
MPI-ESM-LR	969	3.7	231	412	3.6
CESM1-BGC	1142	4.1	−145	541	3.6
NorESM1-M	934	3.8	−173	649	3.4
BCC-CSM-1*	967	3.5	471*	490	3.3
INM-CM4.0*	914	2.5	201	861	2.6
MRI-ESM1*	794	2.9	758	528	3.3
Models average	985 ± 97	3.9 ± 0.9	91 ± 218**	557 ± 112	3.7 ± 0.7
MAGICC6	941	4.0	204	617	4.0

* F_{Ln} estimated as no simulated LUC carbon flux in these ESMs.

** Multimodel average for land carbon is only based on the eight ESMs simulating F_L. HadGEM2-ES and GFDL-ESM2G simulations start in 1860 and 1861, respectively. Note that BCC-CSM-1 simulations end in 2099; the 2099 − 2098 atmospheric CO_2 difference was used to infer atmospheric CO_2 by 2100.

Murphy et al., 2014

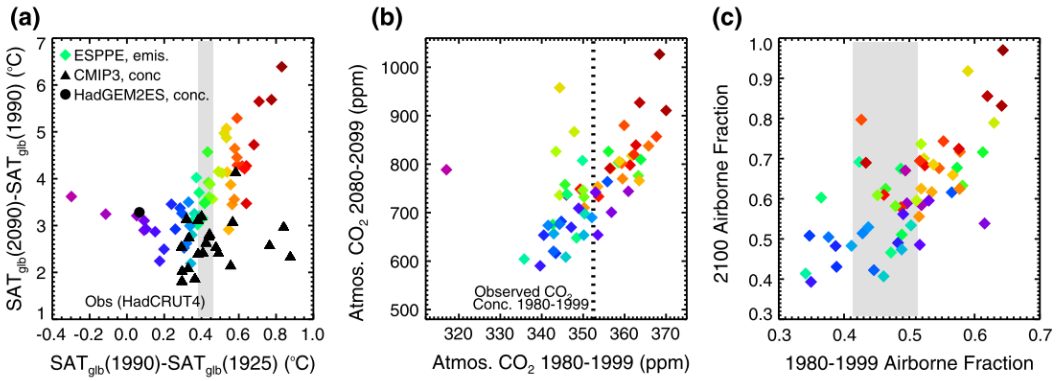

Fig. 9 **a** Future global mean surface air temperature (SAT) changes for 2080–2099 relative to 1980–1999 for members of the ESPPE and CMIP3 ensembles, plotted against corresponding historical changes for 1980–1999 relative to 1900–1949. Future forcing is from the A1B scenario, with CO_2 changes prescribed as emissions in the ESPPE, and atmospheric concentrations in CMIP3. *Grey shading* indicates the range for the median plus or minus two standard deviations of the observed historical change in SAT, obtained using 100 alternative realisations from the HadCRUT4 dataset. ESPPE model variants are colour-coded by simulated historical change in SAT. **b** Average historical and future CO_2 concentrations corresponding to the ESPPE simulations in **a**. The average observed global mean CO_2 concentration for the period 1980–1999 is indicated by the *dotted line* (Masarie and Tans 1995). **c** The average fraction of emitted CO_2 remaining in the atmosphere for the periods 1980–1999 and 2080–2099 for the ESPPE simulations in **a**. *Grey shading* corresponds shows the median plus or minus two standard deviation uncertainty range for average airborne CO_2 fraction for 1980–1999, derived from the observational estimates of Sabine et al. (2004)

Friedlingstein et al., 2006

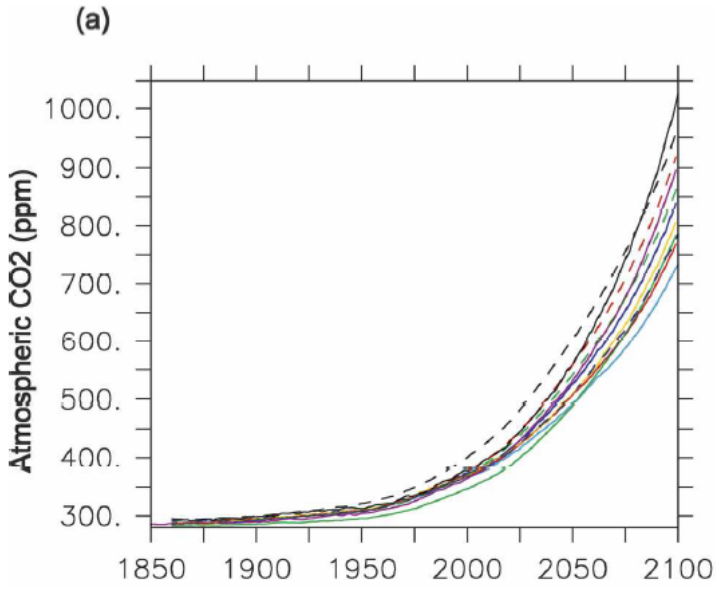

5. The paper is still quite long. In the minor comments I will make another set of suggestions to make the paper easier to understand. This will not be an exhaustive list. There are good guides on the internet for writing concisely, that have helped me become a better writer. For instance: https://writingcenter.gmu.edu/guides/writing-concisely.

We thank the reviewer for pointing us to some guides on writing concisely. We agree that the paper is long and have attempted to shorten the manuscript. We moved the description of the Gregory et al. (2004) method for computing ECS from the CMIP6 GCMs in Sect. 2.4 to the supplement. We added a sentence on lines 593-594 of the supplement: **For the estimate of ECS from the CMIP6**

multi-model ensemble, we use the method described by Gregory et al. (2004) (See the supplement and Fig. 15 for more information).

We removed some of the discussion of Table 1 and Table 2. We also moved Fig. S13 and the description of Fig. 13 to the supplement. In the main paper, we added a sentence on lines 1026-1027 to refer the reader to the supplement for Fig. 13 (which is now Fig. S21): **We use the probabilistic forecasts in Fig. S21 to determine the carbon budgets in Table 2.**

6. The EM-GC model does not model the carbon cycle explicitly, and discussion of the carbon cycle may also be an option to remove. I don't see the value of showing all SSPs in f.i. Figure 9. Consider dropping those with few CMIP6 models.

Discussion of the carbon cycle in lines 987-992 of the previous version of the revised paper (included here for reference) was added upon request by the reviewer: **Examination of (Friedlingstein et al., (2014); and Murphy et al., (2014) led to our determination that the uncertainty in estimates of atmospheric CO2 from emissions driven runs of CMIP5 coupled atmospheric / carbon cycle models is about 10% (1-sigma). We therefore use 10% as the uncertainty in how atmospheric CO2 will respond to the prescribed carbon emissions. We apply the 10% uncertainty estimate to the future remaining carbon budget.**

We have shortened the text and added more information into supplement. We have added the following text on lines 1049-1053 to the main manuscript: **We include a 10% uncertainty, determined from examination of CMIP5 coupled atmospheric / carbon cycle models from Friedlingstein et al. (2014) and Murphy et al. (2014) (see the supplement for more information), within each probability of attaining the Paris goals to represent how atmospheric CO_2 will respond to the prescribed carbon emissions.**

See our response to the previous comment on the information we added to the supplement to address the uncertainties in our carbon budget estimates.

We would like to keep all four panels of Fig. 9, because they illustrate the CMIP6 GMST projections for the four SSP scenarios analyzed in the main part of the manuscript. The multi-model mean, minimum, and maximum displayed in this figure for the four SSPs are shown again in Fig. 11. We would like to retain all panels of Fig. 9 so that the reader can see how we derived the CMIP6 multi-model mean, minimum, and maximum shown in Fig. 11.

Geoffroy, O., Saint-Martin, D., Bellon, G., Voldoire, A., Olivié, D. J. L., & Tytéca, S. (2013). Transient climate response in a two-layer energy-balance model. Part II: Representation of the efficacy of deep-ocean heat uptake and validation for CMIP5 AOGCMs. Journal of Climate, 26(6), 1859–1876. https://doi.org/10.1175/JCLI-D-12-00196.1

Goodwin, P. (2018). On the Time Evolution of Climate Sensitivity and Future Warming. Earth's Future, 6(9), 1336–1348. https://doi.org/10.1029/2018EF000889

Armour, K. C., Bitz, C. M., & Roe, G. H. (2013). Time-Varying Climate Sensitivity from Regional Feedbacks. Journal of Climate, 26(13), 4518–4534. https://doi.org/10.1175/JCLI-D-12-00544.1

Minor comments:

79: Replace ‘to designate future’ with ‘for the’: future and scenarios are redundant

Change made.

101: ‘land-use change’: check hyphens throughout the entire paper

We have ensured all instances of land-use change include a hyphen.

131: remove ‘of climate’

Change made.

132: remove ‘because’, start new sentence at ‘this’

Change made.

142: consider removing ‘Bony et al.’ sentence, I don’t see the use

The sentence has been removed.

150: due to this update, our model is

Change made.

186: which update

We have modified this paragraph based on our update to use HadCRUT5 as the main data set, so the corresponding sentence has been removed.

202-205: long sentence

We have split this sentence into two separate sentences. The new sentences are as follows: **The equation for all three formulations of χ^2 is based on annual averages, rather than monthly time series. We calculate χ^2 with annual values because the autocorrelation functions of ΔT_{OBS} and ΔT_{MDL} display similar shapes using annual averages, and do not match utilizing monthly averages (see supplement of Canty et al. (2013) for further explanation).**

209: ‘that is our primary data source’, maybe replace with: ‘which we use as default’

We have changed the sentence to be: **The average of five OHC data sets, which we use as our primary OHC series, extends from 1955-2017, a total of 63 years.**

220: rung→panel

Change made.

235-237: unnecessary sentence

This sentence does seem unnecessary as written, but it is referring to the dotted black line on Fig. 1e. We have changed the sentence to make it clear what we are referring to. The new sentence is: **Furthermore, the contribution of AMOC to the rise in GMST over 1975-2014 (the same time period used to define AAWR) is also specified on Fig. 1e (dotted black line).**

240: reword: for this simulation, kappa =1.28, W/m^2/C fits the OHC data best

Change made.

242: remove 'the' before 'IOD'

Change made.

243: remove 'temporal variations in'

Change made.

245: slight -> small

Change made.

343: remove 'consequently'

Change made.

347: remove 'multiplicative': factor is by definition multiplicative

Change made.

348: split sentence after '2015'

Change made.

354: remove 'thus'

Change made.

367: remove sentence, already clear

Change made.

379: remove ‘scientific’: what else?

We have removed the words “slight” and “scientific”.

408: consider replacing ‘upon’ with ‘on’ throughout: make it easy for your reviewers and readers to read your text

Change made.

419: consider using the improved HadSST4, which removes biases in the ship measurements.

We will replace HadSST3 with HadSST4 to derive the AMOC time series used in the regression, since we are using HadCRUT5 as our primary data set.

420: remove ‘variations in the strength’?

Change made.

421: I’m not sure whether it’s appropriate to detrend using RF. Temperature lags RF quite a bit, especially in oceans.

Thank you for this inquiry. The Atlantic multidecadal variability (AMV) that we use as a proxy for AMOC is the change in SST between the equator and 60° N. The SSTs represent the upper ocean, or top 100 m. The response of the upper ocean to a change in radiative forcing is almost instantaneous, so a time delay is not needed.

Several studies (Mann and Emanuel, 2006; Ting et al., 2009; Trenberth and Shea, 2006) are critical of using linear detrending to remove the forced trend in the AMV index. This method assumes that the forced trend is linear over time, which may not be correct. Ting et al. (2009) say that the use of the linear detrending method of the AMV index may result in including a global warming signal into the index. All three studies suggest using a detrending method of regressing SST against the AMV index to remove the forced trend over time. We derived an anthropogenic detrending method to remove the influence of anthropogenic activities on SST in the North Atlantic. We achieve similar results if we use the anthropogenic or SST detrending methods (Response Fig. 1) but get different results if we use the linear detrending method.

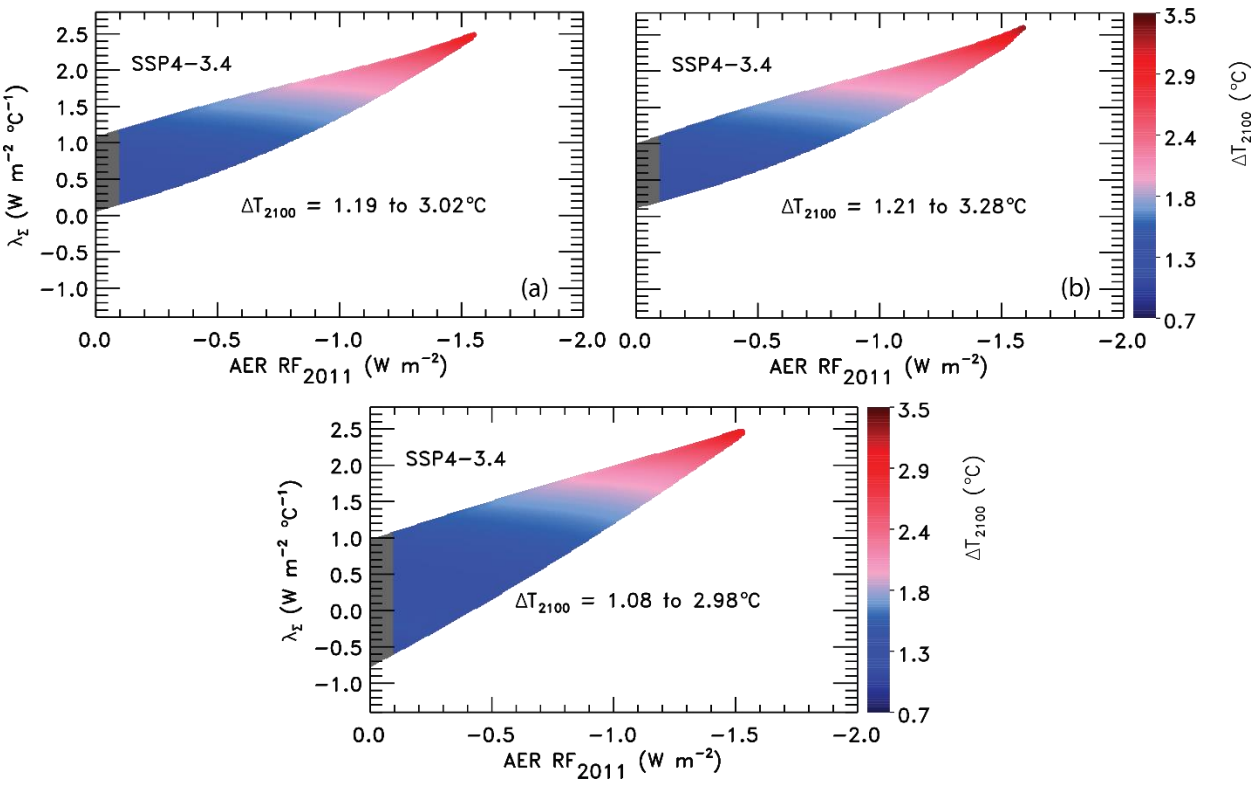

Response Figure 1. GMST anomaly in 2100 from pre-industrial as a function of climate feedback parameter and AER RF_{2011} for SSP4-3.4. (a) AMV index was detrended using the anthropogenic detrending option. (b) AMV index was detrended using the SST detrending method. (c) AMV index was detrended using the linear detrending method.

Response Figure 2 shows that some of the global warming signal is probably being aliased into the AMOC signal when using the linear detrending method. The AMOC contribution of the rise in GMST from 1975-2014 is 0.025°C/decade when using the anthropogenic detrending method but is 0.037°C when using the linear detrending method. The value of AAWR decreases from 0.167 to 0.160°C/decade upon switching from the anthropogenic to linear detrending method.

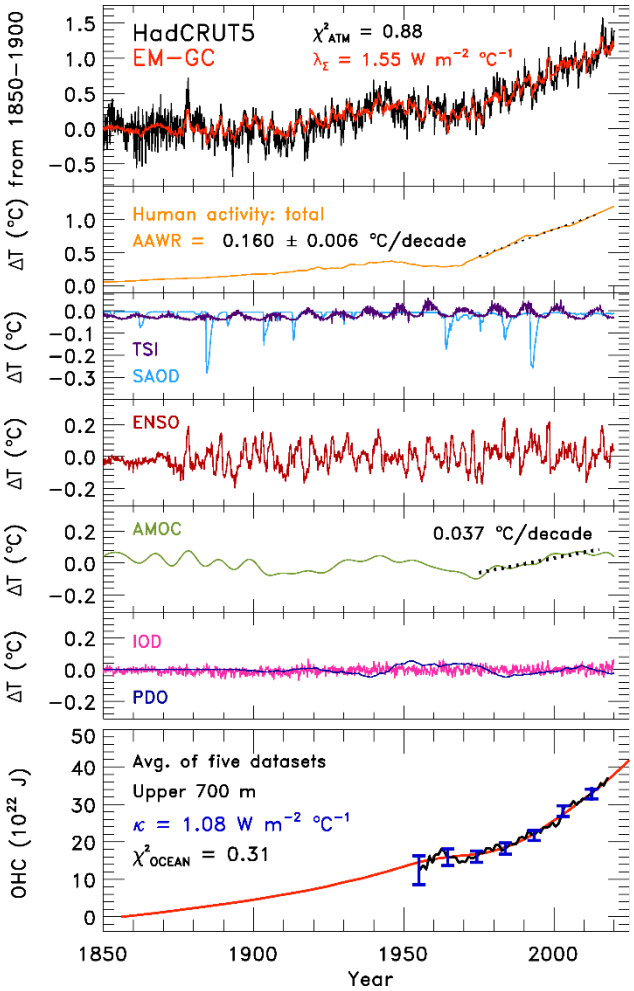

Response Figure 2. Measured and modeled GMST anomaly (ΔT) relative to a pre-industrial (1850-1900) baseline. (a) Observed (black) and modeled (red) ΔT from 1850-2019. (b) Contributions from total human activity. This panel also denotes the best estimate value of the attributable anthropogenic warming rate from 1975-2014 (black dashed) as well as the 2σ uncertainty in the slope for a model run that uses the best estimate of AER RF_{2011} of −0.9 W m^{-2}. (c) TSI (purple) and SAOD (light blue). (d) Influences from ENSO on ΔT. (e) Contributions from AMOC to ΔT and to observed warming from 1975-2014 using the Linear detrending option. (f) Influences from PDO (blue) and IOD (pink) on ΔT. (g) Measured (black) and modeled (red) ocean heat content (OHC) as a function of time for the average of five data sets (see text), the value of χ^2_{OCEAN} for this run, as well as the ocean heat uptake efficiency, κ, needed to provide the best-fit to the OHC record.

433: remove everything between brackets

Change made.

435: surely the numbers are altered. I cannot imagine that the feedback parameter isn't dependent on AMOC in the fit.

Thank you for prompting us to make this sentence clearer. Our major scientific conclusions are not altered if we neglect AMV as a regression variable. As explained in the first author response, our value of λ_Σ only changes slightly when we neglect AMV, IOD, and PDO as regression variables. The value of χ^2_{ATM} substantially increases. The increase in the value of χ^2_{ATM} indicates there will be less combinations of λ_Σ and AER RF_{2011} that provide a good fit to the historical climate record. This

would narrow our range of parameter space (Fig. 10), and slightly change our future temperature projections, AAWR, and ECS. However, we will still arrive at the same conclusions, that the CMIP6 GCMs warm too quickly, and the EM-GC provides more optimistic probabilities of achieving the Paris Agreement target and upper limit.

We have added some clarifying text to this sentence, Sect. 2.3 where we mention the impact of the inclusion of AMV on AAWR, and New Figure S11 to supplement (shown below) to show that AAWR does not change if AMOC is or is not included in the regression. The new text is: **We stress, as explained in Sect. 2.3, none of our major scientific conclusions are altered if we neglect AMV as a regression variable.**

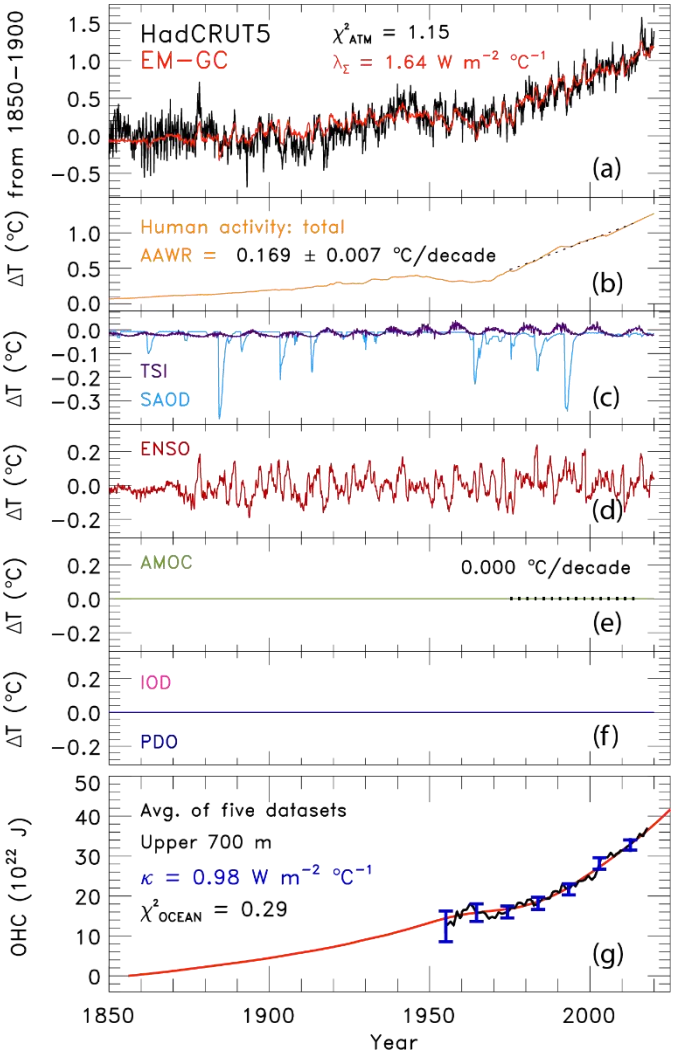

New Figure S11. Measured (HadCRUT5) and modeled GMST anomaly (ΔT) relative to a pre-industrial (1850-1900) baseline without AMOC, PDO, and IOD. (a) Observed (black) and modeled (red) ΔT from 1850-2019. This panel also displays the values of λ_Σ and χ^2_{ATM} (see text) for this best-fit simulation. (b) Contributions from total human activity. This panel also denotes the numerical value of the attributable anthropogenic warming rate from 1975-2014 (black dashed) as well as the 2σ uncertainty in the slope. The estimates of AAWR show similar results if AMOC is or is not included (see Fig. 1). (c) Solar irradiance (light blue) and major volcanoes (purple). (d) Influences from ENSO on ΔT. (e-f) Contributions from AMOC, PDO, and IOD to ΔT are set to zero (g) Measured (black) and modeled (red) ocean

heat content (OHC) as a function of time for the average of five data sets (see text), the value of χ^2_{OCEAN} for this run, as well as the ocean heat uptake efficiency, κ, needed to provide the best-fit to the OHC record. The error bars (blue) denote the uncertainty in OHC used in this analysis (see Sect. 2.2.8).

438: consider using 'use' throughout instead of 'utilising'

Thank you for this suggestion. We have decided to retain both "use" and "utilize" in the manuscript, so the text is not repetitive with "use" repeated multiple times in one sentence.

453: is this old factor still valid?

Thank you for this question. An article posted on climate.gov website published in August of 2020 explains that warming in the ocean below 700 m accounted for 30% of the total increase in OHC from 1971 – 2010 (https://www.climate.gov/news-features/understanding-climate/climate-change-ocean-heat-content). This estimate of 30% is from chapter 3 of IPCC 2013. If the ocean below 700 m accounts for 30% of the heat, then we can infer that the upper 700 m of the ocean holds 70% of the heat. We have verified this estimate ourselves by comparing the OHC in the upper 700 m to the OHC below 700 m from the Cheng et al. (2017) OHC record we use in our analysis. Response Figure 3 shows the change in OHC from 1955-2017 from the Cheng et al. (2017) OHC record for the upper 700 m and above 2000 m. We can divide the OHC in the upper 700 m by the OHC above 2000 m to obtain the ratio between the two time series, and average these values to determine the mean difference between the value of OHC in the upper 700 m and above 2000 m. If we exclude the baseline period (1991-2005) from the calculation, we determine that the ratio is 0.68, indicating the upper 700 m holds about 68% of the heat in the world's oceans. This result supports the assumption of the upper 700 m of the world's oceans holding 70% of the heat in our analysis.

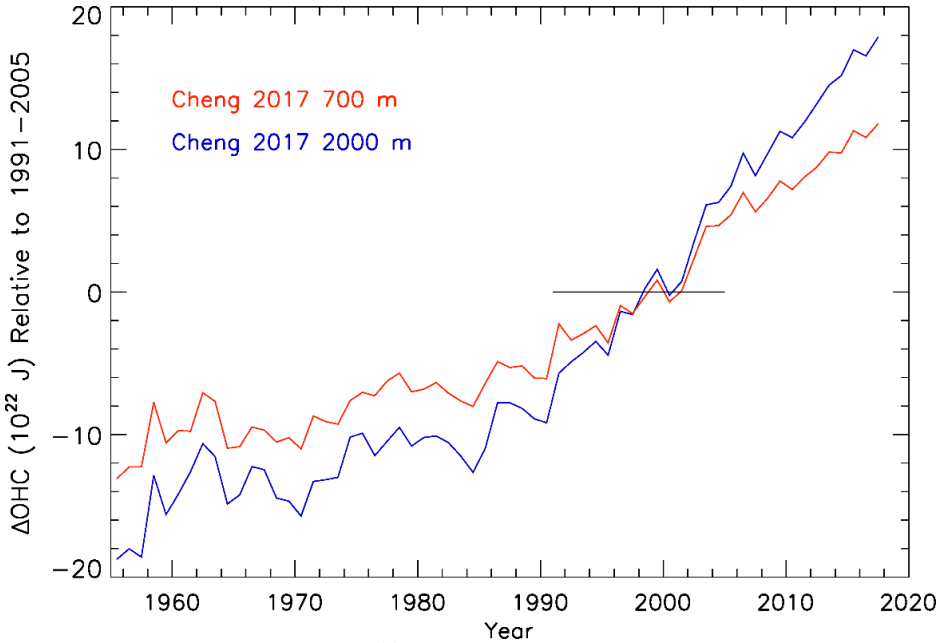

Response Figure 3. Change in OHC (10^{22} J) from 1955-2017 relative to 1991-2005 for the upper 700 m and above 2000 m from Cheng et al. (2017).

455: remove sentence 'since ... whole atmosphere', redundant.

Thank you for this suggestion. We would like to retain this sentence for clarity, to ensure the reader understands our method.

459: remove ‘temporal’

Change made.

481: remove ‘however’

Change made.

505: equal to→of

Thank you for this suggestion. We would like to retain the sentence as currently written to avoid using several instances of the word “of” in one sentence.

510: upon consideration of→by including

Change made.

534: colouring seems to be off in figure S10

We are not exactly sure what the reviewer is referring to here. We have reviewed Fig. S10 and the displayed colors seem fine on our monitors.

539: remove ‘the computation of’

Change made.

552: remove sentence, redundant

Change made.

Section 3.1: move methodology to methodology section 2.2.1 (the bit about blending)

We moved the methodology on the blending effect to Sect. 2.3 where we discuss our method to calculate AAWR.

Figure 8: what interval is plotted for each study?

Thank you for bringing this to our attention. The confidence intervals/percentiles for each of the studies that are plotted are as follows: Lewis and Grunwald 2018 – 5^{th} to 95^{th} percentile, Skeie et al. (2018) – 90% confidence interval, Otto et al. (2013) – 5^{th} to 95^{th} confidence interval, Nijsse et al. (2020) – 5^{th} to 95^{th} % confidence interval, Cox et al. (2018) – 95% confidence limits, Dessler et al. (2018) – minimum and maximum, Armour (2018) – 90% confidence interval, Sherwood et al. (2020) – 5 to 95% confidence intervals, Rugenstein et al. (2020) – minimum and maximum,

Tokarska et al. (2020) – 5th and 95th percentiles, IPCC 2013 – 66% confidence interval, Proistosescu and Huybers (2017) – 5 to 95% confidence interval, and Zelinka et al. (2020) – minimum and maximum. We have decided to include this information in supplement, so the interested reader can find this information without making the main manuscript longer. There is a reference in the Fig. 8 caption to point the reader to the supplement that reads: **See the supplement for the confidence intervals shown for each study.**

772: changed word order, it seems like we're coupling a two-box model to 2.6

Change made.

793: Cox et al. based on CMIP5

Change made.

834: remove 'indicated on each plot', redundant

Change made.

834-835: remove sentence, the reader will know how to do a global average

We would like to maintain this information for anyone trying to reproduce our results. We have moved the sentence to the Fig. 9 caption to help shorten the manuscript.

858: I don't think bimodality is clear here. There seems to be outliers, but not two roughly equal- sized groups of models. With so few models, passing any statistical test on bimodality would be tough. Drop it?

We have replaced "bimodality" with "two groups" so the sentence reads: **Figure 9 illustrates there are two groups of CMIP6 multi-model projections of ΔT, with a few GCMs having future values of ΔT that are considerably higher than others.**

863: remove 'apparent in figure 9', redundant

Change made

918: remove 'our', redundant

Change made: "our" was replaced with "the".

Figure 12: choose bigger bin size: CMIP models displayed weirdly

The bin size in Fig. 12 is consistent between the PDF for the EM-GC and PDF for the CMIP6 GCMs. The CMIP6 PDF looks different from the EM-GC because results are available for only 6 to 33 GCMs depending on the scenario. Conversely, thousands of simulations for the EM-GC allow rigorous sampling of the parameter space.

We prefer to keep the bin size the same between the EM-GC and CMIP6 PDFs. Response Fig. 4 shows the PDF for SSP4-3.4 with a bigger bin size for the CMIP6 GCMs. The bigger bin size looks awkward and makes the figure look like there are only 3 GCMs for SSP4-3.4, whereas there are actually 6.

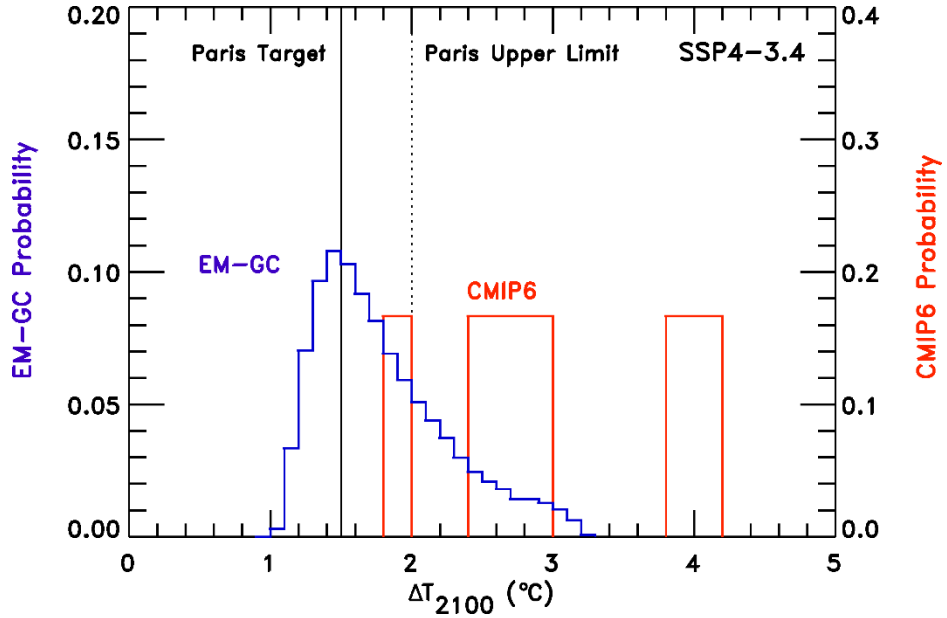

Response Figure 4. Probability density functions (PDF) for ΔT_{2100} found using the EM-GC with the CW14 temperature record (dark blue) and CMIP6 multi-model results (red).

934: three significant digits not justified, two better

Change made.

Table 1: same

Change made.

991-1003: you seem to be repeating the table, making the prose difficult to read, condense to half the size?

We have eliminated some of the discussion of the table, so we are not repeating the same information.

1015: since -> from / from ... onwards

We have changed "since" to "after" so the sentence reads: **Their analysis indicates only 228 Gt C can be released after 2010 to have a 66% probability of achieving the Paris Agreement target of limiting the rise in ΔT below 1.5°C in 2100.**

1023: I don't think either of them studied the entire climate system. Instead, those studies were about the atmosphere.

Upon the changes from switching to HadCRUT5 for our primary GMST data record, this sentence was deleted.

In our revised supplement, Fig. S1 has slightly changed. The figure shows output from the EM-GC that is trained using the HadCRUT4 GMST record but is adjusted to be on the HadCRUT5 pre-industrial baseline, to be consistent with other figures in the manuscript. The new baseline causes the values of ΔT_{2100} shown on the left panel to increase a negligible amount. We fixed a small indexing error in the plotting code used to make Fig. S1, which causes the maximum value of ΔT_{2100} shown on the right panel to decrease slightly.

Reviewer comments are in black, author responses in blue

After a careful reading of the manuscript, I found the authors have addressed most of my comments and questions, and the revised manuscript has been improved. However, there is still one issue that deserves more attention. In the previous review, I asked about the comparison of the AAWRs that are obtained from EM-GC and CMIP6 models. My concern was whether the AAWR from the EM-GC and the AAWR from the CMIP6 can be compared fairly, as the AAWRs were calculated by different methods (For EM-GC, using Eq. (9); For CMIP6 models, using REG method). The authors have revised this part, but if I understand correctly, they compared the AAWR from REG method with the AAWR from LIN method. There is no direct comparison between the REG method and the method used in EM-GC. The confidence in using REG method comes from the "close agreement of AAWR" found using both the REG and the LIN methods, which I find not very convincing. I would suggest that, if possible, the authors may apply the REG method to the EM-GC simulations (Note, do not use the coefficient C1 from Eq. (2). Use the new coefficient obtained from the REG method). Then, compare the AAWR from the REG method and the AAWR calculated from Eq. (9).

> We thank the reviewer for taking the time to read through our changes and are delighted to read that the reviewer finds the manuscript improved.
>
> To address the remaining concern, we applied the REG method to the EM-GC simulations as suggested by the reviewer. We regressed the modeled GMST time series output from the EM-GC against SAOD (after applying a 6-month lag) and a linear function used to represent the anthropogenic effect on temperature from 1975-2014. New Fig. S13 below shows the resulting simulations of ΔT.
>
> The value of AAWR from the EM-GC determined using the REG method is 0.188°C/decade, compared to 0.167°C/decade using Eq. (9) in the main paper (New Fig. S13c and Fig. 1). There is a 0.021°C/decade difference between these two estimates of AAWR. This difference arises because the REG method, when applied to the EM-GC modeled ΔT time series, includes the contribution of AMOC in the value of AAWR (New Fig. S13c). Figure 1 of our paper shows that AMOC contributes about 0.025°C/decade to the rise in ΔT from 1975-2014. If the effect of AMOC is not removed before applying the REG method to the output from the EM-GC, then the influence of AMOC will be erroneously included in the value of AAWR. These results shown on the left hand panels of Fig. S13 are similar to the approach by Foster and Rahmstorf (2011), who included the effect of AMOC by taking the linear fit of a residual. If we include AMOC as a regressor variable to the REG method, we obtain a value of AAWR of 0.161°C/decade (Fig. S13g). This new value of AAWR is within the uncertainty estimate of AAWR using Eq. 9, which is 0.167 ± 0.007°C/decade.
>
> The close agreement of values of AAWR from the REG method once we account for AMOC and that found using Eq. (9) supports the validity of the REG method to determine AAWR from CMIP6 output. We do not explicitly use AMOC as a regressor variable when applying the REG method to CMIP6 GCMs for two reasons. The first

reason is that GCMs have been shown to underestimate key aspects of the Atlantic multidecadal oscillation and are unable to simulate the many oceanic and atmospheric footprints of AMOC (Kavvada et al., (2013). The second reason is that CMIP6 GCM historical runs do not use prescribed SSTs. If the CMIP6 GCMs are representing AMOC, it is a random signal that is averaged out when we analyze the 50 GCMs in order to calculate AAWR.

We have included New Fig. S13 in the supplement and added the following text on lines 541-543 to Sect. 2.3 of the main paper in reference to this figure:

Figure S13 and the supplement compare values of AAWR found using the REG method applied to EM-GC output with values of AAWR found using Eq. (9), as support for the validity of using the REG method to determine AAWR from CMIP6 output.

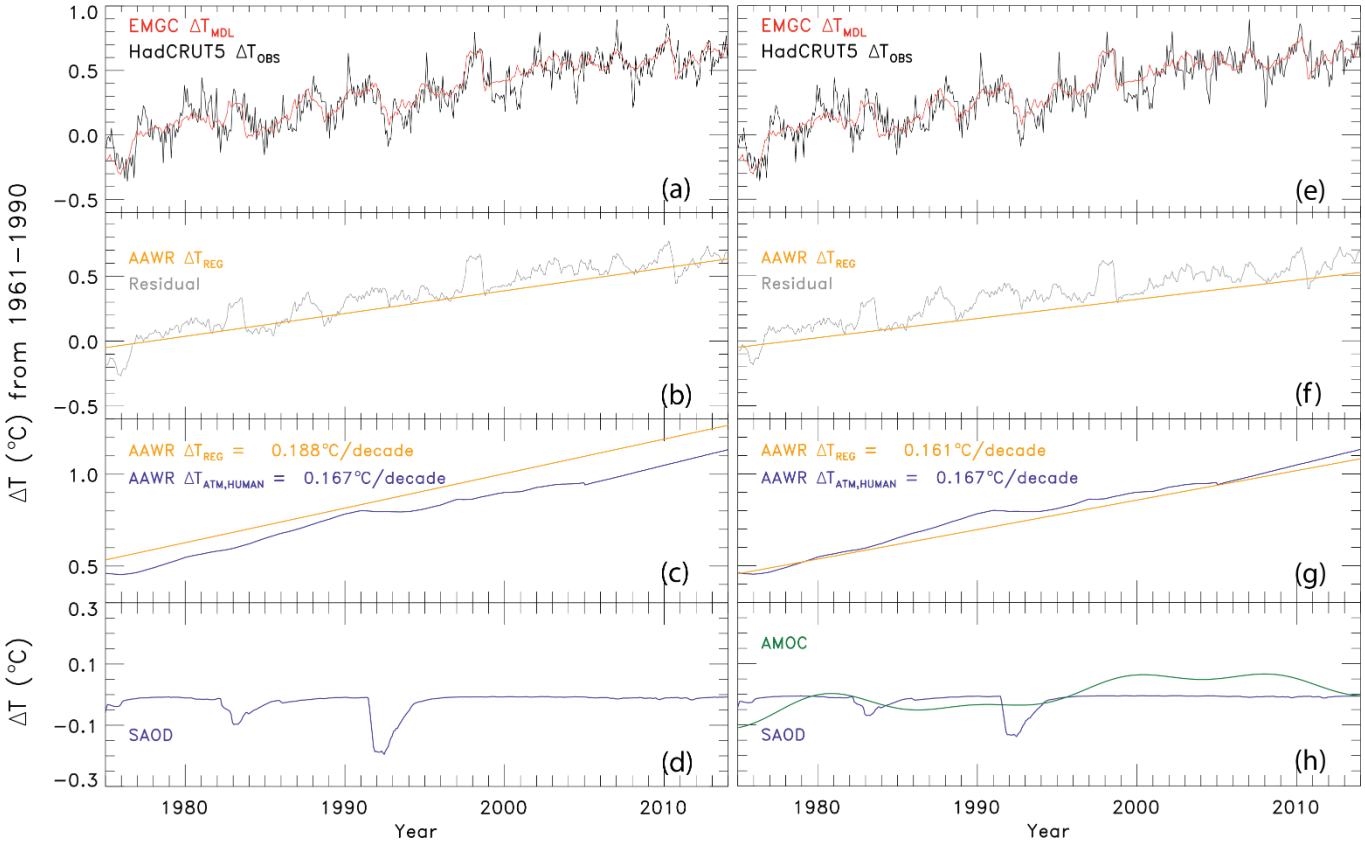

New Figure S13. The change in GMST relative to 1961-1990 from observations and modeled output. (a) Change in GMST from HadCRUT5 and EM-GC simulation. (b) The residual in the change of GMST from the EM-GC simulation after subtracting the contribution of SAOD determined by the REG method (grey) and the change in GMST due to humans from the REG method (orange). (c) The change in GMST due to humans from the REG method (orange) and from the EM-GC (blue). The values of AAWR determined using the REG method and Eq. (9) are shown. (d) The contribution of SAOD to GMST. (e) Same as (a). (f) Same as (b) but also subtracting the contribution of AMOC determined by the REG method. (g) Same as (c) but using AMOC as a regressor variable. (h) Same as (d) and also including the contribution of AMOC to ΔT determined by the REG method.

We have added the following text beginning on line 203 to the supplement to explain our justification of the use of the REG method for the determination of AAWR from the GCMs:

> **We applied the REG method to the EM-GC simulations to check the validity of the REG method. We regressed the modeled ΔT time series from the EM-GC for an AER RF_{2011} = −0.9 W m^{-2} simulation with SAOD and applied a 6 month lag. A linear function is used to represent the anthropogenic effect on temperature from 1975-2014. Fig. S13 shows the results of using the REG method on output of the EM-GC.**
>
> **The value of AAWR from the EM-GC determined using the REG method is 0.188°C/decade, compared to 0.167°C/decade using Eq. (9) (Fig. S13c and Fig. 1). There is a 0.021°C/decade difference between the two methods. This difference arises because the REG method, when applied to the EM-GC modeled ΔT time series, includes the contribution of AMOC in the value of AAWR (Fig. S13c). Figure 1 of our paper illustrates that AMOC contributes about 0.025°C/decade to the rise in ΔT. If we include AMOC as a regressor variable to the REG method, we obtain a value of AAWR of 0.161°C/decade from the output of the EM-GC (Fig. S13g).**
>
> **The close agreement of values of AAWR from the REG method once we account for AMOC and Eq. (9) supports the validity of the REG method to determine AAWR from CMIP6 output. We do not explicitly use AMOC as a regressor variable when applying the REG method to CMIP6 GCMs for two reasons. The first reason is that GCMs have been shown to underestimate key aspects of the Atlantic multidecadal oscillation and are unable to simulate the many oceanic and atmospheric footprints of AMOC (Kavvada et al., 2013). The second reason is that CMIP6 GCM historical runs do not use prescribed SSTs. If the CMIP6 GCMs are representing AMOC, it is a random signal that is averaged out when we analyze the 50 GCMs in order to calculate AAWR.**

In our revised supplement, Fig. S1 has slightly changed. The figure shows output from the EM-GC that is trained using the HadCRUT4 GMST record but is adjusted to be on the HadCRUT5 pre-industrial baseline, to be consistent with other figures in the manuscript. The new baseline causes the values of ΔT_{2100} shown on the left panel to increase a negligible amount. We fixed a small indexing error in the plotting code used to make Fig. S1, which causes the maximum value of ΔT_{2100} shown on the right panel to decrease slightly.

Comparison of CMIP6 Historical Climate Simulations and Future Projected Warming to an Empirical Model of Global Climate

Laura A. McBride[1], Austin P. Hope[2], Timothy P. Canty[2], Brian F. Bennett[2], Walter R. Tribett[2], Ross J. Salawitch[1,2,3]

[1]Department of Chemistry and Biochemistry, University of Maryland College Park, College Park, 20740, USA
[2]Department of Atmospheric and Oceanic Science, University of Maryland College Park, College Park, 20740, USA
[3]Earth System Science Interdisciplinary Center, University of Maryland College Park, College Park, 20740, USA

Correspondence to: Laura McBride (mcbridel@umd.edu)

Abstract.

The sixth phase of the Coupled Model Intercomparison Project (CMIP6) is the latest modeling effort for general circulation models to simulate and project various aspects of climate change. Many of the general circulation models (GCMs) participating in CMIP6 provide archived output that can be used to calculate equilibrium climate sensitivity (ECS) and forecast future temperature change based on emissions scenarios from several Shared Socioeconomic Pathways (SSPs). Here we use our multiple linear regression energy balance model, the Empirical Model of Global Climate (EM-GC), to simulate and project changes in global mean surface temperature (GMST), calculate ECS, and compare to results from the CMIP6 multi-model ensemble. An important aspect of our study is comprehensive analysis of uncertainties due to radiative forcing of climate from tropospheric aerosols (AER RF) in the EM-GC framework. We quantify the attributable anthropogenic warming rate (AAWR) from the climate record using the EM-GC and use AAWR as a metric to determine how well CMIP6 GCMs replicate human-driven global warming over the last forty years. The CMIP6 multi-model ensemble indicates a median value of AAWR over 1975-2014 of 0.221°C/decade (range of 0.151 to 0.299°C/decade; all ranges given here are for 5th and 95th confidence intervals), which is notably faster warming than our median estimate for AAWR of 0.~~135~~157°C/decade (range of 0.~~097~~ 120 to 0.195°C/decade) inferred from analysis of the Hadley Center Climatic Research Unit Version 5 data record for GMST. Estimates of ECS found using the EM-GC (best estimate 2.~~01~~33°C; range of 1.~~12~~ 40 to ~~4.12~~3.57°C) are generally consistent with the range of ECS of 1.5 to 4.5°C given by IPCC's Fifth Assessment Report. The CMIP6 multi-model

ensemble exhibits considerably larger values of ECS (median 3.74°C; range of 2.19~~-~~ to 5.65°C). The dominant factor in the uncertainty for our empirical determinations of AAWR and ECS is imprecise knowledge of AER RF for the contemporary atmosphere. We calculate the likelihood of achieving the Paris Agreement target (1.5°C) and upper limit (2.0°C) of global warming relative to pre-industrial for seven of the SSPs using both the EM-GC and the CMIP6 multi-model ensemble. In our model framework, SSP1-2.6 ~~is the 1.5°C pathway with~~has a ~~64.8~~53% probability of limiting warming ~~at this level~~at or below the Paris target by the end of century and SSP4-3.4 ~~is the 2.0°C pathway, with~~has a ~~74.0~~64% probability of achieving the Paris upper limit. These estimates are based on the assumptions that climate feedback has been and will remain constant over time since the prior temperature record can be fit so well assuming constant climate feedback.~~-~~ In addition, we quantify the sensitivity of future warming to the curbing of the current rapid growth of atmospheric methane and show major near-term limits on the future growth of methane are especially important for achievement of the 1.5°C goal of future warming. We also quantify warming scenarios assuming climate feedback will rise over time, a feature common among many CMIP6 GCMs; under this assumption, it becomes more difficult to achieve any specific warming target. Finally, we assess warming projections in terms of future anthropogenic emissions of atmospheric carbon. In our model framework, humans can emit only another ~~268~~ 150 ± ~~91~~ 79 Gt C after 2019 to have a 66% likelihood of limiting warming to 1.5°C, and another ~~565~~ 400 ± ~~120~~ 104 Gt C to have the same probability of limiting warming to 2.0°C. Given the estimated emission of 11.7 Gt C per year for 2019 due to combustion of fossil fuels and deforestation, our EM-GC simulations suggest the 1.5°C warming target of the Paris Agreement will not be achieved unless carbon and methane emissions are severely curtailed in the next ~~two decades~~10 years.

1 Introduction

The goals of the Paris Agreement, negotiated in December of 2015, are to keep global warming below 2.0°C relative to the start of the Industrial Era and pursue efforts to limit global warming to 1.5°C. General circulation models (GCMs) project future temperature change using various evolutions of greenhouse gases and determine the likelihood of achieving the goals of the agreement. Many GCMs are participating

in the sixth phase of the Coupled Model Intercomparison Project (CMIP6) to quantify how the models represent different aspects of climate change (Eyring et al., 2016). ~~Having accurate~~Accurate projections of future temperature ~~is~~ are critical for achieving the goals of the Paris Agreement. Chapter 11 of IPCC's Fifth Assessment Report shows that some of the previous generations of these models participating in phase 5 of the Coupled Model Intercomparison Project (CMIP5) (Taylor et al., 2012) tended to overestimate the increase in global mean surface temperature (GMST) for the 21st century (Kirtman et al., 2013). In this analysis we use a multiple linear regression energy balance model to quantify the change in GMST from 1850-2019, project future changes in GMST, compare to the CMIP6 multi-model ensemble, and determine the likelihood of achieving the goals of the Paris Agreement.

Several prior studies have used a multiple linear regression approach to model the GMST anomaly in order to quantify the impact of anthropogenic and natural factors on climate (Foster and Rahmstorf, 2011; Lean and Rind, 2008, 2009; Zhou and Tung, 2013). Typically, total solar irradiance, volcanoes, and El Niño southern oscillation (ENSO) are the natural components represented in the multiple linear regression~~,~~. ~~and g~~Greenhouse gases and aerosols are the anthropogenic factors. We use multiple linear regression, in connection with a dynamic ocean module that accounts for the export of heat from the atmosphere to the ocean, to represent the natural and anthropogenic components of the climate system. In addition to the typical natural factors listed above, we include the Atlantic meridional overturning circulation (AMOC), Pacific decadal oscillation (PDO), and Indian Ocean dipole (IOD) to provide a robust representation of the natural climate system (Canty et al., 2013; Hope et al., 2017). Our anthropogenic components also include the effect of ~~land use~~land-use change (i.e., deforestation) on Earth's albedo and the export of heat from the atmosphere to the ocean as the atmosphere warms.

Our analysis builds on the work of Canty et al. (2013) and Hope et al. (2017) and includes several key updates. One is the extension back in time of our analysis to 1850. The Hadley Center Climatic Research Unit (Morice et al., 2012, 2021), Berkley Earth Group (Rohde and Hausfather, 2020), and Cowtan and Way (2014) provide GMST records starting in 1850, which now allows for ~~a~~ simulations of GMST that cover~~s~~ 170 years. The second update is the use of the Shared Socioeconomic Pathways (SSPs) (O'Neill et al., 2017) as our climate scenarios ~~to designate future~~for ~~evolution of~~ greenhouse gas and aerosol abundances. The third is the adoption of an upper ocean to our model, formulated in a manner

that matches the equations of Bony et al. (2006) and Schwartz (2012). A description of the model, the various input parameters used, and the updates listed above is given in Sect. 2. Section 3 ~~provides~~ shows results of CMIP6 and EM-GC ~~comparing~~ comparisons to the historical climate record, estimations of equilibrium climate sensitivity (ECS), as well as comparisons of our model and CMIP6 projections of future GMST change. Discussion of these results is provided in Sect. 4, along with concluding remarks.

2 Data and Methodology

2.1 Empirical model of global climate

In this analysis we use the empirical model of global climate (EM-GC), which provides a multiple linear regression, energy balance simulation of GMST. As detailed in the following paragraphs, the EM-GC solves for ocean heat uptake efficiency (κ) and six regression coefficients to minimize the cost function in Eq. (1).

$$Cost\ Function = \sum_{i=1}^{N_{MONTHS}} \frac{1}{\sigma_{OBSi}^2} (\Delta T_{OBSi} - \Delta T_{MDLi})^2 \qquad (1)$$

In this equation, ΔT_{OBS} represents a time series of observed monthly GMST anomalies, ΔT_{MDL} is the modeled monthly change in GMST, σ_{OBS} is the 1-sigma uncertainty associated with each temperature observation, *i* is the index for each month, and N_{MONTHS} is the total number of months used in the analysis. For this analysis, we trained the model from 1850-2019. The observed GMST anomalies are blended near surface air and sea surface temperature differences relative to the GMST anomaly over 1850-1900, which is assumed to represent pre-industrial conditions.

We consider several anthropogenic and natural factors as components of $\Delta T_{MDL.}$ The radiative forcing (RF) due to greenhouse gases (GHGs), anthropogenic aerosols (AER), ~~land use~~land-use change (LUC), and the export of heat from the atmosphere to the world's oceans are the anthropogenic components of ΔT_{MDL}. The influence on GMST from total solar irradiance (TSI), El Niño southern oscillation (ENSO), the Atlantic meridional overturning circulation (AMOC), volcanic eruptions that reach the stratosphere and enhance stratospheric aerosol optical depth (SAOD), the Pacific decadal oscillation, (PDO) and the Indian Ocean dipole (IOD) are the natural components of ΔT_{MDL}. Equation (2) shows how we calculate ΔT_{MDL}, the modeled monthly change in GMST.

$$\Delta T_{MDLi} = \frac{1+\gamma}{\lambda_P}\{GHG\ \Delta RF_i + AER\ \Delta RF_i + LUC\ \Delta RF_i - Q_{OCEAN\ i}\} + C_0 + C_1 \times SAOD_{i-6} +$$

$$C_2 \times TSI_{i-1} + C_3 \times ENSO_{i-2} + C_4 \times AMOC_i + C_5 \times PDO_i + C_6 \times IOD_i \quad (2)$$

In Eq. (2), GHG ΔRF_i , AER ΔRF_i, and LUC ΔRF_i represent monthly time series of the increase in the stratospheric adjusted values of the RF of climate (Solomon, 2007) since 1750. The parameter λ_P represents the response of a blackbody to a perturbation in the absence of climate feedback (3.2 W m^{-2}, (Bony et al., 2006)). The SAOD, TSI, and ENSO are lagged by 6, 1, and 2 months respectively. The lag of 6 months for SAOD is representative of the time needed for the surface temperature to respond to a change in the aerosol loading due to a volcanic eruption (Douglass and Knox, 2005). This lag is the same as used by Lean and Rind (2008) and Foster and Rahmstorf (2011). The 1 month delay for TSI yields the maximum value of C_2, the solar irradiance regression coefficient. Lean and Rind (2008) and Foster and Rahmstorf (2011) also use a 1 month lag for TSI in their analyses. The 2 month delay for the response of GMST to ENSO is the lag needed to obtain the largest value of the correlation coefficient of the Multivariate ENSO Index version 2 (MEI.v2) (Wolter and Timlin, 1993; Zhang et al., 2019) versus the value of T_{ENSO} calculated by Thompson et al. (2009). In Thompson et al. (2009), T_{ENSO} is the simulated response of GMST to variability induced by ENSO, taking into consideration the effective heat capacity of the atmospheric-ocean mixed layer. Lean and Rind (2008) used a 4-month lag for ENSO.

The term $AMOC_i$ represents the influence of the change in the strength of the thermohaline circulation on GMST (Knight et al., 2005; Medhaug and Furevik, 2011; Stouffer et al., 2006; Zhang and Delworth, 2007). We use the Atlantic multidecadal variability, based on the area weighted monthly mean sea surface temperature (SST) in the Atlantic Ocean between the equator and 60°N (Schlesinger and Ramankutty, 1994), as a proxy for the strength of AMOC. A strong AMOC is characterized by northward flow of energy that would otherwise be radiated to space, which occurs in both the ocean and atmosphere and leads to particularly warm summers in Europe (Kavvada et al., 2013) as well as a number of other well documented influences in other climatic regions (Nigam et al., 2011). The total anthropogenic RF ~~of climate~~ is used to detrend the AMOC signal ~~because~~. T~~t~~his method provides a more realistic approach to infer the changes in the strength of AMOC and its effect on GMST than other detrending options (Canty et al., 2013).

The dimensionless parameter γ represents the sensitivity of the global climate to feedbacks that occur due to a change in the RF of GHGs, AER, and LUC. We relate γ to the climate feedback parameter, λ_{Σ}, as shown in Eq. (3).

$$1 + \gamma = \frac{1}{1 - \left(\frac{\lambda_{\Sigma}}{\lambda_P}\right)}$$

where $\lambda_{\Sigma} = \Sigma$ all climate feedbacks (3)

i.e., $\lambda_{\Sigma} = \lambda_{\text{Water Vapor}} + \lambda_{\text{Lapse Rate}} + \lambda_{\text{Clouds}} + \lambda_{\text{Surface Albedo}}$

The relation between λ_{Σ} and γ in Eq. (3) is commonly used in the climate modeling community (Sect. 8.6 of Solomon (2007)). ~~Bony et al. (2006) and Gregory (2000) use a different formalism to define their climate feedback parameter.~~ Our value of λ_{Σ} is related to the IPCC's Fifth Assessment Report ((Stocker et al., 2013), hereafter IPCC 2013) definition of λ via $\lambda_{\Sigma} = \lambda_P - \lambda$.

Our model explicitly accounts for the export of heat from the atmosphere to the world's oceans (i.e., ocean heat export or OHE). The quantity Q_{OCEAN} in Eq. (2) represents OHE. In our previous analyses (Canty et al., 2013; Hope et al., 2017), Q_{OCEAN} was subtracted outside of the climate feedback multiplicative term $(1+\gamma)/\lambda_P$. We have rewritten Eq. (2) to be comparable to the formulation for this term used by Bony et al. (2006) and Schwartz (2012). ~~The effect of this update results in our model being able to~~Due to this update, our model fits the historical climate record with higher values of climate feedback, especially for strong aerosol cooling (see Fig. S1 and supplement for more information). We calculate Q_{OCEAN} by simulating the long-term trend in observed ocean heat content (OHC) as shown in Eq. (4) and Eq. (5).

$$Q_{OCEANi} = \kappa\left(\Delta T_{ATM,HUMANi} - \Delta T_{OCEAN,HUMANi}\right) \quad (4)$$

$$\kappa = \frac{OHE \times \Delta t}{\int_{t_{START}}^{t_{END}} \left(\left[\frac{1+\gamma}{\lambda_P}\{GHG\ RF_{i-72} + AER\ RF_{i-72} + LUC\ RF_{i-72}\}\right] - [f_0 \sum_0^{i-72} Q_{OCEAN}]\right) dt} \quad (5)$$

The κ term is the ocean heat uptake efficiency (W m^{-2} °C^{-1}) and is based on the definition used in Raper et al. (2002), where κ is the ratio between the atmosphere and ocean temperature difference that best fits observed OHC data (Sect. 2.2.8 describes the OHC data records used in our analysis). The value of κ is determined based ~~upon~~ on the best fit (described below) between Q_{OCEAN} and the observed OHC record. The term $\Delta T_{OCEAN,HUMAN}$ represents the temperature response of the well-mixed, top 100 m of the ocean

due to the total anthropogenically driven rise in OHC. This formulation of $\Delta T_{OCEAN,HUMAN}$ allows the model ocean to warm in response to an atmospheric warming. We use a 6 year lag (72 months) for Q_{OCEAN} to account for the time needed for the energy leaving the atmosphere to heat the upper ocean and penetrate to depth, based on Schwartz (2012). Our analysis of modeled GMST is insensitive to whether this 6 year lag or the 10 year lag from Lean and Rind (2009) is used. The t_{START} and t_{END} limits on the integral in Eq. (5) are the start and end years~~,~~ associated with each OHC record. The start and end years vary between the 5 OHC records (see supplement for the different start and end years). The constant f_0 term in Eq. (5) is a combination of the heat capacity of ocean water, the fraction of total ocean volume in the surface layer, and the fraction of total Q_{OCEAN} that warms the surface layer, and is equal to 8.76×10^{-5} °C m^2 W^{-1}. We represent the global ocean as being 1 km deep for 10% of the ocean area (representing the continental shelves) and 4 km deep for the remaining area, which approximates the average depth of the actual world's oceans to within 3%; 3.7 km compared to 3.682-3.814 km from Charette and Smith (2010). Based ~~upon~~ on our analysis of decadal ocean warming as a function of depth extracted from CMIP5 GCMs, we have determined that 13.7% of the rise in total OHC occurs in the well mixed, upper 100 m of the ocean, the term represented by $\Delta T_{OCEAN,HUMAN}$ in equation (4). The bottom ~~rung~~ panel of Fig. 1 compares our modeled OHC to the observed OHC record based ~~upon~~ on the average of five data sets; the value of κ resulting in the best simulation of observed OHC is shown.

We use the reduced chi-squared (χ^2) metric to define the goodness of fit between the modeled and measured GMST anomaly for the atmosphere and also between simulated and observed OHC. Equation (6) and Eq. (7) show the calculations for χ^2 for the atmosphere, and Eq. (8) shows the calculation for χ^2 for the ocean. ~~As noted above, m~~Minimization of the difference between the measured and modeled GMST anomaly results in the EM-GC being able to replicate the observed rise in temperature over the past 170 years quite well, as shown in Fig. 1. We have added two additional new features to the model to assure accurate representation of the rise in OHC as well as the rise in GMST since 1940. The first new feature, Eq. (7), was added to ensure all simulations matched the past 80 years of observations well ~~because of a change in the specification of the uncertainty of the GMST anomaly ($\sigma_{OBS,i}$ in Eq. (2).) given by the Hadley Center Climatic Research Unit (HadCRUT). A recent update resulted in much larger uncertainties being ascribed to the GMST anomaly for the entire data record,~~Without the χ^2_{RECENT}

constraint, ~~which caused~~ some solutions ~~to yield~~with a value of χ^2_{ATM} less than or equal to 2 have visually poor simulations of the rise in GMST over the past 4 to 5 decades. The second new feature, Eq. (8), was added because ~~for~~ in the original model formulation some selections of the radiative forcing due to tropospheric aerosols (AER ΔRF_i in Eq. (2)) converged~~, the original model formulation was converging but~~in a way that ~~producing~~ produced simulations of OHC that seemed physically improper~~,~~ based on visual inspection of observed and modeled OHC. As a result of these two issues, all calculations shown here are subject to three goodness-of-fit constraints, described by Eq. (6) to (8):

$$\chi^2_{ATM} = \frac{1}{N_{YEARS} - N_{FITTING\ PARAMETERS} - 1} * \sum_{j=1}^{N_{YEARS}} \frac{1}{\langle \sigma_{OBSj} \rangle^2} \left(\langle \Delta T_{OBSj} \rangle - \langle \Delta T_{MDLj} \rangle \right)^2 \quad (6)$$

$$\chi^2_{RECENT} = \frac{1}{N_{YEARS,REC} - N_{FITTING\ PARAMETERS} - 1} * \sum_{j=1}^{N_{YEARS,REC}} \frac{1}{\langle \sigma_{OBSj} \rangle^2} \left(\langle \Delta T_{OBSj} \rangle - \langle \Delta T_{MDLj} \rangle \right)^2 \quad (7)$$

$$\chi^2_{OCEAN} = \frac{1}{N_{YEARS} - N_{FITTING\ PARAMETERS} - 1} * \sum_{j=1}^{N_{YEARS,OHC}} \frac{1}{\langle \sigma_{OBSj} \rangle^2} \left(\langle OHC_{OBSj} \rangle - \langle OHC_{MDLj} \rangle \right)^2 \quad (8)$$

Here, $<\Delta T_{OBS}>$, $<\Delta T_{MDL}>$, and $<\sigma_{OBS}>$ in Eq. (6) and Eq. (7) represent the annually averaged observed, modeled, and uncertainty in the GMST anomaly, respectively. The variable $N_{FITTING\ PARAMETERS}$ is equal to 9 for typical simulations, the sum of 7 (the number of regression coefficients) plus 2 (model output parameters γ and κ). In Eq. (8), $<OHC_{OBS}>$ and $<OHC_{MDL}>$ represent the annual averaged observed and modeled OHC. The σ_{OBS} term in Eq. (8) is the uncertainty in the OHC record (see Sect. 2.2.8 for more information). The equation for all three formulations of χ^2 is based on annual averages, rather than monthly time series~~,~~. ~~because t~~We calculate χ^2 with annual values~~he~~ because the autocorrelation functions of ΔT_{OBS} and ΔT_{MDL} display similar shapes using annual averages, and do not match utilizing monthly averages (see supplement of Canty et al. (2013) for further explanation). The Hadley Center Climate Research Unit (HadCRUT) version 4 uncertainties for GMST are used for the σ_{OBS} in Eq. (6) to (8) for all of the GMST records analyzed here (see Sect. 2.2.1 and the supplement for more information). For Eq. (6) to (8), we define an acceptable fit to the climate record as $\chi^2 \leq 2$. The number of years (N_{YEARS}) varies across the three equations. Equation (6) uses the total number of years in the GMST record, which for HadCRUT5 is 170 years. The number of years in Eq. (8), $N_{YEARS,OHC}$, depends on the OHC data set used, as each data set spans a different range. The average of five OHC data sets ~~that is our primary,~~ which we use as our primary ~~data source~~OHC series, extends from 1955-2017, a total of 63 years. The value of χ^2_{OCEAN} found using Eq. (8) is displayed on the bottom ~~rung~~ panel of Fig. 1. All model simulations

shown throughout this paper have $\chi^2_{OCEAN} \leq 2$, representing a good fit to the observed rise in OHC over the time of the data record.

The calculation of χ^2_{RECENT} shown in Eq. (7) is used to constrain the model to match the observed changes in GMST over the time frame 1940-2019, a total of 80 years ($N_{YEARS,REC}$ equals 80). This time frame was chosen to include a full cycle of AMOC, as the strength of the thermohaline circulation tends to vary on a period of 60-80 years (Chen and Tung, 2018; Kushnir, 1994; Schlesinger and Ramankutty, 1994). As noted above, the χ^2_{RECENT} constraint was added to our model framework because without this constraint the model is able to provide numerically good but poor visual fits to the GMST anomaly under certain conditions ~~the large temperature uncertainties associated with v4.6 of the HadCRUT data set allowed the original model to provide numerically good fits but poor visual fits to GMST changes in the recent time period~~ (i.e. the red line in the top ~~rung~~ panel of Fig. 1 starts to strongly deviate from the black line beginning in about 2000 under certain conditions). All model simulations shown below have $\chi^2_{RECENT} \leq 2$ representing a good fit to the observed rise in GMST over the past 80 years, which results in modeled GMST that replicates observed GMST for the entire time series.

Figure 1 shows the observed (HadCRUT5) and modeled GMST anomaly from 1850-2019, and the various anthropogenic and natural components that constitute modeled GMST ~~(see Fig. S3 for results using Cowtan and Way (2014) GMST record and the Cheng et al. (2017) OHC record (hereafter Cheng 2017))~~. Figure 1a shows the value of climate feedback, 1.~~38~~ 62 W m^{-2} °C^{-1}, that is needed to achieve a best fit to the climate record for this simulation, resulting in values of χ^2_{ATM} = 0.~~71~~ 80 and χ^2_{OCEAN} = 0.~~32~~31. Figure 1b is the total contribution of human activity to variations in GMST, which includes GHGs, AER, LUC, and the export of heat from the atmosphere to the ocean. For the simulation shown, the aerosol radiative forcing is −0.9 W m^{-2}, the best estimate given by IPCC 2013 (Myhre et al., 2013). This panel also notes the best estimate of the time rate of change of GMST attributed to humans from 1975-2014, or the attributable anthropogenic warming rate (AAWR (see Sect. 2.3)). Figure 1c illustrates the contribution to the GMST anomaly from TSI ~~(Solar)~~ and SAOD ~~(Volcano)~~ over the 170-year period. The influences of ENSO and AMOC are indicated in Figs. 1d and 1e, respectively. Furthermore, ~~T~~the contribution of AMOC to the rise in GMST over 1975-2014 (the same time period used to define AAWR) is also specified on Fig. 1e (dotted black line). Figure 1f indicates the small effect of IOD and PDO on

GMST in our model framework. The last panel, Fig. 1g, shows the time series of observed OHC based ~~upon~~ on the average of five data sets for the upper 700 m of the ocean (black points and blue error bars; see Sect. 2.2.8) and the modeled value of OHC (red line). For this simulation, ~~the OHC data is best fit for~~ a value of κ equal to 1.~~28~~ 17 W m^{-2} °C^{-1} fits the OHC data best.~~,~~ ~~which~~ This value of κ falls within the range of empirical estimates for this parameter given by Raper et al. (2002). The sum of the contributions of human activity, TSI, SAOD, ENSO, AMOC, PDO and ~~the~~ IOD to ~~temporal variations in~~ the GMST anomaly shown in Fig. 1b to 1f plus the value of C_0 equals the modeled GMST anomaly, shown by the red line in Fig. 1a.

Altering the training period of our model has a slight effect on our results (see Fig. S2, S3, and the supplement for information on various training periods). We project relatively similar results for end of century warming for training periods that start in 1850 and end in either 2009 or 1999, compared to results shown throughout the paper for a training period of 1850 to 2019, indicating the stability of our approach. As detailed in the supplement, we do find some differences from the results shown in the paper upon use of a training period of 1850 to 1989 due to the reduction in the number of years considered from the available OHC records.

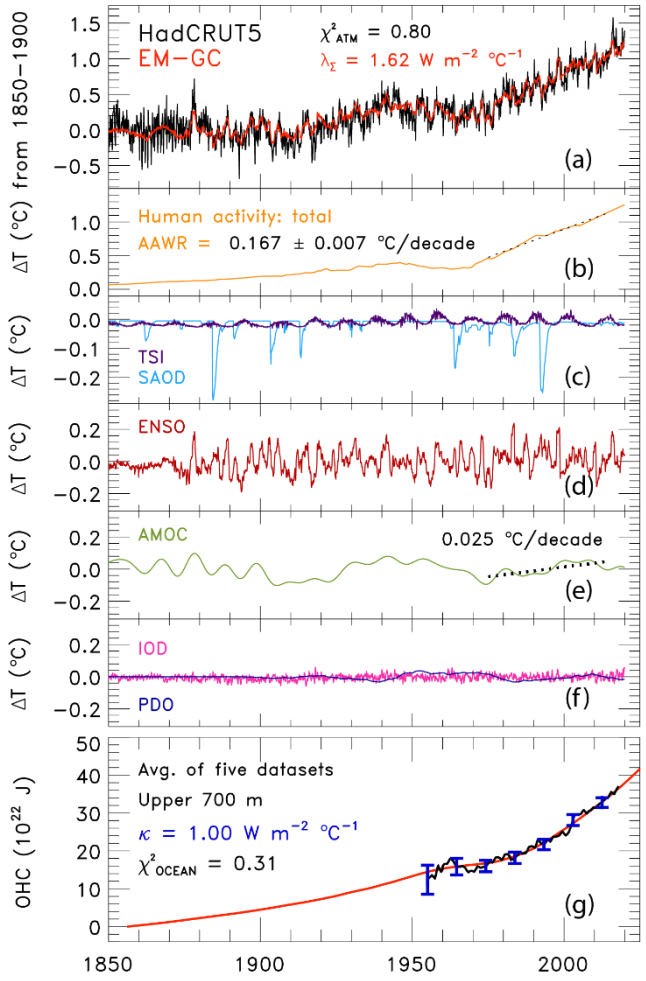

Figure 1. Measured and modeled GMST anomaly (ΔT) relative to a pre-industrial (1850-1900) baseline. (a) Observed (black) HadCRUT5 and modeled (red) ΔT from 1850-2019. This panel also displays the values of λ_Σ and χ^2_{ATM} (see text) for this best-fit simulation. (b) Contributions from total human activity. This panel also denotes the best estimate ~~numerical~~ value of the attributable anthropogenic warming rate from 1975-2014 (black dashed) as well as the 2σ uncertainty in the slope for a model run that uses the best estimate of AER RF_{2011} of −0.9 W m^{-2}. (c) ~~Solar~~ TSI ~~irradiance~~ (~~light blue~~purple) and ~~major volcanoes~~SAOD (~~purple~~light blue). (d) Influences from ENSO on ΔT. (e) Contributions from AMOC to ΔT and to observed warming from 1975-2014. (f) Influences from PDO (blue) and IOD (pink) on ΔT. (g) Measured (black) and modeled (red) ocean heat content (OHC) as a function of time for the average of five data sets (see text), the value of χ^2_{OCEAN} for this run, as well as the ocean heat uptake efficiency, κ, needed to provide the best-fit to the OHC record. The error bars (blue) denote the uncertainty in OHC used in this analysis (see Sect. 2.2.8).

2.2 Model Inputs

2.2.1 Temperature data

We use ~~five~~ seven global mean surface temperature ~~anomalies~~anomaly records. These records include ~~from~~ the Hadley Centre Climatic Research Unit version 4 (HadCRUT4, (Morice et al., 2012)) and version 5 (HadCRUT5 (Morice et al., 2021)) from 1850-2019, National Centers for Environmental Information NOAAGlobalTemp v5 (NOAAGT, (Smith et al., 2008; Zhang et al., 2019)) from 1880-2019, NASA Goddard Institute of Space Studies Surface Temperature Analysis v4 (GISTEMP, (Hansen et al., 2010)) from 1880-2019, Berkeley Earth Group (BEG, (Rohde and Hausfather, 2020)) from 1850-2019, ~~and~~ Cowtan and Way (2014) (CW14~~; see Fig. S4 and the supplement for information on CW14 GMST record~~) from 1850-2019, and the Japanese Meteorological Agency (JMA (Ishihara, 2006)) from 1891-2019. We use the uncertainty time series from HadCRUT4 for all GMST records because the HadCRUT4 uncertainty provides a realistic description of the variation in GMST among the seven records (see the supplement, Figs. S4 and S5, and Table S1 for more information). Our analysis primarily uses the HadCRUT5 GMST data set, ~~because this GMST record is the central focus of some contemporary studies (Liang et al., 2020; Nicholls et al., 2020a, 2020b),~~ but in some sections~~,~~ results are shown for ~~all five~~ the other data sets. All temperature anomalies are with respect to a pre-industrial baseline (1850-1900). To alter each data record so that the temperature anomaly is relative to the same pre-industrial baseline, we adjust all data sets relative to the HadCRUT5 baseline of 1961-1990. ~~because we primarily use the HadCRUT data record in this analysis.~~ We then adjust each data set by the same amount to the HadCRUT5 pre-industrial baseline~~,~~ as described in the ~~methods section of Hope et al. (2017)~~supplement.

2.2.2 Shared Socioeconomic Pathways

For this analysis, we use the estimates of the future abundances of greenhouse gases and aerosols provided by the SSPs. There are twenty-six scenarios, five baseline pathways and twenty-one mitigation scenarios. The baseline pathways follow specific narratives for factors such as population, education, economic growth, and technological developments of sources of renewable energy (Calvin et al., 2017; Fricko et al., 2017; Fujimori et al., 2017; Kriegler et al., 2017; van Vuuren et al., 2017) to represent several possible futures spanning different challenges for adaptation and mitigation to climate change as illustrated in Fig. 1 of O'Neill et al. (2014). The twenty-one mitigation scenarios follow one of the baseline pathways but include specific climate policy to reach a designated radiative forcing at the end of the century.

As part of CMIP6, the ScenarioMIP experiment (O'Neill et al., 2016) includes eight SSPs (SSP1-1.9, SSP1-2.6, SSP4-3.4, SSP2-4.5, SSP4-6.0, SSP3-7.0, SSP5-8.5, and SSP5-3.4-OS) that GCMs use to project future GMST. The first number is the reference pathway that the scenario follows (i.e. SSP1 follows the first SSP narrative) and the numbers after the dash are the target radiative forcing at the end of the century (i.e. SSP1-2.6 reaches around 2.6 W m^{-2} in 2100). The ScenarioMIP experiment designates Tier 1 and Tier 2 scenarios. The Tier 1 scenarios are SSP1-2.6, SSP2-4.5, SSP3-7.0, and SSP5-8.5 , and the Tier 2 scenarios are SSP1-1.9, SSP4-3.4, SSP4-6.0, and SSP5-3.4-OS (an overshoot pathway that follows SSP5-8.5 until around 2040, where carbon dioxide emissions drastically decrease and become negative in 2065). Our analysis includes seven of the eight ScenarioMIP SSPs: all but the overshoot pathway. We highlight four in the main paper: two Tier 1 (SSP1-2.6 and SSP2-4.5) and two Tier 2 (SSP1-1.9 and SSP4-3.4) scenarios. Analysis of the other three SSPs is included in the supplement. Figure 2 shows the ~~time evolution of the~~ atmospheric abundance of the three major anthropogenic GHGs (carbon dioxide, methane, and nitrous oxide) for each of the seven SSPs we consider as well as observations of the global mean atmospheric abundance for these gases to the end of 2019 (Dlugokencky, 2020; Dlugokencky and Tans, 2020).

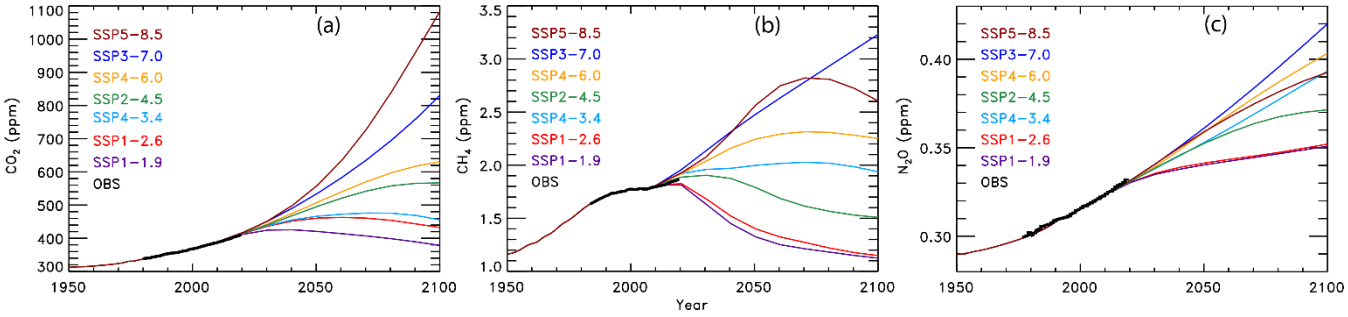

Figure 2. Observed and projected greenhouse gas mixing ratios. (a) Carbon dioxide abundances from observations (black) and seven of the ScenarioMIP SSPs (colors, as indicated). (b) Methane abundances from observations and ScenarioMIP SSPs. (c) Nitrous oxide abundances from observations and ScenarioMIP SSPs.

2.2.3 Greenhouse gases

The historical values of GHG mixing ratios were provided by Meinshausen et al. (2017) from 1850-2014. We used the equations from Myhre (1998) to calculate the change in RF due to carbon dioxide (CO_2), methane (CH_4), nitrous oxide (N_2O), ozone depleting substances (ODS), hydrofluorocarbons,

perfluorocarbons, and sulfur hexafluoride relative to RF in year 1850. We also used the updated pre-industrial values of CH_4 and N_2O from IPCC 2013 and the radiative efficiencies from WMO (2018). The radiative forcing of CH_4 also includes the 15% enhancement from the increase in stratospheric water vapor due to rising atmospheric CH_4 (Myhre et al., 2007). Values of GHG mixing ratios, other than ODSs, from 2015-2100 are from the SSP Database (Calvin et al., 2017; Fricko et al., 2017; Fujimori et al., 2017; Kriegler et al., 2017; Rogelj et al., 2018; van Vuuren et al., 2017) and are provided on a decadal basis. These mixing ratios were interpolated onto a monthly time scale. We used the estimates of future ODS abundances provided in Table 6-4 of the 2018 Ozone Assessment Report (Carpenter et al., 2018), because the SSP database did not provide these estimates. We also include tropospheric ozone (O_3^{TROP}) as a GHG, because tropospheric ozone rivals N_2O as the third most important anthropogenic GHG (Fig 8.15 of Myhre et al. (2013)). The RF due to O_3^{TROP} from the RCPs provided by the Potsdam Institute for Climate Impact Research (Meinshausen et al., 2011) is used, because the SSP database does not provide estimates. Values of RF due to O_3^{TROP} from RCP2.6, RCP4.5, RCP6.0, and RCP8.5 are substituted in for SSP1-2.6, SSP2-4.5, SSP4-6.0, and SSP5-8.5, respectively. We created new time series for the RF due to O_3^{TROP} for SSP4-3.4 and SSP3-7.0 using linear combinations of RF time series from RCP2.6 and RCP8.5, with weights based on the end of century total RF value due to all GHGs of the respective time series. Finally, the RF time series for O_3^{TROP} from RCP2.6 was also used for SSP1-1.9. Figure ~~S5~~ S6 shows the ozone RF time series used in this analysis and the supplement provides more information about the creation of the time series for the RF due to O_3^{TROP}.

2.2.4 Aerosol radiative forcing

The value of the change in total aerosol radiative forcing (direct and indirect) in 2011 relative to pre-industrial (AER RF_{2011}) is highly uncertain. Chapter 8 of the IPCC 2013 report gives a best estimate of AER RF_{2011} as −0.9 W m^{-2}, a likely range between −0.4 and −1.5 W m^{-2}, and a 5^{th} to 95^{th} percent confidence interval between −0.1 and − 1.9 W m^{-2} (Myhre et al., 2013). This substantial range in AER RF_{2011} results in a large spread in future projections of global GMST. Figure 3 shows the effect of varying the value of AER RF_{2011} on projections of GMST in our EM-GC framework, for the same SSP4-3.4 GHG scenario. The middle panel on Figs. 3a, 3b, and 3c shows the contribution to GMST of GHGs, LUC,

AER, as well as net human activities. As the value of AER RF_{2011} decreases and aerosols cool more strongly, the value of climate feedback (model parameter λ_Σ) rises, and the net contribution of human impact on GMST by the end of the century increases. Depending on which value of AER RF_{2011} is used, the rise in GMST by year 2100 for the SSP4-3.4 pathway could range from 1.~~3~~5°C (Fig. 3a) to 2.~~6~~8°C (Fig. 3c) relative to pre-industrial. Strong aerosol cooling offsets a substantial fraction of GHG-induced warming, and a large value of climate feedback (λ_Σ = 2.~~32~~ 41 W m^{-2} $°C^{-1}$) is needed to fit the historical climate record (Fig. 3c). In this case, future warming is large, well above the goals of the Paris Agreement by the end of the century. Conversely, weak aerosol cooling offsets only a small fraction of GHG-induced warming, resulting in a small value of climate feedback (λ_Σ = ~~0.73~~ 1.08 W m^{-2} $°C^{-1}$) needed to fit the observed GMST record (Fig. 3a). The use of any of the values of AER RF_{2011} in Fig. 3 can result in a very good fit to the climate record (i.e., $\chi^2_{ATM} \leq 2$, $\chi^2_{RECENT} \leq 2$, and $\chi^2_{OCEAN} \leq 2$).

We use the total aerosol RF time series provided by the SSP database for each SSP scenario. The database provides AER RF from 2005-2100, with values for all SSPs nearly identical until about 2010 (Riahi et al., 2017; Rogelj et al., 2018). In the EM-GC, we calculate temperature projections over the entire observational period, beginning in 1850. ~~Consequently, we~~We create AER RF time series that begin in 1850 and span the range of uncertainty given by Chapter 8 of IPCC 2013. We use historical estimates of AER RF from 1850-2014 for the four RCPs provided by the Potsdam Institute for Climate Research (Meinshausen et al., 2011). The AER RF value in 2014 from the appropriate historical estimate (i.e. RCP 4.5 is used for SSP2-4.5) is scaled by a constant ~~multiplicative~~ factor, such that the historical RCP value at the end of 2014 matches the SSP time series at the start of 2015.~~,~~ This scaling ~~yielding~~ yields a continuous time series for the RF of climate due to tropospheric aerosols. This scaled time series has AER RF_{2011} nearly equal to −1.0 W m^{-2}, which we take as the SSP-based best estimate of the change in total aerosol radiative forcing in 2011 relative to pre-industrial. Next, the single continuous time series is scaled, again by a constant multiplicative factor, to match the IPCC 2013 best estimate and range of uncertainty for AER RF_{2011} (Myhre et al., 2013). This procedure results in five additional time series of AER RF. Six time series of AER RF are ~~thus~~ created for each SSP, having values of AER RF_{2011} equal to −0.1, −0.4, −0.9, −1.0, −1.5, and −1.9 W m^{-2}. Figure S7 shows these six AER RF time series for SSP1-

2.6 and SSP4-3.4. In the EM-GC framework, we further scale these six time series to create a total of 400 AER RF time series to fully analyze the range of AER RF_{2011} given by Myhre et al. (2013).

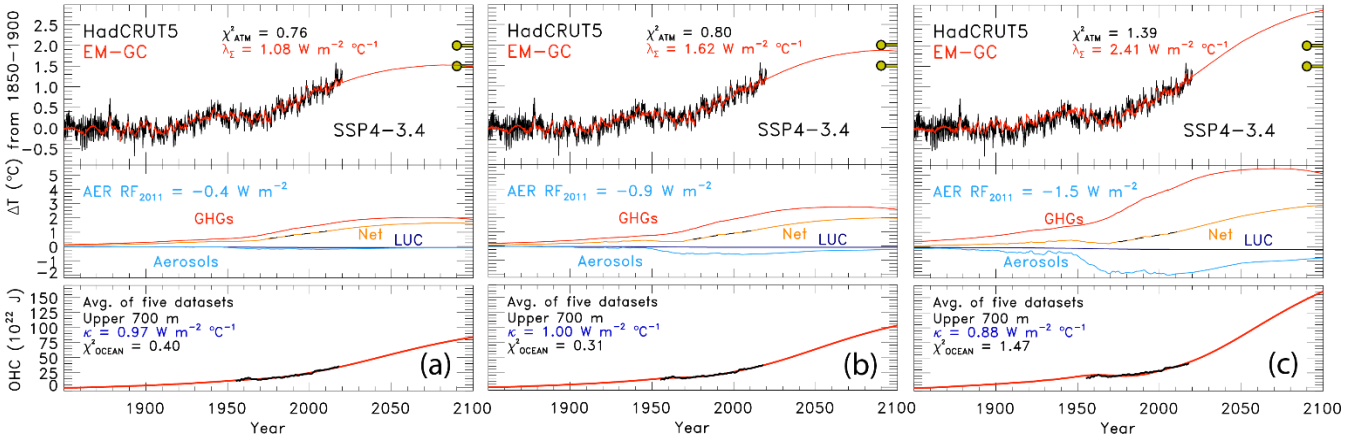

Figure 3. Measured (HadCRUT5) and EM-GC simulated GMST anomaly (ΔT) relative to a pre-industrial (1850-1900) baseline, as well as projected ΔT to end of century for SSP4-3.4. Top panel of each plot displays observed (black) and simulated (red) ΔT, as well as the values of λ_Σ and χ^2_{ATM} for each model run. The Paris Agreement target (1.5°C) and upper limit (2.0°C) are shown (gold circles). The second panel shows the contribution of GHGs, aerosols, and ~~land use~~land-use change to ΔT, as well as the net human component. The bottom panel compares observed (black) and modeled (red) values of OHC for simulations constrained by the average of five data sets (see text) and also provides the numerical values of κ needed to obtain best-fits to the OHC record as well as best-fit values of χ^2_{OCEAN}. The only difference between (a), (b), and (c) is the time series for RF due to tropospheric aerosols used to constrain the EM-GC; values of AER RF_{2011} for each time series are (a) −0.4 W m^{-2}, (b) −0.9 W m^{-2}, (c) −1.5 W m^{-2}.

2.2.5 Total solar irradiance and stratospheric aerosol optical depth

We use the TSI time series provided for the CMIP6 models from 1850-2014 (Matthes et al., 2017) and append values from the Solar Radiation and Climate Experiment (SORCE) (Dudok de Wit et al., 2017) for 2015 to the end of 2019. The values of TSI_i used in Eq. (2) are differences of monthly mean values minus the long-term average (i.e., TSI anomalies). Consistent with prior studies (e.g., Lean and Rind (2008) and Foster and Rahmstorf (2011)) variations in solar irradiance due to the 11-year solar cycle have a small but noticeable effect on the EM-GC simulation of the GMST anomaly (Fig. 1c). For projections of future warming, we set the term TSI_i in Eq. (2) equal to zero from the start of 2020 until 2100 ~~(i.e., we do not propagate 11-year variations of TSI forward in time)~~.

The time series for SAOD is a combination of values computed from extinction coefficients for the CMIP6 GCMs (Arfeuille et al., 2014) from 1850-1978 and the Global Space-based Stratospheric

Aerosol Climatology (GloSSAC v2.0) (Thomason et al., 2018) from 1979-2018. Extinction coefficients at 550 nm were integrated from the tropopause to 39.5 km and averaged over the globe using a cosine of latitude weighting. The CMIP6 and GloSSAC extinction coefficients span 80°S to 80°N. To extend the SAOD time series to the end of 2019, we use the level 3, gridded SAOD product from the Cloud-Aerosol Lidar and Infrared Pathfinder Satellite Observations (CALIPSO) (Vaughan et al., 2004). Time series of globally averaged SAOD from CALIPSO have a very similar shape to the GloSSAC time series over the period of overlap (2006-2018)~~,~~ with a slight offset because GloSSAC uses estimates of CALIPSO data for SAOD. To append the ~~CALIPSO~~ SAOD ~~for~~ after 2018~~-2019~~, we took the average difference between the two time series for the overlapping months and then adjusted the CALIPSO time series by this offset. This slight adjustment to the CALIPSO record has no bearing on our ~~scientific~~ results, since the effect of volcanic activity on GMST has been small over the past 2 decades (Fig. 1c). We set the term $SAOD_i$ in Eq. (2) equal to the value in December 2019 from the start of 2020 until 2100.

2.2.6 El Niño southern oscillation, Pacific decadal oscillation, and Indian Ocean dipole

We use the MEI.v2 (Wolter and Timlin, 1993; Zhang et al., 2019) to characterize the influence of ENSO on GMST. In order to obtain a time series that spans the entire training period of our model, 1850-2019, we append three time series to create an MEI.v2 index over the full ~~time~~ extent of our model training period. The MEI.v2 provides two month averages of empirical orthogonal functions of five different climatic variables from 1979 to present (Zhang et al., 2019). To have the ENSO index extend back to 1850, we compute differences in SST anomalies over the tropical Pacific basin as defined by the MEI.v2 from 1850-1870 using HadSST3 (Kennedy et al., 2011). Our internal computation of this surrogate for the MEI index is then appended to the MEI.ext of Wolter and Timlin (2011), which extends from 1871-1978, and the MEI.v2 index of (Zhang et al., 2019) (1979-2019). This full time series provides a representation of ENSO that covers from 1850 to present. Consistent with prior regression-based approaches (Foster and Rahmstorf, 2011; Lean and Rind, 2008), we find a significant portion of the monthly and at times annual variation in GMST is well explained by ENSO (Fig. 1d). As for the other natural terms, we assume $ENSO_i$ in Eq. (2) is zero for 2020-2100.

The Pacific decadal oscillation is the leading principal component of North Pacific monthly SST variability poleward of 20°N (Barnett et al., 1999). The PDO index maintained by the University of Washington provides monthly values from 1900-2018. The PDO varies on a multidecadal time scale and affects climate in the North Pacific and North America, and has secondary effects in the tropics (Barnett et al., 1999). In our model framework, the expression of PDO on GMST is dependent on the model specification of the AER RF time series, as shown in Fig. ~~S6~~S8. At low values of AER RF_{2011}, such as −0.1 W m^{-2}, the effect of PDO on GMST is negligible and the contribution from AMOC dominates. At high values of AER RF_{2011} (−1.5 W m^{-2}), the effect of PDO on GMST is equal to the contribution from AMOC. At high values of AER RF_{2011}, we obtain results similar to findings from England et al. (2014) and Trenberth and Fasullo (2013) that shows the PDO exhibits an appreciable influence on GMST, especially for the 2000-2010 time period.

The Indian Ocean dipole is based ~~upon~~ on the difference in the anomalous sea surface temperatures (SST) between the western equatorial Indian Ocean (50°-70° E and 10° S-10° N) and the south eastern equatorial Indian Ocean (90° E-110° E & 10° S-0° N) as defined in Saji et al. (1999). We use 1° × 1° SSTs from the Centennial in situ Observation-Based Estimate (COBE) (Ishii et al., 2005) to create an IOD index from 1850-2019. As noted above and shown on Fig. 1f, the regression coefficients for PDO and IOD are quite small. We find little influence of either PDO or IOD in the HadCRUT5 time series of GMST, but these terms are retained for completeness. We assume PDO_i and IOD_i in Eq. (2) are zero after the start of 2019 and 2020, respectively.

2.2.7 Atlantic meridional overturning circulation

We use the Atlantic multidecadal variability (AMV) index as the area weighted, monthly mean SST from ~~HadSST3~~ HadSST4 (Kennedy et al., 2019)~~(Kennedy et al., 2011)~~, between the equator and 60° N in the Atlantic Ocean (Schlesinger and Ramankutty, 1994) to characterize the influence of ~~variations in the strength of~~ the AMOC on GMST. The AMV index is detrended using the RF anomaly due to anthropogenic activity over the historical time frame of the analysis, as discussed in Sect. 3.2.3 of Canty et al. (2013), because this detrending option removes the influence of long-term global warming on the AMV index. The detrended AMV index serves as a proxy for variations in the strength of the AMOC

(Knight et al., 2005; Medhaug and Furevik, 2011; Zhang and Delworth, 2007), which has particularly noticeable effects on climate in the Northern Hemisphere (Jackson et al., 2015; Kavvada et al., 2013; Nigam et al., 2011). For this analysis, the index has been Fourier filtered to remove frequencies above 9 yr^{-1} to retain only the low frequency, high amplitude component of the thermohaline circulation (Canty et al., 2013). As noted above and shown in Fig. 1, a considerable portion of the long-term variability in GMST is attributed to variations in the strength of AMOC, including about 0.~~036~~025°C/decade over the 1975-2014 time period. There is considerable debate about the validity of the use of a proxy such as the AMV index as a surrogate for the climatic effects of AMOC that is centered mainly around how much of the variability of the index is either internal ~~(i.e., natural variability)~~ or externally forced ~~(i.e., driven by anthropogenic factors)~~ (Haustein et al., 2019; Knight et al., 2005; Medhaug and Furevik, 2011; Stouffer et al., 2006). We stress, as explained ~~below~~in Sect. 2.3, none of our major scientific conclusions are altered if we neglect AMV as a regression variable.

2.2.8 Ocean heat content records

Ocean heat content data records from five recent and independent papers are used in this study. We utilize OHC data from Balmaseda et al. (2013), Carton et al. (2018), Cheng et al. (2017), Ishii et al. (2017), and Levitus et al. (2012), as well as the average of the records to model the export of heat (OHE) from the atmosphere to the ocean. Figure ~~S8~~ S9 shows these five OHC records as well as the multi-measurement average. While most of these data sets have a common origin, they differ in how extensive temporal and spatial gaps in the coverage of ocean temperatures have been handled, ranging from data assimilation (Carton et al., 2018) to an iterative radius of influence mapping method (Cheng et al., 2017). The five data sets are all set to zero in 1986, which is the midpoint of the multi-measurement time series, by applying an offset for visual comparison. Since OHE, in units of W m^{-2}, is based ~~upon~~ on the slope of each OHC data set, this offset has no impact on the computation of OHE from OHC that is central to our study. For the computation of OHE from OHC, we use a value of the surface area of the world's oceans equal to 3.3×10^{14} m^2 (Domingues et al., 2008). The OHC records we analyze are for the upper 700 m of the ocean. To calculate the OHE for the whole ocean, we multiply the OHE by 1/0.7 to account for the fact that the upper 700 m of the ocean holds 70% of the heat (Sect. 5.2.2.1 (Solomon, 2007)). When we

subtract the amount of heat going into the ocean in Eq. 2 (Q_{OCEAN}), we also must account for the difference in surface area between the global atmosphere and the world's oceans. Since the Q_{OCEAN} term is computed for the surface area of the ocean, but the forcing is applied to the whole atmosphere, we multiply the Q_{OCEAN} term by the ratio of the surface area of the ocean to the surface area of the atmosphere, which is 0.67.

As noted above, the calculation of χ^2_{OCEAN} shown in Eq. (8) is used to constrain our model representation of the ~~temporal~~ rise in OHC. Only model runs that provide a good fit to the observed OHC record are shown below. For these five OHC data sets, uncertainty estimates are not always provided. Furthermore, some studies that do provide uncertainties give estimates that seem unreasonably small (see Fig. ~~S9~~ S10 and the supplement). Because of the discrepancy in uncertainties between OHC records, we create a new uncertainty time series using both the 1~~-sigma~~σ standard deviation of the average of the five OHC records and the uncertainties from the Cheng et al. (2017) (hereafter Cheng 2017) OHC record. We create this new uncertainty from 1955-2019 by a monthly time step and use either the 1~~-sigma~~σ standard deviation of the average of the five OHC records or the uncertainties from the Cheng 2017 OHC record, whichever is larger, for that month. We use the Cheng 2017 OHC uncertainties because these estimates are the largest of the five data sets. Additionally, the standard deviation from the mean of the five OHC records is very low in the 1980s, which is an artifact of our normalization treatment, not inherent to any of the records. This combined uncertainty estimate is substituted in for each individual data set and the average, resulting in our use of the same time varying uncertainty in OHC for all data sets. Figure ~~S9~~ S10 and the supplement provide more detail on the creation of this time dependent uncertainty estimate for OHC.

The choice of OHC record has only a small effect on future projections of GMST using the EM-GC. Figure 4 illustrates the effect of varying OHC record on future temperature. The bottom panels show the observed and modeled OHC, the value of κ needed to best fit the OHC data record, ~~as well as the~~and the resulting value of χ^2_{OCEAN}. Of the two OHC records shown, Balmaseda et al. (2013) (Fig. 4a) yields the lowest value of κ and Ishii et al. (2017) (Fig. 4b) results in the highest estimate of κ. For the same value of AER RF_{2011} (i.e., −0.9 W m^{-2}) and GHG scenario (SSP4-3.4), we find a difference of 0.25°C in the modeled rise in GMST in year 2100 for these two simulations (red lines on top panels). For most of

the remaining analysis, we use the multi-measurement average of the five OHC data records. ~~However, in~~ In Sects. 3.1 and 3.2 we quantify the effect of OHC data record on both attributable anthropogenic warming rate and equilibrium climate sensitivity.

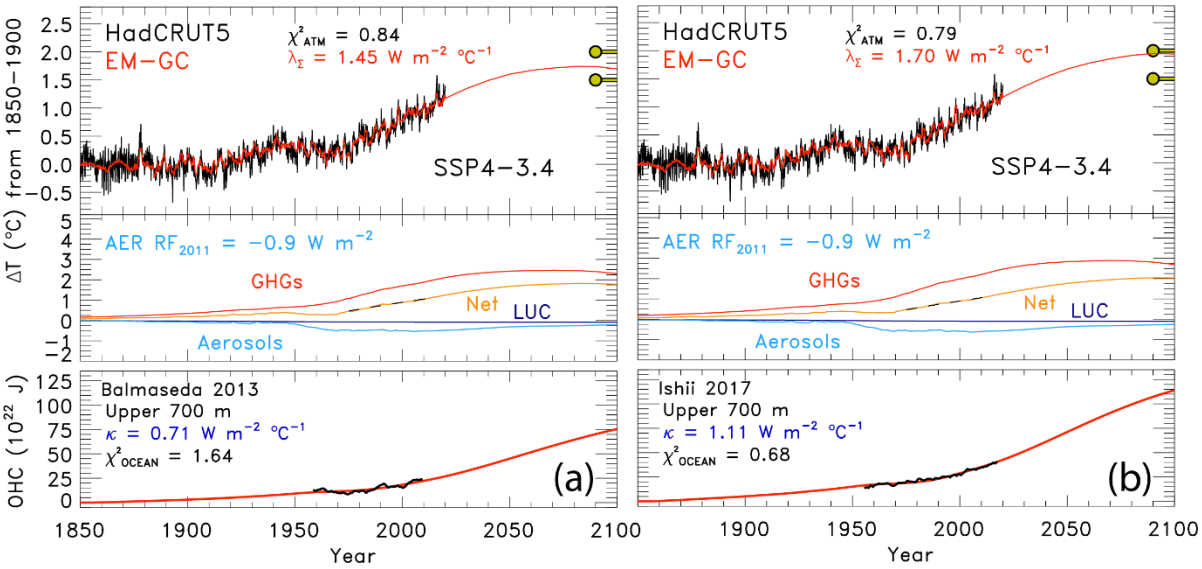

Figure 4. Measured (HadCRUT5) and EM-GC simulated GMST change (ΔT) from 1850-2019, as well as projected ΔT to year 2100 for SSP4-3.4. Top panel of each plot shows observed (black) and simulated (red) ΔT, the λ_{Σ} and χ^2_{ATM} values, and the Paris Agreement target and upper limit. The second panel displays the contribution of GHGs, aerosols, and ~~land use~~land-use change on ΔT. The bottom panel compares the observed (black) and modeled (red) OHC for two different OHC records and displays the value of κ needed to provide best-fits to the OHC record, as well as best-fit values of χ^2_{OCEAN}. Both use an aerosol RF in 2011 of −0.9 W m^{-2}. (a) OHC record from Balmaseda et al. (2013). (b) OHC record from Ishii et al. (2017).

2.3 Attributable anthropogenic warming rate

The attributable anthropogenic warming rate, or AAWR, is the time rate of change of GMST due to humans from 1975-2014. We use AAWR as a metric in the EM-GC framework to quantify the human influence on global warming over the past few decades, and most importantly to also assess how well the CMIP6 GCMs can replicate this quantity. This analysis is motivated by the study of Foster and Rahmstorf (2011), who examined the human influence on the time rate of change of GMST from 1979-2010 using a residual method. We extend the end year of our analysis to 2014 because this is the last year of the CMIP6 Historical simulation. We pushed the start year back to 1975 so that our analysis covers a forty-

year period, over which the effect of human activity on GMST rose nearly linear with respect to time (Fig. 1b and Fig. S10c).

We calculate AAWR utilizing the EM-GC by computing a linear fit to the $\Delta T_{HUMAN,ATM}$ term:

$$\Delta T_{ATM,HUMANi} = \frac{1+\gamma}{\lambda_p} \{GHG\ \Delta RF_i + AER\ \Delta RF_i + LUC\ \Delta RF_i - Q_{OCEAN}\} \quad (9)$$

for a regression that spans 1850-2019. The $\Delta T_{HUMAN,ATM}$ term represents the net impact of the change in GMST due to RF of climate by anthropogenic GHGs, tropospheric aerosols, as well as the variation in surface reflectivity due to ~~land use~~land-use change (deforestation), taking into account that for each model time step, a portion of the human-induced climate forcing is exported to the world's oceans. For each simulation, the slope of the linear least squares fit to the 480 monthly values of $\Delta T_{HUMAN,ATM}$ is used to determine AAWR. For the time period 1975-2014, a value for AAWR of 0.144 ± 0.005 °C/decade is found using a value of AER RF_{2011} equal to −0.9 W m^{-2}, where the uncertainty corresponds to the 2-~~sigma~~σ standard error of a linear least squares fit. The computation of AAWR found by fitting monthly values of $\Delta T_{HUMAN,ATM}$ is insensitive to modest changes in start and end year for the AAWR calculation (see Table S1)~~.~~, -The value of λ_{Σ}, and therefore AAWR, is also insensitive whether ~~as well as whether~~ or not the AMOC, PDO, or IOD terms are included in the regression framework (Canty et al., 2013; Hope et al., 2017). We are able to fit the climate record better (i.e. smaller values of χ^2 in Eqs. (6), (7), and (8)) ~~upon consideration~~by including ~~of~~ the AMOC term. However, computed values of AAWR are insensitive to whether ~~this term~~AMOC is used in the regression because whatever contributions the variation in the strength of the thermohaline circulation may have had on GMST are not considered in Eq. (9) (see ~~Sect. 2.3 of Hope et al. (2017)~~Fig. S11 for further explanation).

The determination of AAWR from historical CMIP6 near surface air temperature output involves conducting -a regression of deseasonalized, globally averaged, monthly ΔT ($\Delta T^{DES,GLB}$) from each GCM (Hope et al., 2017), termed the REG method. The archived CMIP6 Historical runs are constrained by observed variations in SAOD and influenced by other factors such as internal model generated ENSOs. The $\Delta T^{DES,GLB}$ time series for all of the runs from each CMIP6 GCM are averaged together to obtain one time series of $\Delta T^{DES,GLB}$ for each GCM. This average $\Delta T^{DES,GLB}$ time series is used to compute AAWR. The regression approach is used to compute the influence of SAOD on GMST from CMIP6 GCMs. The

time needed for GMST to respond to a change in the aerosol loading in the stratosphere due to a volcanic eruption in each GCM can exhibit a significant difference compared to the empirically determined response time of 6 months discussed in Sect. 2.1. A lag was determined for each GCM by calculating the value of the monthly delay between volcanic eruptions and the surface temperature response that resulted in the largest regression coefficient for SAOD. We regress the $\Delta T^{DES,GLB}$ against SAOD and the anthropogenic effect on temperature, which is approximated as a linear function from 1975-2014. The value of AAWR is the slope of the anthropogenic effect on temperature. Figure ~~S10~~ S12 illustrates the REG method used to determine AAWR from the CMIP6 GCMs. Table ~~S2~~ S3 depicts the slight effect on values of AAWR for the CMIP6 GCMs of changing the start or end year for the regression. At the time of analysis, there are 50 CMIP6 GCMs with the necessary archived output to calculate AAWR, with the values of AAWR found using REG shown in Table S3. Figure S13 and the supplement compare values of AAWR found using the REG method applied to EM-GC output with values of AAWR found using Eq. (9), as support for the validity of using the REG method to determine AAWR from CMIP6 output.

We also use a second method to extract the value of AAWR from the CMIP6 multi-model ensemble. This method, termed LIN, involves ~~the computation of~~ a linear regression of global, annual average values of GMST from the CMIP6 multi-model ensemble (Hope et al., 2017). For LIN, we exclude the years of obvious volcanic influence on the rise in GMST from the CMIP6 multi-model ensemble Historical simulations: i.e. data for 1982 and 1983 (following the eruption of El Chichón) and 1991 and 1992 (following the eruption of Mount Pinatubo) are excluded. Archived global, annual average values of GMST covering 1975-2014, excluding these four years, are fit using linear regression, with the AAWR set equal to the slope of the fit. Values of AAWR for 1975-2014 found using LIN are also shown in Table ~~S3~~ S4 for each GCM. Analysis of AAWR for these 50 GCMs of LIN versus REG (see Fig. ~~S11~~S14) results in a correlation coefficient (r^2) of 0.995 and a mean ratio of 1.009 ± 0.015, with LIN-based AAWR exceeding REG-based AAWR by about 1%. The close agreement of AAWR found using both methods provides strong evidence for the accurate determination of AAWR from the CMIP6 GCMs. We use the REG method in this analysis because it provides a more rigorous technique to remove the influence of SAOD on GMST from the CMIP6 multi-model ensemble compared to the LIN method. ~~All of our~~

~~scientific conclusions are unchanged had we used LIN based values of AAWR from the CMIP6 multi-model ensemble.~~

The CMIP6 multi-model ensemble provides simulations of near surface air temperature (TAS), which we use to calculate AAWR. The EM-GC uses blended near surface air temperature to determine values of AAWR. Cowtan et al. (2015) provide a method to create blended near surface air temperature output from the GCMs. The CMIP6 multi-model ensemble contains archived fields of TAS and the temperature at the interface of the atmosphere and the upper boundary of the ocean (TOS) (Griffies et al., 2016), whereas only a subset of GCM groups provide the archived land fraction needed to calculate blended near surface air temperature using the Cowtan et al. (2015) method. Cowtan et al. (2015) compare the modeled and measured trend in global temperature over 1975-2014 and found a 4.0% difference in the trend upon the use of blended temperature from CMIP5 GCMs, rather than global modeled TAS. Their analysis focused on a comparison of modeled and measured temperature, not just the anthropogenic component. We have used the method of Cowtan et al. (2015) to create blended CMIP6 temperature output, for the CMIP6 GCMs that provide TAS, TOS, and the land fraction. Upon our use of blended CMIP6 temperature output for these GCMs, and calculation of AAWR for 1975-2014, we find that AAWR based on blended CMIP6 temperature is 3.5% lower than AAWR found when using only TAS. Tokarska et al. (2020) estimate an effect of 0.013°C/decade in the trend of CMIP6 temperature output upon the use of blended CMIP6 temperature instead of TAS, while Cowtan et al. (2015) report a difference of 0.030°C/decade between the trend in observations and modeled output. Since the difference between values of AAWR found using blended CMIP6 temperature output and TAS is so small and does not affect any of our conclusions, we use TAS output from the CMIP6 multi-model archive because this choice allows many more GCMs to be examined.

2.4 Equilibrium climate sensitivity

The equilibrium climate sensitivity (ECS), which represents the warming that would occur after climate has equilibrated with atmospheric CO_2 at the 2×pre-industrial level (Kiehl, 2007; Otto et al., 2013; Schwartz, 2012) is also used to compare results of our EM-GC to CMIP6 multi-model output. To calculate ECS from the EM-GC, we use the following equation:

$$ECS = \frac{1+\gamma}{\lambda_P} \times 5.35\ \mathrm{W\,m^{-2}} \times \ln(2) \quad (10)$$

That represents the rise in GMST for a doubling of CO_2, assuming no other perturbations as well as equilibrium in other components of the climate system (i.e., Q_{OCEAN} = 0) (Mascioli et al., 2013). The expression for the radiative forcing of CO_2 is from Myhre (1998). The quantity γ in Eq. (10), which represents the sensitivity of the GMST to feedbacks within the climate system, is the only variable component of ECS. We only use values of γ that result in good fits ($\chi^2 \leq 2$ for Eq. (6) to (8)) between modeled and observed GMST and modeled and observed OHC.

For the estimate of ECS from the CMIP6 multi-model ensemble, we use the method described by Gregory et al. (2004) (See the supplement and Fig. S15 for more information). At the time of this analysis, 28 models released the necessary output to the CMIP6 archive (see Table S5 for the list of models and individual values of ECS). There have been some recent analyses that suggest the Gregory method may underestimate ECS (Rugenstein et al., 2020). However, ~~W~~we use the Gregory method to calculate ECS from the CMIP6 GCMs because this procedure is preferred by Eyring et al. (2016) for the use by CMIP6.

~~There have been some recent analyses that suggest the Gregory method may underestimate ECS . However, we use the Gregory method to be consistent with the approach for CMIP6 recommended by Eyring et al. (2016).~~

~~To use the Gregory method, near surface air temperature output from the Abrupt 4×CO_2 and piControl simulations, as well as net downward radiative flux output from the Abrupt 4×CO_2 simulation is used to calculate ECS. At the time of this analysis, 28 models released the necessary output to the CMIP6 archive (see Table S4 for the list of models and individual values of ECS). The near surface air temperature and net downward radiative flux was converted from monthly gridded output to annual global averages. We calculate the temperature change for the Abrupt 4×CO_2 simulation by subtracting the piControl near surface air temperature (Chen et al., 2019) (Fig. S12). This computed temperature anomaly is then regressed against the net downward radiative flux, with the x-intercept yielding the equilibrium response of ΔT to a quadrupling of CO_2. This equilibrium response is then divided by two (Jones et al., 2019) to arrive at the equilibrium climate sensitivity (Fig. S12).~~

2.5 Aerosol weighting method

Probabilistic forecasts of the future rise in GMST for various SSPs are an important part of our analysis. Probabilities of AAWR and ECS are computed by considering the uncertainty in AER RF_{2011}. We also provide probabilistic estimates of AAWR and ECS. All of these quantities are computed by incorporating the uncertainty in the radiative forcing of climate due to tropospheric aerosols within results of our EM-GC simulations. We use an asymmetric Gaussian to assign weights to the value of GMST, AAWR or ECS found for various time series of radiative forcing by aerosols associated with particular values of AER RF_{2011}. Figure 5a shows the asymmetric Gaussian function we use to maximize the values of AAWR or ECS at the best estimate of AER RF_{2011} of −0.9 W m^{-2}, accomplished by giving these values the highest weighting. The IPCC 2013 "likely" range limits of AER RF_{2011} of −0.4 and −1.5 W m^{-2} (Myhre et al., 2013) are assigned to the ~~one~~ 1~~sigma~~σ values of the Gaussian, and the AAWR or ECS estimates occurring at the "likely" range AER RF_{2011} limits are given the same weighting. The −0.1 and −1.9 W m^{-2} limits of the AER RF_{2011} range are assigned as the ~~two~~ 2~~sigma~~σ values of the asymmetric Gaussian, based ~~upon~~ on the IPCC 2013 description of these two values as being 5 and 95% uncertainty limits (Myhre et al., 2013). The Gaussian we use is asymmetric due to the fact that the distribution of the likely range and 5th and 95th percentiles of the values of AER RF_{2011} are not distributed symmetrically from the best estimate of −0.9 W m^{-2}. For example, the likely ranges of AER RF_{2011} are given as −0.4 W m^{-2} and −1.5 W m^{-2}; the −0.4 W m^{-2} value is 0.5 W m^{-2} from the best estimate whereas −1.5 W m^{-2} is 0.6 W m^{-2} from the best estimate. We fit a Gaussian to the likely range and 5th and 95th percentiles that has slightly different shape on either side of the best estimate, as shown in Fig. 5a.

Figure 5b shows the value of AAWR in °C/decade as a function of the climate feedback parameter, λ_Σ, and AER RF_{2011}. We are able to find more good fits to the observed GMST for small values of AER RF_{2011} than at larger values of AER RF_{2011}. Therefore, we bin values of AAWR (Fig. 5b), ECS (Fig. 5c), or future GMST (described in Sect. 3.3) by AER RF_{2011} and find the probability distribution for values of AAWR, ECS, or future GMST within each bin. The resulting probability distributions are assigned the weights associated with each value of AER RF_{2011} in the bins to arrive at the probabilistic estimates of AAWR or ECS shown in Sect. 3. If we did not use this procedure and instead simply averaged all of the values for AAWR and ECS shown in Fig. 5, undue emphasis would be given to model results that occur

at small AER RF_{2011} (see Fig. ~~S14~~ S16 for unweighted ECS values). This aerosol weighting method allows the expert assessment of the likely range of RF due to tropospheric aerosols given in Chapter 8 of IPCC 2013 (Myhre et al., 2013) to be quantitatively incorporated into our computations of AAWR, ECS, and GMST.

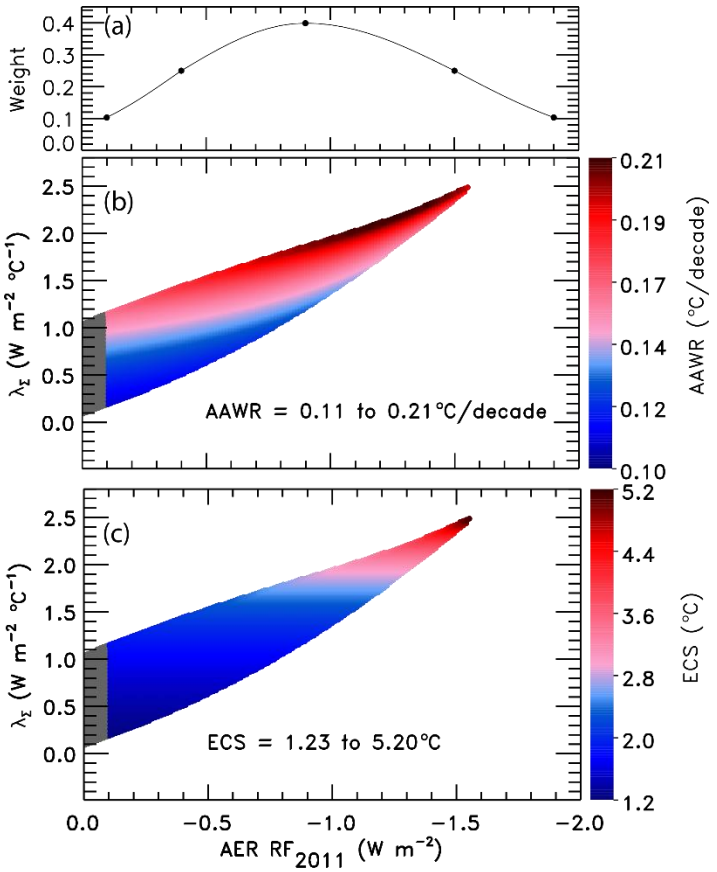

Figure 5. Aerosol weighting method. (a) The weights assigned to an asymmetric Gaussian distribution of AER RF_{2011} based on values provided by chapter 8 of IPCC 2013. The five black circles indicate the assigned weights for the AER RF_{2011} best estimate of −0.9 W m^{-2}, likely range of −0.4 and −1.5 W m^{-2}, and the 5th and 95th confidence intervals of −0.1 and −1.9 W m^{-2}. (b) Values of AAWR in °C/decade as a function of climate feedback parameter, λ_Σ, and the value of AER RF_{2011} associated with various time series for the RF of climate due to tropospheric aerosols. The colors denote the ~~various~~ values of AAWR calculated from 1975-2014 using the EM-GC trained with the HadCRUT5 ΔT record. (c) ECS in °C as a function of λ_Σ and the value of AER RF_{2011}. The colors denote ~~various~~ values of ECS found using the EM-GC. For panels (b) and (c), model results are shown only for combinations of λ_Σ and RF due to tropospheric aerosols for which good fits to the climate record could be achieved.

3 Results

3.1 AAWR, comparison to CMIP6 multi-model ensemble

An important measure of any climate model is the ability to accurately simulate the human influence on the global mean surface temperature (GMST) anomaly. We use the attributable anthropogenic warming rate (AAWR) found by our highly constrained Empirical Model of Global Climate (EM-GC) to quantify how well the CMIP6 multi-model ensemble (see Table ~~S5~~ S7 for a list of CMIP6 GCMs analyzed in this study) is able to simulate the human influence on global warming over the past several decades. ~~The EM-GC results in Fig. 6 have been constrained by blended near surface air temperature (TAS) and the temperature at the interface of the atmosphere and the upper boundary of the ocean (TOS) (Griffies et al., 2016). The CMIP6 multi-model output contains archived fields of TAS and TOS, whereas only a subset of GCM groups provide the archived land fraction needed to calculate blended near surface air temperature. Cowtan et al. (2015) compare the modeled and measured trend in global temperature over 1975-2014 and found a 4.0% difference in the trend upon the use of blended temperature from CMIP5 GCMs, rather than global modeled TAS. Their analysis focused on a comparison of modeled and measured temperature, not just the anthropogenic component. We have used the method of Cowtan et al. (2015) to create blended CMIP6 temperature output, for the CMIP6 GCMs that provide TAS, TOS, and the land fraction. Upon our use of blended CMIP6 temperature output for these GCMs, and calculation of AAWR for 1975-2014 as described in Sect. 2.3, we find that AAWR based upon blended CMIP6 temperature is 3.5% lower than AAWR found when using only TAS. Tokarska et al. (2020) estimate an effect of 0.013°C/decade in the trend of CMIP6 temperature output upon the use of blended CMIP6 temperature instead of TAS, while Cowtan et al. (2015) report a difference of 0.030°C/decade between the trend in observations and modeled output. Since the difference between values of AAWR found using blended CMIP6 temperature output and TAS is so small and does not affect any of our conclusions, we use TAS output from the CMIP6 multi-model archive because this choice allows the behavior of many more GCMs to be examined.~~

Figure 6 compares values of AAWR from 1975-2014 computed using our EM-GC with AAWR found utilizing archived output from the CMIP6 multi-model ensemble. ~~Five~~ Seven GMST data sets and five OHC records can be used to estimate AAWR with the EM-GC~~;~~. ~~for~~ For each choice, AAWR exhibits sensitivity to the variation of the time series of radiative forcing due to tropospheric aerosols. Each box

and whisker plot found using our EM-GC shows, for a particular choice of GMST and OHC data record, the 25th, 50th, and 75th percentiles of AAWR (box), and 5th and 95th percentiles (whiskers) found using the aerosol weighting method described in Sect. 2.5. The star symbol indicates the minimum and maximum values of AAWR for each value of GMST data set and OHC record. The choice of OHC record and GMST data set has a slight effect on AAWR, as shown by the colored EM-GC symbols in Fig. 6. ~~For example, switching from using the HadCRUT record to the CW14 record increases the values of λ_{Σ} that result in good fits to the climate record, which in turn affects the values of AAWR. The estimate of the value of AAWR increases from 0.143°C/decade to 0.153°C/decade when using the Cheng OHC record and changing the GMST record from HadCRUT to CW14.~~ The averages of the five 25th, 50th, and 75th percentiles of AAWR found using the HadCRUT5 data set for GMST are 0.~~115~~138, 0.~~135~~157, and 0.~~160~~176°C/decade, respectively. The 5th and 95th percentile values of AAWR from HadCRUT5 are 0.~~097~~ 120 and 0.195°C/decade.

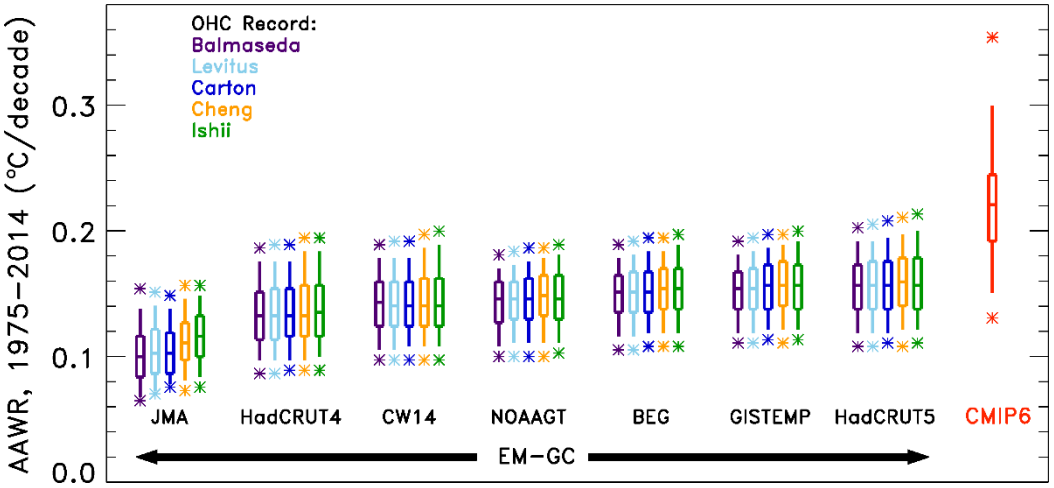

Figure 6. AAWR from the EM-GC and CMIP6 multi-model ensemble for 1975-2014. ~~Five~~ Seven temperature data sets and five ocean heat content records are used to compare values of AAWR computed from the EM-GC. The box represents the 25th, 50th, and 75th percentiles, the whiskers denote the 5th and 95th percentiles, and the stars show the minimum and maximum values of AAWR from the EM-GC based ~~upon~~ on the aerosol weighting method described in Sect. 2.5. The red box labeled "CMIP6" shows the 25th, 50th, and 75th percentiles, the whiskers represent the 5th and 95th percentiles, and the stars denote the minimum and maximum values of AAWR from the 50 member CMIP6 multi-model ensemble.

The box and whisker symbol labeled CMIP6 in Fig. 6 shows the 5th, 25th, 50th, 75th, and 95th percentiles of AAWR calculated from 50 GCMs, also from 1975-2014, as described in Sect. 2.3. The

stars denote the minimum and maximum values of AAWR from the GCMs. Two CMIP6 models exhibit values of AAWR similar to the median values we infer from the HadCRUT4, CW14, NOAAGT, BEG, ~~BEG,~~ GISTEMP, and HadCRUT5~~, NOAAGT, and CW14~~ data records using the EM-GC~~,~~. I~~i~~n particular INM-CM5-0 (Volodin and Gritsun, 2018) yields 0.147°C/decade and MIROC6 (Tatebe et al., 2019) results in 0.157°C/decade (Table ~~S3~~ S4 provides values of AAWR for all individual CMIP6 GCMs). The median value of AAWR from the CMIP6 multi-model ensemble is 0.221°C/decade, about ~~60~~40% larger than the 50th percentile value of AAWR found using the HadCRUT5 data set for GMST ~~noted above~~. The 5th, 25th, 75th, and 95th percentiles of AAWR from the CMIP6 multi-model ensemble are 0.151, 0.192, 0.245, and 0.299°C/decade, respectively. Some CMIP6 GCMs exhibit values of AAWR that are ~~almost~~ 0.14°C/decade larger than our largest empirical estimates for 1975-2014; the maximum value of AAWR from the GCMs is 0.354 °C/decade. The maximum value of AAWR based off the historical climate record using the EM-GC is 0.~~257~~213°C/decade (~~NOAAGT~~ HadCRUT5 data set using the ~~Cheng~~ Ishii et al. (2017) OHC record and a time series for RF due to tropospheric aerosols consistent with AER RF_{2011} equal to −1.~~6~~5 W m^{-2}). ~~The 95th percentiles of all~~ All of the EM-GC based values of AAWR in Fig. 6 are below the ~~75th~~ 50th percentile of AAWR from the CMIP6 multi-model ensemble of 0.~~245~~221°C/decade, supporting the notion that CMIP6 GCMs tend to exhibit a faster rate of anthropogenic warming over the past four decades than the actual atmosphere.

Our determination that the rate of global warming from the CMIP6 multi-model ensemble over the time period 1975-2014 significantly exceeds the rise in GMST attributed to human activity is aligned with a similar finding highlighted in Figure 11.25b of chapter 11 of the IPCC 2013 report that CMIP5 models tend to warm too quickly compared to the actual climate system over the time period 1975-2014 (Kirtman et al., 2013). The values of AAWR from the CMIP6 multi-model ensemble from our analysis present a similar finding as Tokarska et al. (2020) and ~~(~~CONSTRAIN~~,~~ (2020), that some of the CMIP6 models over estimate recent warming trends.~~,~~ ~~with~~ Tokarska et al. (2020) examin~~e~~~~ing~~ the trend in the human component of GMST from 1981-2014. We arrive at a similar conclusion as these studies that CMIP6 ~~models~~ GCMs overestimate the rate of global warming for the 1982-2014 time period of AAWR as shown in Table S2 and ~~2~~S3. Our results, the finding by the IPCC 2013 report, ~~and~~ Tokarska et al. (2020), and CONSTRAIN (2020) appear to be quite different than the conclusion of Hausfather et al.

(2020) that past climate models have matched recent temperature observations quite well. The Hausfather et al. (2020) study does not examine CMIP5 GCMs, let alone CMIP6 GCMs, and the last two rows of their Table 1 indicate that the skill of climate models forecasting the change in GMST over time decreased considerably between the Third Assessment Report (TAR) and the Fourth Assessment Report (AR4). The change in temperature over time for the TAR and AR4 only span 17 and 10 years, respectively (Hausfather et al., 2020). In Fig. 6, we examine the ability of the GCMs to simulate the rise in GMST attributed to humans over a 40 year time period, which provides a better measure of how well the models simulate the observations than ~~when using a~~the shorter time period. The temperature change over time for the TAR and AR4 examined by Hausfather et al. (2020) ends in 2017, which was right after a very strong ENSO, so their analysis may be influenced by the 2015 to 2016 ENSO event. In contrast, our analysis of AAWR is not influenced by natural variability such as ENSO because we examine the human component of global warming after explicitly accounting for and removing the influence of ENSO on GMST. Consequently, our determination of AAWR from observations (Table ~~S1~~S2) and GCMs (Table ~~S2~~S3) depends only to a small extent on the specification of start year (for values ranging from 1970 to 1984) and end year (2004 to 2018). Our analysis shows that upon quantification of the human driver to global warming within both the data record and climate models, the CMIP6 GCMs warm faster than observed GMST over the past four decades, regardless of precise specification of start and end year.

3.2 ECS

Equilibrium climate sensitivity (ECS) is a metric often used to compare the sensitivity of warming among GCMs, as well as with warming inferred from the historical climate record. Figure 7 shows values of ECS inferred from the climate record using our EM-GC, ~~five~~ seven GMST data sets, and five OHC records. As for AAWR, the largest variation in ECS is driven by uncertainty in AER RF_{2011}. The colored circles represent the ECS values found using the IPCC 2013 best estimate of AER RF_{2011} of −0.9 W m^{-2} (Myhre et al., 2013). The ECS values found utilizing the EM-GC are displayed using a box and whisker symbol. The middle line represents the median values of ECS, and the box is bounded by the 25^{th} and 75^{th} percentiles. The whiskers connect to the 5^{th} and 95^{th} percentiles, and the stars denote the minimum and maximum values. We use the aerosol weighting method described in Sect. 2.5 to calculate the percentiles

for ECS; values of ECS found without aerosol weighting are shown in Fig. ~~S14~~S16. Varying the choice of GMST data record has a slight effect on the value of ECS, whereas the choice of OHC record has a larger effect, as indicated by the various heights of the box and whiskers and the maximum values of ECS. In the EM-GC framework, the ocean heat export term (Q_{OCEAN}) represents disequilibrium in the climate system. We compute values of Q_{OCEAN} from various records of OHC. If the current value of Q_{OCEAN} is as large as suggested by the Cheng 2017 and Ishii et al. (2017) OHC records, then Earth's climate will exhibit a larger rise in GMST to reach equilibrium than if the value of Q_{OCEAN} inferred from the OHC record of Balmaseda et al. (2013) is correct. The averages of the 25th, 50th, and 75th percentiles of ECS found using the HadCRUT5 data set for GMST are 1.~~49~~74, ~~1.85~~2.12, and 2.~~50~~67°C, respectively. The average best estimate of ECS using the HadCRUT5 data set and an AER RF_{2011} value of −0.9 W m^{-2} is 2.~~01~~33°C.

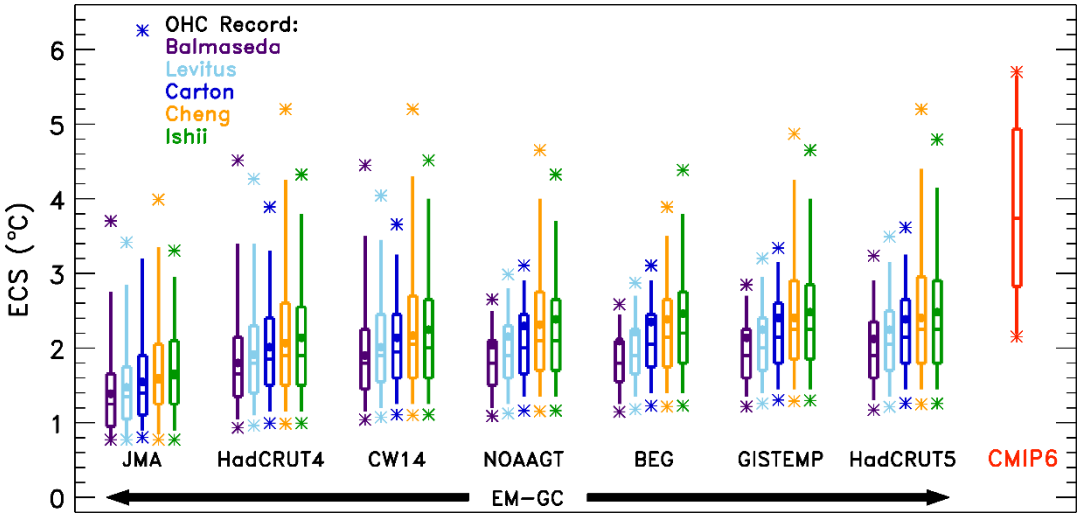

Figure 7. ECS from the EM-GC and the CMIP6 multi-model ensemble. ~~Five~~ Seven GMST data sets and five ocean heat content records are used to compare values of ECS computed from the EM-GC. The box represents the 25th, 50th, and 75th percentiles, the whiskers denote the 5th and 95th percentiles, and the stars indicate the minimum and maximum values of ECS using the EM-GC based ~~upon~~ on the weighting method described in Sect. 2.5. The circles denote the value of ECS associated with the best estimate of AER RF_{2011} of −0.9 W m^{-2}. The red box labeled "CMIP6" represents the 25th, 50th, and 75th percentiles, the whiskers denote the 5th and 95th percentiles, and the stars indicate the minimum and maximum values of ECS from the 28 member CMIP6 multi-model ensemble.

The box and whisker symbol labeled CMIP6 in Fig. 7 shows the 25th, 50th, 75th, and 5th and 95th percentiles of ECS calculated from output of 28 CMIP6 models, as described in Sect. 2.4. Minimum and maximum values are represented by the stars. The values of ECS from the CMIP6 multi-model ensemble

are larger than the majority of values inferred from the climate record using the EM-GC. The height of the box for the CMIP6 multi-model ensemble estimate of ECS is larger than the height of the boxes for ECS inferred from the climate record using the EM-GC, indicating that the GCMs exhibit a wide range of ECS values. The 25th and 75th percentiles of ECS from the CMIP6 multi-model ensemble are 2.84°C and 4.93°C, respectively. The 5th percentile of ECS from the CMIP6 multi-model ensemble is 2.19°C, and the 95th percentile is 5.65°C (see Table S4 for ECS values for specific models). In contrast, the average 5th and 95th percentiles from the EM-GC are 1.~~12~~40°C and ~~4.12~~3.57°C, respectively. The median value of ECS from the CMIP6 multi-model ensemble is 3.74°C, ~~more than double~~ 1.6 times the ~~median value~~best estimate of ~~1.85~~2.33°C found using the HadCRUT5 temperature record.

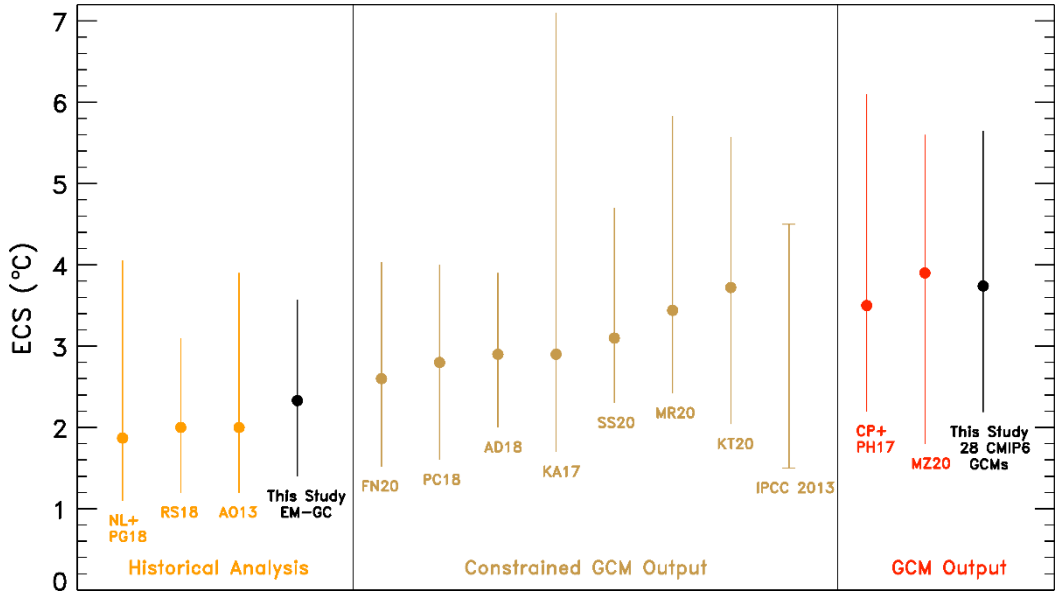

Figure 8. Values of ECS from the EM-GC (black) trained using the HadCRUT5 GMST record, our analysis of the CMIP6 multi-model ensemble (black), and 13 other studies grouped by type of analysis. The studies are listed by lead author (first initial of their first name and first initial of their last name) and the year of publication, unless there are only two authors, in which case initials of both authors are listed. Historical analysis includes Lewis and Grünwald (2018) NL+PG18, Otto et al. (2013) AO13, and Skeie et al. (2018) RS18. Constrained GCM output includes Armour (2017) KA17, Cox et al. (2018) PC18, Dessler et al. (2018) AD18, Nijsse et al. (2020) FN20, Rugenstein et al. (2020) MR20, Sherwood et al. (2020) SS20, Stocker et al. (2013) IPCC 2013, and Tokarska et al. (2020) KT20. GCM output includes Proistosescu and Huybers (2017) CP+PH17 and Zelinka et al. (2020) MZ20. See the supplement for the confidence intervals shown for each study.

~~We tested our approach of calculating ECS utilizing the EM-GC to CMIP6 GCMs by altering the EM-GC framework to include CMIP6 output (see the supplement for details). Our results in Fig. S13~~

~~show the validity of our approach. We obtain similar values of ECS for the CMIP6 GCMs using the EM-GC framework as the Gregory method. The EM-GC method is insensitive to which OHC record is used, as indicated in Fig. S13a and S13b.~~

Figure 8 summarizes values of ECS found utilizing the analysis of the century and a half long climate record using our EM-GC, our examination of a 28 member CMIP6 GCM ensemble, and 13 other recent studies. The studies are divided into three categories: those that estimated ECS based on observations (Historical Analysis), others that used GCM output but constrained the output in some way (Constrained GCM Output), and studies that examined raw GCM output (GCM Output). We obtain a best estimate for ECS of 2.~~01~~33°C using the HadCRUT5 data record and a value of AER RF_{2011} = −0.9 W m^{-2} with a range of ECS of 1.~~12~~40-~~4.12~~3.57°C (5th and 95th percent confidence interval). This estimate of ECS largely falls within the range provided by IPCC 2013 of 1.5°C to 4.5°C for ECS and is supported by three other derivations of ECS from the empirical climate record: 2.0°C (range of 1.2-3.9°C) given by Otto et al. (2013), 1.87°C (range of 1.1-4.05°C) given by Lewis and Grünwald (2018), and 2.0°C (range of 1.2-3.1°C) given by Skeie et al. (2018) (all range values are for the 5th and 95th percent confidence interval). Our estimate of ECS covers ~~the same~~a similar range of values given by Cox et al. (2018), Dessler et al. (2018), and Nijsse et al. (2020), as illustrated in Fig. 8. Our determination of ECS from the CMIP6 GCMs resembles that from Proistosescu and Huybers (2017) and Zelinka et al. (2020) as indicated in the GCM Output category of Fig. 8.

Recent studies have shown that the CMIP6 multi-model ensemble exhibits higher values of ECS than the CMIP5 models because of larger, positive cloud feedbacks within the latest models (Gettelman et al., 2019; Meehl et al., 2020; Sherwood et al., 2020; Zelinka et al., 2020). The IPCC 2013 report gives a likely range of 1.5°C to 4.5°C for ECS (Stocker et al., 2013), and some of the CMIP6 GCMs analyzed in this study have values of ECS more than 1°C above this range. However, some in the climate community seem to currently doubt whether the very large values of ECS are representative of the real world (CONSTRAIN, 2020; Forster et al., 2020; Lewis and Curry, 2018; Tokarska et al., 2020). Gettelman et al. (2019) found that the newest version of the Community Earth System Model (CESM2) has a higher value of ECS than CESM1 (5.3°C versus 4.0°C) and urge the climate community to work together to determine the plausibility of such high values of ECS. Zhu et al. (2020) found that the high

values of ECS in CESM2 and other GCMs is not supported by the paleoclimate record and are biased too warm. An analysis by Nijsse et al. (2020) coupled the CMIP6 multi-model ensemble to a two-box energy balance model and the climate record and ~~obtains~~ obtained a median value of ECS ~~from the CMIP6 multi-model ensemble~~ of 2.6°C and range of 1.52-4.03°C (5^{th} and 95^{th} percentiles) ~~coupled to a two-box energy balance model and the climate record~~. Similarly, Sherwood et al. (2020) conclude cooling during the Last Glacial Maximum provides strong evidence against ECS being greater than 4.5°C and conclude ECS lies within the range of 2.3 to 4.7°C at the 5^{th} to 95^{th} percent confidence intervals.

We obtain a wide range of ECS values from our EM-GC simulations of the climate record due to consideration of the uncertainty in the radiative forcing of climate ~~due to~~from tropospheric aerosols (Figs. 5c and ~~8~~7). However, under one circumstance, we find values of ECS using the EM-GC that are similar to the maximum value of ECS from the CMIP6 multi-model ensemble. Our ~~very~~ large estimate of ECS occurs if we assume that anthropogenic aerosols have exhibited ~~very~~ strong cooling and offset a large amount of greenhouse gas warming, such that the observed GMST record can only be well simulated under the condition of large climate feedback (i.e., values of λ_Σ in Eq. (3) greater than or equal to 2.~~5~~ 45 W m^{-2} $°C^{-1}$). If aerosols have truly strongly cooled the climate, offsetting the vast majority of the rise in RF due to greenhouse gases as suggested by Shen et al. (2020), the actual value of ECS may lie close to 5°C or larger. Under the ~~more likely~~ scenario that aerosols have not cooled this strongly (~~as suggested by~~ Bond et al., ~~(~~2013)), then it is ~~more~~ feasible that ECS lies well below 5°C. The highest values of ECS found using our analysis (red portion of Fig 5c) are assigned low weights due to the assessment by Myhre et al. (2013) that the large AER RF_{2011} associated with these ECS values is unlikely.

Four empirical determinations of ECS (our study plus Lewis and Grünwald (2018), Otto et al. (2013), and Skeie et al. (2018)) and the CMIP5 or CMIP6-constrained estimates of Cox et al. (2018), Dessler et al. (2018), and Nijsse et al. (2020) are in slight contrast with the 2.3-4.7°C range for ECS (5^{th} and 95^{th} confidence interval) published recently by Sherwood et al. (2020) (Fig 8). As noted above, Sherwood et al. (2020) use paleoclimate data to rule out the high range of ECS. They rely on a determination that the feedback due to clouds is moderately to strongly positive to rule out the low range of ECS found by our analysis and the studies noted above. We caution that knowledge of the cloud feedback from observations is generally limited to databases such as the International Satellite Cloud

Climatology Project (ISCCP) (Schiffer and Rossow, 1983) and Pathfinder Atmospheres Extended (PATMOS-x) (Foster and Heidinger, 2013). ~~that,~~ W~~w~~hile these databases are monumental in terms of complexity and scope, they cover only a fairly short (i.e., about 36 years) part of the century and a half climate record (Klein et al., 2017; Sherwood et al., 2020). Most assessments of total cloud feedback rely on some combination of observations such as ISCCP, PATMOS-x, or other satellite records together with the results of regression analysis, GCM projections, and large eddy simulations that are able to resolve some of the convective processes involved in cloud formation (Klein et al., 2017; Sherwood et al., 2020). The most important component of the global cloud feedback is tropical low clouds, which Sherwood et al. (2020) consider to exert a positive feedback on climate based largely on the results of Klein et al. (2017). The determination by Klein et al. (2017) of a likely positive feedback for tropical low altitude clouds is based on the mean and standard deviation of the central value of this feedback determined by five studies, even though four of these studies exhibit uncertainties that encompass zero feedback and the fifth nearly reaches zero (their Fig. 3). This fact, combined with the recent study by Weaver et al. (2020) who report no long term statistically significant trend in global cloud reflectivity at 340 nm averaged between 45° S and 45° N based on analysis of data collected by a variety of NOAA and NASA satellite instruments, causes us to suggest the true value of ECS may lie below the 2.3°C lower limit given by Sherwood et al. (2020).

In our model framework, the largest uncertainty in ECS is driven by imprecise knowledge of the radiative forcing of climate by tropospheric aerosols. As shown in Fig. 5c, a wide range of ECS values can be inferred from the century and a half long climate record. We stress that each value of ECS shown in Fig. 5c is based ~~upon~~ on a simulation for which χ^2_{ATM}, χ^2_{RECENT}, and χ^2_{OCEAN} are all less than or equal to 2. Better knowledge of AER RF for the contemporary atmosphere would lead to a reduction in the uncertainty of ECS. Numerous studies of the climate record, including our century and a half simulations, infer the possibility of lower values of ECS than was given by a recent analysis of studies that involve examination of data from compendiums such as ISCCP and PATMOS-x (Sherwood et al., 2020). However, the analysis by Sherwood et al. (2020) did not examine consistency of the inferred value of ECS with the ability of models to accurately simulate the GMST anomaly between 1850 and present or over the past 40 years.

We conclude this section by commenting on the relationship between ECS and AAWR in our model framework. Eight of the CMIP6 GCMs (GFDL-ESM4, GISS-E2-1-G, INM-CM5-0, INM-CM4-8, MIROC6, MIROC-ES2L, NorESM2-LM, and NorESM2-MM) exhibit values of ECS and AAWR consistent with the minimum and maximum estimates based on our EM-GC constrained by the HadCRUT5 GMST record (Table S5 and Fig. S17). An analysis of the relationship between AAWR and ECS from the CMIP6 GCMs illustrates that 78% of the variance in ECS among the 28 CMIP6 GCMs that provide both quantities is explained by AAWR (see Fig. S17). This result indicates CMIP6 GCMs that accurately simulate the rise in observed ΔT over the past few decades exhibit values of ECS that are in line with our empirically based estimate.

3.3 Future projections

3.3.1 CMIP6

The CMIP6 multi-model archive provides future projections of the GMST anomaly relative to pre-industrial (ΔT) using the ScenarioMIP Shared Socioeconomic Pathways (SSPs). Figure 9 shows the CMIP6 multi-model ensemble projections of ΔT for the four SSPs (SSP1-1.9, SSP1-2.6, SSP4-3.4, and SSP2-4.5) highlighted in our analysis. Each SSP scenario has varying amounts of gridded, monthly mean TAS projections submitted to the CMIP6 archive by GCMs ~~(indicated on each plot)~~. ~~Global, monthly ΔT was created by averaging the TAS output over the globe with a cosine latitude weighting.~~ The global, monthly ΔT time series for all of the runs for each CMIP6 GCM were averaged together to obtain one time series of ΔT. The varying amount of GCM output available for each SSP scenario is due to the fact that: a) SSP1-2.6 and SSP2-4.5 are Tier 1 scenarios (O'Neill et al., 2016) and are designated as priority over the other SSPs (as described in Sect. 2.2.2), and b) not all GCMs have provided results to the CMIP6 archive at the time of the analysis. More CMIP6 multi-model output will likely become available as modeling groups who have not submitted output to the CMIP6 archive finalize their results. However, we do not expect additional GCM simulations will affect our conclusions unless the GCM output is significantly different than that currently available.

The red trapezoid in Fig. 9 labeled as the IPCC 2013 likely range is the same trapezoid as that displayed on Figure 11.25b from chapter 11 of the IPCC 2013 report (Kirtman et al., 2013). ~~All of t~~The

recent observations of ΔT from HadCRUT5 lie ~~within~~ towards the top of the likely range of warming designated by this trapezoid. Many of the projections of the rise in ΔT from the CMIP6 multi-model ensemble lie above the IPCC 2013 likely range of warming. The Paris Agreement target of 1.5°C and upper limit of 2.0°C are shown as yellow circles, included to allow for comparison of the future projections of ΔT from the CMIP6 multi-model ensemble with the goals of the agreement. The thick blue line on each plot is the CMIP6 multi-model mean of ΔT, and the dashed blue lines are the minimum and maximum ΔT projections from the CMIP6 multi-model ensemble. For SSP1-1.9, the multi-model mean projection of ΔT in 2100 from the CMIP6 GCMs lies just above the Paris Agreement target at 1.6°C, whereas for SSP1-2.6 the CMIP6 multi-model mean reaches the Paris Agreement upper limit of 2.0°C at the end of this century. For both SSP4-3.4 and SSP2-4.5, the end of century CMIP6 multi-model mean lies above the Paris Agreement upper limit at 3.0°C and 3.1°C, respectively.

Figure 9 illustrates there ~~is a bimodality~~are two groups of CMIP6 multi-model projections of ΔT, with a few GCMs having future values of ΔT that are considerably higher than others. This divergence for GCM projections of ΔT is especially evident in Fig. 9a, c, and d. The two CMIP6 GCMs that have the highest values of ΔT across the four SSPs are CanESM5 (Swart et al., 2019) and UKESM1 (Sellar et al., 2020). The CanESM5 and UKESM1 GCMs have the highest values of AAWR (0.354°C/decade and 0.299°C/decade, respectively), large values of ECS (5.70°C and 5.40°C, respectively), and exceed observed ΔT reported by HadCRUT5 for the past few decades ~~(apparent in Fig. 9)~~.

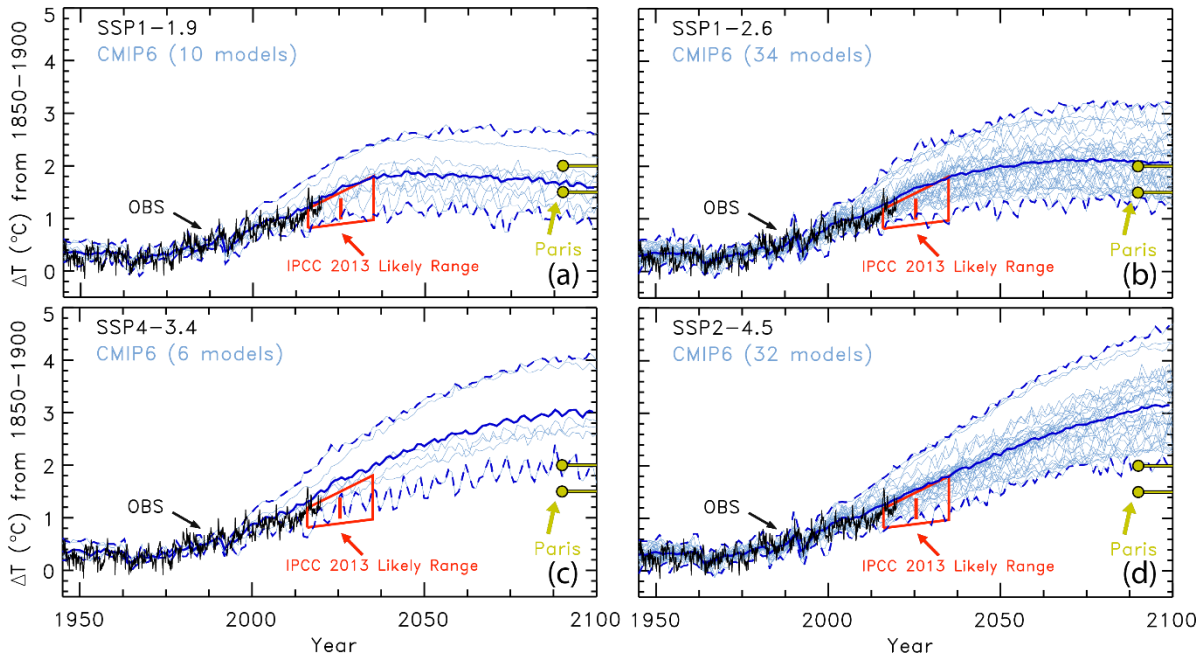

Figure 9. Historical simulations and future projections of GMST from the CMIP6 multi-model ensemble for several SSP scenarios. (a) GCM simulations from the Historical experiment, and future model projections from SSP1-1.9. Observations (black) are from ~~HadCRUT~~ HadCRUT5 to the end of 2019. The IPCC 2013 likely range of warming (red) is from Figure 11.25b from chapter 11 of the IPCC 2013 report. The CMIP6 multi-model mean (thick, blue) and minimum and maximum (dashed, blue) lines are shown. Global, monthly ΔT was created by averaging the TAS output over the globe with a cosine latitude weighting. The Paris Agreement target of 1.5°C and upper limit (yellow) of 2.0°C are included to demonstrate how the GCM projections compare. (b) Future GMST projections from SSP1-2.6. (c) Future GMST projections from SSP4-3.4. (d) Future GMST projections from SSP2-4.5.

3.3.2 EM-GC

The EM-GC is also used to project future changes in ΔT using the SSPs. Figure 10 shows the GMST anomaly in 2100 from pre-industrial (ΔT_{2100}) as a function of the climate feedback parameter and AER RF_{2011}, for the four SSPs highlighted throughout. Only model runs from the EM-GC that achieved a good fit to the climate record ($\chi^2_{ATM} \leq 2$, $\chi^2_{RECENT} \leq 2$, $\chi^2_{OCEAN} \leq 2$) are shown. The EM-GC runs that satisfy these three χ^2 constraints but fall outside of the IPCC 2013 range for AER RF_{2011} (Myhre et al., 2013) are shaded grey (left hand side of each panel). We do not consider the EM-GC projections that lie outside of the IPCC 2013 range for AER RF_{2011} in our projections of ΔT, yet these results are shown to illustrate that the EM-GC can fit the climate record with estimates of the RF due to tropospheric aerosols that lie below (i.e., less cooling) of the 5th confidence interval of −0.1 W m^{-2} for AER RF_{2011} given by IPCC 2013. We cannot establish any good fits of the ~~climate~~ HadCRUT5 GMST record for AER RF_{2011} with a

cooling stronger than about −1.~~6~~55 W m^{-2}. The range of ΔT_{2100} we compute using the EM-GC for SSP1-1.9, SSP1-2.6, SSP4-3.4, and SSP2-4.5 are 0.~~65~~75-2.~~16~~06°C, 0.~~82~~96-2.~~78~~58°C, 1.~~00~~18-3.~~28~~01°C, and 1.~~21~~45-3.~~78~~47°C, respectively. Results for SSP4-6.0, SSP3-7.0, and SSP5-8.5 are shown in Fig. ~~S15~~S18: ΔT_{2100} ranges are 1.~~41~~70-4.~~47~~02°C, ~~1.84~~2.26-~~5.56~~4.93°C, and 2.~~13~~62-~~6.75~~6.02°C for these three scenarios.

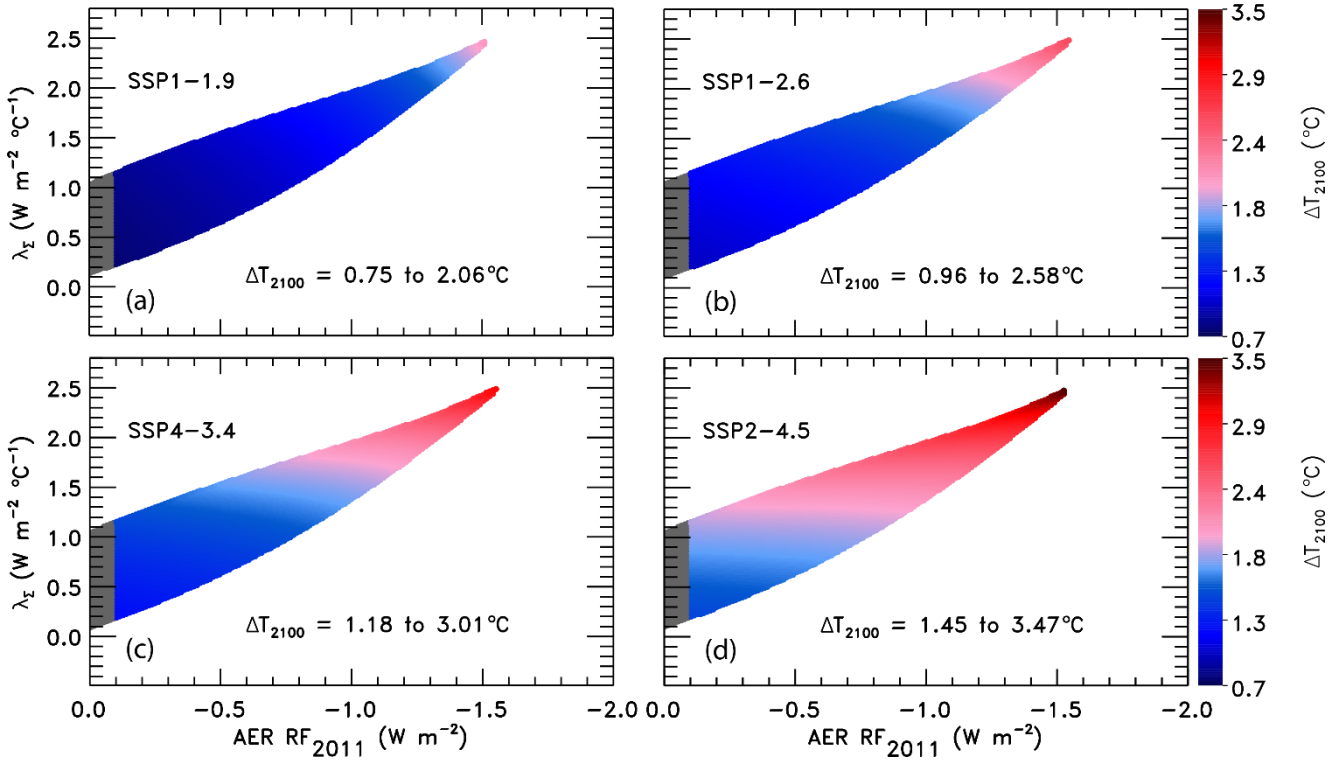

Figure 10. ΔT_{2100} as a function of climate feedback parameter and tropospheric aerosol radiative forcing in 2011 using the EM-GC trained with the HadCRUT5 ΔT record. (a) Future GMST change for SSP1-1.9. The region outside of the AER RF_{2011} range provided by IPCC 2013 is shaded (grey). Colors denote the GMST change in year 2100 relative to pre-industrial. The color bar is the same across all four panels for comparison. (b) GMST anomaly for SSP1-2.6. (c) Future temperature change for SSP4-3.4. (d) GMST anomaly for SSP2-4.5.

The large range of ΔT_{2100} found for any given SSP scenario ~~(i.e., a factor of 3.1 difference between the smallest and largest end of century warming for SSP2-4.5)~~ is caused by the fact that the climate record can be fit nearly equally well by a considerably large combination of the climate feedback parameter (our λ_Σ) and scenarios for radiative forcing due to tropospheric aerosols. The more aerosols have cooled, offsetting the relatively well-known warming due to GHGs, the larger λ_Σ must be to fit the climate record.

Since the RF of aerosols is set to diminish in the future due largely to public health concerns (Lelieveld et al., 2015; Shindell et al., 2016; Smith and Bond, 2014), the part of our model ensemble requiring relatively large values of λ_{Σ} to achieve a good fit to the climate record will result in higher values of ΔT_{2100} than other members of our model ensemble with small values of λ_{Σ}. Most GCMs sample only a small portion of the possible combinations of λ_{Σ} and AER RF_{2011} shown in Figs. 10 and ~~S8~~S18.

3.3.3 Comparing CMIP6 and EM-GC

Time series of future projections of ΔT from the EM-GC can be illustrated as probabilistic forecasts. Figure 11 shows the change in future ΔT for SSP1-1.9, SSP1-2.6, SSP4-3.4, and SSP2-4.5 colored by the probability of reaching at least that rise in ΔT by the end of the century. The EM-GC probabilities are computed from ensemble members for model runs constrained by the HadCRUT5 data records for GMST and the average of 5 OHC data records (Fig. ~~S8~~S9) based ~~upon~~ on the aerosol weighting method, described in Sect. 2.5. The trapezoid from chapter 11 of IPCC 2013 (Kirtman et al., 2013) is shown on Fig. 11 in black to highlight that the EM-GC projections of the future rise in ΔT lie within the IPCC 2013 likely range of warming. The Paris Agreement target and upper limit are included to compare the EM-GC projections of future ΔT to the Paris Agreement goals. The white shaded region is the EM-GC's median estimate of future ΔT for each SSP scenario. The median estimate for ΔT_{2100} for simulations using SSP1-1.9 and SSP1-2.6 falls below the Paris Agreement target at 1.~~0~~1°C and 1.~~3~~4°C, respectively. The median estimate of ΔT_{2100} from the EM-GC for SSP4-3.4 is between the Paris Agreement target and upper limit at 1.~~6~~8°C. For SSP2-4.5 the median estimate of ΔT_{2100} is 2.1°C, which is just ~~just below~~above the Paris Agreement upper limit ~~at 1.9°C~~. The CMIP6 minimum, multi-model mean, and maximum projections of ΔT, based on the ensembles ~~identical to those~~ in Fig. 9, are also shown in Fig. 11. The CMIP6 minimum projection of the rise in ΔT falls near the EM-GC median estimate of ΔT for each SSP scenario. The CMIP6 multi-model mean value of the future change in ΔT falls below the EM-GC maximum value of ΔT, while the CMIP6 maximum value is far above the maximum projections of the future rise in ΔT using the EM-GC. Results for SSP4-6.0, SSP3-7.0, and SSP5-8.5 are provided in Fig. ~~S16~~S19.

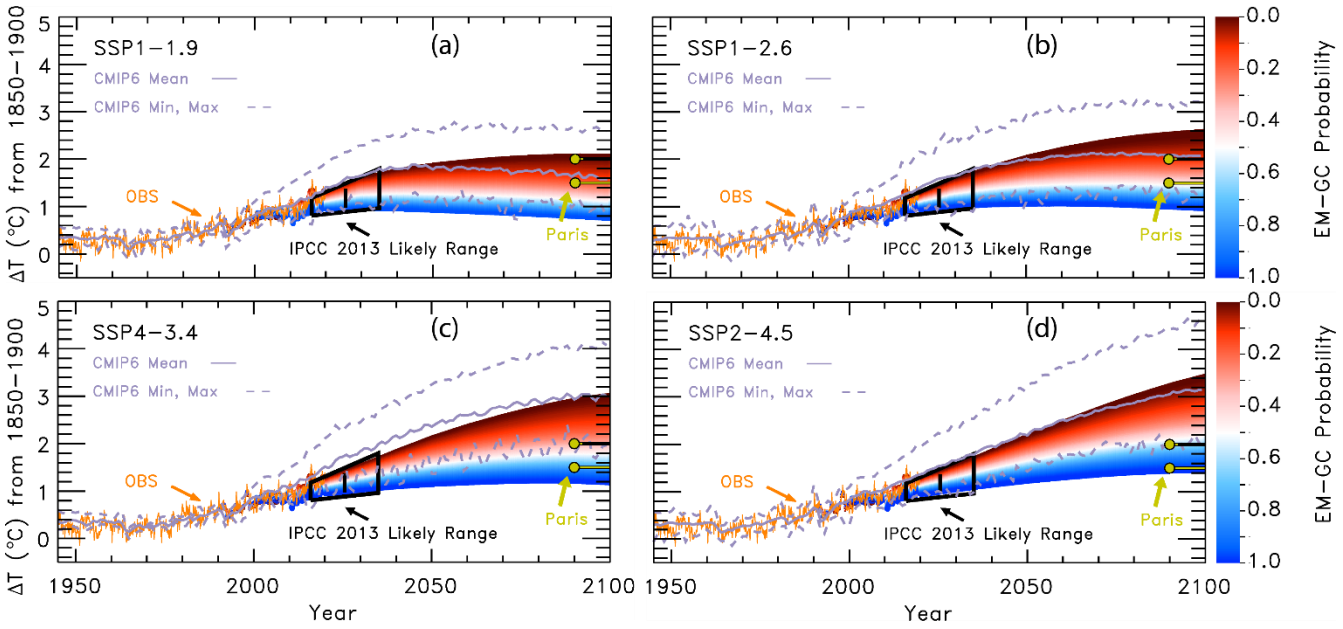

Figure 11. Probabilistic forecasts of the future rise in ΔT from the EM-GC trained using the HadCRUT5 ΔT record for several SSPs. (a) Future projections of ΔT for SSP1-1.9. Observations (orange) are from HadCRUT5. The IPCC 2013 likely range of warming (black) is from Figure 11.25b of chapter 11 of IPCC 2013. The Paris Agreement target and upper limit (yellow) are shown for comparison to EM-GC projections. The CMIP6 minimum, multi-model mean, and maximum values of ΔT are shown to compare to EM-GC projections. Colors denote the probability of reaching at least that temperature by the end of the century. (b) Future projections of ΔT for SSP1-2.6. (c) Future projections of ΔT for SSP4-3.4. (d) Future projections of ΔT for SSP2-4.5.

Figure 12 compares probability distribution functions (PDFs) for the projection of ΔT_{2100} utilizing the EM-GC with the HadCRUT5 GMST record and average of the five OHC data sets ~~and the CW14 GMST record combined with the Cheng 2017 OHC record,~~ and the CMIP6 multi-model ensemble. ~~The CW14 PDF is shown to illustrate the slight sensitivity of our projections of ΔT_{2100} to the choice of GMST and OHC records.~~ For the CMIP6 multi-model results, we compute the probabilities of achieving the Paris Agreement target of 1.5°C and upper limit of 2.0°C (at the end of the century) by calculating how many of the GCMs participating in each scenario have projections of ΔT_{2100} below the target or upper limit. ~~In contrast, the~~ The probabilities for the projections of ΔT_{2100} using ~~our~~ the EM-GC are computed using the aerosol weighting method, described in Sect. 2.5. The height of each histogram represents the probability that a particular range of ΔT_{2100}, defined by the width of each line segment, will occur. The left-hand y-axis displays the probability of ΔT_{2100} using the EM-GC, while the right-hand y-axis represents the probability of ΔT_{2100} using the CMIP6 multi-model simulations. The values on the CMIP6

multi-model ensemble y-axis are double the values on the EM-GC y-axis, for visual comparison. The solid black line denotes the Paris Agreement target and the dotted black line signifies the upper limit on each panel. The PDFs for SSP4-6.0, SSP3-7.0, and SSP5-8.5 are shown in Fig. ~~S17~~S20.

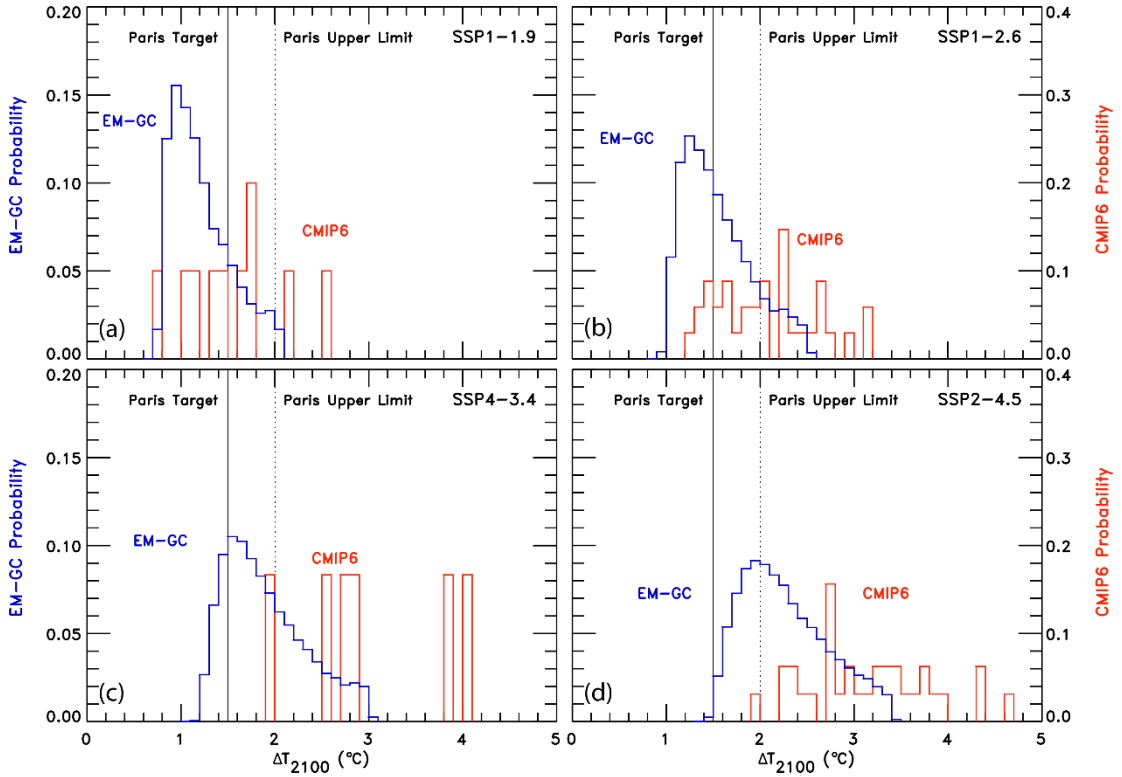

Figure 12. Probability density functions (PDF) for ΔT_{2100} found using the EM-GC ~~with the HadCRUT temperature record (dark blue), the EM-GC~~ trained with the ~~CW14~~ HadCRUT5 temperature record (~~light~~ dark blue)~~,~~ and CMIP6 multi-model results (red). (a) PDF for EM-GC results and CMIP6 multi-model results for SSP1-1.9. The left-hand y-axis is for EM-GC probabilities and the righthand y-axis is for the CMIP6 multi-model ensemble probabilities. (b) PDF for SSP1-2.6. (c) PDF for SSP4-3.4. (d) PDF for SSP2-4.5.

Numerical values of probabilities for staying at or below the Paris Agreement target for SSP1-2.6 or upper limit for SSP4-3.4 ~~for all seven~~are given for ~~SSP scenarios are given in~~the seven GMST records using the EM-GC and CMIP6 multi-model ensemble in Table 1. Projections of ΔT_{2100} based on the EM-GC provide more optimism for achieving the Paris Agreement goals than the CMIP6 multi-model ensemble, regardless of which GMST data record is used. For simulations constrained using the HadCRUT5 record, ~~T~~the SSP1-2.6 scenario provides a 53% (Table 1) likelihood of ΔT_{2100} staying at or below 1.5°C and SSP4-3.4 results in a 64% likelihood of limiting warming to 2.0°C by end of century.

The probability of achieving the Paris Agreement target or upper limit increases upon using HadCRUT4 rather than HadCRUT5 in the EM-GC framework. The probability of achieving the 1.5°C target for SSP1-2.6 and 2.0°C upper limit for SSP4-3.4 using the HadCRUT4 GMST record are 64% and 74%, respectively (Table 1). This decline in attainment of the goals of the Paris Agreement upon use of HadCRUT5 reflects more rapid warming of this data record compared to HadCRUT4 (Fig. S4e versus S4c). The rapid warming in HadCRUT5 is driven by more accurate buoy records for SST and a statistical gap filling procedure to attain global coverage (Morice et al., 2021). The impact on the likelihood of achieving the Paris Agreement goals of for the other SSP scenarios upon using the HadCRUT4 or HadCRUT5 data records is detailed in Table S6.

An analysis ~~SSP1-1.9 scenario results in an 84.1% probability of ΔT_{2100} staying at or below 1.5°C, while SSP1-2.6 gives a 64.8% likelihood of global warming staying at or below 1.5°C by end of century (Table 1) using the HadCRUT temperature record. The probabilities decrease to 82.4% and 57.0% upon the use of the CW14 temperature record and OHC from Cheng 2017. The SSP1-1.9 scenario involves extreme climate mitigation that is unlikely to happen in the next few years with atmospheric CO_2 peaking close to present day values (Fig. 2a). The SSP1-2.6 scenario requires less climate mitigation than SSP1-1.9 (though still requires net negative emissions towards the end of the century) and provides greater than a 50% likelihood of staying at or below the Paris Agreement target, thus we designate SSP1-2.6 as the 1.5°C pathway in our model framework instead of SSP1-1.9. by This result is supported by~~ Tokarska et al. (2020) supports our finding of a higher likelihood of attaining the goals of the Paris Agreement than suggested by the CMIP6 multi-model ensemble. Tokarska et al. (2020) ~~, who~~ filter the CMIP6 multi-model output on the level of agreement with observations to show that the SSP1-2.6 scenario has a likely range of warming at 1.33-1.99°C above preindustrial by end of century.~~, based upon filtering CMIP6 GCM output on the level of agreement with the observed climate record.~~ Previous studies suggested that a 2.6 W m^{-2} scenario was in line with the 2.0°C goal (Kriegler et al., 2014, 2015; O'Neill et al., 2016; Riahi et al., 2015). ~~However, o~~Our analysis suggests the 2.6 W m^{-2} scenario provides between ~~between a 57-65~~a 86-98% probability of limiting warming to 2.0°C and a 53-78% probability of achieving the more stringent 1.5°C target, depending on the GMST record (Table 1) ~~depending on the choice of GMST and~~

~~OHC data records.~~, ~~and~~ If GHGs were to follow SSP4-3.4, we find a 19-58% probability of limiting warming to 1.5°C and~~that a 3.4 W m^{-2} scenario (i.e., SSP4-3.4) is in line with the 2.0°C goal and has~~ ~~about~~ a ~~70-74~~64-87% probability of limiting warming to 2.0°C ~~(Table 1) depending on the choice of the same data records~~. ~~We therefore designate SSP4-3.4 as the 2.0°C pathway.~~ Significant climate mitigation efforts will be required to keep the growth of CO_2, CH_4, and N_2O below the trajectories shown for SSP1-2.6 ~~(1.5°C pathway in our model framework)~~ and SSP4-3.4 ~~(2.0°C pathway)~~ (Fig. 2).~~Results utilizing the EM-GC and HadCRUT GMST combined with the average OHC are shown in the top half of the table, and probabilities using the CW14 GMST and Cheng 2017 OHC records are shown in the bottom half. The CMIP6 multi-model projections exhibit lower probabilities of achieving the goals of the Paris Agreement than the projections using the EM-GC. In the creation of ScenarioMIP, SSP1-2.6 was designed to be a scenario that achieved the Paris Agreement goals and likely (greater than 66% probability (Stocker et al., 2013)) limited warming below 2.0°C, and was expected to produce a future rise in ΔT_{2100} of 1.7°C (O'Neill et al., 2016). The CMIP6 multi-model probability of SSP1-2.6 to stay at or below 2.0°C is 51.5%, as shown in Table 1. Based on our analysis, the CMIP6 multi-model ensemble does not indicate SSP1-2.6 as being a 2.0°C pathway, because it will only provide about a 50:50 likelihood of limiting warming below 2.0°C.~~

Table 1. Probability of achieving the Paris Agreement target (SSP1-2.6) or upper limit (SSP4-3.4) for seven GMST records using the EM-GC and the CMIP6 multi-model ensemble.~~List of SSP scenarios analyzed in this study and the probabilities of achieving the Paris Agreement target or upper limit based on the EM-GC using the HadCRUT4 GMST data set and average of the five OHC records and the CMIP6 multi-model ensemble. The second half of the table shows the probabilities of achieving the Paris Agreement target or upper limit based on the EM-GC using the CW14 GMST record and Cheng 2017 OHC data set.~~ The probabilities using the EM-GC are computed using the aerosol weighting method. The probabilities using the CMIP6 models are computed by calculating how many of the models for that scenario are below the temperature limits compared to the total number of models.

	Probability of Staying at or Below 1.5°C		Probability of Staying at or Below 2.0°C	
	SSP1-2.6	SSP4-3.4	SSP1-2.6	SSP4-3.4
CMIP6	18%	0%	47%	17%
HadCRUT5	53%	19%	86%	64%
GISTEMP	55%	20%	88%	69%
CW14	60%	29%	89%	71%
NOAAGT	61%	27%	90%	74%
BEG	62%	26%	98%	76%
HadCRUT4	64%	35%	90%	74%

JMA	78%	58%	95%	87%
SSP1-1.9	82.4%			97.5%
SSP1-2.6	57.0%			85.5%
SSP4-3.4	28.1%			69.6%
SSP2-4.5	4.2%			43.2%
SSP4-6.0	0.0%			17.4%
SSP3-7.0	0.0%			0.0%
SSP5-8.5	0.0%			0.0%

3.3.4 Transient climate response and cCarbon budgets

The transient climate response to cumulative emissions (TCRE) relates the rise in ΔT to the cumulative amount of carbon released into the atmosphere by human activities. We illustrate TCRE from the EM-GC as probabilistic forecasts, as shown in Fig. 13S21, to analyze future projections of ΔT. We use the probabilistic forecasts in Fig. S21 to determine the carbon budgets in Table 2. Figure 13 displays the GMST anomaly from pre-industrial versus the cumulative emissions of CO_2, in Gt C, since 1870. The orange line represents observations of ΔT from HadCRUT plotted against cumulative carbon emissions from the Global Carbon Budget project (Friedlingstein et al., 2019). The colors represent the probability that ΔT will rise to the indicated level, considering only acceptable fits to the climate record, for the EM-GC ensemble run constrained to match GMST from HadCRUT and the mean OHC record from the five OHC data records (Fig. S8) and using the aerosol weighting method. The dotted and dashed horizontal lines are placed at ΔT values of 1.5°C and 2.0°C, the target and upper limit of the Paris Agreement. The intersections of the light grey curve with the dotted horizontal line represent the 95% probability of the Paris Agreement target being achieved, and the intersections of the light grey curve with the dashed horizontal line represent the 95% probability of the Paris Agreement upper limit being achieved. The intersection of these horizontal lines with the dark grey and the black curves are the 66% and 50% probabilities, respectively of the Paris Agreement target or upper limit being attained. The SSP5-8.5 scenario was used to calculate TCRE because this scenario has the highest cumulative carbon emissions needed to provide the most complete relation between ΔT and future emissions.

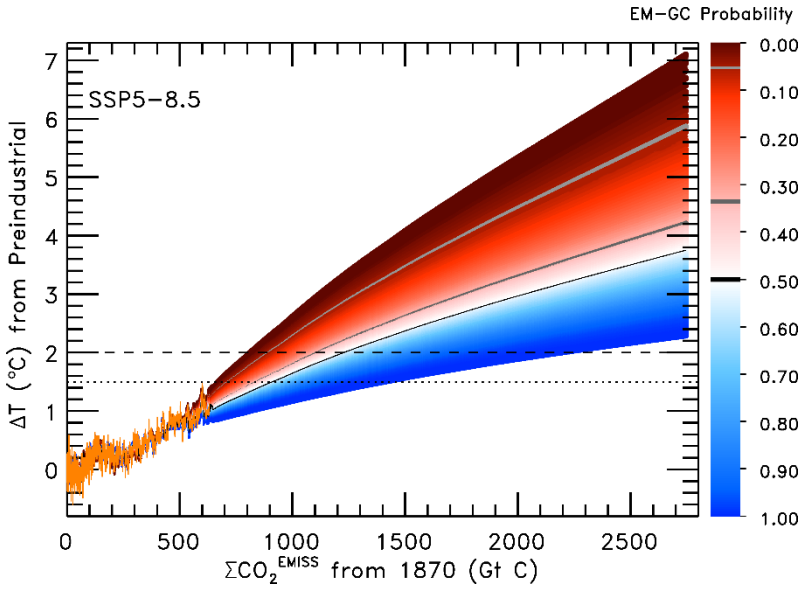

Figure 13. Transient climate response to cumulative CO_2 emissions for SSP5-8.5 using the EM-GC. Simulations of the rise in ΔT versus cumulative CO_2 emissions in units of Gt C. The orange line is observations of ΔT from HadCRUT plotted against cumulative carbon emissions from the Global Carbon Budget project (Friedlingstein et al., 2019). The dotted and dashed lines denote the Paris Agreement target and upper limit, respectively. The EM-GC projections represent the probability that the future value of ΔT will rise to the indicated level, considering only acceptable fits to the climate record. The light grey, dark grey, and black curves denote the 95, 66, and 50% probabilities of either the Paris target (intersection of dotted horizontal lines) or upper limit (intersection of dashed lines with curves) being achieved.

Table 2 contains estimated carbon budgets from our analysis in the form of the total CO_2 emissions (Gt C) since 1870 that result in a 95%, 66%, and 50% probability of the future rise in ΔT staying below the Paris Agreement target of 1.5°C and upper limit of 2.0°C and the future CO_2 emissions since 2019. Examination of Friedlingstein et al. (2014) and Murphy et al. (2014) led to our determination that the uncertainty in estimates of atmospheric CO_2 from emissions driven runs of CMIP5 coupled atmospheric / carbon cycle models is about 10% (1-sigma). The largest variation in our carbon budget estimates is driven by the uncertainty in AER RF, which is incorporated into the probability of achieving the Paris Agreement target and upper limit (see Fig. S21 and the supplement). We therefore useinclude a 10% as the uncertainty, determined from examination of CMIP5 coupled atmospheric / carbon cycle models from Friedlingstein et al. (2014) and Murphy et al. (2014) (see the supplement for more information), within each probability of attaining the Paris goals to represent in how atmospheric CO_2 will respond to the prescribed carbon emissions.

~~We apply the 10% uncertainty estimate to the future remaining carbon budget.~~ To obtain a ~~a 95% likelihood of limiting the rise in future ΔT below 1.5°C, only 746 ± 75 Gt C since 1870 can be released into the atmosphere. For a~~ 66% likelihood of limiting the rise in future ΔT below 1.5°C, only ~~906~~ 790 ± ~~91~~ 79 Gt C can be released.~~, while for a 50% probability 974 ± 97 Gt C in total can be emitted. To have~~For a ~~95% probability of ΔT staying below the 2.0°C upper limit, 933 ± 93 Gt C since 1870 can be released into the atmosphere. For a~~ 66% likelihood of the rise in ΔT staying below the 2.0 °C upper limit, 1,~~203~~ 040 ± ~~120~~ 104 Gt C can be emitted~~, whereas for a 50% likelihood 1,323 ± 132 Gt C can be released~~. To place these numbers in their proper perspective, about ~~638~~ 640 Gt C have been released from 1870 through the end of 2019 due to ~~land use~~land-use change, fossil fuel emissions, gas flaring, and cement production according to the Global Carbon Budget project (Friedlingstein et al., 2019). In our model framework, after 2019 society can therefore only emit ~~another 108 ± 75, 268~~ 150 ± ~~91~~79 Gt C~~, or 336 ± 97 Gt C~~ to have ~~either~~ a ~~95%,~~ 66%~~, or 50%~~ chance of limiting warming to 1.5°C. ~~These~~ This future emissions estimate~~s~~ rise~~s~~ to ~~to 295 ± 93, 565~~ 400 ± ~~120~~104 Gt C~~, and 685 ± 132 Gt C~~ to have a ~~95%,~~ 66%~~, or 50%~~ chance of limiting warming to 2.0°C.

Table 2. Total cumulative and future carbon emissions that will lead to crossing the Paris temperature thresholds based on the EM-GC trained using the HadCRUT5 ΔT record. Estimates of $\Sigma CO_2^{EMISSIONS}$ that would cause global warming to stay below indicated thresholds for 95%, 66%, and 50% probabilities and are rounded to the nearest 10 Gt C. The values in the top half of the table are the estimates of total cumulative carbon emissions that will lead to crossing the Paris Agreement thresholds with the 10% uncertainty for how atmospheric CO2 responds to prescribed carbon emissions (see text) included~~with the 10% uncertainty included~~. The values in the bottom half of the table are the estimates of future cumulative carbon emissions after 2019 that will lead to crossing the Paris Agreement thresholds, with the same 10% uncertainty. The range of years given represents when the Paris Agreement thresholds will be passed based ~~upon~~ on the rate of emissions from SSP5-8.5 or continuing the 2019 rate of emissions of 11.7 Gt C yr^{-1} (Friedlingstein et al., 2019).

Total $\Sigma CO_2^{EMISSIONS}$ since 1870 from the EM-GC			
	95%	**66%**	**50%**
1.5°C	~~746~~ 730 ± ~~75~~ 73 Gt C	~~906~~ 790 ± ~~91~~ 79 Gt C	~~974~~ 830 ± ~~97~~ 83 Gt C
2.0°C	~~933~~ 920 ± ~~93~~ 92 Gt C	~~1203~~ 1040 ± ~~120~~ 104 Gt C	~~1323~~ 1110 ± ~~132~~ 111 Gt C
Future $\Sigma CO_2^{EMISSIONS}$ (assuming ~~638~~ 640 Gt C released between 1870-2019)			
	95%	**66%**	**50%**

1.5°C	~~108~~ 90 ± ~~75~~ 73 Gt C (~~2022~~[a]2021[a]-~~2032~~[a]2031[a]) (2021[b]-~~2034~~[b]2033[b])	~~268~~ 150 ± ~~91~~ 79 Gt C (~~2032~~2025-~~2042~~2035) (~~2034~~2026-~~2049~~2039)	~~336~~ 190 ± ~~97~~ 83 Gt C (~~2036~~2027-~~2045~~2038) (~~2039~~2029-~~2056~~2043)
2.0°C	~~295~~ 280 ± ~~93~~ 92 Gt C (~~2033~~[a]2033[a]-~~2043~~[a]2043[a]) (~~2036~~[b]2036[b]-~~2052~~[b]2051[b])	~~565~~ 400 ± ~~120~~ 104 Gt C (~~2046~~2039-~~2056~~2049) (~~2057~~2045-~~2077~~2063)	~~685~~ 470 ± ~~132~~ 111 Gt C (~~2051~~2047-~~2061~~2052) (~~2066~~2050-~~2088~~2069)

[a] Year the 1.5°C target or 2.0°C upper limit will be exceeded assuming the rate of emission inferred from SSP5-8.5 and the 1-~~sigma~~σ uncertainty. Applies to the 66% and 50% probabilities.

[b] Year the 1.5°C target or 2.0°C upper limit will be exceeded assuming the 2019 rate of emission of 11.7 Gt C yr^{-1} and the 1-~~sigma~~σ uncertainty Applies to the 66% and 50% probabilities.

An analysis by van Vuuren et al. (2020) assesses ~~TCRE~~ remaining carbon budgets based on cumulative emissions after 2010. Their analysis indicates only 228 Gt C can be released ~~since~~ after 2010 to have a 66% probability of achieving the Paris Agreement target of limiting the rise in ΔT below 1.5°C in 2100. They base this estimate on an analysis of climate sensitivity and carbon cycle components, including an adjustment to TCRE for the tendency of CMIP5 GCMs to warm too quickly that had been suggested by Millar et al. (2017). ~~In our model framework, w~~We find a 66% probability of limiting warming to 1.5°C upon the release of ~~369~~ 250 ± ~~91~~ 79 Gt C between 2010 and 2100. ~~It is not surprising our analysis provides somewhat more latitude for the probabilistic forecasts of limiting warming to 1.5°C compared to estimates based on analyses of GCM output, given the tendency of CMIP5 GCMs (Hope et al., 2017) and CMIP6 GCMs (Sect. 3.1) to warm so much faster than the observed climate system.~~ Our results are similar to the findings in van Vuuren et al. (2020). ~~Regardless, between~~ Between 2010 and 2019, about ~~101~~ 100 Gt C has been released to the atmosphere (Friedlingstein et al., 2019), so the remaining budget after 2019 for limiting warming to 1.5°C is about ~~127~~ 128 Gt C according to van Vuuren et al. (2020). The remaining budget from our analysis is 150 ± 79 Gt C. Our analysis and that by van

Vuuren et al. (2020) suggest ~~A~~at the pace of emissions in 2019 of 11.7 Gt C yr^{-1} (Friedlingstein et al., 2019), society will cross this threshold in ~~about a decade~~the next 10 years. ~~Our model framework suggests a remaining budget of 268 ± 91 Gt C (Table 2). Society has at most about 20 years, or 15-29 years based on the 10% uncertainty, to severely limit carbon emissions to have a 66% probability to achieve the target of the Paris Agreement.~~

3.3.5 Blended methane

Atmospheric abundances of methane will likely continue to increase as society expands natural gas production and agriculture, making it important to analyze the impact of various methane scenarios on the rise of GMST. It is unlikely future atmospheric methane abundances will progress as indicated by SSP1-2.6 (see Fig. 2), a low radiative forcing scenario. Current observations shown in Fig. 2 illustrate that the methane mixing ratio is following SSP2-4.5 and has missed the initial decline needed to follow the SSP1-2.6 pathway. To analyze the effect varying future methane abundance pathways will have on GMST, we have generated linear interpolations of the SSP1-2.6 and SSP3-7.0 methane ~~future~~ abundances and created four alternate scenarios (see Fig. ~~S18~~S22), which we call blended methane scenarios. We can substitute one of the blended methane scenarios into the EM-GC instead of using the projection of methane specified by the SSP database to quantify the sensitivity of future warming to various evolutions of methane on the rise in GMST.

Figure ~~14~~ 13 shows the probability of staying at or below the Paris Agreement target (gold colors) or upper limit (purple colors) for SSP1-2.6 (solid) and SSP4-3.4 (dotted) as a function of the methane mixing ratio in 2100. The lowest atmospheric methane mixing ratio value in 2100 of 1.15 ppm is from the SSP1-2.6 methane pathway, the highest mixing ratio in 2100 of 3.20 ppm is from the SSP3-7.0 methane pathway~~, . and t~~The four in between are the blended methane scenarios. As the atmospheric methane abundance increases, the likelihood of achieving the goals in the Paris Agreement decreases. For SSP1-2.6, the probability of limiting the rise in GMST below the 1.5°C target begins at ~~65~~53% for HadCRUT5 using the SSP1-2.6 designated methane pathway and decreases as the blended scenarios are considered. The probability of achieving the Paris Agreement target declines to ~~just under 50~~30% if methane reaches 2.4 ppm in 2100 and to ~~34~~16% if methane increases to 3.2 ppm in 2100. Even though

~~we have labeled~~ SSP1-2.6 ~~the 1.5°C pathway in our model framework~~can have a 53% probability of limiting warming to 1.5°C, ~~limiting future warming to this challenging amount~~achieving this goal can likely only be ~~achieved~~ attained by strict limits on both emissions of carbon dioxide and methane.

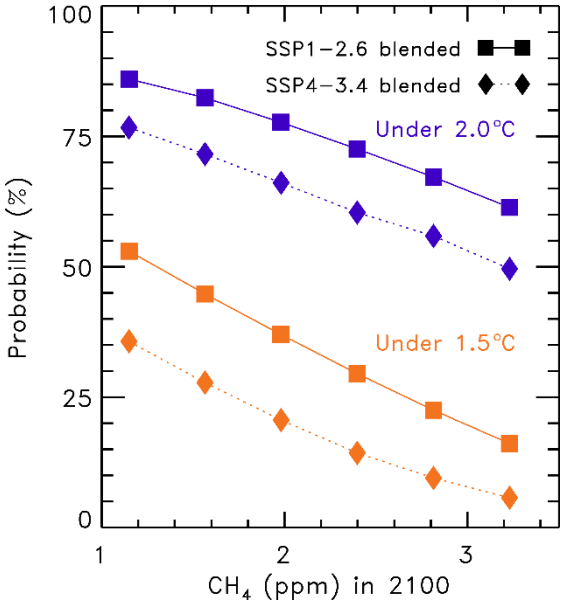

Figure ~~14~~13. Probability of staying at or below the Paris Agreement target and upper limit for SSP1-2.6 and SSP4-3.4 as a function of varying methane scenarios using the EM-GC trained with the HadCRUT5 ΔT record. The atmospheric methane scenarios are calculated using linear combinations of methane abundances from SSP1-2.6 and SSP3-7.0 to span the range of future methane abundances.

In Sect. 3.3.3, we showed that if all GHGs follow the SSP4-3.4 scenario there would be a ~~74~~64% probability of limiting warming to 2.0°C. If the methane pathway instead follows SSP1-2.6, which has an end of century mixing ratio of only 1.15 ppm, then the probability of achieving the Paris Agreement goal rises to ~~82~~77%. ~~However, I~~if the methane pathway follows SSP3-7.0 and the end of century mixing ratio increases to 3.2 ppm, then the probability of achieving the Paris Agreement goal declines to ~~65~~50%.

Reducing the future anthropogenic emissions of methane might be more challenging than controlling future emissions of carbon dioxide, ~~simply~~ because methane has such a wide variety of sources related to energy, agriculture, and ruminants (Kirschke et al., 2013). Given the current widespread use of methane as a source of energy in the United States and parts of Europe (Saunois et al., 2020), combined with the continued growth in the global number of ruminants (Wolf et al., 2017), it seems unrealistic for atmospheric methane to follow the peak and sharp decline starting in 2025 of the SSP1-2.6 pathway (Fig.

3b). Our analysis suggests failure to limit methane to the SSP1-2.6 trajectory will have a larger impact on the achievement of the 1.5°C Paris goal compared to the 2.0°C upper limit. Figure ~~14~~ 13 is designed to provide some perspective on the importance of ~~future controls on~~ limiting the growth of methane in the atmosphere~~on projections of end of century warming~~.

3.3.6 Climate feedback

In our analysis above, we have assumed the value of λ_Σ (and thus λ, see Eq (3) and corresponding text in Sect. 2.1) is constant over time. Time-constant λ_Σ is the simplest assumption one can make. The climate record can be fit very well based on this conjecture, as shown in Fig. 1a ~~and Fig. S3a~~. However, many GCMs suggest that climate feedback may vary over time (Marvel et al., 2018; Rugenstein et al., 2020). An analysis by ~~(~~Goodwin~~,~~ (2018) finds there is a delay in the response of climate feedback to a change in radiative forcing, on the order of a few days to several decades. In our EM-GC framework, we are able to conduct calculations allowing the value of λ_Σ to vary over time with a delay between the change in radiative forcing and the response of λ_Σ (see Fig. S23 and the supplement for results without the time delay), and to project future temperature with such an assumption. Up until this point, our simulations have used time-invariant λ_Σ to be consistent with how our model results had been presented in prior publications (Canty et al., 2013; Hope et al., 2017). Recall from Sect. 2.1 that $\lambda_\Sigma = \lambda_P - \lambda$. To assess the effect of time varying climate feedback on our projections of global warming, we examine the sensitivity in terms of λ^{-1}, because this quantity scales proportionally with ΔT and ~~also~~ our use of the inverse λ allows for direct comparison to the results of Marvel et al. (2018) and Rugenstein et al. (2020).

Figure ~~15~~ 14 shows the change in observed and modeled GMST under ~~several~~ four assumptions regarding λ^{-1}. ~~The first assumption is that~~First, the value of λ^{-1} is constant over time (Figs. ~~15a~~14a, e). Second, the value of λ^{-1} varies by 50% between 1850-2100 (Figs. 14b, f: further discussion of Fig. 14b and f will occur at the end of the section). The third assumption involves λ^{-1} varying over time while χ^2_{RECENT} is always less than or equal to two (Figs 14c, g). Fourth, λ^{-1} varies over time while χ^2_{ATM} is always less than or equal to two (Figs. 14d, h).~~.~~ In all cases for time varying feedback, we also assume the value of λ^{-1} has the same shape as the SSP4-3.4 RF time series along with a lag of 20 years and that the new time series for λ^{-1} maintains an average value over the observational record identical to the

constant value for λ^{-1} of 0.63 °C / W m^{-2}. We chose a lag of 20 years to represent the longest delay in response of climate feedback to a change in RF suggested by Goodwin (2018). If we use the shorter delays represented in Goodwin (2018), then our results would be between those from the instantaneous response of climate feedback to a change in RF (Fig. S23) and the 20-year delay. Finally, in the simulations described below, the value of λ^{-1} is assumed to continue to rise into the future at the same proportionality to $\Delta T_{ATM,HUMAN}$ as the prior increase.

~~We are able to fit the climate record over the past 170 years (χ^2_{ATM}) and past 80 years (χ^2_{RECENT}) extremely well for constant λ^{-1}. To simulate variations of λ^{-1} over time, we alter runs from the EM-GC that were conducted with constant λ^{-1}, by modifying the $\Delta T_{ATM,HUMAN}$ component of these original EM-GC simulations. The value of λ^{-1} takes the same shape as the SSP4-3.4 RF time series, scaled, and shifted so that the new time series maintains an average value of λ^{-1} over the observational record that is identical to the constant λ^{-1} value. In simulations described below, the value of λ^{-1} is assumed to continue to rise into the future, at the same proportionality to $\Delta T_{ATM,HUMAN}$ as the prior increase.~~

We fit the climate record over the past 170 years (χ^2_{ATM}) and past 80 years (χ^2_{RECENT}) extremely well for constant λ^{-1}. If we allow the value of λ^{-1} to scale with anthropogenic forcing such that the maximum value of ~~χ^2_{ATM}~~ χ^2_{RECENT} is always less than or equal to ~~2~~two, we obtain the result shown in Fig. ~~15b~~14c. This scaling of λ^{-1} results in a value of ΔT_{2100} of 2.8°C, about ~~50%~~1.0°C higher than when a constant value of λ^{-1} is used and an increase in λ^{-1} by nearly a factor of ~~2~~two~~.5 at the end of century~~ in 2100. The modeled change in GMST starts to deviate from the observations around year ~~2000~~2010. This deviation is seen in the residual between modeled and observed GMST in Fig. ~~15f~~14g. If we allow the value of λ^{-1} to scale with anthropogenic forcing so that the maximum value of ~~χ^2_{RECENT}~~ χ^2_{ATM} is less than or equal to ~~2~~two, we arrive at the result shown in Fig. ~~15c~~14d~~,~~. This variation in λ^{-1} ~~yielding~~ yields a value of ΔT_{2100} of 3.5°C that is nearly double~~s~~ the estimate of ΔT_{2100} for the time invariant λ^{-1} (Fig 14a) and ~~over two and a half centuries and~~ a rise in λ^{-1} over two and a half centuries by a factor of ~~4~~3.5. The modeled change in GMST starts to deviate ~~dramatically~~ from observations around year ~~1990~~2005. Th~~is starke~~ deviation is seen in the residual between modeled and observed GMST in Fig. ~~15g~~14h. The ~~χ^2_{ATM}~~ χ^2_{RECENT} value in Fig. ~~15g~~ 14h is 3.~~63~~85, which does not satisfy our reduced chi-squared constraints~~, and~~

~~interestingly appears to resemble the behavior of some CMIP6 GCMs (see Fig. 9 as well as Tokarska et al. (2020))~~.

Several other studies have investigated the degree of change in λ^{-1}. Marvel et al. (2018) suggest that the median value of ECS from the CMIP5 GCMs may ~~increase~~ rise ~~from 1.8 to 2.3°C or 1.8 to 3.1°C~~ due to time varying λ^{-1}~~, which corresponds to an~~ increasinge ~~in λ^{-1}~~ from 1850-2100 ~~of~~ by 28 to 72%~~, respectively~~. Rugenstein et al. (2020) estimates a median increase of 17% for values of ECS from CMIP6 GCMs when examining millennial length simulations compared to the 150-year Gregory et al. (2004) method, which is consistent with about an 11% rise in λ^{-1} (Fig. 2b of Rugenstein et al. (2020)). A doubling (Fig. ~~15b~~14c) or ~~quadrupling~~ tripling of λ^{-1} (Fig. ~~15c~~14d) over two and a half centuries is faster than the increase indicated by Marvel et al. (2018) and the millennia order timescale in Sect. 12.5.3 of IPCC 2013 and Rugenstein et al. (2020). ~~A~~An increase of 50% ~~increase~~ or lower in λ^{-1} (Fig. ~~15d~~14b) is in line with the estimate of the change in ECS due to time-variant λ^{-1} indicated by Marvel et al. (2018) and Rugenstein et al. (2020). The use of a 20-year delay in the response of the feedback to a change in RF results in good fits to the HadCRUT5 GMST record (Fig. 14b). However, we are not able to achieve as low values of χ^2_{RECENT} and χ^2_{ATM} to this record for time variant feedback if we assume an instantaneous response (Fig. 14 a-d versus Fig. S23 a-d).

The assumption of constant feedback within the EM-GC framework is reasonable because there is no strong evidence from the climate record for a noticeable increase in λ^{-1} on the multidecadal time scale associated with the simulations ~~shown~~ in Fig. ~~15~~14. If the true value of λ^{-1} actually rises over time as suggested by some of the CMIP6 (Rugenstein et al., 2020) and CMIP5 GCMs (Marvel et al., 2018), our projections of global warming would be a few tenths of a degree warmer than our current best estimates assuming constant λ^{-1}, as shown in Fig. ~~15d~~14b. ~~Interestingly, i~~Increasing λ^{-1} by 50% results in a similar value of ΔT_{2100} as when utilizing a higher value of AER RF_{2011} (i.e. AER RF_{2011} less than −0.9 W m^{-2}) in the EM-GC framework ~~(see Fig. 3)~~.

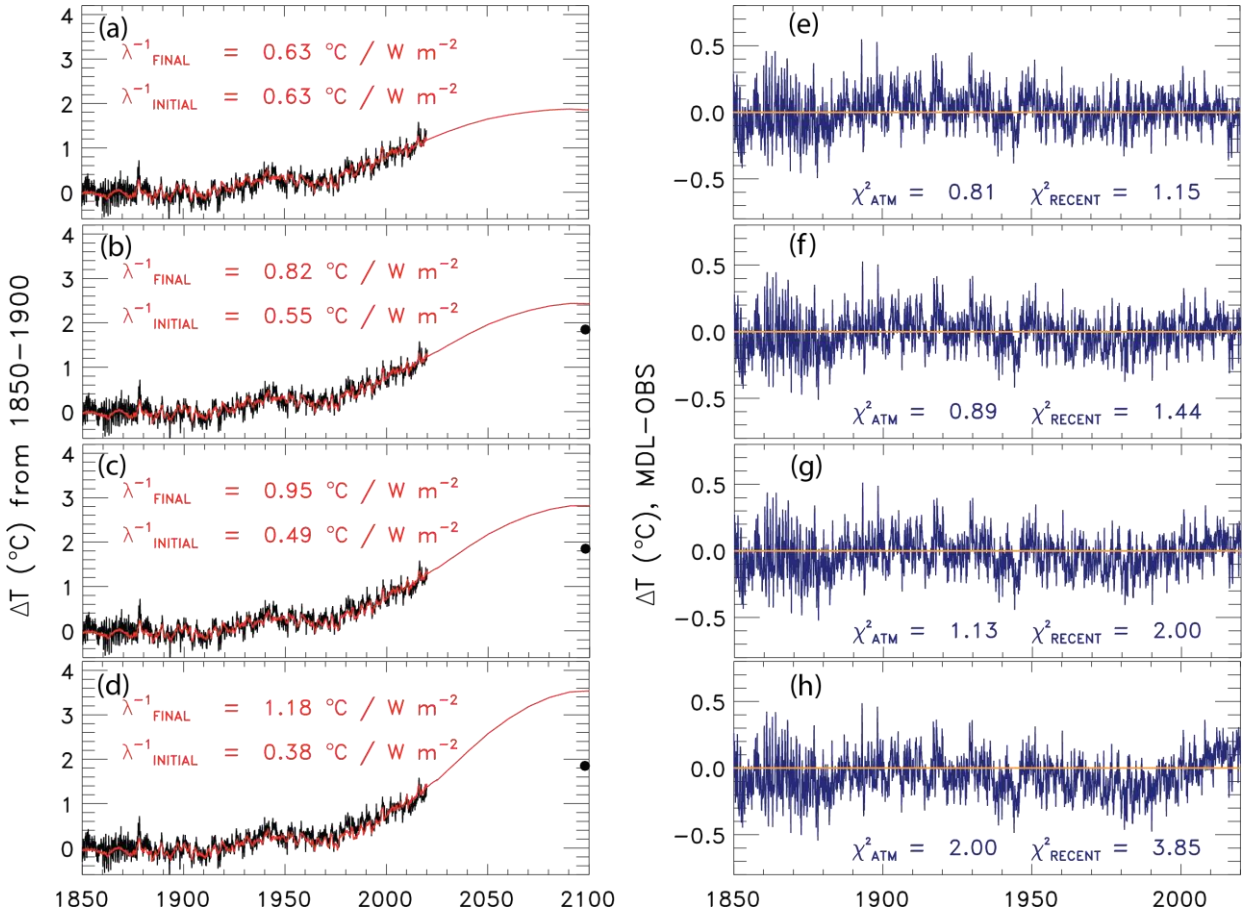

Figure ~~15~~14. Change in GMST from 1850-2019 for observations from ~~HadCRUT~~ HadCRUT5 (black) and 1850-2100 for modeled (red) using SSP4-3.4 and the residual between modeled and observations incorporating a 20 year delay between λ^{-1} and a change in RF. (a) Rise in GMST assuming a constant value of λ^{-1}. (b) Rise in GMST allowing λ^{-1} to increase by 50%. ~~Rise in GMST allowing λ^{-1} to vary while the value of χ^2_{ATM} is kept below 2.~~ (c) Rise in GMST allowing λ^{-1} to vary while the value of χ^2_{RECENT} is kept below 2. (d) ~~Rise in GMST allowing λ^{-1} to increase by 50%.~~ Rise in GMST allowing λ^{-1} to vary while the value of χ^2_{ATM} is kept below 2. (e) Residual between modeled and observed rise in GMST from 1850-2019 for constant λ^{-1}. (f) Same as (e) but for increasing λ^{-1} by 50%~~but for varying λ^{-1} while the value of χ^2_{ATM} is kept below 2~~. (g) Same as (f) but for varying λ^{-1} while the value of χ^2_{RECENT} is kept below 2. (h) same as (g) but for varying λ^{-1} while the value of χ^2_{ATM} is kept below 2~~but for increasing λ^{-1} by 50%~~.

4 Conclusions

In this paper we use a multiple linear regression energy balance model (EM-GC), to analyze and project changes in the future rise in global mean surface temperature (GMST), calculate the attributable anthropogenic warming rate (AAWR, the component of the rise in GMST caused by human activities)

over the past four decades, and compute the equilibrium climate sensitivity (ECS, the rise in GMST that would occur after climate has equilibrated with atmospheric CO_2 at the 2×pre-industrial level). Projections of the rise in GMST (ΔT) are conducted for seven of the Shared Socioeconomic Pathway (SSP) projections of GHGs (O'Neill et al., 2017). We compare computations of AAWR, ECS, and projections of ΔT to values for each quantity computed from archived output provided by GCMs as part of CMIP6 (Eyring et al., 2016). A critical component of our study is comprehensive analysis of uncertainties in AAWR, ECS, and projections of ΔT in our EM-GC framework, due to the rather large uncertainty in radiative forcing of climate from tropospheric aerosols (AER RF).

The ~~best estimate of~~median value~~s~~ of AAWR from 1975-2014 computed using our EM-GC constrained by the century and a half long record for GMST provided by ~~the HadCRUT~~ HadCRUT5~~data record (Cowtan and Way, 2014)~~ is 0.~~135~~157°C/decade and the 5th, and 95th percentiles are 0.~~097~~ 120 and 0.195°C/decade, respectively. The median value of AAWR from the CMIP6 multi-model ensemble is 0.221°C/decade and the 5th, and 95th percentiles are 0.151 and 0.299°C/decade, respectively. We show that the component of GMST attributed to human activity within the CMIP6 multi-model ensemble warms considerably faster than observations over the past four decades, a result that is consistent with ~~a~~ recent ~~analysis~~ analyses of output from the CMIP6 multi-model ensemble (CONSTRAIN, 2020; Tokarska et al., 2020) as well as output from CMIP5 GCMs assessed in AR5 (i.e, Fig. 11.25b of Kirtman et al. (2013)). This finding differs from the conclusion of Hausfather et al. (2020), who showed fairly good agreement between projections of global warming from GCMs and observed ΔT. As detailed in Sect. 3.1, this paper examined GCMs that proceeded CMIP5 and examined ΔT for a time period that ends in 2017, a time when global temperature was influenced by a strong ENSO event that ended in 2016. The majority of the uncertainty in our EM-GC based estimate of AAWR is due to imprecise knowledge of the true value of AER RF.

In our model framework, the best estimate of ECS is 2.~~01~~33°C and the 5th and 95th percentiles are 1.~~12~~ 40 and ~~4.12~~3.57°C, respectively. The median value of ECS from the CMIP6 multi-model ensemble is 3.74°C, which is ~~almost double~~around 1.6 times the best estimate value of ECS inferred from the observed climate record. The 5th and 95th percentiles of ECS from the CMIP6 multi-model ensemble are

2.19 and 5.65°C, respectively. We obtain a wide range of ECS values using the EM-GC because of the uncertainty in AER RF. With an AER RF_{2011} equal to −1.6 W m^{-2}, the EM-GC calculates a value of ECS similar to the maximum value of ECS from the CMIP6 multi-model mean. We cannot rule out the very high value of ECS, but we assign a low probability based on the IPCC 2013 low likelihood for the needed value of AER RF_{2011}. Our empirically based determination of ECS is in good overall agreement with the recent empirical determinations of Lewis and Grünwald (2018) (1.87°C, range of 1.1-4.05°C) and Skeie et al. (2018) (2.0°C, range of 1.2-3.1°C) and the slightly older empirically determination reported by Otto et al. (2013) (2.0°C, range of 1.2-3.9°C) (all range values are for the 5th and 95th percent confidence interval). A recent review of climate feedback and climate sensitivity published by Sherwood et al. (2020) reported ECS lies within the range of 2.3 to 4.7°C at the 5th to 95th percent confidence intervals; their lower bound for ECS is quite a bit higher than the lower bound found in our analysis, as well as by Cox et al. (2018), Dessler et al. (2018), Lewis and Grünwald (2018), Nijsse et al. (2020), Otto et al. (2013), Skeie et al. (2018), and Tokarska et al. (2020).

We also examined the probability of limiting the future rise in GMST below the Paris Agreement target of 1.5°C and upper limit of 2.0°C. Our probabilistic forecasts of projections of ΔT include a comprehensive treatment of the uncertainty in AER RF, a capability outside the scope of the GCM intercomparisons conducted for CMIP6. Our analysis indicates that if GHGs were to follow the ~~the~~ SSP1-2.6 pathway, there would be ~~scenario is the 1.5°C pathway, providing between~~ a ~~57.0-64.8~~53% likelihood ~~of keeping~~that the ~~the end of century~~ rise in ΔT would remain below the Paris Agreement target of 1.5°C (relative to pre-industrial) by the end of century based on HadCRUT5 ~~depending on the choice of GMST and OHC record~~. We find that the SSP4-3.4 scenario ~~is the 2.0°C pathway, as this scenario~~ provides a ~~69.6-74.0~~64% likelihood of limiting global warming to below the Paris Agreement upper limit of 2.0°C by end of century. These probabilities have declined upon our use of HadCRUT5 compared to the GMST record of HadCRUT4 to 64% and 74% for the SSP1-2.6 and SSP4-3.4 scenarios, respectively. In contrast, the CMIP6 multi-model mean only suggests ~~a~~a 1~~5.2~~8% probability of achieving the Paris Agreement target for SSP1-2.6 and a 1~~6.7~~7% probability of attaining the Paris Agreement goal for SSP4-3.4. ~~This result~~The lower probabilities suggested by the CMIP6 multi-model ensemble is not surprising, given the

tendency of most CMIP6 GCMs to warm faster ~~than has been observed~~vations over the past four decades. Our projections of ΔT using a physically based model tied to observations of ocean heat content, quantification of natural as well as anthropogenic drivers of variations in GMST, and consideration of uncertainty in AER RF are shown to be remarkably similar to the expert assessment of the future rise in GMST that was sketched out in Fig. 11.25b of AR5 (Kirtman et al., 2013), and the empirically-based filtering of CMIP6 model output recently published by Tokarska et al. (2020). Finally and most importantly, our estimates are based on the assumption that climate feedback has been and will continue to remain constant over time, since the prior temperature record can be fit so well under this assumption. As described in Section 3.3.6, if climate feedback rises over time, larger warming will be realized than that found under ~~the~~ this assumption of temporally invariant feedback.

We also quantify the sensitivity of the probability of achieving the Paris Agreement target (1.5°C) or upper limit (2.0°C) to future atmospheric abundances of methane. The end of century mixing ratio of methane in the SSP1-2.6 scenario is 1.15 ppm, considerably less than the contemporary abundance of 1.88 ppm. The likelihood of attaining the 1.5°C target for SSP1-2.6 decreases as future methane emissions increase, declines to ~~just under 50~~30% if methane reaches 2.4 ppm in 2100 and to ~~34~~16% if methane increases to 3.2 ppm at end of century. Our analysis described in Sect. 3.3.5 demonstrates that major near-term limits on the future growth of methane are especially important for achievement of the 1.5°C limit to future warming that constitutes the goal of the Paris Agreement.

Finally, we have also quantified in the EM-GC framework the remaining budgets of carbon (i.e., CO_2) emissions that can occur while attaining either the goal or upper limit of the Paris Agreement. We find that after 2019, society can only emit another ~~108 ± 75, 268~~ 150 ± ~~91~~79~~, or 336 ± 97~~ Gt C to have ~~either~~ a ~~95%,~~ 66%~~, or 50% chance~~ likelihood of limiting warming to 1.5°C. ~~These~~ This future emissions estimate~~s~~ rise~~s~~ to ~~295 ± 93, 565~~ 400 ± ~~120~~104~~, and 685 ± 132~~ Gt C to have a ~~95%,~~ 66%~~, or 50% chance~~ probability of limiting warming to 2.0°C. Given the anthropogenic emissions of carbon due to combustion of fossil fuels, cement production, gas flaring, and ~~land use~~land-use change ~~are~~ were about 11.7 Gt C per year in 2019 (Friedlingstein et al., 2019), our study indicates that the target (1.5°C warming) of the Paris Agreement will not be achieved unless carbon emissions are severely curtailed in the next ~~two decades~~10 years.

We conclude by noting that the CMIP6 multi-model ensemble provides many useful parameters such as sea level rise, sea ice decline, and precipitation changes, that provide a great societal understanding of the impact of climate change. We do not mean to undermine the importance of the CMIP6 GCMs by this analysis. Rather, we hope that studies such as this, along with other recent evaluations of CMIP6 multi-model output such as Nijsse et al. (2020) and Tokarska et al. (2020) will provide improved use of the CMIP6 multi-model ensemble for policy decisions. Our EM-GC was built to specifically simulate and project changes in GMST; we do not examine numerous other components of the climate system that affect society. ~~Our study indicates that unless society~~We emphasize that our projections show that unless society can implement steep reductions in the emissions of carbon (CO_2) and methane (CH_4) ~~rather soon~~in the next 10 years, 1.5°C global warming goal of the~~the~~ Paris Agreement will ~~fail to~~not be achieved. ~~We suggest there is slighly more time to achieve these steep reductions than indicated by the CMIP6 multi-model mean. The incredibly valuable output of the CMIP6 GCMs is important for determining the consequences for society of 1.5°C, 2.0°C, or even larger rises in GMST.~~

5 Acronyms

AAWR – Attributable anthropogenic warming rate

AR4 – Fourth Assessment Report

AER – Anthropogenic aerosols

AER RF_{2011} – Radiative forcing due to anthropogenic aerosols in 2011

AMOC – Atlantic meridional overturning circulation

AMV – Atlantic multidecadal variability

BEG – Berkley Earth Group

CALIPSO – Cloud-Aerosol Lidar and Infrared Pathfinder Satellite Observations

CMIP5 – Coupled Model Intercomparison Project Phase 5

CMIP6 – Coupled Model Intercomparison Project Phase 6

COBE - Centennial in situ Observation-Based Estimate

CW14 – Cowtan and Way (2014) temperature record

ECS – Equilibrium climate sensitivity

EM-GC – Empirical Model of Global ~~climate~~Climate

ENSO – El Niño ~~southern~~ Southern ~~oscillation~~Oscillation

GCM – General Circulation Model

GHG – Greenhouse gas

GISTEMP – Goddard Institute for Space Studies Surface Temperature Analysis v4

GloSSAC – Global Space-based Stratospheric Aerosol Climatology

GMST – Global mean surface temperature

HadCRUT – Hadley Center Climatic Research Unit

IPCC – Intergovernmental Panel on Climate Change

ISCCP – International Satellite Cloud Climatology Project

IOD – Indian Ocean dipole

LIN – Linear method

LUC – ~~Land use~~Land-use change

MEI – Multivariate ENSO index

NOAAGT – National Center for Environmental Information NOAAGlobalTemp v5

ODS – Ozone depleting substances

OHC – Ocean heat content

OHE – Ocean heat export

PATMOS-X - Pathfinder Atmospheres Extended

PDO – Pacific decadal oscillation

RCP – Representative concentration pathway

REG – Regression method

RF – Radiative forcing

SAOD – Stratospheric aerosol optical depth

SORCE – Solar Radiation and Climate Experiment

SSP – Shared Socioeconomic Pathway

SST – Sea surface temperature

TAR – Third Assessment Report

TAS – Near surface air temperature

TCRE – Transient climate response to cumulative emissions

TOS – Temperature at the interface of the atmosphere and the upper boundary of the ocean

TSI – Total solar irradiance

6 Author Contribution

LAM, APH, and TPC developed the model code used in this analysis, LAM, APH, and BFB collected data, RJS supervised, administrated, and developed the project, LAM wrote the original draft, and RJS, APH, BFB, TPC, and WRT participated in the review and editing of the manuscript.

7 Competing Interests

The authors declare that they have no conflict of interest.

8 Acknowledgements

We would like to acknowledge the World Climate Research Programme for coordinating and promoting CMIP6 through its Working Group on Coupled Modelling. We thank the climate modeling groups participating in CMIP6 for producing and making their model results available, the Earth System Grid Federation (ESGF) for archiving the data and providing access, and the several funding agencies who support ESGF and CMIP6. This project could not occur without the results from CMIP6. We appreciate very much financial support from the NASA Climate Indicators and Data Products for Future National Climate Assessments (INCA) program (award NNX16AG34G). This study was partially supported by NOAA grants NA14NES4320003 and NA19NES4320002 (Cooperative Institute for Satellite Earth System Studies - CISESS) at the University of Maryland/ESSIC. We thank University of Maryland Undergraduate Lauren Borgia for participating in extensive, in-depth discussions of recent papers on cloud feedback and climate sensitivity. Finally, we thank both reviewers for very careful reads of the original paper that led to substantial improvements in the manuscript, as well as Martin Stolpe for contacting us privately, while the paper was in discussion, regarding an erroneous description of the effect of creating blended near surface air temperature that had appeared in the submitted paper.

9 References

Arfeuille, F., Weisenstein, D., MacK, H., Rozanov, E., Peter, T. and Brönnimann, S.: Volcanic forcing for climate modeling: A new microphysics-based data set covering years 1600-present, Clim. Past, 10(1), 359–375, doi:10.5194/cp-10-359-2014, 2014.

Armour, K. C.: Energy budget constraints on climate sensitivity in light of inconstant climate feedbacks, Nat. Clim. Chang., 7(5), 331–335, doi:10.1038/nclimate3278, 2017.

Balmaseda, M. A., Trenberth, K. E. and Källén, E.: Distinctive climate signals in reanalysis of global ocean heat content, Geophys. Res. Lett., 40(9), 1754–1759, doi:10.1002/grl.50382, 2013.

Barnett, T. P., Pierce, D. W., Latif, M., Dommenget, D. and Saravan, R.: Interdecadal interactions between the tropics and midlatitudes in the Pacific basin, Geophys. Res. Lett., 26(5), 615–618, 1999.

Bond, T. C., Doherty, S. J., Fahey, D. W., Forster, P. M., Berntsen, T., Deangelo, B. J., Flanner, M. G., Ghan, S., Kärcher, B., Koch, D., Kinne, S., Kondo, Y., Quinn, P. K., Sarofim, M. C., Schultz, M. G., Schulz, M., Venkataraman, C., Zhang, H., Zhang, S., Bellouin, N., Guttikunda, S. K., Hopke, P. K., Jacobson, M. Z., Kaiser, J. W., Klimont, Z., Lohmann, U., Schwarz, J. P., Shindell, D., Storelvmo, T., Warren, S. G. and Zender, C. S.: Bounding the role of black carbon in the climate system: A scientific assessment, J. Geophys. Res. Atmos., 118(11), 5380–5552, doi:10.1002/jgrd.50171, 2013.

Bony, S., Colman, R., Kattsov, V. M., Allan, R. P., Bretherton, C. S., Dufresne, J. L., Hall, A., Hallegatte, S., Holland, M. M., Ingram, W., Randall, D. A., Soden, B. J., Tselioudis, G. and Webb, M. J.: How well do we understand and evaluate climate change feedback processes?, J. Clim., 19(15), 3445–3482, doi:10.1175/JCLI3819.1, 2006.

Calvin, K., Bond-Lamberty, B., Clarke, L., Edmonds, J., Eom, J., Hartin, C., Kim, S., Kyle, P., Link, R., Moss, R., McJeon, H., Patel, P., Smith, S., Waldhoff, S. and Wise, M.: The SSP4: A world of deepening inequality, Glob. Environ. Chang., 42, 284–296, doi:10.1016/j.gloenvcha.2016.06.010, 2017.

Canty, T., Mascioli, N. R., Smarte, M. D. and Salawitch, R. J.: An empirical model of global climate – Part 1: A critical evaluation of volcanic cooling, Atmos. Chem. Phys., 13(8), 3997–4031, doi:10.5194/acp-13-3997-2013, 2013.

Carpenter, L. J., Daniel, J. S. (Lead A., Fleming, E. L., Hanaoka, T., Ravishankara, A. R., Ross, M. N., Tilmes, S., Wallington, T. J. and Wuebbles, D. J.: Scenarios and information for policymakers., 2018.

Carton, J. A., Chepurin, G. A. and Chen, L.: SODA3: A New Ocean Climate Reanalysis, J. Clim., 31(17), 6967–6983, doi:10.1175/jcli-d-18-0149.1, 2018.

Charette, M. A. and Smith, W. H. F.: The Volume of Earth ' s Ocean, Oceanography, 23(2), 112–114, 2010.

Chen, X. and Tung, K. K.: Global surface warming enhanced by weak Atlantic overturning circulation, Nature, 559(7714), 387–391, doi:10.1038/s41586-018-0320-y, 2018.

Chen, X., Guo, Z., Zhou, T., Li, J., Rong, X., Xin, Y., Chen, H. and Su, J.: Climate Sensitivity and Feedbacks of a New Coupled Model CAMS-CSM to Idealized CO2 Forcing: A Comparison with CMIP5 Models, J. Meteorol. Res., 33(1), 31–45, doi:10.1007/s13351-019-8074-5, 2019.

Cheng, L., Trenberth, K. E., Fasullo, J., Boyer, T., Abraham, J. and Zhu, J.: Improved estimates of ocean heat content from 1960 to 2015, Sci. Adv., 3(3), 1–11, doi:10.1126/sciadv.1601545, 2017.

Church, J. A., White, N. J., Konikow, L. F., Domingues, C. M., Graham Cogley, J., Rignot, E., Gregory, J. M., Van Den Broeke, M. R., Monaghan, A. J. and Velicogna, I.: Revisiting the Earth's sea-level and energy budgets from 1961 to 2008, Geophys. Res. Lett., 40(15), 4066, doi:10.1002/grl.50752, 2013.

CONSTRAIN: ZERO IN ON: A new generation of climate models, COVID-19 and the Paris Agreement, CONSTRAIN Proj. Annu. Rep. 2020, doi:10.5281/zenodo.428461, 2020.

Cowtan, K. and Way, R. G.: Coverage bias in the HadCRUT4 temperature series and its impact on recent temperature trends, Q. J. R. Meteorol. Soc., 140(683), 1935–1944, doi:10.1002/qj.2297, 2014.

Cowtan, K., Hausfather, Z., Hawkins, E., Jacobs, P., Mann, M. E., Miller, S. K., Steinman, B. A., Stolpe, M. B. and Way, R. G.: Robust comparison of climate models with observations using blended land air and ocean sea surface temperatures, Geophys. Res. Lett., 42(15), 6526–6534, doi:10.1002/2015GL064888, 2015.

Cox, P. M., Huntingford, C. and Williamson, M. S.: Emergent constraint on equilibrium climate sensitivity from global temperature variability, Nature, 553(7688), 319–322, doi:10.1038/nature25450, 2018.

Dessler, A. E., Mauritsen, T. and Stevens, B.: The influence of internal variability on Earth's energy balance framework and implications for estimating climate sensitivity, Atmos. Chem. Phys., 18(7), 5147–5155, doi:10.5194/acp-18-5147-2018,

2018.
Dlugokencky, E.: Trends in Atmospheric Methane, [online] Available from: www.esrl.noaa.gov/gmd/ccgg/trends_ch4/, 2020.
Dlugokencky, E. and Tans, P.: Trends in Atmospheric Carbon Dioxide, [online] Available from: www.esrl.noaa.gov/gmd/ccgg/trends/, 2020.
Domingues, C. M., Church, J. A., White, N. J., Gleckler, P. J., Wijffels, S. E., Barker, P. M. and Dunn, J. R.: Improved estimates of upper-ocean warming and multi-decadal sea-level rise, Nature, 453(7198), 1090–1093, doi:10.1038/nature07080, 2008.
Douglass, D. H. and Knox, R. S.: Climate forcing by the volcanic eruption of Mount Pinatubo, Geophys. Res. Lett., 32(5), 1–5, doi:10.1029/2004GL022119, 2005.
Dudok de Wit, T., Kopp, G., Fröhlich, C. and Schöll, M.: Methodology to create a new total solar irradiance record: Making a composite out of multiple data records, Geophys. Res. Lett., 44(3), 1196–1203, doi:10.1002/2016GL071866, 2017.
England, M. H., Mcgregor, S., Spence, P., Meehl, G. A., Timmermann, A., Cai, W., Gupta, A. Sen, Mcphaden, M. J., Purich, A. and Santoso, A.: Recent intensification of wind-driven circulation in the Pacific and the ongoing warming hiatus, Nat. Clim. Chang., 4(3), 222–227, doi:10.1038/nclimate2106, 2014.
Eyring, V., Bony, S., Meehl, G. A., Senior, C. A., Stevens, B., Stouffer, R. J. and Taylor, K. E.: Overview of the Coupled Model Intercomparison Project Phase 6 (CMIP6) experimental design and organization, Geosci. Model Dev., 9(5), 1937–1958, doi:10.5194/gmd-9-1937-2016, 2016.
Forster, P. M., Maycock, A. C., McKenna, C. M. and Smith, C. J.: Latest climate models confirm need for urgent mitigation, Nat. Clim. Chang., 10(1), 7–10, doi:10.1038/s41558-019-0660-0, 2020.
Foster, G. and Rahmstorf, S.: Global temperature evolution 1979–2010, Environ. Res. Lett., 6(4), 044022, doi:10.1088/1748-9326/6/4/044022, 2011.
Foster, M. J. and Heidinger, A.: PATMOS-x: Results from a diurnally corrected 30-yr satellite cloud climatology, J. Clim., 26(2), 414–425, doi:10.1175/JCLI-D-11-00666.1, 2013.
Fricko, O., Havlik, P., Rogelj, J., Klimont, Z., Gusti, M., Johnson, N., Kolp, P., Strubegger, M., Valin, H., Amann, M., Ermolieva, T., Forsell, N., Herrero, M., Heyes, C., Kindermann, G., Krey, V., McCollum, D. L., Obersteiner, M., Pachauri, S., Rao, S., Schmid, E., Schoepp, W. and Riahi, K.: The marker quantification of the Shared Socioeconomic Pathway 2: A middle-of-the-road scenario for the 21st century, Glob. Environ. Chang., 42, 251–267, doi:10.1016/j.gloenvcha.2016.06.004, 2017.
Friedlingstein, P., Meinshausen, M., Arora, V. K., Jones, C. D., Anav, A., Liddicoat, S. K. and Knutti, R.: Uncertainties in CMIP5 climate projections due to carbon cycle feedbacks, J. Clim., 27(2), 511–526, doi:10.1175/JCLI-D-12-00579.1, 2014.
Friedlingstein, P., Jones, M. W., Sullivan, M. O., Andrew, R. M., Hauck, J., Peters, G. P., Peters, W., Pongratz, J., Sitch, S., Quéré, C. Le, Bakker, D. C. E., Canadell, J. G., Ciais, P., Jackson, R. B., Anthoni, P., Barbero, L., Bastos, A., Bastrikov, V., Becker, M., Bopp, L., Buitenhuis, E., Chandra, N., Chevallier, F., Chini, L. P., Currie, K., Feely, R. A., Gehlen, M., Gilfillan, D., Gkritzalis, T., Goll, D. S., Gruber, N., Gutekunst, S., Harris, I., Haverd, V., Houghton, R. A., Hurtt, G., Ilyina, T., Jain, A. K., Joetzjer, E., Kaplan, J. O., Kato, E., Goldewijk, K. K., Korsbakken, J. I., Landschützer, P., Lauvset, S. K., Lefevre, N., Lenton, A., Lienert, S., Lombardozzi, D., Marland, G., McGuire, P. C., Melton, J. R., Metzl, N., Munro, D. R., Nabel, J. E. M. S., Nakaoka, S., Neill, C., Omar, A. M., Ono, T., Peregon, A., Pierrot, D., Poulter, B., Rehder, G., Resplandy, L., Robertson, E., Rodenbeck, C., Seferian, R., Schwinger, J., Smith, N., Tans, P. P., Tian, H., Tilbrook, B., Tubiello, F. N., Van Der Werf, G. R., Wiltshire, A. J. and Zaehle, S.: Global Carbon Budget 2019, Earth Syst. Sci. Data, (11), 1783–1838, 2019.
Fujimori, S., Hasegawa, T., Masui, T., Takahashi, K., Herran, D. S., Dai, H., Hijioka, Y. and Kainuma, M.: SSP3: AIM implementation of Shared Socioeconomic Pathways, Glob. Environ. Chang., 42, 268–283, doi:10.1016/j.gloenvcha.2016.06.009, 2017.
Gettelman, A., Hannay, C., Bacmeister, J. T., Neale, R. B., Pendergrass, A. G., Danabasoglu, G., Lamarque, J. F., Fasullo, J. T., Bailey, D. A., Lawrence, D. M. and Mills, M. J.: High Climate Sensitivity in the Community Earth System Model Version 2 (CESM2), Geophys. Res. Lett., 46(14), 8329–8337, doi:10.1029/2019GL083978, 2019.
Goodwin, P.: On the Time Evolution of Climate Sensitivity and Future Warming, Earth's Futur., 6(9), 1336–1348, doi:10.1029/2018EF000889, 2018.
Gregory, J. M., Ingram, W. J., Palmer, M. A., Jones, G. S., Stott, P. A., Thorpe, R. B., Lowe, J. A., Johns, T. C. and Williams,

K. D.: A new method for diagnosing radiative forcing and climate sensitivity, Geophys. Res. Lett., 31(3), 2–5, doi:10.1029/2003GL018747, 2004.

Griffies, S. M., Danabasoglu, G., Durack, P. J., Adcroft, A. J., Balaji, V., Böning, C. W., Chassignet, E. P., Curchitser, E., Deshayes, J., Drange, H., Fox-Kemper, B., Gleckler, P. J., Gregory, J. M., Haak, H., Hallberg, R. W., Heimbach, P., Hewitt, H. T., Holland, D. M., Ilyina, T., Jungclaus, J. H., Komuro, Y., Krasting, J. P., Large, W. G., Marsland, S. J., Masina, S., McDougall, T. J., George Nurser, A. J., Orr, J. C., Pirani, A., Qiao, F., Stouffer, R. J., Taylor, K. E., Treguier, A. M., Tsujino, H., Uotila, P., Valdivieso, M., Wang, Q., Winton, M. and Yeager, S. G.: OMIP contribution to CMIP6: Experimental and diagnostic protocol for the physical component of the Ocean Model Intercomparison Project, Geosci. Model Dev., 9(9), 3231–3296, doi:10.5194/gmd-9-3231-2016, 2016.

Hansen, J., Ruedy, R., Sato, M. and Lo, K.: Global surface temperature change, Rev. Geophys., 48(4), RG4004, doi:10.1029/2010RG000345.1.INTRODUCTION, 2010.

Hausfather, Z., Drake, H. F., Abbott, T. and Schmidt, G. A.: Evaluating the Performance of Past Climate Model Projections, Geophys. Res. Lett., 47(1), 0–3, doi:10.1029/2019GL085378, 2020.

Haustein, K., Otto, F. E. L., Venema, V., Jacobs, P., Cowtan, K., Hausfather, Z., Way, R. G., White, B., Subramanian, A. and Schurer, A. P.: A limited role for unforced internal variability in twentieth-century warming, J. Clim., 32(16), 4893–4917, doi:10.1175/JCLI-D-18-0555.1, 2019.

Hope, A. P., Canty, T. P., Salawitch, R. J., Tribett, W. R. and Bennett, B. F.: Forecasting Global Warming, in Paris Climate Agreement: Beacon of Hope, pp. 51–114, Springer Climate., 2017.

Ishihara, K.: Calculation of global surface temperature anomalies with COBE-SST, Weather Serv. Bull., 73, S19–S25, 2006.

Ishii, M., Shouji, A., Sugimoto, S. and Matsumoto, T.: Objective analyses of sea-surface temperature and marine meteorological variables for the 20th century using ICOADS and the Kobe Collection, Int. J. Climatol., 25(7), 865–879, doi:10.1002/joc.1169, 2005.

Ishii, M., Fukuda, Y., Hirahara, S., Yasui, S., Suzuki, T. and Sato, K.: Accuracy of Global Upper Ocean Heat Content Estimation Expected from Present Observational Data Sets, Sci. Online Lett. Atmos., 13(0), 163–167, doi:10.2151/sola.2017-030, 2017.

Jackson, L. C., Kahana, R., Graham, T., Ringer, M. A., Woollings, T., Mecking, J. V. and Wood, R. A.: Global and European climate impacts of a slowdown of the AMOC in a high resolution GCM, Clim. Dyn., 45(11–12), 3299–3316, doi:10.1007/s00382-015-2540-2, 2015.

Jones, C., Sellar, A., Tang, Y. and Rumbold, S.: Results from the UKESM1 CMIP6 DECK and historical simulations, UKESM [online] Available from: https://ukesm.ac.uk/portfolio-item/ukesm1-cmip6-deck-and-historical/# (Accessed 9 October 2019), 2019.

Kavvada, A., Ruiz-Barradas, A. and Nigam, S.: AMO's structure and climate footprint in observations and IPCC AR5 climate simulations, Clim. Dyn., 41(5–6), 1345–1364, doi:10.1007/s00382-013-1712-1, 2013.

Kennedy, J. J., Rayner, N. A., Smith, R. O., Parker, D. E. and Saunby, M.: Reassessing biases and other uncertainties in sea surface temperature observations measured in situ since 1850: 2. Biases and homogenization, J. Geophys. Res., 116(D14), 1–22, doi:10.1029/2010jd015220, 2011.

Kennedy, J. J., Rayner, N. A., Atkinson, C. P. and Killick, R. E.: An Ensemble Data Set of Sea Surface Temperature Change From 1850: The Met Office Hadley Centre HadSST.4.0.0.0 Data Set, J. Geophys. Res. Atmos., 124(14), 7719–7763, doi:10.1029/2018JD029867, 2019.

Kiehl, J. T.: Twentieth century climate model response and climate sensitivity, Geophys. Res. Lett., 34(22), 1–4, doi:10.1029/2007GL031383, 2007.

Kirschke, S., Bousquet, P., Ciais, P., Saunois, M., Canadell, J. G., Dlugokencky, E. J., Bergamaschi, P., Bergmann, D., Blake, D. R., Bruhwiler, L., Cameron-Smith, P., Castaldi, S., Chevallier, F., Feng, L., Fraser, A., Heimann, M., Hodson, E. L., Houweling, S., Josse, B., Fraser, P. J., Krummel, P. B., Lamarque, J. F., Langenfelds, R. L., Le Quéré, C., Naik, V., O'doherty, S., Palmer, P. I., Pison, I., Plummer, D., Poulter, B., Prinn, R. G., Rigby, M., Ringeval, B., Santini, M., Schmidt, M., Shindell, D. T., Simpson, I. J., Spahni, R., Steele, L. P., Strode, S. A., Sudo, K., Szopa, S., Van Der Werf, G. R., Voulgarakis, A., Van Weele, M., Weiss, R. F., Williams, J. E. and Zeng, G.: Three decades of global methane sources and sinks, Nat. Geosci., 6(10), 813–823, doi:10.1038/ngeo1955, 2013.

Kirtman, B., Power, S. B., Adedoyin, A. J., Boer, G. J., Bojariu, R., Camilloni, I., Doblas-Reyes, F., Fiore, A. M., Kimoto, M., Meehl, G., Prather, M., Sarr, A., Schär, C., Sutton, R., van Oldenborgh, G. J., Vecchi, G. and Wang, H. J.: Near-term

climate change: Projections and predictability, Clim. Chang. 2013 Phys. Sci. Basis Work. Gr. I Contrib. to Fifth Assess. Rep. Intergov. Panel Clim. Chang., 9781107057, 953–1028, doi:10.1017/CBO9781107415324.023, 2013.

Klein, S. A., Hall, A., Norris, J. R. and Pincus, R.: Low-Cloud Feedbacks from Cloud-Controlling Factors: A Review, Surv. Geophys., 38(6), 1307–1329, doi:10.1007/s10712-017-9433-3, 2017.

Knight, J. R., Allan, R. J., Folland, C. K., Vellinga, M. and Mann, M. E.: A signature of persistent natural thermohaline circulation cycles in observed climate, Geophys. Res. Lett., 32(20), 1–4, doi:10.1029/2005GL024233, 2005.

Kriegler, E., Weyant, J. P., Blanford, G. J., Krey, V., Clarke, L., Edmonds, J., Fawcett, A., Luderer, G., Riahi, K., Richels, R., Rose, S. K., Tavoni, M. and van Vuuren, D. P.: The role of technology for achieving climate policy objectives: Overview of the EMF 27 study on global technology and climate policy strategies, Clim. Change, 123(3–4), 353–367, doi:10.1007/s10584-013-0953-7, 2014.

Kriegler, E., Riahi, K., Bauer, N., Schwanitz, V. J., Petermann, N., Bosetti, V., Marcucci, A., Otto, S., Paroussos, L., Rao, S., Arroyo Currás, T., Ashina, S., Bollen, J., Eom, J., Hamdi-Cherif, M., Longden, T., Kitous, A., Méjean, A., Sano, F., Schaeffer, M., Wada, K., Capros, P., P. van Vuuren, D. and Edenhofer, O.: Making or breaking climate targets: The AMPERE study on staged accession scenarios for climate policy, Technol. Forecast. Soc. Change, doi:10.1016/j.techfore.2013.09.021, 2015.

Kriegler, E., Bauer, N., Popp, A., Humpenöder, F., Leimbach, M., Strefler, J., Baumstark, L., Bodirsky, B. L., Hilaire, J., Klein, D., Mouratiadou, I., Weindl, I., Bertram, C., Dietrich, J. P., Luderer, G., Pehl, M., Pietzcker, R., Piontek, F., Lotze-Campen, H., Biewald, A., Bonsch, M., Giannousakis, A., Kreidenweis, U., Müller, C., Rolinski, S., Schultes, A., Schwanitz, J., Stevanovic, M., Calvin, K., Emmerling, J., Fujimori, S. and Edenhofer, O.: Fossil-fueled development (SSP5): An energy and resource intensive scenario for the 21st century, Glob. Environ. Chang., 42, 297–315, doi:10.1016/j.gloenvcha.2016.05.015, 2017.

Kushnir, Y.: Interdecadal Variations in North Atlantic Sea Surface Temperature and Associated Atmospheric Conditions, J. Clim., 7(1), 141–157, doi:10.1175/1520-0442(1994)007<0141:IVINAS>2.0.CO;2, 1994.

Lean, J. L. and Rind, D. H.: How natural and anthropogenic influences alter global and regional surface temperatures: 1889 to 2006, Geophys. Res. Lett., 35(18), 1–6, doi:10.1029/2008GL034864, 2008.

Lean, J. L. and Rind, D. H.: How will Earth's surface temperature change in future decades?, Geophys. Res. Lett., 36(15), 1–5, doi:10.1029/2009GL038932, 2009.

Lelieveld, J., Evans, J. S., Fnais, M., Giannadaki, D. and Pozzer, A.: The contribution of outdoor air pollution sources to premature mortality on a global scale, Nature, 525(7569), 367–371, doi:10.1038/nature15371, 2015.

Levitus, S., Antonov, J. I., Boyer, T. P., Baranova, O. K., Garcia, H. E., Locarnini, R. A., Mishonov, A. V., Reagan, J. R., Seidov, D., Yarosh, E. S. and Zweng, M. M.: World ocean heat content and thermosteric sea level change (0-2000m), 1955-2010, Geophys. Res. Lett., 39(10), 1–5, doi:10.1029/2012GL051106, 2012.

Lewis, N. and Curry, J.: The impact of recent forcing and ocean heat uptake data on estimates of climate sensitivity, J. Clim., 31(15), 6051–6071, doi:10.1175/JCLI-D-17-0667.1, 2018.

Lewis, N. and Grünwald, P.: Objectively combining AR5 instrumental period and paleoclimate climate sensitivity evidence, Clim. Dyn., 50(5), 2199–2216, doi:10.1007/s00382-017-3744-4, 2018.

Marvel, K., Pincus, R., Schmidt, G. A. and Miller, R. L.: Internal Variability and Disequilibrium Confound Estimates of Climate Sensitivity From Observations, Geophys. Res. Lett., 45(3), 1595–1601, doi:10.1002/2017GL076468, 2018.

Mascioli, N. R., Canty, T. and Salawitch, R. J.: An empirical model of global climate – Part 2: Implications for future temperature, Atmos. Chem. Phys., 2013.

Matthes, K., Funke, B., Andersson, M. E., Barnard, L., Beer, J., Charbonneau, P., Clilverd, M. A., Dudok de Wit, T., Haberreiter, M., Hendry, A., Jackman, C. H., Kretzschmar, M., Kruschke, T., Kunze, M., Langematz, U., Marsh, D. R., Maycock, A. C., Misios, S., Rodger, C. J., Scaife, A. A., Seppala, A., Shangguan, M., Sinnhuber, M., Tourpali, K., Usoskin, I., van de Kamp, M., Verronen, P. T. and Versick, S.: Solar forcing for CMIP6 (v3.2), Geosci. Model Dev., 10, 2247–2302, 2017.

McBride, L. A., Hope, A. P., Canty, T. P., Bennett, B. F., Tribett, W. R. and Salawitch, R. J.: Input and Output Files EMGC, , doi:10.5281/zenodo.4300780, 2021.

Medhaug, I. and Furevik, T.: North Atlantic 20th century multidecadal variability in coupled climate models: Sea surface temperature and ocean overturning circulation, Ocean Sci., 7(3), 389–404, doi:10.5194/os-7-389-2011, 2011.

Meehl, G. A., Senior, C. A., Eyring, V., Flato, G., Lamarque, J. F., Stouffer, R. J., Taylor, K. E. and Schlund, M.: Context for

interpreting equilibrium climate sensitivity and transient climate response from the CMIP6 Earth system models, Sci. Adv., 6(26), 1–11, doi:10.1126/sciadv.aba1981, 2020.

Meinshausen, M., Smith, S. J., Calvin, K., Daniel, J. S., Kainuma, M. L. T., Lamarque, J., Matsumoto, K., Montzka, S. A., Raper, S. C. B., Riahi, K., Thomson, A., Velders, G. J. M. and van Vuuren, D. P. P.: The RCP greenhouse gas concentrations and their extensions from 1765 to 2300, Clim. Change, 109(1), 213–241, doi:10.1007/s10584-011-0156-z, 2011.

Meinshausen, M., Vogel, E., Nauels, A., Lorbacher, K., Meinshausen, N., Etheridge, D. M., Fraser, P. J., Montzka, S. A., Rayner, P. J., Trudinger, C. M., Krummel, P. B., Beyerle, U., Canadell, J. G., Daniel, J. S., Enting, I. G., Law, R. M., Lunder, C. R., O'Doherty, S., Prinn, R. G., Reimann, S., Rubino, M., Velders, G. J. M., Vollmer, M. K., Wang, R. H. J. and Weiss, R.: Historical greenhouse gas concentrations for climate modelling (CMIP6), Geosci. Model Dev., 10(5), 2057–2116, doi:10.5194/gmd-10-2057-2017, 2017.

Millar, R. J., Fuglestvedt, J. S., Friedlingstein, P., Rogelj, J., Grubb, M. J., Matthews, H. D., Skeie, R. B., Forster, P. M., Frame, D. J. and Allen, M. R.: Emission budgets and pathways consistent with limiting warming to 1.5°C, Nat. Geosci., 11(6), 454–455, doi:10.1038/s41561-018-0153-1, 2017.

Morice, C. P., Kennedy, J. J., Rayner, N. A. and Jones, P. D.: Quantifying uncertainties in global and regional temperature change using an ensemble of observational estimates: The HadCRUT4 data set, J. Geophys. Res. Atmos., 117(8), 1–22, doi:10.1029/2011JD017187, 2012.

Morice, C. P., Kennedy, J. J., Rayner, N. A., Winn, J. P., Hogan, E., Killick, R. E., Dunn, R. J. H., Osborn, T. J., Jones, P. D. and Simpson, I. R.: An updated assessment of near-surface temperature change from 1850: the HadCRUT5 dataset, J. Geophys. Res. Atmos., doi:10.1029/2019jd032361, 2021.

Murphy, J. M., Booth, B. B. B., Boulton, C. A., Clark, R. T., Harris, G. R., Lowe, J. A. and Sexton, D. M. H.: Transient climate changes in a perturbed parameter ensemble of emissions-driven earth system model simulations, Clim. Dyn., 43(9–10), 2855–2885, doi:10.1007/s00382-014-2097-5, 2014.

Myhre, G., Highwood, E. J., Shine, K. P. and Stordal, F.: New estimates of radiative forcing due to wel mixed greenhouse gases, Geophys. Res. Lett., 25(14), 2715–2718, 1998.

Myhre, G., Nilsen, J. S., Gulstad, L., Shine, K. P., Rognerud, B. and Isaksen, I. S. A.: Radiative forcing due to stratospheric water vapour from CH4 oxidation, Geophys. Res. Lett., 34(1), 3–7, doi:10.1029/2006GL027472, 2007.

Myhre, G., Shindell, D., Bréon, F.-M., Collins, W., Fuglestvedt, J., Huang, J., Koch, D., Lamarque, J.-F., Lee, D., Mendoza, B., Nakajima, T., Robock, A., Stephens, G., Takemura, T. and Zhang, H.: Anthropogenic and Natural Radiative Forcing, Clim. Chang. 2013 Phys. Sci. Basis. Contrib. Work. Gr. I to Fifth Assess. Rep. Intergov. Panel Clim. Chang., 659–740, doi:10.1017/ CBO9781107415324.018, 2013.

Nigam, S., Guan, B. and Ruiz-Barradas, A.: Key role of the Atlantic Multidecadal Oscillation in 20th century drought and wet periods over the Great Plains, Geophys. Res. Lett., 38(16), 1–6, doi:10.1029/2011GL048650, 2011.

Nijsse, F. J. M. M., Cox, P. M. and Williamson, M. S.: Emergent constraints on transient climate response (TCR) and equilibrium climate sensitivity (ECS) from historical warming in CMIP5 and CMIP6 models, Earth Syst. Dyn., 11, 737–750, 2020.

O'Neill, B. C., Kriegler, E., Riahi, K., Ebi, K. L., Hallegatte, S., Carter, T. R., Mathur, R. and van Vuuren, D. P.: A new scenario framework for climate change research: The concept of shared socioeconomic pathways, Clim. Change, 122(3), 387–400, doi:10.1007/s10584-013-0905-2, 2014.

O'Neill, B. C., Tebaldi, C., Van Vuuren, D. P., Eyring, V., Friedlingstein, P., Hurtt, G., Knutti, R., Kriegler, E., Lamarque, J. F., Lowe, J., Meehl, G. A., Moss, R., Riahi, K. and Sanderson, B. M.: The Scenario Model Intercomparison Project (ScenarioMIP) for CMIP6, Geosci. Model Dev., 9(9), 3461–3482, doi:10.5194/gmd-9-3461-2016, 2016.

O'Neill, B. C., Kriegler, E., Ebi, K. L., Kemp-Benedict, E., Riahi, K., Rothman, D. S., van Ruijven, B. J., van Vuuren, D. P., Birkmann, J., Kok, K., Levy, M. and Solecki, W.: The roads ahead: Narratives for shared socioeconomic pathways describing world futures in the 21st century, Glob. Environ. Chang., 42, 169–180, doi:10.1016/j.gloenvcha.2015.01.004, 2017.

Otto, A., Otto, F. E. L., Boucher, O., Church, J., Hegerl, G., Forster, P. M., Gillett, N. P., Gregory, J., Johnson, G. C., Knutti, R., Lewis, N., Lohmann, U., Marotzke, J., Myhre, G., Shindell, D., Stevens, B. and Allen, M. R.: Energy budget constraints on climate response, Nat. Geosci., 6(6), 415–416, doi:10.1038/ngeo1836, 2013.

Proistosescu, C. and Huybers, P. J.: Slow climate mode reconciles historical and model-based estimates of climate sensitivity,

Sci. Adv., 3(7), 1–7, doi:10.1126/sciadv.1602821, 2017.

Raper, S. C. B., Gregory, J. M. and Stouffer, R. J.: The role of climate sensitivity and ocean heat uptake on AOGCM transient temperature response, J. Clim., 15(1), 124–130, doi:10.1175/1520-0442(2002)015<0124:TROCSA>2.0.CO;2, 2002.

Riahi, K., Kriegler, E., Johnson, N., Bertram, C., den Elzen, M., Eom, J., Schaeffer, M., Edmonds, J., Isaac, M., Krey, V., Longden, T., Luderer, G., Méjean, A., McCollum, D. L., Mima, S., Turton, H., van Vuuren, D. P., Wada, K., Bosetti, V., Capros, P., Criqui, P., Hamdi-Cherif, M., Kainuma, M. and Edenhofer, O.: Locked into Copenhagen pledges - Implications of short-term emission targets for the cost and feasibility of long-term climate goals, Technol. Forecast. Soc. Change, 90(PA), 8–23, doi:10.1016/j.techfore.2013.09.016, 2015.

Riahi, K., van Vuuren, D. P., Kriegler, E., Edmonds, J., O'Neill, B. C., Fujimori, S., Bauer, N., Calvin, K., Dellink, R., Fricko, O., Lutz, W., Popp, A., Cuaresma, J. C., KC, S., Leimbach, M., Jiang, L., Kram, T., Rao, S., Emmerling, J., Ebi, K., Hasegawa, T., Havlik, P., Humpenöder, F., Da Silva, L. A., Smith, S., Stehfest, E., Bosetti, V., Eom, J., Gernaat, D., Masui, T., Rogelj, J., Strefler, J., Drouet, L., Krey, V., Luderer, G., Harmsen, M., Takahashi, K., Baumstark, L., Doelman, J. C., Kainuma, M., Klimont, Z., Marangoni, G., Lotze-Campen, H., Obersteiner, M., Tabeau, A. and Tavoni, M.: The Shared Socioeconomic Pathways and their energy, land use, and greenhouse gas emissions implications: An overview, Glob. Environ. Chang., 42, 153–168, doi:10.1016/j.gloenvcha.2016.05.009, 2017.

Rogelj, J., Popp, A., Calvin, K. V., Luderer, G., Emmerling, J., Gernaat, D., Fujimori, S., Strefler, J., Hasegawa, T., Marangoni, G., Krey, V., Kriegler, E., Riahi, K., Van Vuuren, D. P., Doelman, J., Drouet, L., Edmonds, J., Fricko, O., Harmsen, M., Havlík, P., Humpenöder, F., Stehfest, E. and Tavoni, M.: Scenarios towards limiting global mean temperature increase below 1.5 °c, Nat. Clim. Chang., 8(4), 325–332, doi:10.1038/s41558-018-0091-3, 2018.

Rohde, R., Muller, R., Jacobsen, R., Muller, E. and Wickham, C.: A New Estimate of the Average Earth Surface Land Temperature Spanning 1753 to 2011, Geoinformatics Geostatistics An Overv., 01(01), 1–7, doi:10.4172/2327-4581.1000101, 2013.

Rohde, R. A. and Hausfather, Z.: The Berkeley Earth Land/Ocean Temperature Record, Earth Syst. Sci. Data, 12(4), 3469–3479, doi:10.5194/essd-12-3469-2020, 2020.

Rugenstein, M., Bloch-Johnson, J., Gregory, J., Andrews, T., Mauritsen, T., Li, C., Frölicher, T. L., Paynter, D., Danabasoglu, G., Yang, S., Dufresne, J. L., Cao, L., Schmidt, G. A., Abe-Ouchi, A., Geoffroy, O. and Knutti, R.: Equilibrium Climate Sensitivity Estimated by Equilibrating Climate Models, Geophys. Res. Lett., 47(4), 1–12, doi:10.1029/2019GL083898, 2020.

Saji, N. H., Goswami, B. N., Vinayachandran, P. N. and Yamagata, T.: A dipole mode in the tropical Indian ocean, Nature, 401(6751), 360–363, doi:10.1038/43854, 1999.

Saunois, M., Stavert, A., Poulter, B., Bousquet, P., Canadell, J., Jackson, R., Raymond, P., Dlugokencky, E., Houweling, S., Patra, P., Ciais, P., Arora, V., Bastviken, D., Bergamaschi, P., Blake, D., Brailsford, G., Bruhwiler, L., Carlson, K., Carrol, M., Castaldi, S., Chandra, N., Crevoisier, C., Crill, P., Covey, K., Curry, C., Etiope, G., Frankenberg, C., Gedney, N., Hegglin, M., Höglund-Isaksson, L., Hugelius, G., Ishizawa, M., Ito, A., Janssens-Maenhout, G., Jensen, K., Joos, F., Kleinen, T., Krummel, P., Langenfelds, R., Laruelle, G., Liu, L., Machida, T., Maksyutov, S., McDonald, K., McNorton, J., Miller, P., Melton, J., Morino, I., Müller, J., Murguia-Flores, F., Naik, V., Niwa, Y., Noce, S., O'Doherty, S., Parker, R., Peng, C., Peng, S., Peters, G., Prigent, C., Prinn, R., Ramonet, M., Regnier, P., Riley, W., Rosentreter, J., Segers, A., Simpson, I., Shi, H., Smith, S., Steele, L. P., Thornton, B., Tian, H., Tohjima, Y., Tubiello, F., Tsuruta, A., Viovy, N., Voulgarakis, A., Weber, T., van Weele, M., van der Werf, G., Weiss, R., Worthy, D., Wunch, D., Yin, Y., Yoshida, Y., Zhang, W., Zhang, Z., Zhao, Y., Zheng, B., Zhu, Q., Zhu, Q. and Zhuang, Q.: The Global Methane Budget 2000–2017, Earth Syst. Sci. Data, 12(3), 1561–1623, doi:10.5194/essd-12-1561-2020, 2020.

Schiffer, R. A. and Rossow, W. B.: The International Satellite Cloud Climatology Project (ISCCP): The first project of the World Climate Research Programme, Bull. Am. Meteorol. Soc., (76), 779–784, 1983.

Schlesinger, M. E. and Ramankutty, N.: An oscillation in the global climate system of period 65-70 years, Nature, 367, 723–726, 1994.

Schwartz, S. E.: Determination of Earth's Transient and Equilibrium Climate Sensitivities from Observations Over the Twentieth Century: Strong Dependence on Assumed Forcing, Surv. Geophys., 33(3–4), 745–777, doi:10.1007/s10712-012-9180-4, 2012.

Sellar, A. A., Walton, J., Jones, C. G., Wood, R., Abraham, N. L., Andrejczuk, M., Andrews, M. B., Andrews, T., Archibald, A. T., de Mora, L., Dyson, H., Elkington, M., Ellis, R., Florek, P., Good, P., Gohar, L., Haddad, S., Hardiman, S. C.,

Hogan, E., Iwi, A., Jones, C. D., Johnson, B., Kelley, D. I., Kettleborough, J., Knight, J. R., Köhler, M. O., Kuhlbrodt, T., Liddicoat, S., Linova-Pavlova, I., Mizielinski, M. S., Morgenstern, O., Mulcahy, J., Neininger, E., O'Connor, F. M., Petrie, R., Ridley, J., Rioual, J. C., Roberts, M., Robertson, E., Rumbold, S., Seddon, J., Shepherd, H., Shim, S., Stephens, A., Teixiera, J. C., Tang, Y., Williams, J., Wiltshire, A. and Griffiths, P. T.: Implementation of U.K. Earth System Models for CMIP6, J. Adv. Model. Earth Syst., 12(4), 1–27, doi:10.1029/2019MS001946, 2020.

Shen, Z., Ming, Y. and Held, I. M.: Using the fast impact of anthropogenic aerosols on regional land temperature to constrain aerosol forcing, Sci. Adv., (August), 1–8, 2020.

Sherwood, A. S., Webb, M. J., Annan, J. D., Armour, K. C., Forster, P. M., Hargreaves, J. C., Hegerl, G., Klein, S. A., Marvel, K. D., Rohling, E. J., Watanabe, M., Andrews, T., Braconnot, P., Bretherton, C. S., Foster, G. L., Hausfather, Z., von der Heydt, A. S., Knutti, R., Mauritsen, T., Norris, J. R., Proistosescu, C., Rugenstein, M., Schmidt, G. A. and Tokarska, K. B., Zelinka, M. D.: An assessment of Earth ' s climate sensitivity using multiple lines of evidence, Rev. Geophys., 1–166, 2020.

Shindell, D. T., Lee, Y. and Faluvegi, G.: Climate and health impacts of US emissions reductions consistent with 2 °c, Nat. Clim. Chang., 6(5), 503–507, doi:10.1038/nclimate2935, 2016.

Skeie, R., Berntsen, T., Aldrin, M., Holden, M. and Myhre, G.: Climate sensitivity estimates - Sensitivity to radiative forcing time series and observational data, Earth Syst. Dyn., 9(2), 879–894, doi:10.5194/esd-9-879-2018, 2018.

Smith, S. J. and Bond, T. C.: Two hundred fifty years of aerosols and climate: The end of the age of aerosols, Atmos. Chem. Phys., 14(2), 537–549, doi:10.5194/acp-14-537-2014, 2014.

Smith, T. M., Reynolds, R. W., Peterson, T. C. and Lawrimore, J.: Improvements to NOAA's historical merged land-ocean surface temperature analysis (1880-2006), J. Clim., 21(10), 2283–2296, doi:10.1175/2007JCLI2100.1, 2008.

Solomon, S.: Climate change 2007-the physical science basis: Working group I contribution to the fourth assessment report of the IPCC, Cambridge University Press., 2007.

Stocker, T., Qin, D., Plattner, G., Tignor, M., Allen, S., Boschung, J., Nauels, A., Xia, Y., Bex, V. and Midgely, P.: IPCC, 2013: climate change 2013: The physical science basis. Conribution of working group I to the fifth assessment report of the intergovernmental panel on climate change., Cambridge, UK and New York, NY USA., 2013.

Stouffer, R. J., Yin, J., Gregory, J. M., Dixon, K. W., Spelman, M. J., Hurlin, W., Weaver, A. J., Eby, M., Flato, G. M., Hasumi, H., Hu, A., Jungclaus, J. H., Kamenkovich, I. V., Levermann, A., Montoya, M., Murakami, S., Nawrath, S., Oka, A., Peltier, W. R., Robitaille, D. Y., Sokolov, A., Vettoretti, G. and Weber, S. L.: Investigating the cause of the response of the thermohaline circulation to past and future climage changes, J. Clim., 19(8), 1365–1387, doi:10.1175/JCLI3689.1, 2006.

Swart, N. C., Cole, J. N. S., Kharin, V. V., Lazare, M., Scinocca, J. F., Gillett, N. P., Anstey, J., Arora, V., Christian, J. R., Hanna, S., Jiao, Y., Lee, W. G., Majaess, F., Saenko, O. A., Seiler, C., Seinen, C., Shao, A., Sigmond, M., Solheim, L., Von Salzen, K., Yang, D. and Winter, B.: The Canadian Earth System Model version 5 (CanESM5.0.3), Geosci. Model Dev., 12(11), 4823–4873, doi:10.5194/gmd-12-4823-2019, 2019.

Tatebe, H., Ogura, T., Nitta, T., Komuro, Y., Ogochi, K., Takemura, T., Sudo, K., Sekiguchi, M., Abe, M., Saito, F., Chikira, M., Watanabe, S., Mori, M., Hirota, N., Kawatani, Y., Mochizuki, T., Yoshimura, K., Takata, K., O'Ishi, R., Yamazaki, D., Suzuki, T., Kurogi, M., Kataoka, T., Watanabe, M. and Kimoto, M.: Description and basic evaluation of simulated mean state, internal variability, and climate sensitivity in MIROC6, Geosci. Model Dev., 12(7), 2727–2765, doi:10.5194/gmd-12-2727-2019, 2019.

Taylor, K. E., Stouffer, R. J. and Meehl, G. A.: An overview of CMIP5 and the experiment design, Bull. Am. Meteorol. Soc., 93(4), 485–498, doi:10.1175/BAMS-D-11-00094.1, 2012.

Thomason, L. W., Ernest, N., Millán, L., Rieger, L., Bourassa, A., Vernier, J. P., Manney, G., Luo, B., Arfeuille, F. and Peter, T.: A global space-based stratospheric aerosol climatology: 1979-2016, Earth Syst. Sci. Data, 10(1), 469–492, doi:10.5194/essd-10-469-2018, 2018.

Thompson, D. W. J., Wallace, J. M., Jones, P. D. and Kennedy, J. J.: Identifying signatures of natural climate variability in time series of global-mean surface temperature: Methodology and insights, J. Clim., 22(22), 6120–6141, doi:10.1175/2009JCLI3089.1, 2009.

Tokarska, K. B., Stolpe, M. B., Sippel, S., Fischer, E. M., Smith, C. J., Lehner, F. and Knutti, R.: Past warming trend constrains future warming in CMIP6 models, Sci. Adv., 6(12), 1–13, doi:10.1126/sciadv.aaz9549, 2020.

Trenberth, K. E. and Fasullo, J. T.: An apparent hiatus in global warming?, Earth's Futur., 1, 19–32,

doi:10.1002/2013EF000165.Received, 2013.
Vaughan, M. A., Young, S. A., Winker, D. M., Powell, K. A., Omar, A. H., Liu, Z., Hu, Y. and Hostetler, C. A.: Fully automated analysis of space-based lidar data: an overview of the CALIPSO retrieval algorithms and data products, in Proc.SPIE, vol. 5575., 2004.
Volodin, E. and Gritsun, A.: Simulation of observed climate changes in 1850-2014 with climate model INM-CM5, Earth Syst. Dyn., 9(4), 1235–1242, doi:10.5194/esd-9-1235-2018, 2018.
van Vuuren, D. P., Stehfest, E., Gernaat, D. E. H. J., Doelman, J. C., van den Berg, M., Harmsen, M., de Boer, H. S., Bouwman, L. F., Daioglou, V., Edelenbosch, O. Y., Girod, B., Kram, T., Lassaletta, L., Lucas, P. L., van Meijl, H., Müller, C., van Ruijven, B. J., van der Sluis, S. and Tabeau, A.: Energy, land-use and greenhouse gas emissions trajectories under a green growth paradigm, Glob. Environ. Chang., 42, 237–250, doi:10.1016/j.gloenvcha.2016.05.008, 2017.
van Vuuren, D. P., van der Wijst, K.-I., Marsman, S., van den Berg, M., Hof, A. F. and Jones, C. D.: The costs of achieving climate targets and the sources of uncertainty, Nat. Clim. Chang., 10(April), doi:10.1038/s41558-020-0732-1, 2020.
Weaver, C. J., Wu, D. L., Bhartia, P. K., Labow, G. J. and Haffner, D. P.: A long-term cloud albedo data record since 1980 from UV satellite sensors, Remote Sens., 12(12), 1–18, doi:10.3390/rs12121982, 2020.
WMO: World Meteorological Organization, Scientific assessment of ozone depletion: 2018, Glob. Ozone Res. Monit. Proj. #58, 2018.
Wolf, J., Asrar, G. R. and West, T. O.: Revised methane emissions factors and spatially distributed annual carbon fluxes for global livestock, Carbon Balance Manag., 12(1), doi:10.1186/s13021-017-0084-y, 2017.
Wolter, K. and Timlin, M. S.: Monitoring ENSO in COADS with a seasonally adjusted principal component index, Proc 17th Clim. Diagnostics Work., 52–57 [online] Available from: http://www.esrl.noaa.gov/psd/enso/mei/WT1.pdf%5Cnpapers2://publication/uuid/123434A4-48AA-4F4B-A3F7-506504693A80, 1993.
Wolter, K. and Timlin, M. S.: El Niño/Southern Oscillation behaviour since 1871 as diagnosed in an extended multivariate ENSO index (MEI.ext), Int. J. Climatol., 31(7), 1074–1087, doi:10.1002/joc.2336, 2011.
Zelinka, M. D., Myers, T. A., McCoy, D. T., Po-Chedley, S., Caldwell, P. M., Ceppi, P., Klein, S. A. and Taylor, K. E.: Causes of Higher Climate Sensitivity in CMIP6 Models, Geophys. Res. Lett., 47(1), doi:10.1029/2019GL085782, 2020.
Zhang, H.-M., Lawrimore, J., Huang, B., Menne, M. J., Yin, X., Sanchez-Lugo, A., Gleason, B. E., Vose, R., Arndt, D., Rennie, J. J. and Williams, C. N.: Updated Temperature Data Give a Sharper View of Climate Trends, Eos (Washington. DC)., 100, doi:10.1029/2019EO128229, 2019.
Zhang, R. and Delworth, T. L.: Impact of the Atlantic Multidecadal Oscillation on North Pacific climate variability, Geophys. Res. Lett., 34(23), 2–7, doi:10.1029/2007GL031601, 2007.
Zhou, J. and Tung, K. K.: Deducing multidecadal anthropogenic global warming trends using multiple regression analysis, J. Atmos. Sci., 70(1), 3–8, doi:10.1175/JAS-D-12-0208.1, 2013.
Zhu, J., Poulsen, C. J. and Otto-Bliesner, B. L.: High climate sensitivity in CMIP6 model not supported by paleoclimate, Nat. Clim. Chang., 10(5), 378–379, doi:10.1038/s41558-020-0764-6, 2020.

10 Data availability

All data used as inputs into the EM-GC are available from resources on the web. We have provided the links to the resources below. The data are also available along with the EM-GC output data used in this analysis at 10.5281/zenodo.4300780 ~~10.5281/zenodo.3908407~~ (McBride et al., 2021) on Zenodo.org.

IOD: The COBE SST data is provided by the NOAA ESRL physical sciences division from their web site https://www.esrl.noaa.gov/psd/.

Tropospheric ozone RF: http://www.pik-potsdam.de/~mmalte/rcps/ .

MEI.v2 and MEI.ext: https://psl.noaa.gov/enso/mei/data/meiv2.data and https://psl.noaa.gov/enso/mei.ext/table.ext.html

PDO: http://research.jisao.washington.edu/pdo/PDO.latest.txt

SAOD: https://eosweb.larc.nasa.gov/project/glossac/glossac

TSI: http://lasp.colorado.edu/home/sorce/data/tsi-data/

OHC Records:

Balmaseda: http://www.cgd.ucar.edu/cas/catalog/ocean/OHC700m.tar.gz
Carton: https://www.atmos.umd.edu/~ocean/index_files/soda3_readme.htm
Cheng: http://159.226.119.60/cheng/
Ishii: http://159.226.119.60/cheng/
Levitus: https://www.nodc.noaa.gov/OC5/3M_HEAT_CONTENT/

SSP Database: All information for the SSPs obtained from the SSP database is at https://tntcat.iiasa.ac.at/SspDb/dsd?Action=htmlpage&page=about .

CMIP6 Input Data: https://docs.google.com/document/d/1pU9IiJvPJwRvIgVaSDdJ4O0Jeorv_2ekEtted34K9cA/edit#heading=h.jdoykiw7tpen

CMIP6 Model Output Archive: https://esgf-node.llnl.gov/search/cmip6/

Supplement

Section 2.1 states "The effect of this update results in our model being able to fit the historical climate record with higher values of climate feedback, especially for strong aerosol cooling (see Fig. S1 and supplement for more information)". Figure S1 illustrates the impact of updating Eq. (2) in our model to be comparable to the formulation in Bony et al. (2006) and Schwartz (2012). This figure displays the change in GMST anomaly in 2100 relative to pre-industrial (ΔT_{2100}) as a function of λ_{Σ} and AER RF_{2011} for the two formulations of Eq. (2). Figure S1a uses the previous version of the EM-GC, where Q_{OCEAN} was subtracted outside of the climate feedback multiplicative term, and Fig. 1b uses the new version of the EM-GC where Q_{OCEAN} is subtracted within the climate feedback multiplicative term.

In the EM-GC framework, we calculate our value of Q_{OCEAN} by finding the κ needed to multiply the temperature difference between the atmosphere and the ocean to fit the observed OHC record. The model iterates over the ocean module, specifically the value of $\Delta T_{OCEAN,HUMAN}$ in Eq. (4), until the EM-GC converges on an estimate of κ for a single OHC record and value of AER RF_{2011}. Figure S1 illustrates that the effect of changing Eq. (2) in the EM-GC impacts our estimates of the rise in ΔT_{2100} at high values of AER RF_{2011}. Strong aerosol cooling results in the ocean taking up more heat from the atmosphere than in the previous version of the EM-GC. The larger value of Q_{OCEAN} results in a higher value of climate feedback needed to fit the historical climate record, because both AER RF_{2011} and Q_{OCEAN} are acting to cool the climate system. The higher values of climate feedback increase our maximum value of ΔT_{2100}. This change brings some of the projections of ΔT_{2100} from the EM-GC closer to values of ΔT_{2100} from the CMIP6 multi-model ensemble.

Section 2.1 states "Altering the training period of our model has a slight effect on our results (see Fig. S2, S3, and the supplement for information on various training periods)." Figure S2 shows the end of century projected warming as a function of λ_{Σ} and AER RF_{2011}, for four different training periods: 1850-1989 (Fig. S2a), 1850-1999 (Fig. S2b), 1850-2009 (Fig. S2c) and 1850-2019 (Fig. S2d), which is the normal training period used in our analysis. Values of ΔT_{2100} are shown only for combinations of λ_{Σ} and AER RF_{2011} that lead to good fits ($\chi^2 \leq 2$) to the climate record. We project relatively similar results for end of century warming for the training periods that end in 2019~~,~~ and 2009~~, and 1999~~. Our results using the training period from 1850-1999 are similar to observations and other reduced complexity models (Nicholls et al., 2020). The training period that ends in 1989 (Fig. S2a) yields a different "shape" of model parameter space for which good fits to the climate record can be obtained, compared to the other training periods. The different shape for this shorter training period is due to two factors. First, the formulation of the ocean component of our model for the training period that stops in 1989 uses ~~. In training to 1989, we are only considering~~ 35 years

of the observed OHC record. We are able to calculate good fits to the OHC record over this shorter time period that diverge from the OHC record after 1989. Also, for this shorter time period, aerosol radiative forcing of climate cools in a manner that nearly mirrors the warming due to rising GHGs, resulting in a wider range of model parameters that lead to a "good fit" of the climate record, compared to model simulations constrained by data that extend closer to present-day. The highest values of ΔT_{2100} in Fig. S2a are associated with the largest values of λ_{Σ}, which in our model corresponds to excessively high values of κ that we can rule out, based on OHC data collected during 1990 to ~~2020~~2019.

Figure S3 shows the observed (HadCRUT5) and modeled ΔT anomaly from 1945-2060 for the four different training periods described above. Each panel contains three projections of future ΔT for SSP4-3.4: projection using the value of climate feedback that provides the best fit to the historical climate record for a value of AER $RF_{2011} = -0.9$ W m^{-2}, the lowest value of climate feedback that provides a good fit to the observed ΔT record for a value of AER $RF_{2011} = -0.1$ W m^{-2}, and the highest value of climate feedback that provides a good fit to the historical climate record (the associated value of AER RF_{2011} varies depending on the training period). As more years are added to the training period, the range of projection for future temperature decreases (Fig. S3a vs S3d). All of the best fit projections (solid line) and highest value of climate feedback (upper dashed line) closely follow the mid-point of the data, regardless of the training period. Given the nature of this test (i.e., predicting GMST out to 2019 for a series of trainings that stop in either 1989, 1999, or 2009), Figure S3 supports the quantitative accuracy of our approach for simulating and projecting future ΔT.

~~Section 2.2.1 states "see Fig. S4 and the supplement for information on CW14 GMST record". Figure S4 shows the GMST anomaly relative to pre-industrial over time for (a) HadCRUT record with the HadCRUT uncertainties, (b) CW14 record with the CW14 uncertainties, (c) BEG record with the BEG uncertainties, and (d) CW14 record with HadCRUT uncertainties. The uncertainties for CW14 are much smaller than those for the HadCRUT and BEG records. The small values of CW14 uncertainties, especially from 1850-1900, cause the EM-GC to not be able to achieve good fits to this temperature record. We have two choices for use of the CW14 GMST record; either relax the constraint for χ^2_{ATM} (i.e., run with $\chi^2_{ATM} \leq 4$), or modify the CW14 uncertainties. We chose to combine the uncertainties from HadCRUT with the values of GMST from the CW14 record since CW14 is based upon the HadCRUT GMST record. Upon use of this combination of data and uncertainty, we are able to find good fits to the CW14 temperature record that look similar to the fits obtained using the other GMST data sets.~~

Section 2.2.1 states "We use the uncertainty time series from HadCRUT4 for all GMST records (see the supplement, Figs. S4 and S5, and Table S1 for more information)". Figure S4 shows values of ΔT based on

the seven individual GMST records (GISTEMP, BEG, HadCRUT4, CW14, HadCRUT5, NOAAGT, and JMA) with their corresponding 1σ and 2σ uncertainties. A horizontal line at zero denotes the time period of the baseline for each ΔT record. The multi-record mean, excluding the data set that is plotted, is also shown. Since the multi-record mean and individual ΔT record are plotted on the same baseline, these two quantities closely match over this time period. Panels (a), (b), (e), and (f) illustrate that the uncertainties for these GMST records are not large enough to encompass the multi-record mean over 1850-2019. The multi-record mean in panel (a) is below the GISTEMP 1σ uncertainty range between 1880 and 1900, and again between 1980 to 2019. In panel (b), the multi-record mean is above the BEG 1σ range from 1850 until 1865, 1880 to 1895, and below the 1σ uncertainty range from 2000 to 2019. The multi-record mean in panel (e) is below the HadCRUT5 1σ uncertainty range from 1990 until 2019. In panel (f), the multi-record mean is above the NOAAGT 1σ uncertainty range from 1920 until 1955. The JMA GMST record does not provide an uncertainty estimate. We therefore use the HadCRUT4 combined uncertainty (measurement, sampling, bias, and coverage uncertainties (Morice et al., 2012)) estimate for JMA in panel (g). The multi-record mean of ΔT for all data sets other than JMA lies at the edge of the 1σ uncertainty range from 1891 until 2000. After 2000, the multi-record mean falls above both the 1σ and 2σ HadCRUT4 uncertainty range. The HadCRUT4 uncertainty time series shown in panel (c) is the only uncertainty estimate large enough to cover the spread in the various GMST records.

Figure S5 shows ΔT based on all seven GMST records and the multi-record mean relative to three baseline periods. The 1σ and 2σ uncertainties from HadCRUT4 are plotted about the multi-record mean. Panels (a) and (d) show the GMST records relative to 1891-1920, which are the first 30 years all of the data sets have in common. Between 1850-1970, all of the data sets fall within the 1σ HadCRUT4 uncertainty. After 1970, the GMST records start to deviate and some fall outside of the 1σ uncertainty but within the 2σ uncertainty, and JMA falls outside of the 2σ uncertainty. Panels (b) and (e) show the GMST records relative to the HadCRUT baseline period of 1961-1990. We see similar behavior as in panels (a) and (d), where the GMST records largely fall within the HadCRUT4 1σ uncertainty until about 1970. Panels (c) and (f) show the GMST records forced to match HadCRUT5 from 2010-2019, which is baselined to 1961-1990. In these two panels, we see a large spread between the GMST records from the beginning of the time period until 2005.

Table S1 shows the percentage of ΔT data points that lie within the 1σ or 2σ HadCRUT4 uncertainty about the multi-record mean for all seven data records since 1940. Year 1940 is used to be consistent with the definition of our χ^2_{RECENT} parameter. Depending on the choice of baseline period, the number of data points within the uncertainty range varies. For a baseline of 1891-1920, 80% of the data points for all seven records are within the 1σ uncertainty and 95% of the data points are within the 2σ. For a baseline of 1961-1990, 88% and 93% of data points are within the 1σ and 2σ HadCRUT4 uncertainties, respectively. If the

ΔT records are forced to match the average value of the HadCRUT5 data set over the last decade, 72% of the data points are within the 1σ uncertainty and 88% are within the 2σ uncertainty. This analysis shows that depending on which baseline is used, the percentage of points within the 1σ or 2σ uncertainty ranges varies. Overall, these comparisons support the utility of the HadCRUT4 uncertainty for the GMST, since the 1σ and 2σ uncertainty ranges capture a percentage of points approximately correct for a pure Gaussian distribution. Therefore, we have adopted the HadCRUT4 uncertainties in GMST for all of the analyses in the main paper. The uncertainties published by other data centers tend to be smaller than the HadCRUT4 uncertainties. Since only the HadCRUT4 uncertainties span the range of values for ΔT from the seven data records in a somewhat realistic fashion, we have decided to use these uncertainties uniformly throughout the analysis.

Section 2.2.1 also says "We then adjust each data set to the HadCRUT5 pre-industrial baseline as described in the supplement". The mean of the HadCRUT5 GMST record from 1850-1900 is −0.3589°C. We add 0.3589°C to each value of the HadCRUT5 record to adjust the data set onto the pre-industrial baseline. We use this same offset for all of the other data sets. We add 0.3589°C to each value of ΔT from the six data sets to match the HadCRUT5 1850-1900 baseline.

Section 2.2.3 states "Figure ~~S5~~ S6 shows the ozone RF time series used in this analysis and the supplement provides more information about the creation of the time series for the RF due to O_3^{TROP}". Figure ~~S5~~ S6 displays the time series of tropospheric ozone RF used in our analysis for the various SSPs. Tropospheric ozone is an important GHG that rivals nitrous oxide as the third most important anthropogenic GHG. We include the RF due to tropospheric ozone (O_3^{TROP}) in our model for completion, even though the SSP database does not provide RF estimates for the various SSPs. We use values from the RCP scenarios provided by the Potsdam Institute for Climate Impact Research (Meinshausen et al., 2011). The values of the RF due to O_3^{TROP} for SSP1-1.9 and SSP1-2.6 are from the RCP2.6 pathway. The RCP4.5 time series of O_3^{TROP} is used for SSP2-4.5, the RCP6.0 time series is used for SSP4-6.0, and the RCP8.5 time series is used for SSP5-8.5. We create linear combinations of RCP2.6 and RCP8.5 to generate two new time series of the RF due to O_3^{TROP} for SSP4-3.4 and SSP3-7.0. There is a large gap between the time series of the RF due to O_3^{TROP} for RCP6.0 (shown as SSP4-6.0) and RCP8.5 (shown as SSP5-8.5) in Fig. ~~S5~~S6. We created a time series that would split the difference between the two RCPs to represent the RF due to O_3^{TROP} for SSP3-7.0. The SSP4-3.4 time series of the RF due to O_3^{TROP} that was created lies in between the RCP2.6 (shown as SSP1-2.6) and RCP4.5 (shown as SSP2-4.5) time series in Fig. ~~S5~~S6.

Section 2.2.8 states “Figure ~~S8~~ S9 shows the five OHC records as well as the multi-measurement average”. Figure ~~S8~~ S9 displays the five OHC content data sets, as well as the multi-measurement average, plotted as a function of time and normalized to year 1986. This figure illustrates how the shapes of the different OHC records compare. Each of the time series represents the amount of heat stored in the top 700 m of the world’s oceans for that specific data set. Carton et al. (2018) is the shortest data set, and only spans 36 years (1982-2017). The second shortest record is Balmaseda et al. (2013a), which spans 52 years (1958.5-2009.5). Ishii et al. (2017) is the record in the middle with a range of 63 years (1955-2017). Both Cheng et al. (2017) and Levitus et al. (2012) have records that span 65 years (1955-2019). The length of the data set and the shape of the curve affect the estimate of ocean heat export (OHE), because we calculate OHE by taking a linear fit to the full OHC time series. Balmaseda et al. (2013a) has the lowest estimate of OHE because the slope of the curve is relatively shallow, due to the fact that it slightly rises, then decreases at the start of the record. Carton et al. (2018) has the highest estimate of OHE because the slope of the curve is the steepest of the five records.

Section 2.2.8 also says “For these five OHC data sets, uncertainty estimates are not always provided. Furthermore, some studies that do provide uncertainties give estimates that seem unreasonably small (see Fig ~~S9~~ S10 and the supplement)” and “Figure ~~S9~~ S10 and the supplement provide more detail on the creation of this time dependent uncertainty estimate for OHC”. Figure ~~S9~~ S10 shows the multi-measurement average as well as the five OHC data records as a function of time, the uncertainty for each corresponding data set, and the combined uncertainty used in this analysis. Panel (a) shows the multi-measurement OHC average with the standard deviation of the mean plotted around the average time series. The standard deviation is large at the beginning of the time series, due to the spread in the estimates of OHC between the different records (illustrated in Fig. ~~S8~~S9). The standard deviation decreases as the various OHC records converge near a similar estimate. The standard deviation is zero in 1986 because we normalized all of the time series to zero in this year to create the multi-measurement average. Because of this normalization, the standard deviation of the mean is not a realistic measure of uncertainty for the five OHC time series.

Panels (b), (c), (d), (e), and (f) display the uncertainty estimates for the five OHC data records. We use the standard deviation of the mean of five ensemble members of the European Centre for Medium-Range Weather Forecasts Ocean ReAnalysis System 4 (ORSA) (Balmaseda et al., 2013b) for the Balmaseda et al. (2013a) record. The standard deviation is plotted in panel (b) as the dotted blue line. The standard deviation is small at the beginning of the record, because the five ensemble members started at similar values of OHC in 1958 and diverged over time. The combined uncertainty of the standard deviation of the average of the five OHC records and the Cheng et al. (2017) estimate is plotted as a dashed blue line. Panel (c) shows the Levitus et al. (2012) time series for the top 700 m updated to the end of 2019. The Levitus time series utilizes

the standard error over the whole ocean for their uncertainty estimate and is plotted as the dotted light blue line. The standard error is a very small uncertainty estimate compared to the other OHC data records, which is unreasonable considering the large variations in OHC between the different records. We use the standard deviation of eight reanalysis experiments to represent the uncertainty associated with the Carton et al. (2018) OHC record and is plotted as a dotted orange line in panel (e). The standard deviation of the eight reanalysis experiments is rather small, which also is unrealistic. Panel (f) displays the Cheng et al. (2017) OHC record updated through the end of 2019 with the 1σ ~~sigma~~ uncertainty. This uncertainty does not vary much throughout the data record, making it more realistic as an estimate for such an uncertain quantity as OHC. We created the combined uncertainty estimate of the standard deviation of the average of the five OHC records and the Cheng et al. (2017) 1σ ~~sigma~~ uncertainty to have the largest uncertainty possible due to the fact that OHC varies between the different records. The EM-GC cannot achieve $\chi^2_{OCEAN} \leq 2$ for Balmaseda et al. (2013a), Levitus et al (2012), and Carton et al. (2018) using their own respective estimates of uncertainty. Creating one uncertainty estimate to be used for all of the OHC records provides consistency and allows the EM-GC to achieve good fits between the observed and modeled OHC.

Section 2.3 states "Figure ~~S10~~ S12 illustrates the REG method used to determine AAWR from the CMIP6 GCMs" ~~and "Analysis of AAWR for these 50 GCMs of LIN versus REG (see Fig. S11)…"~~. Figure ~~S10~~ S12 shows the change in ΔT~~G~~MST from 1975-2014 from the CMIP6 GCMs and the contribution of SAOD from 1975-2014. There was about a 6 month lag between the response of ΔT~~G~~MST and enhancements of SAOD following the eruption of Mount Pinatubo in June 1991 (Douglass and Knox, 2005; Thompson et al., 2009); a 6 month delay for the response of ΔT~~G~~MST to SAOD is commonly used in regression analyses of the actual temperature record (Foster and Rahmstorf, 2011; Lean and Rind, 2008). The time needed for ΔT~~G~~MST to respond to a change in the aerosol loading in the stratosphere due to a volcanic eruption in each GCM can exhibit a significant difference compared to this empirically determined response time. Therefore, a lag was determined for each GCM by calculating the value of the monthly delay that resulted in the largest regression coefficient for SAOD (versus ΔT~~G~~MST). Due to the difference in model physics between the various GCMs, the value of the delay between the volcanic forcing and surface temperature response ranged from 0 to 11 months. The effect of SAOD on ΔT~~G~~MST for the 50 GCMs is shown in Fig. ~~S10d~~S12d. Figure ~~S10b~~ S12b shows the residual in ΔT~~G~~MST after removing the influence of SOAD, and the median value of AAWR from the CMIP6 multi-model ensemble is plotted as a linear line. Figure ~~S10c~~ S12c shows the human component of global warming, $\Delta T_{ATM,HUMAN}$, from the EM-GC. A linear fit and quadratic fit are shown to illustrate that $\Delta T_{ATM,HUMAN}$ is almost nearly linear from 1975-2014, supporting the approximation of $\Delta T_{ATM,HUMAN}$ as a linear function from 1975-2014 for the REG calculation.

Section 2.3 also states "Figure S13 and the supplement compare values of AAWR found using the REG method applied to EM-GC output with values of AAWR found using Eq. (9), as support for the validity of using the REG method to determine AAWR from CMIP6 output". We applied the REG method to the EM-GC simulations to check the validity of the REG method. We regressed the modeled ΔT time series from the EM-GC for an AER RF_{2011} = −0.9 W m^{-2} simulation with SAOD and applied a 6 month lag. A linear function is used to represent the anthropogenic effect on temperature from 1975-2014. Fig. S13 shows the results of using the REG method on output of the EM-GC.

The value of AAWR from the EM-GC determined using the REG method is 0.188°C/decade, compared to 0.167°C/decade using Eq. (9) (Fig. S13c and Fig. 1). There is a 0.021°C/decade difference between the two methods. This difference arises because the REG method, when applied to the EM-GC modeled ΔT time series, includes the contribution of AMOC in the value of AAWR (Fig. S13c). Figure 1 of our paper illustrates that AMOC contributes about 0.025°C/decade to the rise in ΔT. If we include AMOC as a regressor variable to the REG method, we obtain a value of AAWR of 0.161°C/decade from the output of the EM-GC (Fig. S13g).

The close agreement of values of AAWR from the REG method once we account for AMOC and Eq. (9) supports the validity of the REG method to determine AAWR from CMIP6 output. We do not explicitly use AMOC as a regressor variable when applying the REG method to CMIP6 GCMs for two reasons. The first reason is that GCMs have been shown to underestimate key aspects of the Atlantic multidecadal oscillation and are unable to simulate the many oceanic and atmospheric footprints of AMOC (Kavvada et al., 2013). The second reason is that CMIP6 GCM historical runs do not use prescribed SSTs. If the CMIP6 GCMs are representing AMOC, it is a random signal that is averaged out when we analyze the 50 GCMs in order to calculate AAWR.

Section 2.3 also says "Analysis of AAWR for these 50 GCMs of LIN versus REG (see Fig. S14)…". Figure ~~S11~~ S14 shows the similarity between the values of AAWR determined using the LIN and REG methods. The ratio between the values of AAWR determined utilizing LIN and REG is 1.009, indicating there is only about a 0.9% difference in the values of AAWR using the two methods. Figure ~~S11~~ S14 also shows the values of AAWR that are below the maximum value of AAWR determined by the EM-GC utilizing the HadCRUT5 temperature record (blue) and the values that are above the maximum (red). ~~About~~ Less than half of the GCMs result in values of AAWR less than the maximum value from the EM-GC and ~~half~~ more than half of the GCMs result in values of AAWR greater than the maximum value from the EM-GC utilizing the HadCRUT5 GMST record.

Section 2.4 states “For the estimate of ECS from the CMIP6 multi-model ensemble, we use the method described by Gregory et al. (2004) (See the supplement and Fig. S15 for more information)”. To use the Gregory method, near surface air temperature output from the Abrupt 4×CO_2 and piControl simulations, as well as net downward radiative flux output from the Abrupt 4×CO_2 simulation is used to calculate ECS. The near surface air temperature and net downward radiative flux was converted from monthly gridded output to annual global averages. We calculate the temperature change for the Abrupt 4×CO_2 simulation by subtracting the piControl near surface air temperature (Chen et al., 2019) (Fig. S15). This computed temperature anomaly is then regressed against the net downward radiative flux, with the x-intercept yielding the equilibrium response of ΔT to a quadrupling of CO_2. This equilibrium response is then divided by two (Jones et al., 2019) to arrive at the equilibrium climate sensitivity (Fig. S15).

Section 2.5 states “See Fig. ~~S14~~ S16 for unweighted ECS values and Section 3.2 states “See Fig ~~S14~~ S16 for results without aerosol weighting”. Figure ~~S14~~ S16 displays the values of ECS using the EM-GC and the CMIP6 multi-model ensemble. The EM-GC box contains the 25th, 50th, and 75th percentiles, the whiskers denote the 5th and 95th percentiles, and the stars represent the minimum and maximum values of ECS. The box labeled CMIP6 is unchanged from Fig. ~~8~~7. The values of ECS are not treated with the aerosol weighting described in Sect. 2.5. This figure shows that most of the estimates of ECS found using the EM-GC are concentrated towards small values of ECS, due to the fact that the majority of the EM-GC model runs with good fits to the climate record (χ^2_{ATM}, χ^2_{RECENT}, and χ^2_{OCEAN}) have weak aerosol cooling and low values of λ_Σ (Fig. 5b). We use the aerosol weighting method to assign the same weights for the IPCC 2013 “likely” range limits of AER RF_{2011} of −0.4 and −1.5 W m^{-2} at the one sigma values of a Gaussian, and the −0.1 and −1.9 W m^{-2} are at the two sigma values of a Gaussian. Using the aerosol weighting method adjusts our estimates of ECS so that the calculated percentiles occur at higher values.

~~Section 3.2 states “We tested our approach of calculating ECS utilizing the EM-GC to CMIP6 GCMs by altering the EM-GC framework to include CMIP6 output (see the supplement for details)”. To use the EM-GC framework with the CMIP6 output, we calculated the CMIP6 multi-model mean change in GMST from 1850-2100 using the SSP2-4.5 scenario. We used the standard deviation of the CMIP6 multi-model mean to represent the uncertainty in the rise in GMST for our reduced chi-squared calculations. We trained the EM-GC from 1850-2100, included the CMIP6 prescribed values of SAOD and TSI, and did not include any natural variability, since effects on GMST due to factors such as ENSO should be randomly distributed within the various CMIP6 GCM runs that constitute the CMIP6 multi-model mean. We used the average of the five (Fig. S13a) and the Cheng OHC (Fig. S13b) records to calculate the amount of heat exported to the world’s oceans. Our results in Fig. S13a,b show ΔT_{2100} for the values of AER RF_{2011} and λ_Σ that the EM-GC~~

~~finds good fits to the CMIP6 multi-model GMST output for SSP2-4.5. Figure S13c shows the 5th, 25th, 50th, 75th, and 95th percentile values of ECS for the Gregory method and the altered EM-GC framework with the Cheng OHC record and the average of the five OHC records. The comparison of ECS found using quite different approaches, illustrated in Figure S13, provides strong support for the veracity of ECS inferred from GCMs and from the climate record throughout our analysis.~~

Section 3.2 in the Fig. 8 caption says, "See supplement for the confidence intervals plotted for each study". All of the studies except Dessler et al. (2018), Rugenstein et al. (2020), IPCC 2013, and Zelinka et al. (2020) have the 5 to 95% confidence intervals shown. The 66% confidence intervals are shown for IPCC 2013, and the minimum and maximum are shown for Dessler et al. (2020), Rugenstein et al. (2020) and Zelinka et al. (2020).

Section 3.3.4 states "see Fig. S21 and the supplement" and "see the supplement for more information". Figure S21 shows the rise in ΔT from pre-industrial for SSP5-8.5 versus the cumulative emissions of CO_2, in Gt C, since 1870. The colored lines denote the probability of reaching at least that temperature by the end of century. The large spread in projections of future ΔT is driven by the uncertainty in AER RF. The computed probabilities are based on the aerosol weighting method, so the uncertainty in AER RF is considered when determining the likelihood of achieving the Paris Agreement target of 1.5°C and upper limit of 2.0°C for the cumulative carbon emissions.

We use the uncertainty suggested by coupled atmospheric / carbon cycle models in how atmospheric CO_2 will respond to the prescribed carbon emissions. Examination of Fig. 2 and Table 3 from Friedlingstein et al. (2014) and Fig. 9b from Murphy et al. (2014) led to our determination that the uncertainty in estimates of atmospheric CO_2 from emissions driven runs of CMIP5 coupled atmospheric / carbon cycle models is about 10% (1σ). We include this 10% uncertainty in our determination of the carbon budgets for each probability of achieving the Paris Agreement target and upper limit shown in Table 2.

Section 3.3.6 states "see Fig. S23 and the supplement for results without the time delay". Figure S23 shows the effect of time variant λ^{-1} with an instantaneous response between λ^{-1} and a change in radiative forcing. The instantaneous response causes the modeled ΔT to deviate more from the observed temperature than the results using the 20 year delay in the response (Fig. S23g, h versus Fig. 14g, h). The deviation between the modeled and observed ΔT does not allow for a large change in λ^{-1} over time to still achieve the χ^2_{ATM} and χ^2_{RECENT} constraints. The deviation between modeled and observed ΔT in Fig. 23d resembles the behavior of some CMIP6 GCMs (see Fig. 9 and Tokarska et al. (2020)).

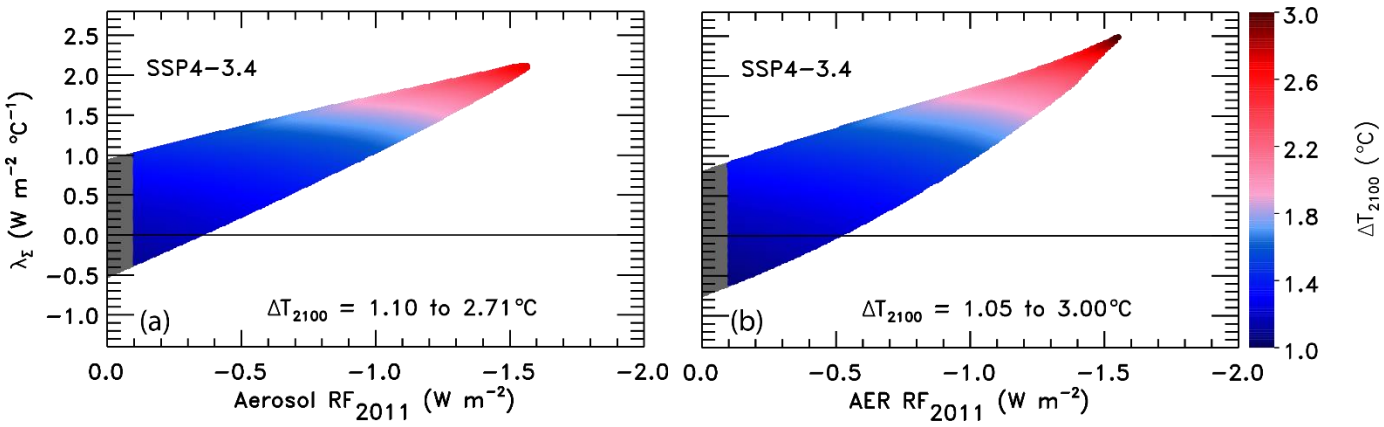

Figure S1. GMST anomaly in 2100 relative to pre-industrial (ΔT_{2100}) as a function of climate feedback parameter and AER RF_{2011} for two versions of the EM-GC trained with the HadCRUT4 ΔT record. (a) The change in ΔT_{2100} for SSP4-3.4 using the original formulation of Eq. (2) where Q_{OCEAN} is subtracted outside of the feedback multiplicative term. (b) The change in ΔT_{2100} for SSP4-3.4 using the updated formulation of Eq. (2) where Q_{OCEAN} is subtracted within the feedback multiplicative term similar to Bony et al. (2006) and Schwartz (2012). The EM-GC is able to fit higher values of λ_Σ at strong aerosol cooling (around −1.5 W m^{-2}) for the new Eq. (2) compared to the original formulation in Canty et al. (2013) and Hope et al. (2017). The maximum value of future warming has increased due to the higher λ_Σ values.

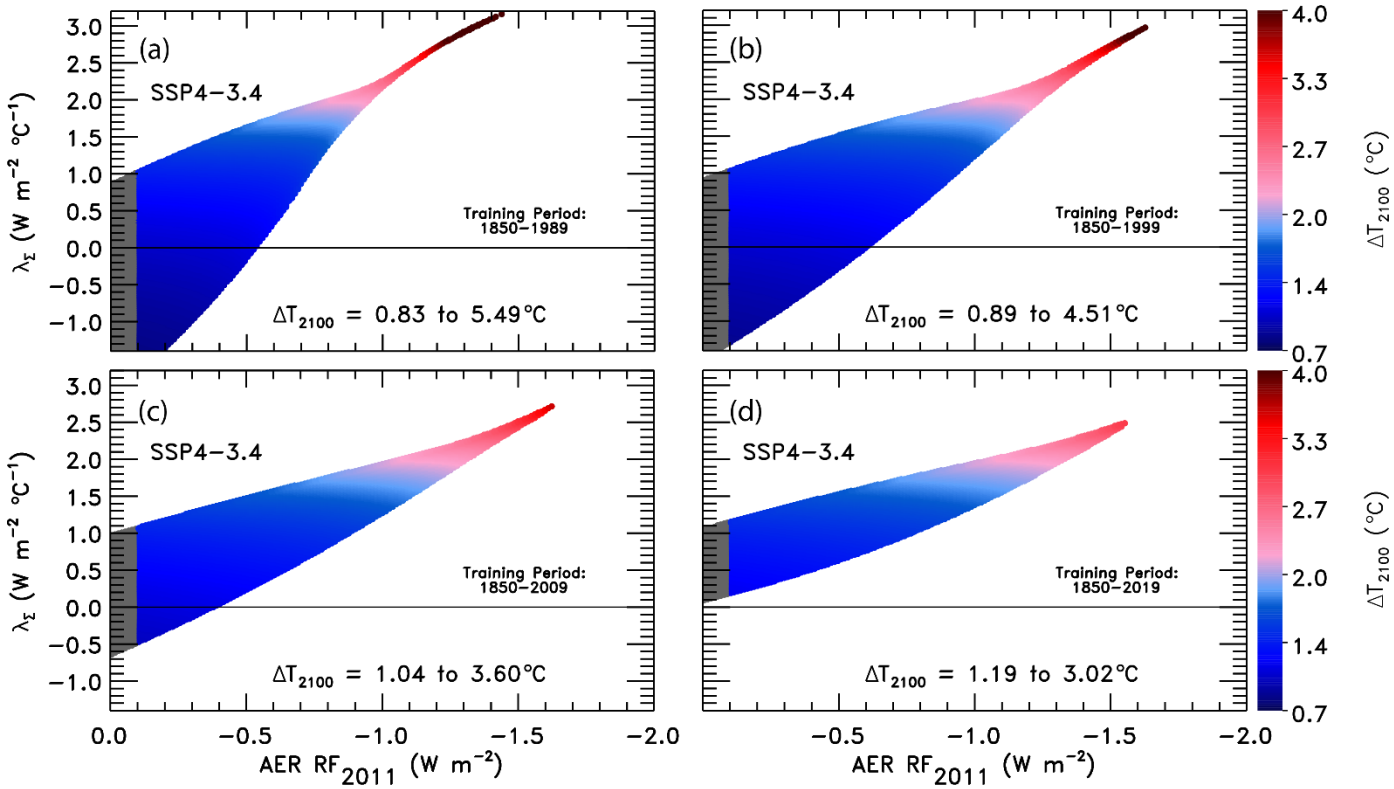

Figure S2. ΔT_{2100} as a function of climate feedback parameter and tropospheric aerosol radiative forcing in 2011 using the EM-GC trained with the HadCRUT5 ΔT record for SSP4-3.4. (a) Training period of 1850-1989. The region outside of the AER RF_{2011} range provided by IPCC 2013 is shaded (grey). Colors denote the GMST change in year 2100 relative to pre-industrial. The color bar is the same across all four panels for comparison. (b) Training period of 1850-1999. (c) Training period of 1850-2009. (d) Training period of 1850-2019, which is the normal training period used in our analysis.

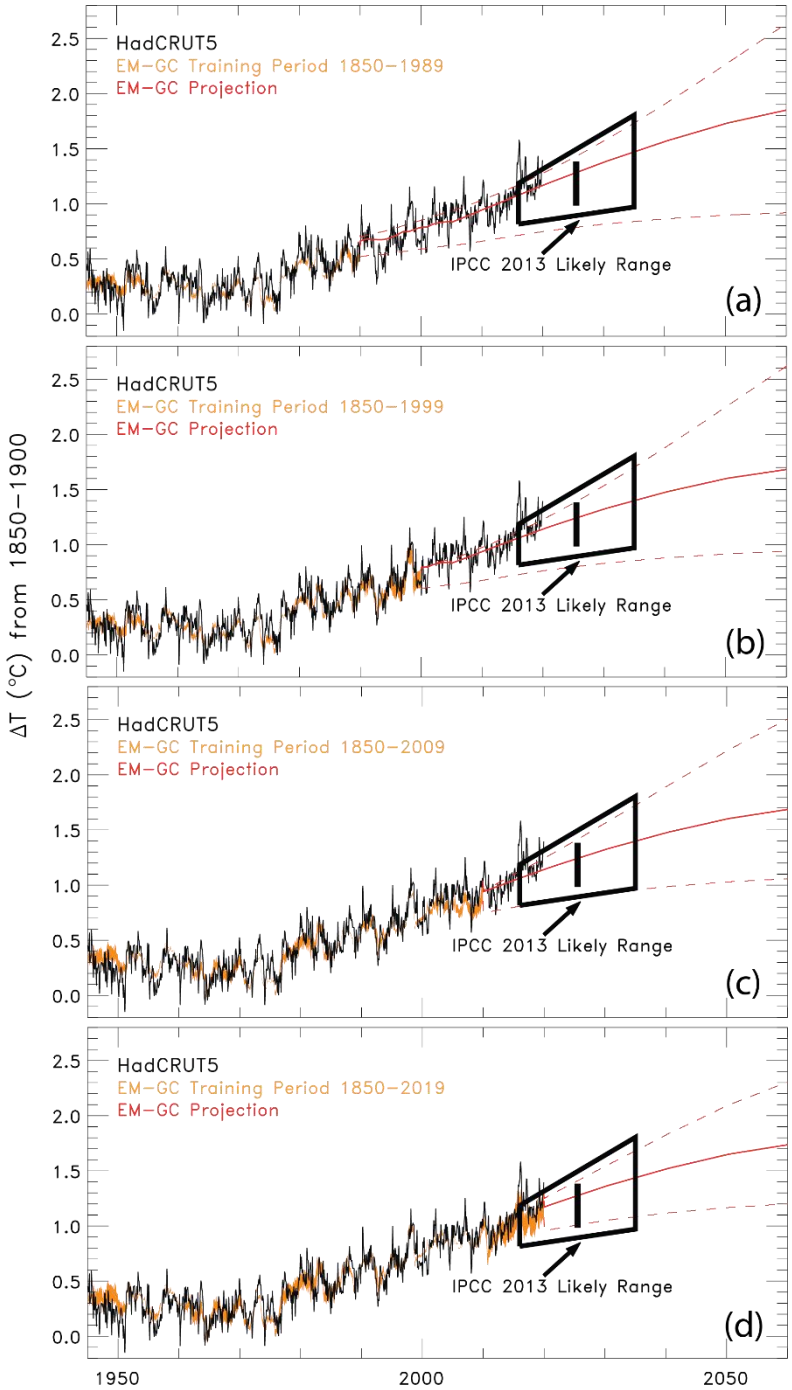

Figure S3. Observed and modeled GMST anomaly relative to 1850-1900 from 1945-2060 for four training periods. (a) Observations from HadCRUT5 (black), the EM-GC ΔT simulation for a training period of 1850-1989 (orange) of HadCRUT5, and the EM-GC projections for SSP4-3.4 out to 2060. Three EM-GC projections are shown in red: The best estimate of climate feedback for AER RF_{2011} = −0.9 W m^{-2}, the lowest value of climate feedback that satisfies the χ^2 constraints for AER RF_{2011} = −0.1 W m^{-2}, and the highest value of climate feedback that satisfies the χ^2 constraints (the value of AER RF_{2011} varies for each training period). The IPCC 2013 likely range of warming is denoted as the black trapezoid. (b) Training period of 1850-1999. (c) Training period of 1850-2009. (d) Training period of 1850-2019.

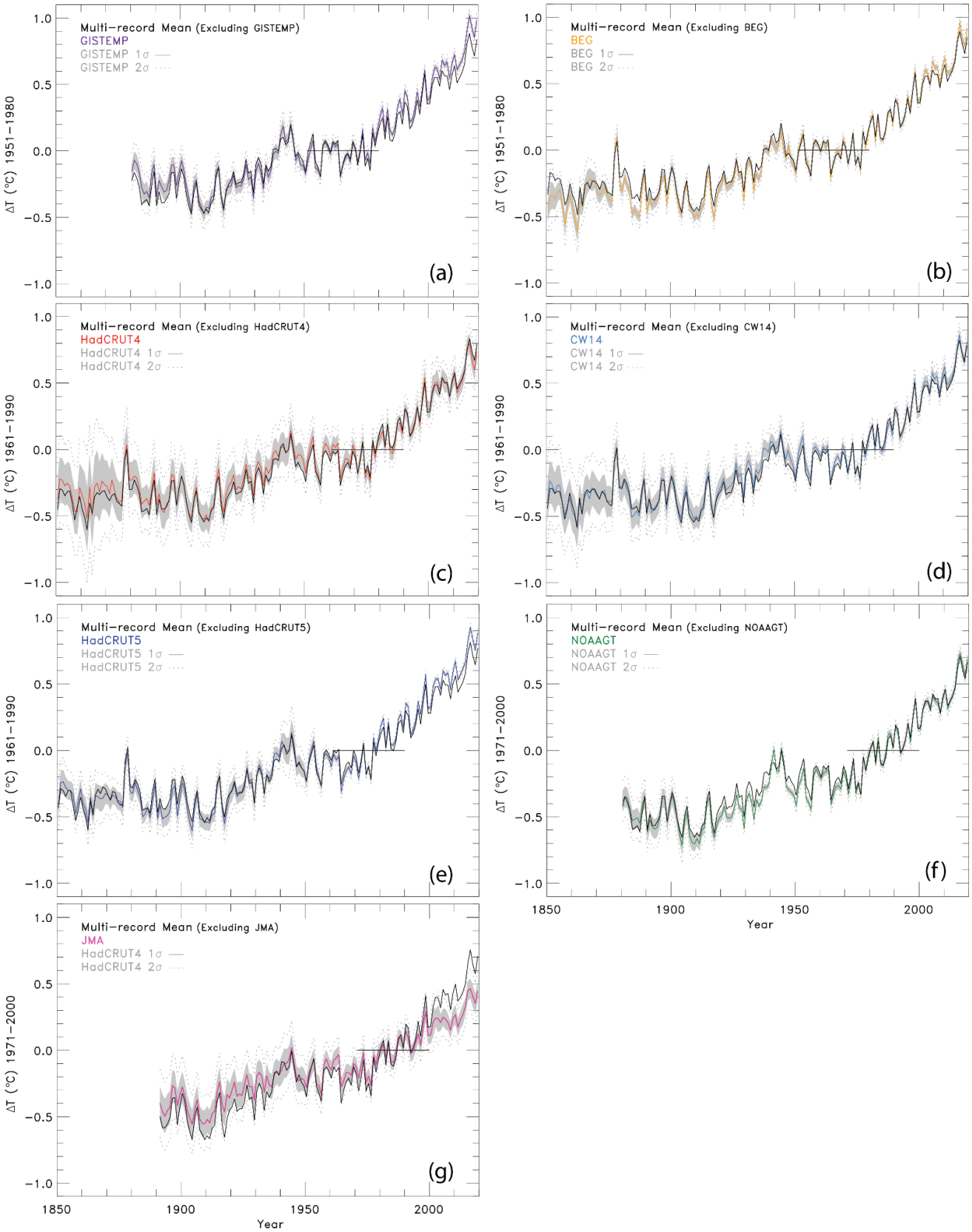

Figure S4. Annual GMST (ΔT) anomaly for seven data records relative to their individual baseline and the multi-record mean. The multi-record mean does not include the data set that is being shown. The 1σ and 2σ uncertainties for each GMST record are shown, and the horizontal line for ΔT=0 spans the baseline used for the specific panel. (a) GISTEMP. (b) BEG. (c) HadCRUT4. (d) CW14. (e) HadCRUT5. (f) NOAAGT. (g) JMA. Since the JMA data provider does not provide an uncertainty time series, the HadCRUT4 uncertainty is used.

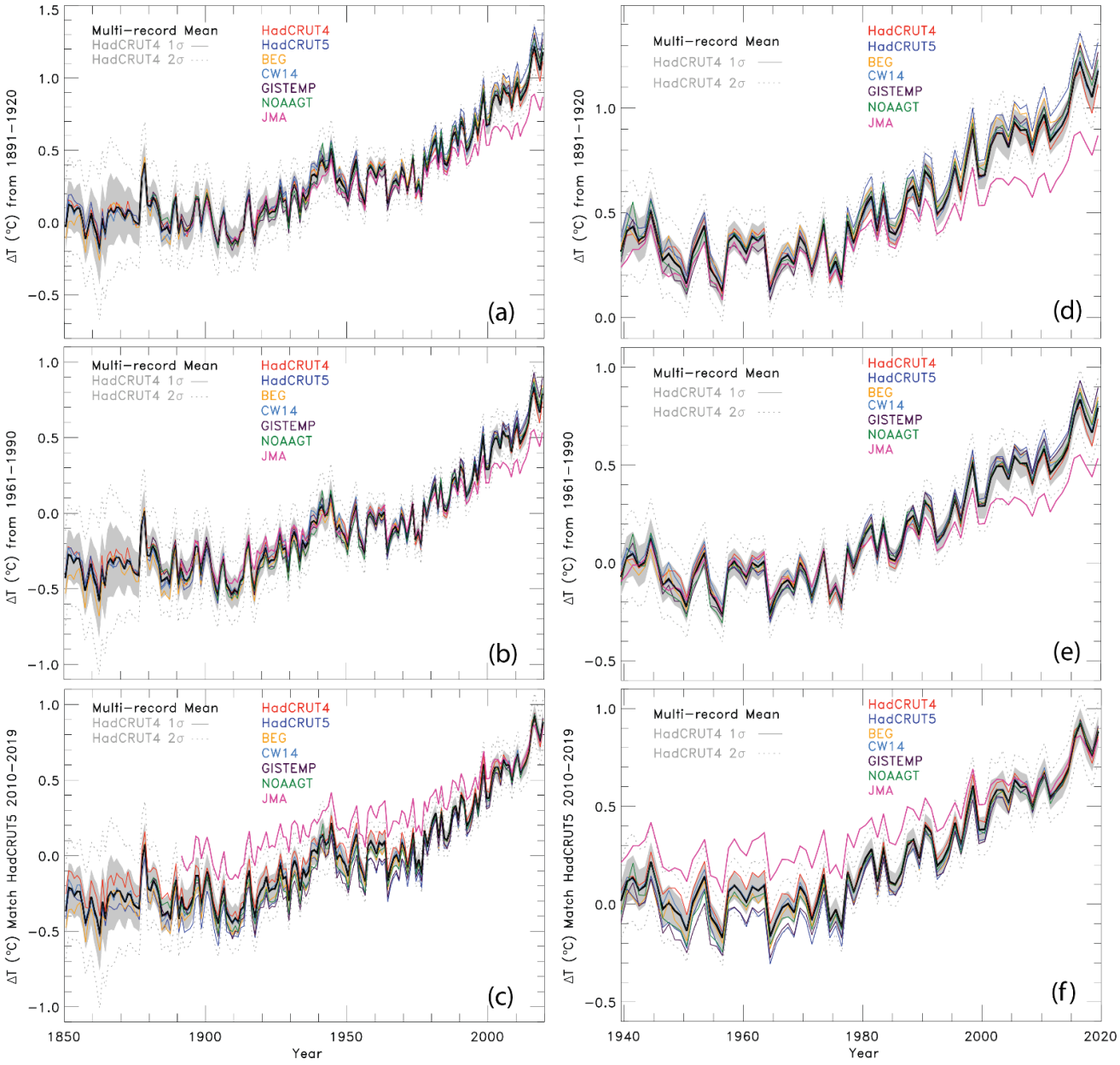

Figure S5. Annual GMST (ΔT) anomaly relative to several baseline periods -for seven data records. The 1σ (shaded grey) and 2σ (dotted grey) HadCRUT4 uncertainties are plotted about the multi-model record mean (black). (a) Baseline of 1891-1920 plotted from 1850-2019. (b) Same as (a) using a baseline of 1961-1990. (c) Same as (a) except all of the ΔT records are forced to match the average ΔT anomaly over 2010-2019 given by HadCRUT5 that is relative to 1961-1990. (d) – (f) Same as (a) – (c) except plotted from 1940-2019.

Table S1. Percentage of annual values between 1940-2019 of the GMST record within the 1 sigma or 2 sigma HadCRUT4 uncertainties about the multi-record mean for each baseline period.

Baseline: 1891-1920	1σ			2σ		
	N_{WITHIN}	N_{TOTAL}	%	N_{WITHIN}	N_{TOTAL}	%
HadCRUT4	77	80	96	80	80	100
HadCRUT5	42	80	53	80	80	100
CW14	80	80	100	80	80	100
BEG	71	80	89	80	80	100
GISTEMP	73	80	91	80	80	100
NOAAGT	76	80	95	80	80	100
JMA	29	80	36	54	80	68
AVERAGE			**80%**			**95%**
Baseline: 1961-1990						
HadCRUT4	80	80	100	80	80	100
HadCRUT5	68	80	85	80	80	100
CW14	80	80	100	80	80	100
BEG	80	80	100	80	80	100
GISTEMP	75	80	94	80	80	100
NOAAGT	80	80	100	80	80	100
JMA	27	80	34	48	80	60
AVERAGE			**88%**			**93%**
Match 2010-2019						
HadCRUT4	68	80	86	80	80	100
HadCRUT5	47	80	59	76	80	95
CW14	78	80	98	80	80	100
BEG	77	80	96	80	80	100
GISTEMP	47	80	59	79	80	99
NOAAGT	73	80	61	80	80	100
JMA	11	80	14	18	80	23
AVERAGE			**72%**			**88%**

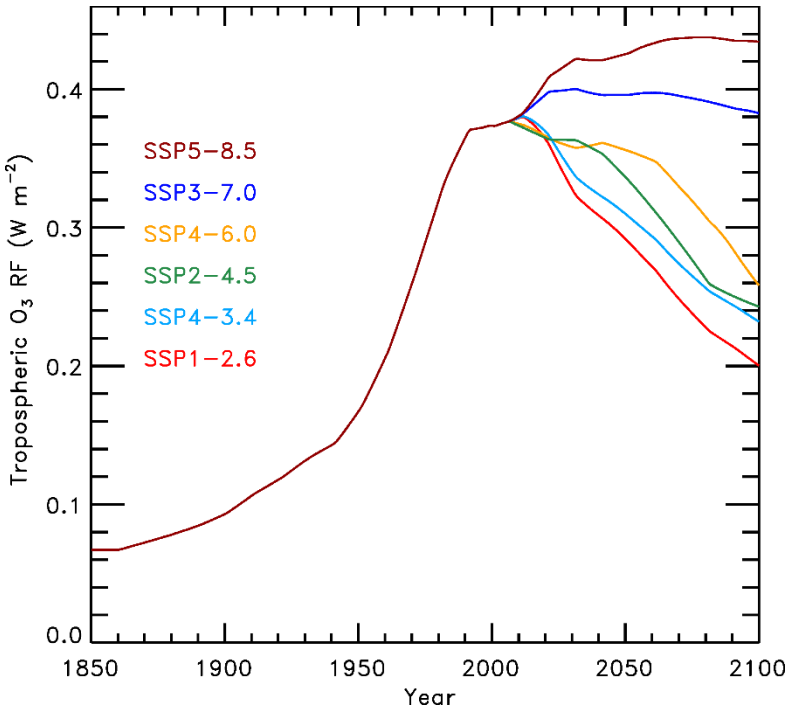

Figure ~~S5~~S6. Radiative forcing of tropospheric ozone for the various SSPs analyzed in our study. The time series labeled SSP1-2.6, SSP2-4.5, SSP4-6.0, and SSP5-8.5 are from the corresponding RCP scenarios. We created the time series from SSP4-3.4 and SSP3-7.0 using linear combinations of the SSP1-2.6 and SSP5-8.5 time series.

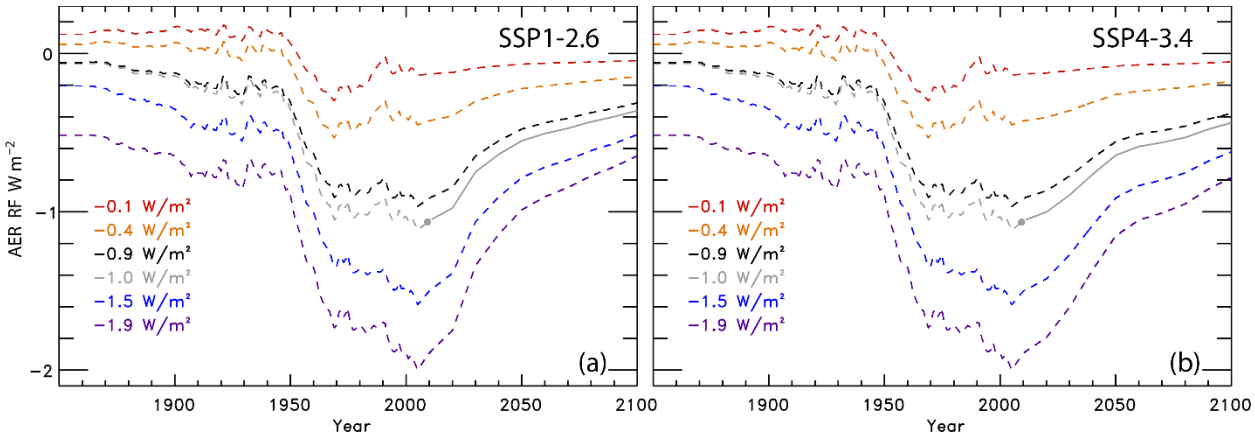

Figure S7. Radiative forcing time series due to tropospheric aerosols. (a) The RF time series due to tropospheric aerosols for SSP1-2.6. The solid grey circle denotes the value of AER RF_{2011} given by the SSP database. The solid grey lined labeled the −1.0 W m^{-2} time series is the AER RF time series given by the SSP database for SSP1-2.6. We appended a historical AER RF time series from the RCP scenarios and created five additional AER RF time series as described in Sect. 2.2.4. (b) Anthropogenic aerosol radiative forcing time series for SSP4-3.4.

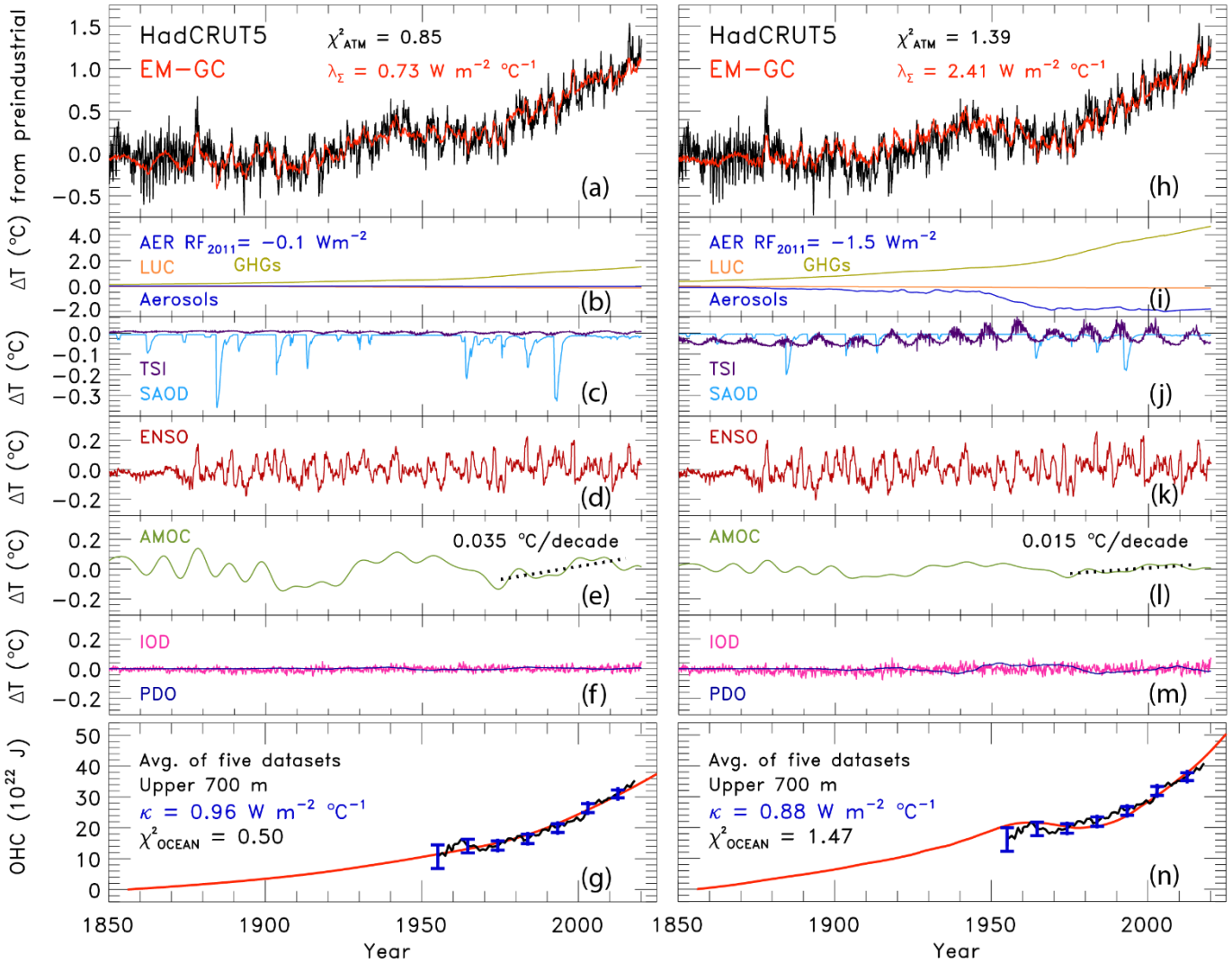

Figure S68. Measured (HadCRUT5) and modeled GMST anomaly (ΔT) relative to a pre-industrial (1850-1900) baseline for an AER RF$_{2011}$ = −0.1 W m^{-2} and −1.5 W m^{-2}. (a) Observed (black) and modeled (red) ΔT from 1850-2019. This panel also displays the values of λ_Σ and χ^2_{ATM} (see text) for this best-fit simulation. (b) Contributions from total human activity. This panel also denotes the numerical value of the attributable anthropogenic warming rate from 1975-2014 (black dashed) as well as the 2σ uncertainty in the slope. (c) Solar irradiance (light blue) and major volcanoes (purple). (d) Influences from ENSO on ΔT. (e) Contributions from AMOC to ΔT and to observed warming from 1975-2014. (f) Influences from PDO (blue) and IOD (pink) on ΔT. (g) Measured (black) and modeled (red) ocean heat content (OHC) as a function of time for the average of five data sets (see text), the value of χ^2_{OCEAN} for this run, as well as the ocean heat uptake efficiency, κ, needed to provide the best-fit to the OHC record. The error bars (blue) denote the uncertainty in OHC used in this analysis (see Sect. 2.2.8). (h)-(n) Same as (a)-(g), except for AER RF$_{2011}$ = −1.5 W m^{-2}.

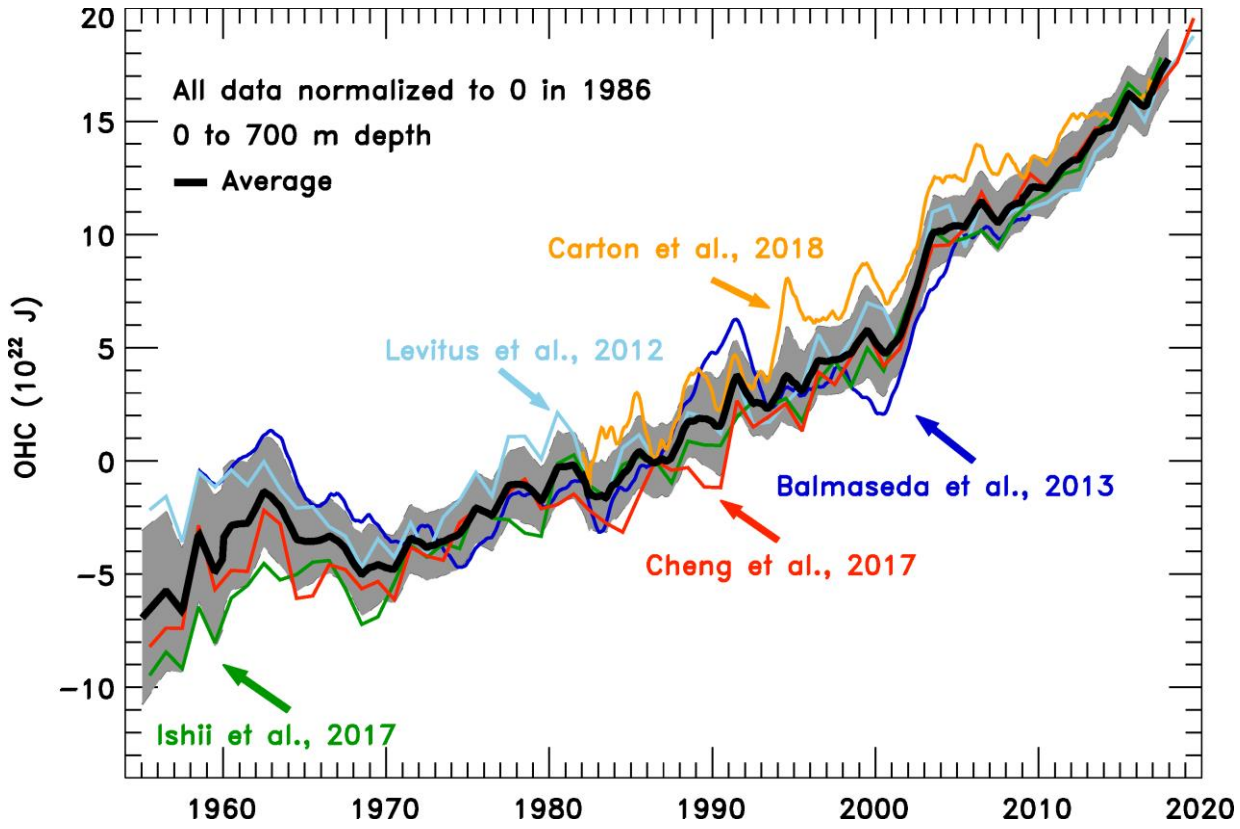

Figure ~~S8~~S9. Ocean heat content time series. The five ocean heat content data records used in this analysis, normalized to the year 1986 because this year is in the middle of the average time series. The grey shaded region is the combined uncertainty estimate used in this analysis, centered around the average of the five data sets. The average of the ocean heat content records (1955 – 2017) is computed when there are three or more data sets available for a given year.

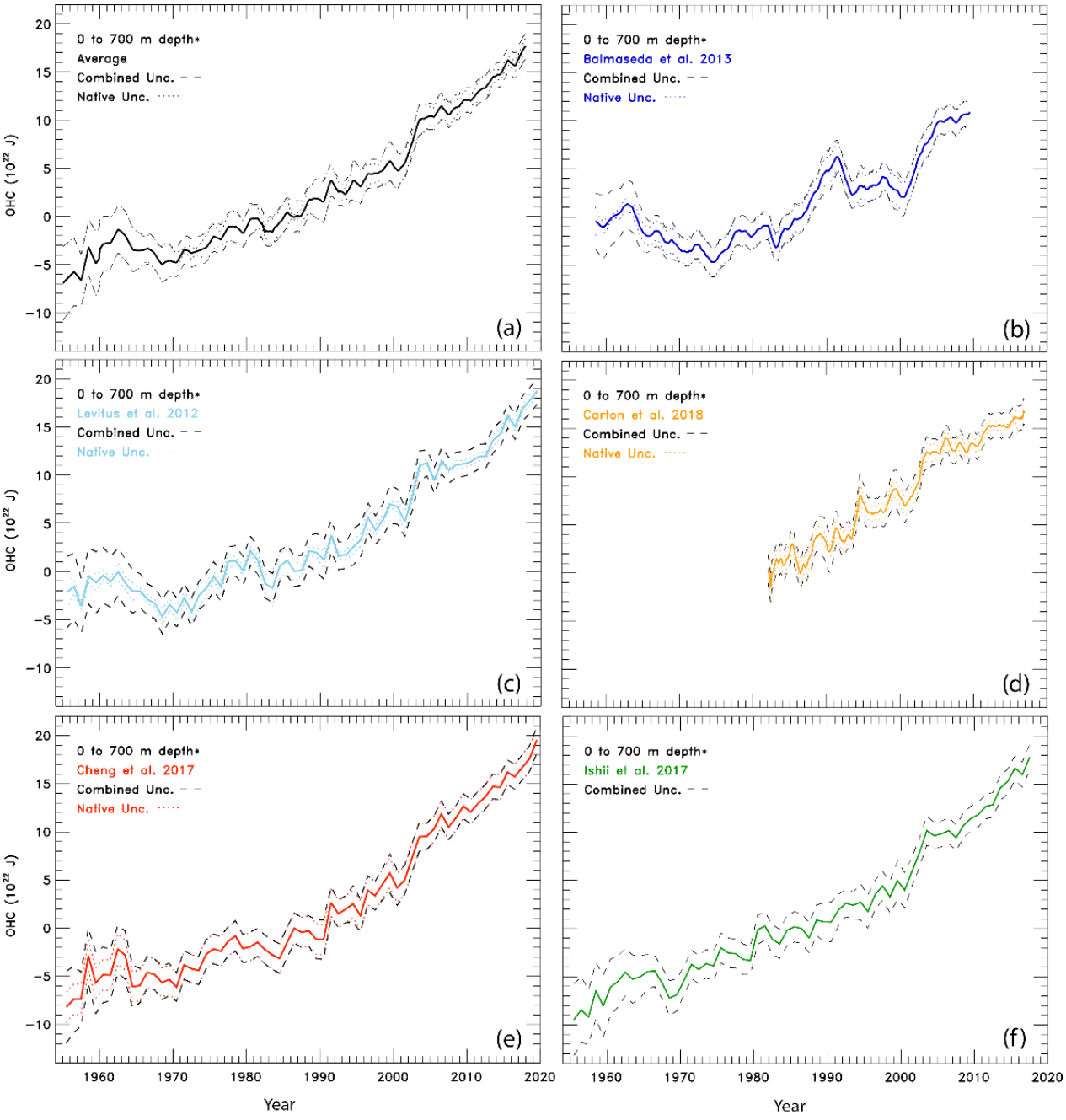

Figure ~~S9~~S10. The ocean heat content records and uncertainty estimates analyzed in this study. (a) The average OHC record along with the standard deviation of the mean represented by the dotted black line, and the combined uncertainty of the 1σ ~~sigma~~ standard deviation of the average of the five OHC records and the Cheng et al. (2017) estimates shown as the dashed black line. (b) Balmaseda OHC record with the standard deviation of the five ORSA ensemble members as the dotted line, and the combined uncertainty as the dashed line. (c) Levitus OHC record with the standard error as the native uncertainty, and the combined uncertainty. (d) Carton OHC record with the standard deviation of the mean of multiple ensemble members, and the combined uncertainty. (e) Cheng OHC record with the 1σ native uncertainty and the combined uncertainty. (f) Ishii OHC record with the combined uncertainty as the dashed line.

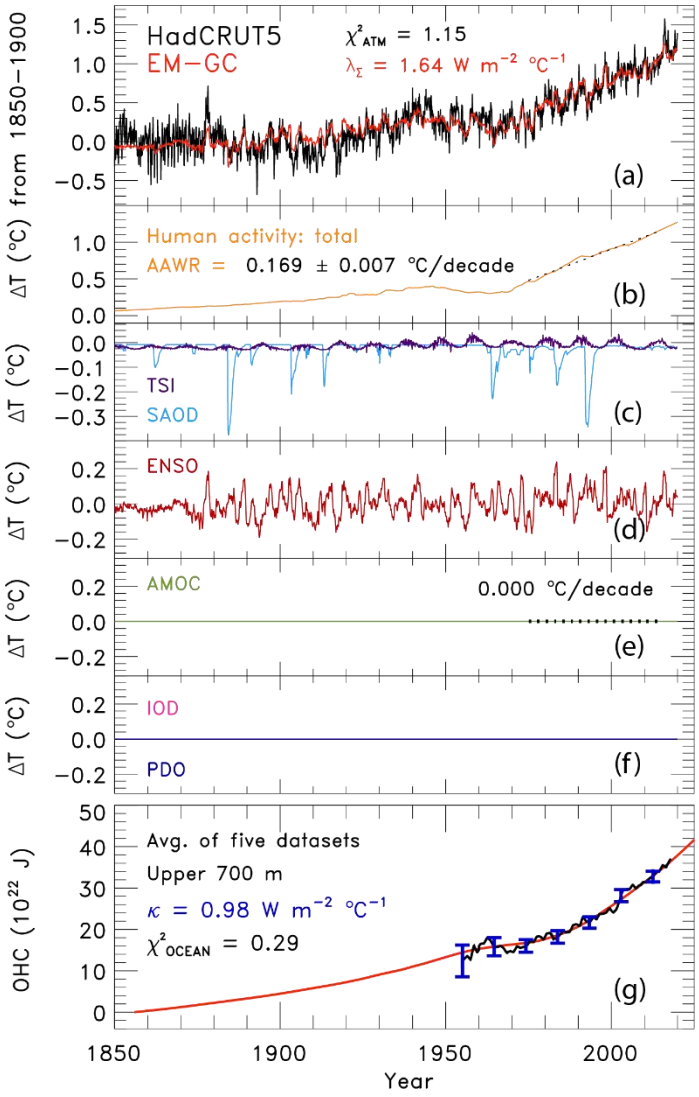

Figure S11. Measured (HadCRUT5) and modeled GMST anomaly (ΔT) relative to a pre-industrial (1850-1900) baseline without AMOC, PDO, and IOD. (a) Observed (black) and modeled (red) ΔT from 1850-2019. This panel also displays the values of λ_Σ and χ^2_{ATM} (see text) for this best-fit simulation. (b) Contributions from total human activity. This panel also denotes the numerical value of the attributable anthropogenic warming rate from 1975-2014 (black dashed) as well as the 2σ uncertainty in the slope. The estimates of AAWR show similar results if AMOC is or is not included (see Fig. 1b). (c) Solar irradiance (light blue) and major volcanoes (purple). (d) Influences from ENSO on ΔT. (e-f) Contributions from AMOC, PDO, and IOD to ΔT are set to zero (g) Measured (black) and modeled (red) ocean heat content (OHC) as a function of time for the average of five data sets (see text), the value of χ^2_{OCEAN} for this run, as well as the ocean heat uptake efficiency, κ, needed to provide the best-fit to the OHC record. The error bars (blue) denote the uncertainty in OHC used in this analysis (see Sect. 2.2.8).

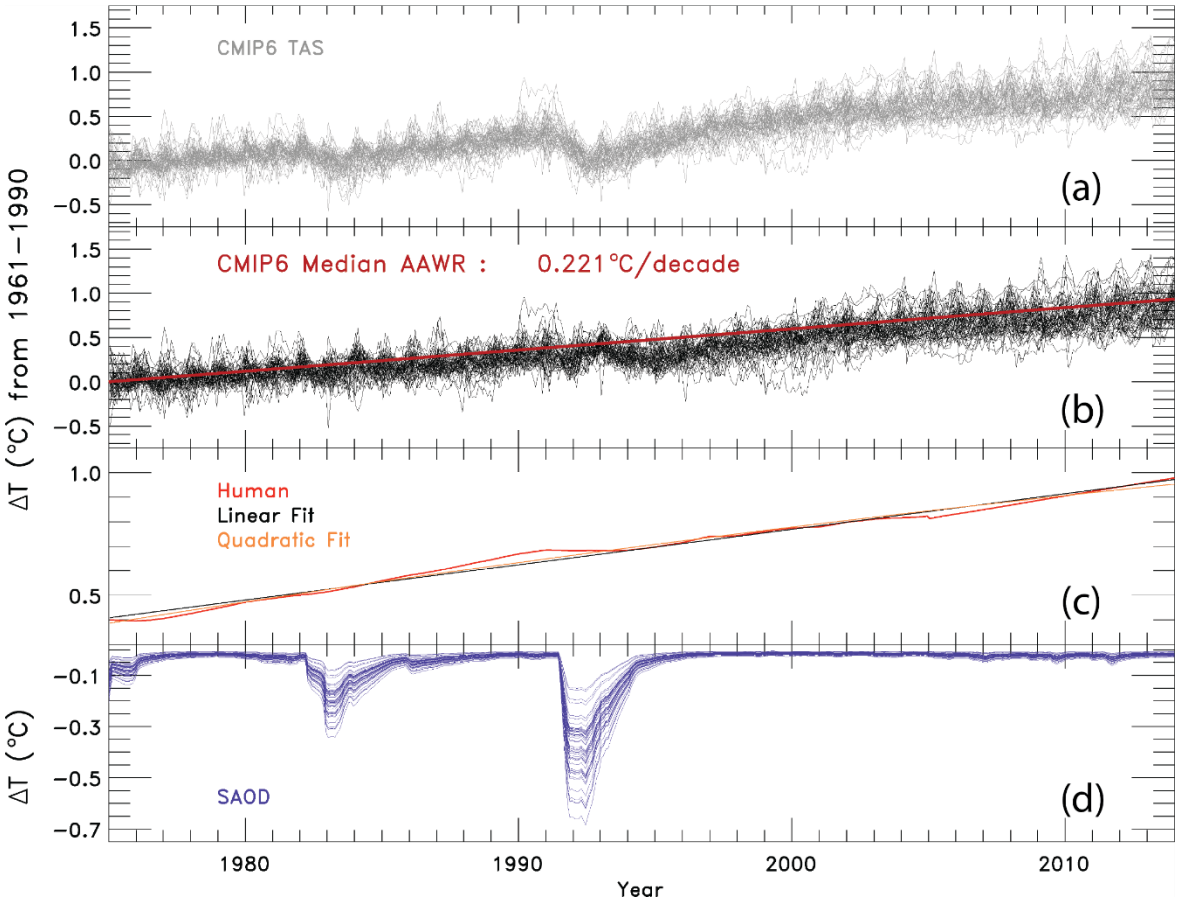

Figure ~~S10~~S12. The change in GMST (ΔT) relative to 1961-1990 from the CMIP6 GCMs and the contribution from SAOD from 1975-2014. (a) ΔT~~The change in GMST~~ from the 50 CMIP6 GCMs. (b) The residual in the change of GMST from the 50 CMIP6 GCMs after subtracting the contribution of SAOD determined by the updated REG method. The median value of AAWR is written on this panel and plotted in red. (c) The human component of global warming, $\Delta T_{ATM,HUMAN}$, from the EM-GC. A linear fit (black) and quadratic fit (red) are plotted on top to show that $\Delta T_{ATM,HUMAN}$ is almost exactly linear. (d) The contribution of SAOD in the 50 CMIP6 GCMs using a lag month calculated for each model.

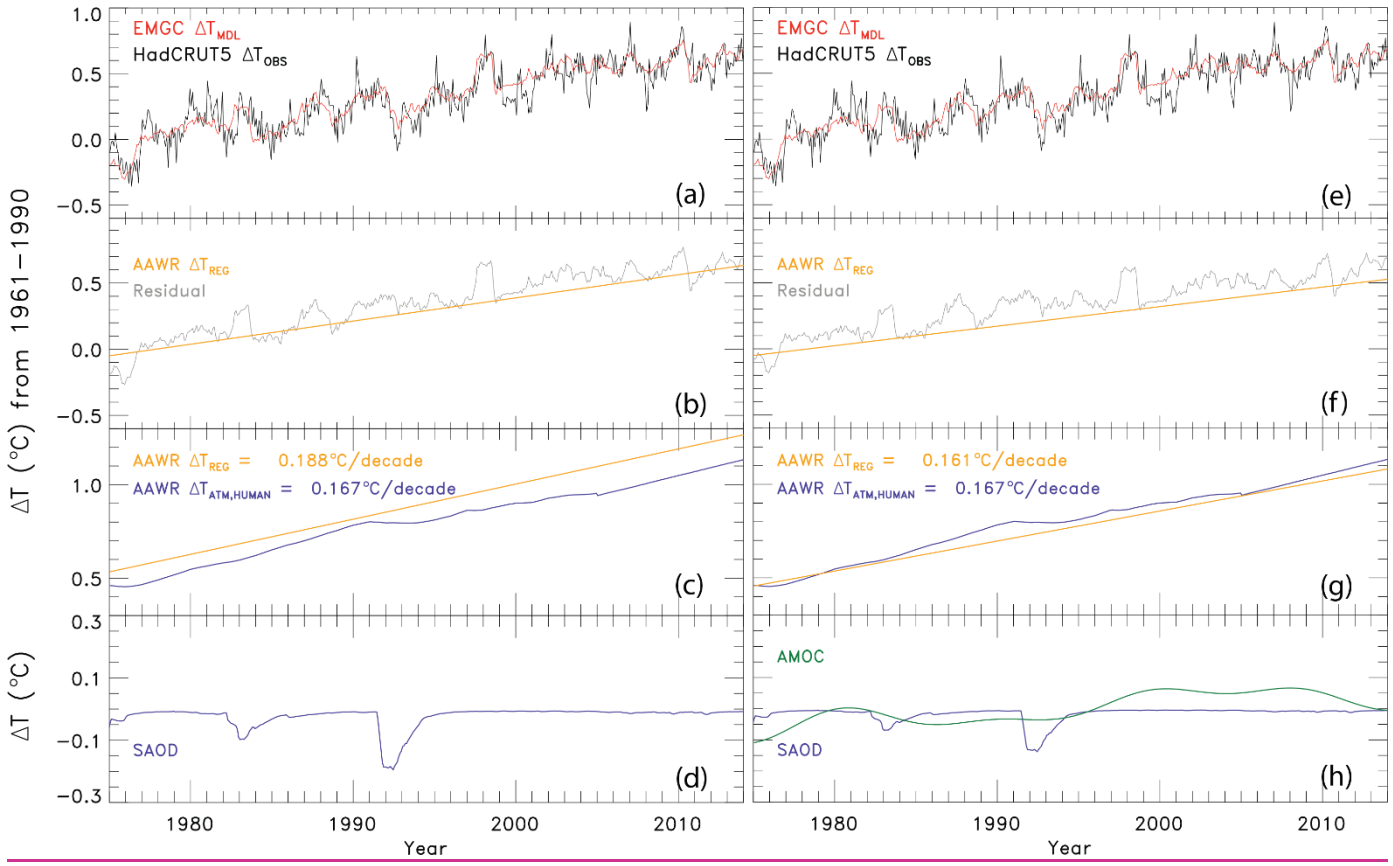

Figure S13. The change in GMST (ΔT) relative to 1961-1990 from observations and modeled output. (a) ΔT from HadCRUT5 and EM-GC simulation. (b) The residual in ΔT from the EM-GC simulation after subtracting the contribution of SAOD determined by the REG method (grey) and ΔT due to humans from the REG method (orange). (c) ΔT due to humans from the REG method (orange) and from the EM-GC (blue). The values of AAWR determined using the REG method and Eq. (9) are shown. (d) The contribution of SAOD to ΔT. (e) Same as (a). (f) Same as (b) but also subtracting the contribution of AMOC determined by the REG method. (g) Same as (c) but using AMOC as a regressor. (h) Same as (d) also showing the contribution of AMOC to ΔT found using the REG method.

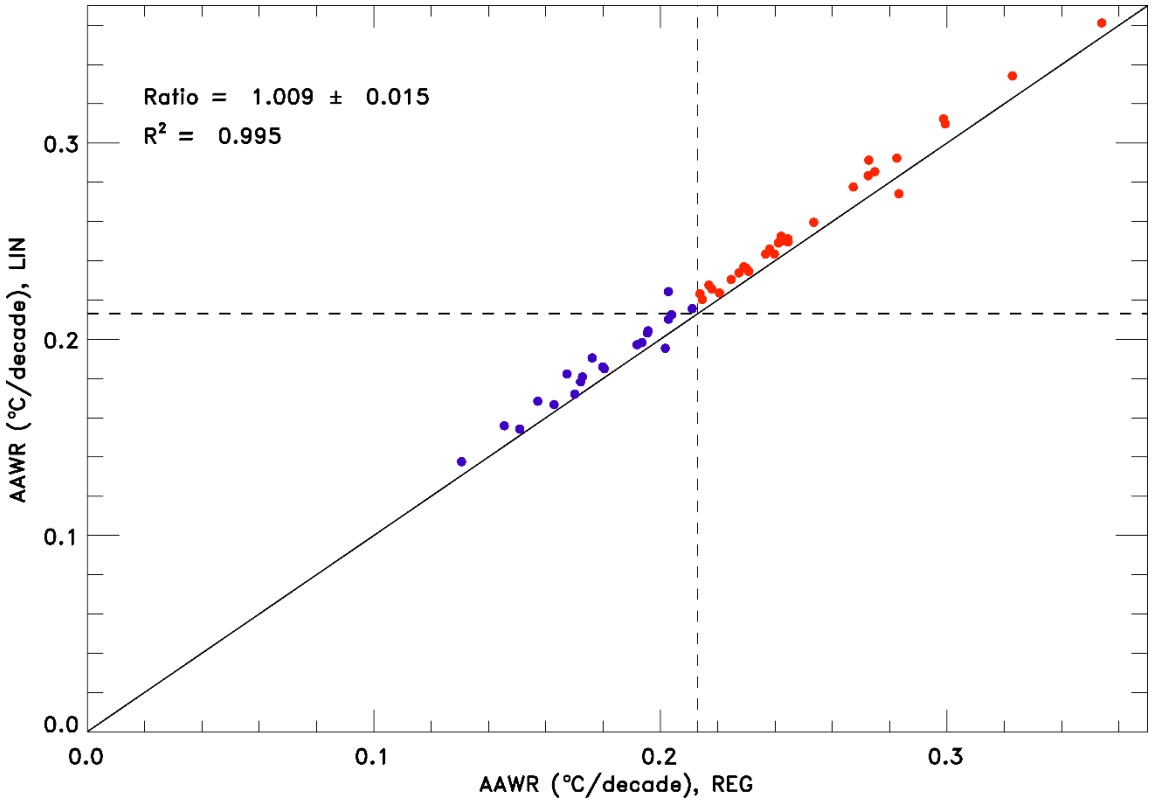

Figure ~~S11~~S14. Values of AAWR for 50 CMIP6 GCMs using the LIN and REG methods. The solid black line is the 1:1 line and the vertical and horizontal dashed lines are the maximum value of AAWR determined using the EM-GC and the HadCRUT temperature record. The CMIP6 GCMs that have values of AAWR less than the maximum value from the EM-GC are blue, and the CMIP6 GCMs that have values of AAWR greater than the maximum value from the EM-GC are red. The slope, 1σ standard deviation, and R^2 of the values of AAWR from the CMIP6 GCMs are shown.

Table S21. Values of AAWR calculated using the EM-GC as a function of start and end year. The value of AAWR from 1975-2014 used in the main manuscript is shown in red. Each model run uses the best estimate of AER RF_{2011} (−0.9 W m^{-2}), the average of five OHC records, and the HadCRUT5 GMST record. The impact on varying the start and end year on AAWR is slight, except when a short record is used (i.e. 1984-2004, a 21 year span). A two-decade time span is not long enough to calculate an accurate estimate of AAWR. The value of AAWR is more sensitive to the choice of OHC or temperature record used than the chosen time span.

		Start Year					
	AAWR (°C/decade)	**1970**	**1973**	**1975**	**1979**	**1982**	**1984**
End Year	**2004**	0.154 181 ± 0.006007	0.153 180 ± 0.007009	0.153 180 ± 0.008010	0.145 169 ± 0.009011	0.138 159 ± 0.010013	0.130 149 ± 0.010012
	2006	0.150 177 ± 0.006008	0.149 175 ± 0.007009	0.149 174 ± 0.008010	0.141 163 ± 0.009011	0.134 153 ± 0.009012	0.126 143 ± 0.009011
	2008	0.148 173 ± 0.006007	0.146 171 ± 0.006008	0.146 169 ± 0.007009	0.138 159 ± 0.008010	0.131 150 ± 0.008010	0.124 141 ± 0.007009
	2010	0.147 172 ± 0.005007	0.145 169 ± 0.006008	0.144 167 ± 0.007008	0.137 158 ± 0.007008	0.131 150 ± 0.007009	0.125 143 ± 0.006008
	2012	0.146 171 ± 0.005006	0.144 168 ± 0.005007	0.144 167 ± 0.006008	0.137 158 ± 0.006008	0.132 152 ± 0.006008	0.128 145 ± 0.006007
	2014	0.146 171 ± 0.004005	0.145 168 ± 0.005006	0.144 167 ± 0.005007	0.139 160 ± 0.005007	0.134 154 ± 0.006007	0.130 149 ± 0.005007
	2016	0.147 171 ± 0.004005	0.145 169 ± 0.004006	0.145 168 ± 0.005006	0.140 161 ± 0.005006	0.137 157 ± 0.005007	0.134 153 ± 0.005007
	2018	0.147 171 ± 0.003005	0.146 170 ± 0.004005	0.146 169 ± 0.004006	0.142 163 ± 0.005006	0.139 159 ± 0.005006	0.137 156 ± 0.005006

Table S32. Average values of AAWR calculated from the CMIP6 multi-model results using the regression method as a function of start and end year. The uncertainty corresponds to the 1σ standard deviation of AAWR found from the 50 GCMs. The value of AAWR from 1975-2014 used in the main manuscript is shown in red. The values of AAWR from the CMIP6 multi-model ensemble is more sensitive to the choice of start and end year than the EM-GC due to the small number of models. We use the same start and end year, 1975-2014, for the determination of AAWR for both the EM-GC and the CMIP6 multi-model ensemble for consistency.

		Start Year					
	AAWR (°C/decade)	**1970**	**1973**	**1975**	**1979**	**1982**	**1984**
End Year	**2004**	0.185	0.196	0.200	0.208	0.224	0.230
	2006	0.192	0.203	0.207	0.216	0.232	0.238
	2008	0.196	0.207	0.211	0.220	0.234	0.241
	2010	0.200	0.209	0.214	0.222	0.236	0.241
	2012	0.204	0.213	0.218	0.226	0.239	0.244
	2014	0.208	0.217	0.222	0.230	0.242	0.247

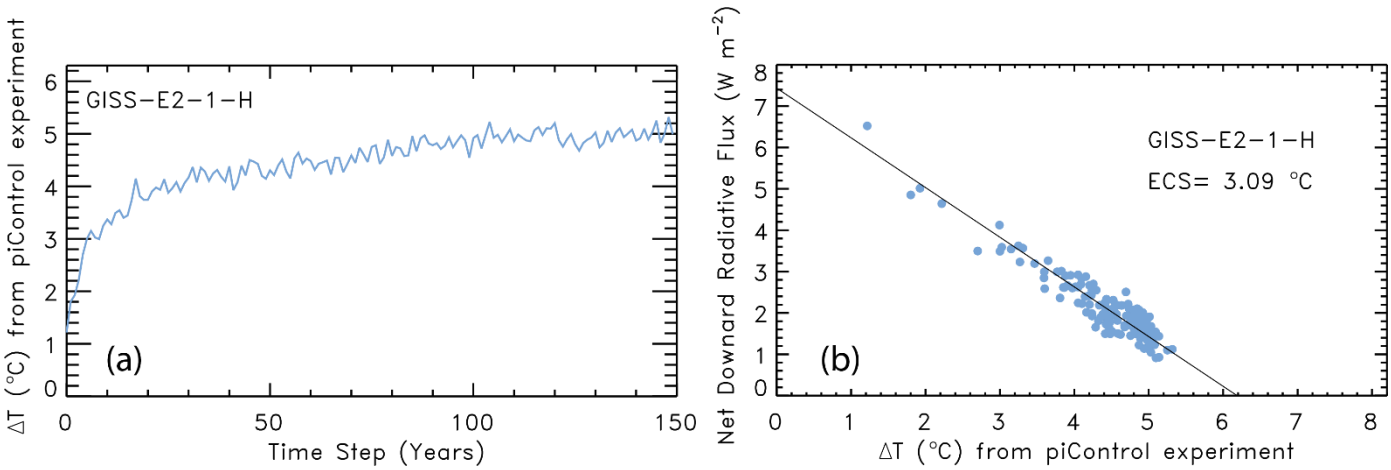

Figure ~~S12~~S15. Steps for the calculation of ECS using the Gregory et al. (2004) method, using GISS-E2-1-H (Kelley et al., 2020) as an example. (a) The change in Abrupt 4×CO_2 GMST (variable: tas) from the piControl experiment for 150 years. (b) Abrupt 4×CO_2 net downward radiative flux (variable: rtmt) versus the Abrupt 4×CO_2 GMST change from the piControl experiment for 150 years. The x-intercept of the orthogonal linear least squares fit of the GCM output shown in panel (b), divided by two yields the equilibrium climate sensitivity, which in this case is 3.09°C.

Table S43. Values of AAWR from 1975-2014 for the 50 CMIP6 multi-model Historical simulations available at time of the analysis (April 2020) for both the REG and LIN methods. The asterisk symbol (*) indicates there is only one run used to compute the value of AAWR for that GCM. No asterisk indicates the AAWR value shown in the table is the average of the values of AAWR for all runs of that model. The average ratio of LIN to REG for all 50 models is 1.009 ± 0.015, shown at the bottom of the table and in Fig. S141. The correlation coefficient (r^2) of 0.995 is also shown. We conclude our determination of AAWR from the CMIP6 multi-model ensemble is accurate to ±1%, which is much smaller than the difference between the CMIP6 multi-model ensemble values of AAWR and those found using the EM-GC framework.

Model	AAWR, REG (°C/decade)	AAWR, LIN (°C/decade)	Model	AAWR, REG (°C/decade)	AAWR, LIN (°C/decade)
ACCESS-CM2	0.211	0.216	GFDL-CM4*	0.243	0.250
ACCESS-ESM1-5	0.238	0.246	GFDL-ESM4	0.203	0.224
AWI-CM-1-1-MR	0.215	0.220	GISS-E2-1-G	0.194	0.198
BCC-CSM2-MR	0.217	0.228	GISS-E2-1-G-CC	0.204	0.213
BCC-ESM1	0.241	0.249	GISS-E2-1-H	0.237	0.244
CAMS-CSM1-0	0.131	0.138	HadGEM3-GC31-LL	0.283	0.292
CanESM5	0.354	0.361	HadGEM3-GC31-MM	0.227	0.234
CanESM5-CanOE	0.323	0.334	INM-CM4-8*	0.173	0.181
CAS-ESM2-0	0.196	0.204	INM-CM5-0	0.146	0.156
CESM2	0.240	0.243	IPSL-CM6A-LR	0.230	0.236
CESM2-FV2	0.221	0.224	KACE-1-0-G	0.254	0.260
CESM2-WACCM	0.273	0.291	MCM-UA-1-0	0.225	0.231
CESM2-WACCM-FV2	0.231	0.235	MIROC6	0.157	0.168
CIESM	0.245	0.251	MIROC-ES2L	0.163	0.167
CNRM-CM6-1	0.202	0.196	MPI-ESM1-2-HAM	0.180	0.186
CNRM-CM6-1-HR*	0.172	0.178	MPI-ESM1-2-HR	0.195	0.203
CNRM-ESM2-1	0.170	0.172	MPI-ESM1-2-LR	0.192	0.197
E3SM-1-0	0.267	0.278	MRI-ESM2-0	0.203	0.210
E3SM-1-1*	0.283	0.285	NESM3	0.242	0.253
E3SM-1-1-ECA*	0.275	0.274	NorCPM1	0.180	0.185
EC-Earth3*	0.299	0.310	NorESM2-LM	0.167	0.182
EC-Earth3-Veg*	0.214	0.223	NorESM2-MM*	0.151	0.154
FGOALS-f3-L	0.218	0.226	SAM0-UNICON*	0.245	0.250
FGOALS-g3	0.176	0.191	TaiESM1*	0.273	0.283
FIO-ESM-2-0	0.229	0.237	UKESM1-0-LL	0.299	0.312
Ratio = 1.009 ± 0.015			R^2 = 0.995		

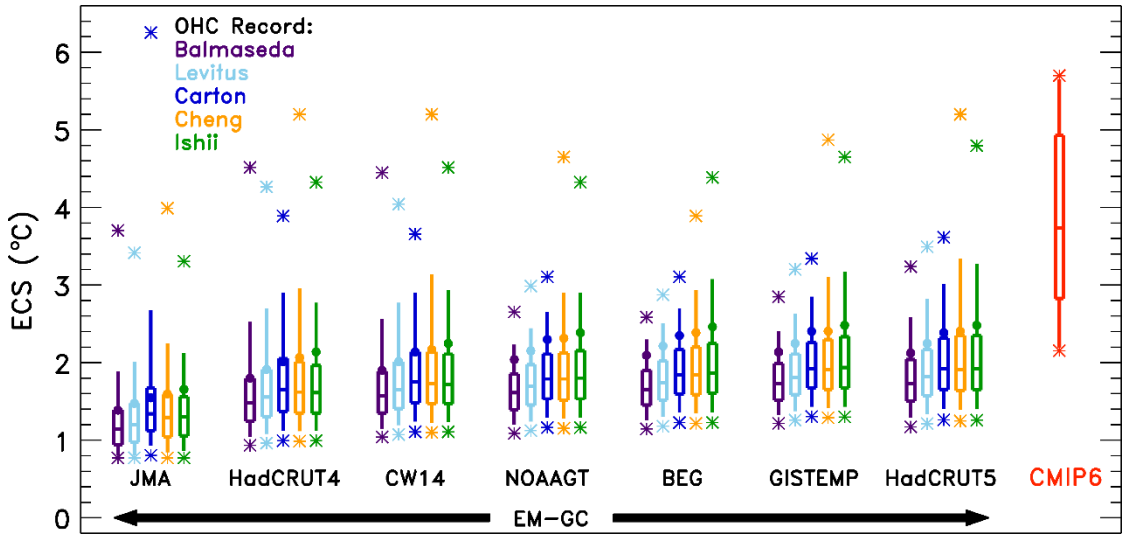

Figure S16. Values of ECS found using the EM-GC and the CMIP6 multi-model ensemble without the aerosol weighting method. Values of ECS utilizing the EM-GC are calculated using seven temperature data sets and five ocean heat content records (as indicated). The box represents the 25th, 50th, and 75th percentiles of the values of ECS and the whiskers denote the 5th and 95th percentiles for the different OHC records and each temperature record without using the aerosol weighting method (unweighted). The stars indicate the minimum and maximum values of ECS. The circles are the values of ECS associated with the best estimate of AER RF_{2011} of −0.9 W m^{-2}. The box labeled CMIP6 is the 25th, 50th, and 75th percentiles of the values of ECS from the CMIP6 multi-model ensemble, the whiskers indicate the 5th and 95th percentiles, and the stars represent the minimum and maximum values of ECS from the CMIP6 multi-model ensemble.

Table S54. Equilibrium climate sensitivity (ECS) from 28 CMIP6 GCMs. We can only calculate ECS for GCMs that provide Abrupt 4×CO_2 near surface air temperature (output variable: tas), net downward radiative flux (output variable: rtmt), and piControl near surface air temperature (output variable: tas) to the CMIP6 archive at time of the analysis (April 2020). All estimates are for one model run except for CanESM5, which is the average of two runs.

Model	ECS (K)
ACCESS-CM2	4.93
ACCESS-ESM1-5	3.63
BCC-CSM2-MR	3.16
BCC-ESM1	3.74
CanESM5	5.70
CESM2	5.32
CESM2-FV2	5.06
CESM2-WACCM	4.73
CESM2-WACCM-FV2	4.56
E3SM-1-0	5.28
EC-Earth3-Veg	4.34
GFDL-CM4	3.78
GFDL-ESM4	2.61
GISS-E2-1-G	2.71
GISS-E2-2-G	2.25
GISS-E2-1-H	3.09
HadGEM3-GC31-LL	5.65
INM-CM4-8	2.32
INM-CM5-0	2.39
IPSL-CM6A-LR	4.97
MCM-UA-1-0	3.68
MIROC6	2.84
MIROC-ES2L	2.83
NorESM2-LM	2.19
NorESM2-MM	2.15
SAM0-UNICON	3.53
TaiESM1	4.33
UKESM1-0-LL	5.40

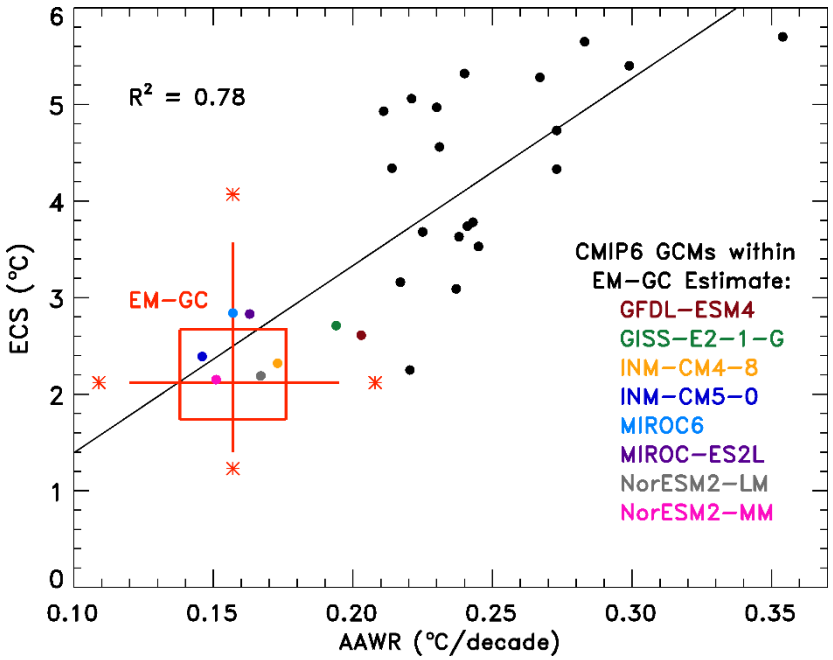

Figure S17. Values of ECS versus AAWR for the CMIP6 multi-model ensemble. The EM-GC estimates of AAWR and ECS based on training to the HadCRUT5 GMST record are plotted as a box and whisker. The box shows the average 25th, 50th, and 75th percentiles for the five OHC records shown for HadCRUT5 in Fig. 6 and Fig. 7. The whiskers represent the average 5th and 95th percentiles. The stars denote the average minimum and maximum values of AAWR or ECS. The eight CMIP6 GCMs that obtain values of AAWR and ECS that are both within the minimum and maximum estimates provided by the EM-GC are identified on the figure. Values of AAWR explain about 78% of the variance in ECS among the CMIP6 GCMs.

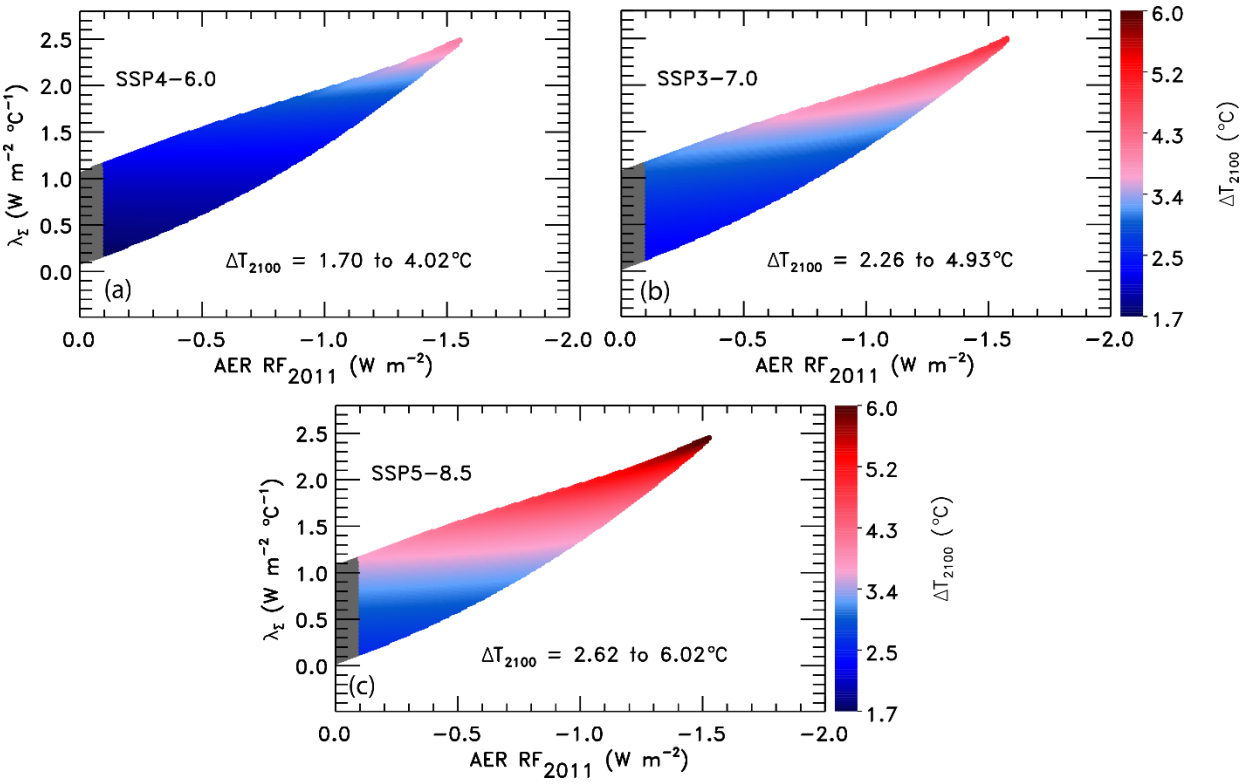

Figure ~~S15~~S18. GMST anomaly in 2100 from pre-industrial (ΔT_{2100}) as a function of climate feedback parameter and AER RF_{2011} found using the EM-GC trained with ΔT from HadCRUT5. (a) ΔT_{2100} for SSP4-6.0. The region outside of the tropospheric aerosol radiative forcing rage provided by IPCC 2013 (Myhre et al., 2013) is shaded grey. Colors denote the change in ΔT_{2100}. (b) ΔT_{2100} for SSP3-7.0. (c) ΔT_{2100} for SSP5-8.5.

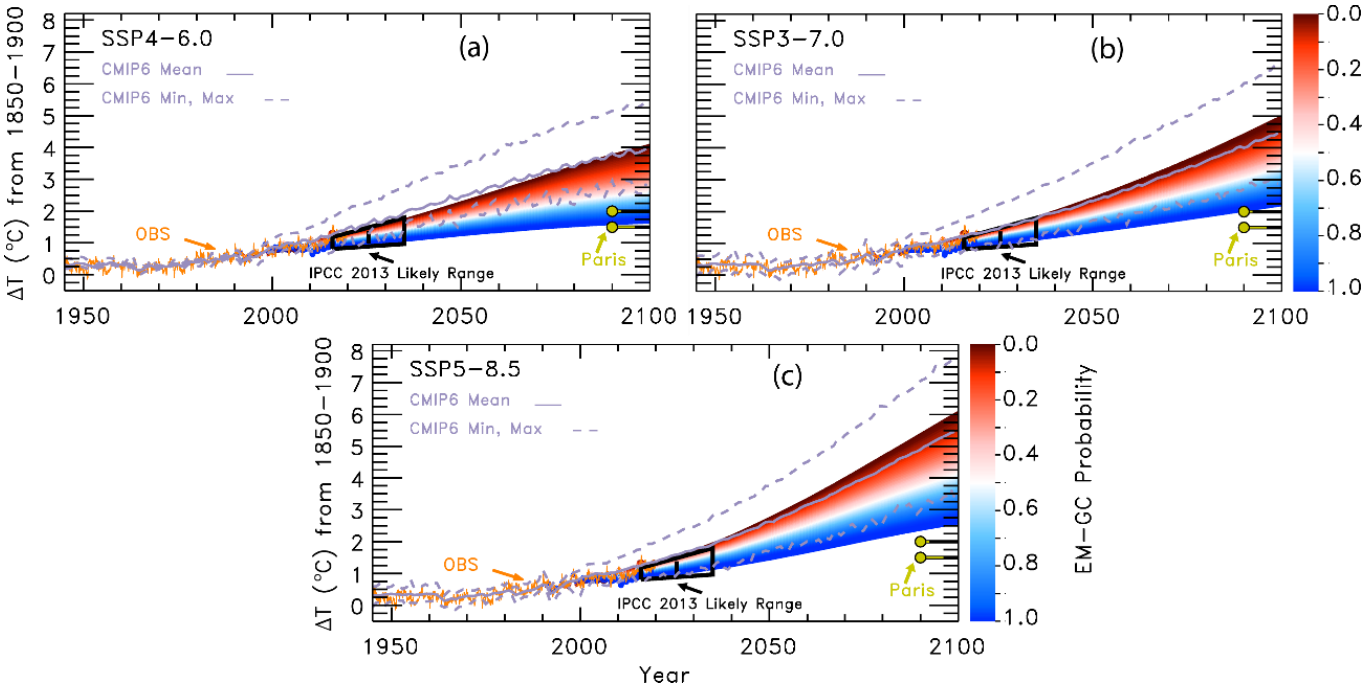

Figure ~~S16~~S19. Probabilistic forecasts of future projections of ΔT using the EM-GC trained with ΔT from HadCRUT5 for the SSP4-6.0, SSP3-7.0, and SSP5-8.5 scenarios. (a) Future projections of ΔT for SSP4-6.0. Observations (orange) are from ~~CRU~~HadCRUT5. The IPCC 2013 likely range of warming (black) is from Figure 11.25b of chapter 11 of the IPCC 2013 report. The Paris Agreement target and upper limit (yellow) are shown for comparison to projections of ΔT using the EM-GC. The CMIP6 minimum, multi-model mean, and maximum values of the rise in ΔT are shown to compare to projections from the EM-GC. Colors denote the probability of reaching at least that temperature by the end of the century and are computed using the aerosol weighting method (see Sect. 2.5). (b) Future projections of ΔT for SSP3-7.0. (c) Future projections of ΔT for SSP5-8.5.

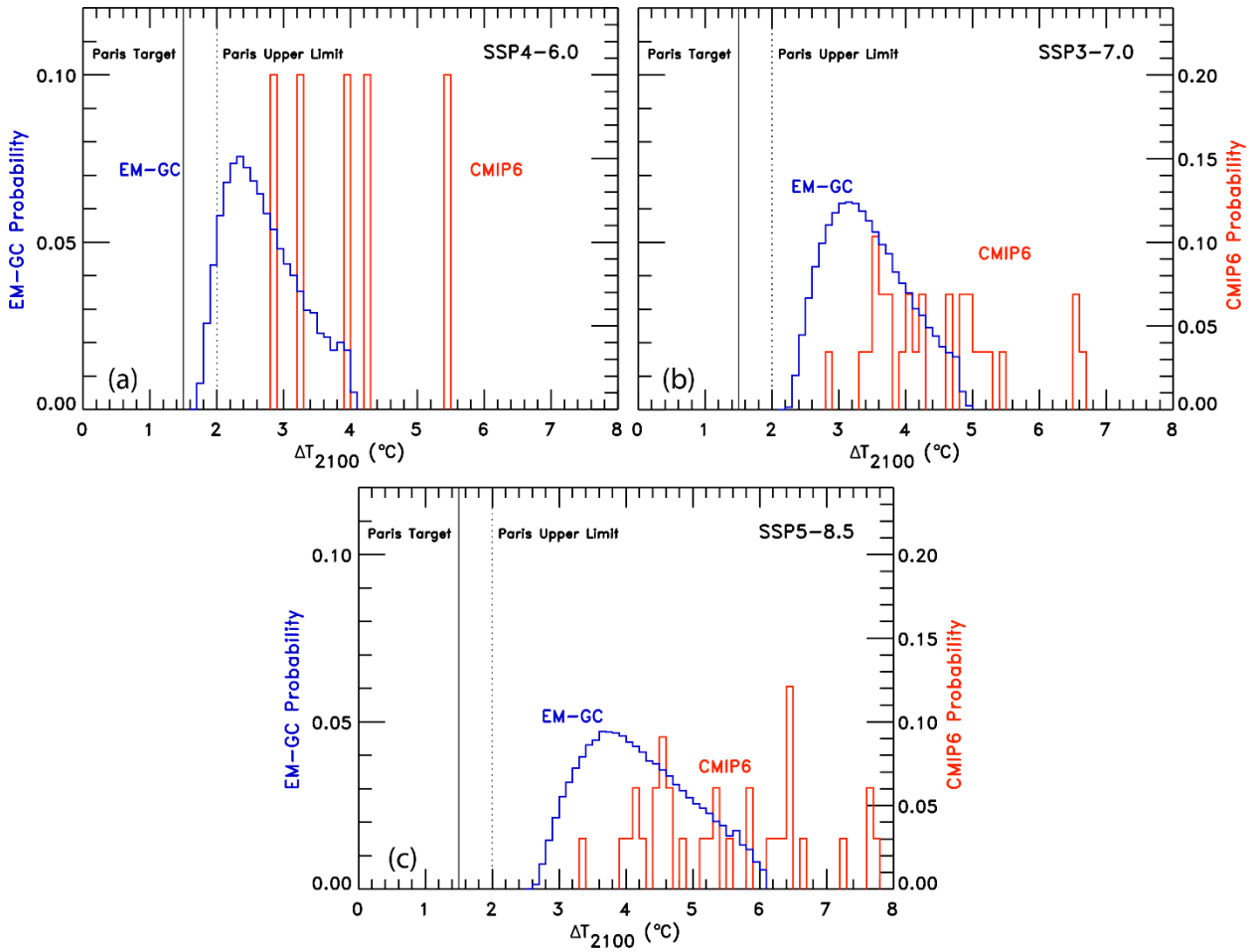

Figure ~~S17~~S20. Probability density functions (PDF) for the increase in ΔT_{2100} using the EM-GC and the CMIP6 multi-model ensemble. (a) PDF for EM-GC (blue) results trained with ΔT from HadCRUT5 and CMIP6 multi-model results (red) for SSP4-6.0. The left-hand y-axis is for EM-GC probabilities and the righthand y-axis is for GCM probabilities. (b) PDF for SSP3-7.0. (c) PDF for SSP5-8.5.

Table S6. Probabilities of achieving the Paris Agreement target and upper limit for the various SSP scenarios based on the EM-GC using the HadCRUT4 or HadCRUT5 GMST data set and the CMIP6 multi-model ensemble. The probabilities using the EM-GC are computed using the aerosol weighting method. The probabilities using the CMIP6 GCMs are computed by calculating how many of the models for that scenario are below the temperature limits compared to the total number of models.

	Probability of Staying at or Below 1.5°C			Probability of Staying at or Below 2.0°C		
	HadCRUT4	**HadCRUT5**	**CMIP6**	**HadCRUT4**	**HadCRUT5**	**CMIP6**
SSP1-1.9	84%	81%	50%	99%	98%	80%
SSP1-2.6	64%	53%	18%	90%	86%	47%
SSP4-3.4	35%	19%	0%	74%	64%	17%
SSP2-4.5	9%	0%	0%	52%	33%	3%
SSP4-6.0	0%	0%	0%	26%	8%	0%
SSP3-7.0	0%	0%	0%	1%	0%	0%
SSP5-8.5	0%	0%	0%	0%	0%	0%

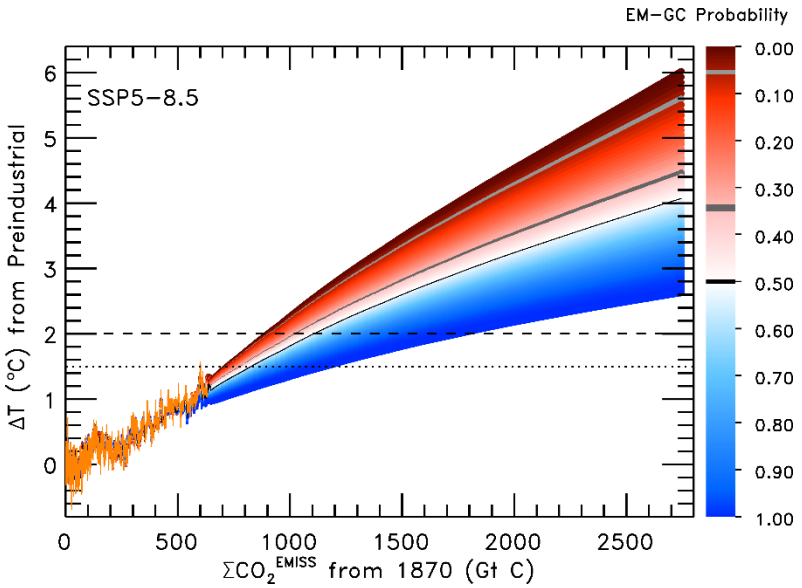

Figure S21. Transient climate response to cumulative CO_2 emissions for SSP5-8.5 using the EM-GC trained with the HadCRUT5 ΔT record. Simulations of the rise in ΔT versus cumulative CO_2 emissions in units of Gt C. The orange line is observations of ΔT from HadCRUT5 plotted against cumulative carbon emissions from the Global Carbon Budget project (Friedlingstein et al., 2019). The dotted and dashed lines denote the Paris Agreement target and upper limit, respectively. The EM-GC projections represent the probability that the future value of ΔT will rise to the indicated level, considering only acceptable fits to the climate record. The probabilities were determined using the aerosol weighting method. The light grey, dark grey, and black curves denote the 95, 66, and 50% probabilities of either the Paris target (intersection of dotted horizontal lines) or upper limit (intersection of dashed lines with curves) being achieved.

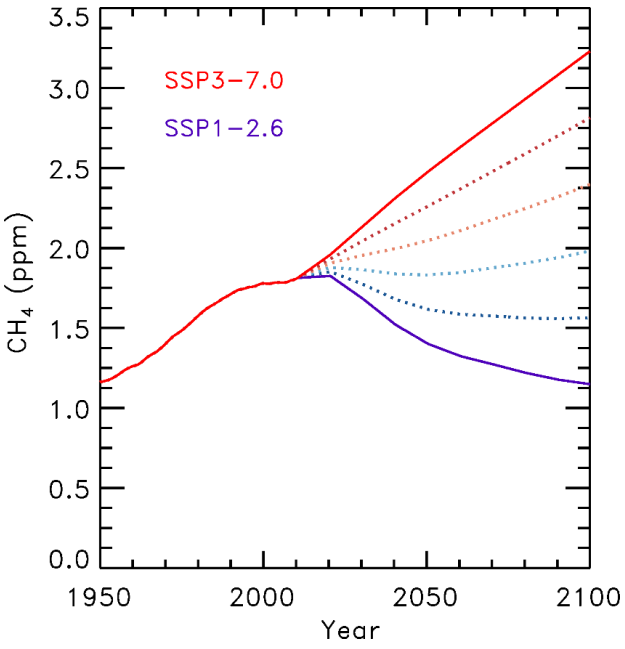

Figure ~~S18~~S22. Blended methane mixing ratios. The dotted lines are linear combinations of the time series of methane abundances using SSP1-2.6 and SSP3-7.0 to span the range of values of future methane. The solid lines are the SSP1-2.6 and SSP3-7.0 methane mixing ratio time series.

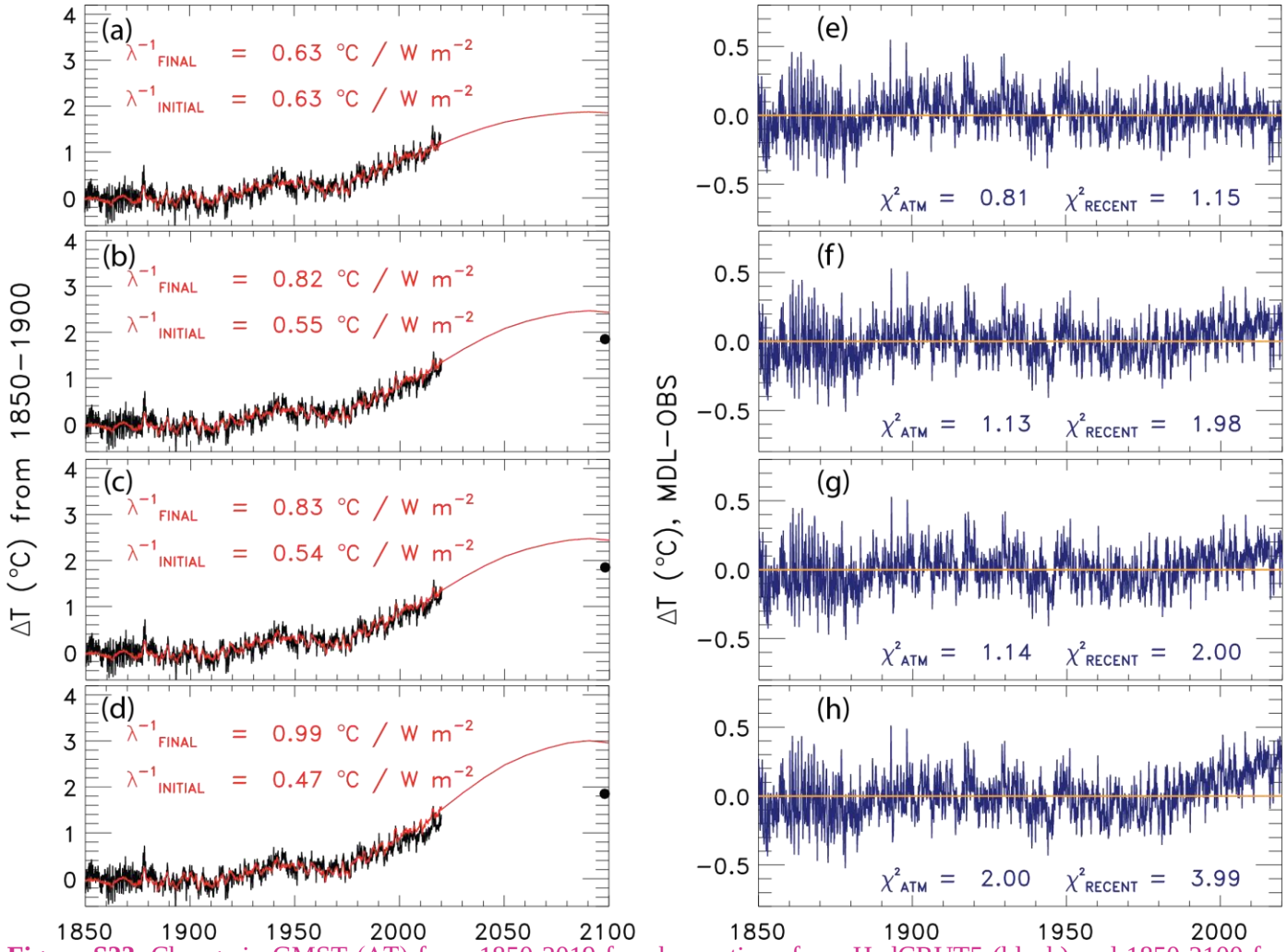

Figure S23. Change in GMST (ΔT) from 1850-2019 for observations from HadCRUT5 (black) and 1850-2100 for modeled (red) using SSP4-3.4 and the residual between modeled and observations using an instantaneous time variant λ^{-1}. (a) ΔT assuming a constant value of λ^{-1}. (b) ΔT allowing λ^{-1} to increase by 50%. (c) ΔT allowing λ^{-1} to vary while the value of χ^2_{RECENT} is kept below 2. (d) ΔT allowing λ^{-1} to vary while the value of χ^2_{ATM} is kept below 2. (e) Residual between modeled and observed ΔT from 1850-2019 for constant λ^{-1}. (f) Same as (e) but for increasing λ^{-1} by 50%. (g) Same as (f) but for varying λ^{-1} while the value of χ^2_{RECENT} is kept below 2. (h) same as (g)but for varying λ^{-1} while the value of χ^2_{ATM} is kept below 2.

Table ~~S5~~S7. Details of the CMIP6 GCMs used in this study.

Institution	Model	Model Output
AS-RCEC	TaiESM1	No reference provided
AWI	AWI-CM-1-1-MR	(Semmler et al., 2018a, 2018b, 2018c, 2019a, 2019b)
BCC	BCC-CSM2-MR	(Wu et al., 2018a, 2018b, 2018c; Xin et al., 2019a, 2019b, 2019c, 2019d)
	BCC-ESM1	(Zhang et al., 2018a, 2018b, 2019)
CAMS	CAMS-CSM1-0	(Rong, 2019a, 2019b, 2019c, 2019d, 2019e, 2019f)
CAS	CAS-ESM2-0	(Chai, 2019)
	FGOALS-f3-L	(YU, 2019a, 2019b, 2019c, 2019d, 2019e)
	FGOALS-g3	(Li, 2019a, 2019b, 2019c, 2019d, 2019e)
CCCma	CanESM5	(Swart et al., 2019f, 2019g, 2019h, 2019i, 2019j, 2019k, 2019l, 2019m, 2019n, 2019o)
	CanESM5-CanOE	(Swart et al., 2019a, 2019b, 2019c, 2019d, 2019e)
CNRM-CERFACS	CNRM-CM6-1	(Voldoire, 2018, 2019c, 2019d, 2019e, 2019f)
	CNRM-CM6-1-HR	(Voldoire, 2019a, 2019b, 2020a, 2020b)
	CNRM-ESM2-1	(Seferian, 2018; Voldoire, 2019g, 2019h, 2019i, 2019j, 2019k, 2019l)
CSIRO	ACCESS-ESM1-5	(Ziehn et al., 2019a, 2019b, 2019c, 2019d, 2019e, 2019f, 2019g)
CSIRO-ARCCSS	ACCESS-CM2	(Dix et al., 2019a, 2019b, 2019c, 2019d, 2019e, 2019f, 2019g)
E3SM-Project	E3SM-1-0	(Bader et al., 2018, 2019a, 2019b)
	E3SM-1-1-ECA	(Bader et al., 2020)
E3SM-Project RUBISCO	E3SM-1-1	(Bader et al., 2019c)
EC-Earth-Consortium	EC-Earth3	(EC-Earth Consortium (EC-Earth), 2019i, 2019j, 2019k, 2019l, 2019m)
	EC-Earth3-Veg	(EC-Earth Consortium (EC-Earth), 2019a, 2019b, 2019c, 2019d, 2019e, 2019f, 2019g, 2019h)

FIO-QLNM	FIO-ESM-2-0	(Song et al., 2019a, 2019b, 2019c, 2019d)
HAMMOZ-Consortium	MPI-ESM1-2-HAM	(Neubauer et al., 2019)
INM	INM-CM4-8	(Volodin et al., 2019a, 2019b, 2019c, 2019d, 2019e, 2019f, 2019g)
	INM-CM5-0	(Volodin et al., 2019m, 2019h, 2019n, 2019i, 2019j, 2019k, 2019l)
IPSL	IPSL-CM6A-LR	(Boucher et al., 2018a, 2018b, 2018c, 2019a, 2019b, 2019c, 2019d, 2019e, 2019f, 2019g)
MIROC	MIROC6	(Shiogama et al., 2019a, 2019b, 2019c, 2019d, 2019e, 2019f, 2019g; Tatebe and Watanabe, 2018a, 2018b, 2018c)
	MIROC-ES2L	(Hajima et al., 2019; Tachiiri et al., 2019a, 2019b, 2019c, 2019d, 2019e)
MOHC	HadGEM3-GC31-MM	(Ridley et al., 2019c)
MOHC NERC	HadGEM3-GC31-LL	(Good, 2019, 2020a, 2020b; Ridley et al., 2018, 2019a, 2019b)
MOHC, NERC, NIMS-KMA, NIWA	UKESM1-0-LL	(Byun, 2020; Good et al., 2019a, 2019b, 2019c, 2019d, 2019e, 2019f; Tang et al., 2019a, 2019b, 2019c)
MPI-M AWI	MPI-ESM1-2-LR	(Wieners et al., 2019a, 2019b, 2019c, 2019d, 2019e)
MPI-M DWD DKRZ	MPI-ESM1-2-HR	(Jungclaus et al., 2019; Schupfner et al., 2019a, 2019b, 2019c, 2019d; Steger et al., 2019)
MRI	MRI-ESM2-0	(Yukimoto et al., 2019a, 2019b, 2019c, 2019d, 2019e, 2019f, 2019g, 2019h)
NASA-GISS	GISS-E2-1-G	(NASA Goddard Institute for Space Studies (NASA/GISS), 2018a, 2018b, 2018c, 2020a, 2020b, 2020c, 2020d)
	GISS-E2-1-G-CC	No reference provided
	GISS-E2-2-G	(NASA Goddard Institute for Space Studies (NASA/GISS), 2019a)
	GISS-E2-1-H	(NASA Goddard Institute for Space Studies (NASA/GISS), 2018d, 2019b, 2019c)
NCAR	CESM2-WACCM-FV2	(Danabasoglu, 2019d, 2019e, 2020a)

	CESM2	(Danabasoglu, 2019c, 2019d, 2019e, 2019f, 2019g, 2019h; Danabasoglu et al., 2019)
	CESM2-FV2	(Danabasoglu, 2019b, 2019c, 2020b)
	CESM2-WACCM	(Danabasoglu, 2019f, 2019g, 2019h, 2019a, 2019i, 2019j, 2019k)
	NorCPM1	(Bethke et al., 2019a, 2019b, 2019c)
NCC	NorESM2-LM	(Seland et al., 2019a, 2019b, 2019c, 2019d, 2019e, 2019f, 2019g)
	NorESM2-MM	(Bentsen et al., 2019a, 2019b, 2019c, 2019d, 2019e, 2019f, 2019g)
NIMS-KMA	KACE-1-0-G	(Byun et al., 2019a, 2019b, 2019c, 2019d, 2019e)
NOAA-GFDL	GFDL-CM4	(Guo et al., 2018a, 2018b, 2018c, 2018d, 2018e)
	GFDL-ESM4	(John et al., 2018a, 2018b, 2018c, 2018d, 2018e; Krasting et al., 2018a, 2018b, 2018c)
NUIST	NESM3	(Cao, 2019a, 2019b, 2019c; Cao and Wang, 2019)
SNU	SAM0-UNICON	(Park and Shin, 2019a, 2019b, 2019c)
THU	CIESM	(Huang, 2019a, 2019b, 2020a, 2020b)
UA	MCM-UA-1-0	(Stouffer, 2019a, 2019b, 2019c, 2019d, 2019e, 2019f, 2019g)

References

Bader, D. C., Leung, R., Taylor, M. and McCoy, R. B.: E3SM-Project E3SM1.0 model output prepared for CMIP6 CMIP piControl, Earth System Grid Federation, , doi:https://doi.org/10.22033/ESGF/CMIP6.4499, 2018.

Bader, D. C., Leung, R., Taylor, M. and McCoy, R. B.: E3SM-Project E3SM1.0 model output prepared for CMIP6 CMIP abrupt-4xCO2, Earth System Grid Federation, , doi:https://doi.org/10.22033/ESGF/CMIP6.4491, 2019a.

Bader, D. C., Leung, R., Taylor, M. and McCoy, R. B.: E3SM-Project E3SM1.0 model output prepared for CMIP6 CMIP historical, Earth System Grid Federation, , doi:https://doi.org/10.22033/ESGF/CMIP6.4497, 2019b.

Bader, D. C., Leung, R., Taylor, M. and McCoy, R. B.: E3SM-Project E3SM1.1 model output prepared for CMIP6 CMIP historical, Earth System Grid Federation, , doi:https://doi.org/10.22033/ESGF/CMIP6.11485, 2019c.

Bader, D. C., Leung, R., Taylor, M. and McCoy, R. B.: E3SM-Project E3SM1.1ECA model output prepared for CMIP6 CMIP historical, Earth System Grid Federation, , doi:https://doi.org/10.22033/ESGF/CMIP6.11486, 2020.

Balmaseda, M. A., Trenberth, K. E. and Källén, E.: Distinctive climate signals in reanalysis of global ocean heat content, Geophys. Res. Lett., 40(9), 1754–1759, doi:10.1002/grl.50382, 2013a.

Balmaseda, M. A., Mogensen, K. and Weaver, A. T.: Evaluation of the ECMWF ocean reanalysis system ORAS4, Q. J. R. Meteorol. Soc., 139(674), 1132–1161, doi:10.1002/qj.2063, 2013b.

Bentsen, M., Oliviè, D. J. L., Seland, Ø., Toniazzo, T., Gjermundsen, A., Graff, L. S., Debernard, J. B., Gupta, A. K., He, Y., Kirkevåg, A., Schwinger, J., Tjiputra, J., Aas, K. S., Bethke, I., Fan, Y., Griesfeller, J., Grini, A., Guo, C., Ilicak, M., Karset, I. H. H., Landgren, O. A., Liakka, J., Moseid, K. O., Nummelin, A., Spensberger, C., Tang, H., Zhang, Z., Heinze, C., Iversen, T. and Schulz, M.: NCC NorESM2-MM model output prepared for CMIP6 CMIP abrupt-4xCO2, Earth System Grid Federation, , doi:https://doi.org/10.22033/ESGF/CMIP6.7840, 2019a.

Bentsen, M., Oliviè, D. J. L., Seland, Ø., Toniazzo, T., Gjermundsen, A., Graff, L. S., Debernard, J. B., Gupta, A. K., He, Y., Kirkevåg, A., Schwinger, J., Tjiputra, J., Aas, K. S., Bethke, I., Fan, Y., Griesfeller, J., Grini, A., Guo, C., Ilicak, M., Karset, I. H. H., Landgren, O. A., Liakka, J., Moseid, K. O., Nummelin, A., Spensberger, C., Tang, H., Zhang, Z., Heinze, C., Iversen, T. and Schulz, M.: NCC NorESM2-MM model output prepared for CMIP6 CMIP historical, Earth System Grid Federation, , doi:https://doi.org/10.22033/ESGF/CMIP6.8040, 2019b.

Bentsen, M., Oliviè, D. J. L., Seland, Ø., Toniazzo, T., Gjermundsen, A., Graff, L. S., Debernard, J. B., Gupta, A. K., He, Y., Kirkevåg, A., Schwinger, J., Tjiputra, J., Aas, K. S., Bethke, I., Fan, Y., Griesfeller, J., Grini, A., Guo, C., Ilicak, M., Karset, I. H. H., Landgren, O. A., Liakka, J., Moseid, K. O., Nummelin, A., Spensberger, C., Tang, H., Zhang, Z., Heinze, C., Iversen, T. and Schulz, M.: NCC NorESM2-MM model output prepared for CMIP6 CMIP piControl, Earth System Grid Federation, , doi:https://doi.org/10.22033/ESGF/CMIP6.8221, 2019c.

Bentsen, M., Oliviè, D. J. L., Seland, Ø., Toniazzo, T., Gjermundsen, A., Graff, L. S., Debernard, J. B., Gupta, A. K., He, Y., Kirkevåg, A., Schwinger, J., Tjiputra, J., Aas, K. S., Bethke, I., Fan, Y., Griesfeller, J., Grini, A., Guo, C., Ilicak, M., Karset, I. H. H., Landgren, O. A., Liakka, J., Moseid, K. O., Nummelin, A., Spensberger, C., Tang, H., Zhang, Z., Heinze, C., Iversen, T. and Schulz, M.: NCC NorESM2-MM model output prepared for CMIP6 ScenarioMIP ssp126, Earth System Grid Federation, , doi:https://doi.org/10.22033/ESGF/CMIP6.8250, 2019d.

Bentsen, M., Oliviè, D. J. L., Seland, Ø., Toniazzo, T., Gjermundsen, A., Graff, L. S., Debernard, J. B., Gupta, A. K., He, Y., Kirkevåg, A., Schwinger, J., Tjiputra, J., Aas, K. S., Bethke, I., Fan, Y., Griesfeller, J., Grini, A.,

Guo, C., Ilicak, M., Karset, I. H. H., Landgren, O. A., Liakka, J., Moseid, K. O., Nummelin, A., Spensberger, C., Tang, H., Zhang, Z., Heinze, C., Iversen, T. and Schulz, M.: NCC NorESM2-MM model output prepared for CMIP6 ScenarioMIP ssp245, Earth System Grid Federation, , doi:https://doi.org/10.22033/ESGF/CMIP6.8255, 2019e.

Bentsen, M., Oliviè, D. J. L., Seland, Ø., Toniazzo, T., Gjermundsen, A., Graff, L. S., Debernard, J. B., Gupta, A. K., He, Y., Kirkevåg, A., Schwinger, J., Tjiputra, J., Aas, K. S., Bethke, I., Fan, Y., Griesfeller, J., Grini, A., Guo, C., Ilicak, M., Karset, I. H. H., Landgren, O. A., Liakka, J., Moseid, K. O., Nummelin, A., Spensberger, C., Tang, H., Zhang, Z., Heinze, C., Iversen, T. and Schulz, M.: NCC NorESM2-MM model output prepared for CMIP6 ScenarioMIP ssp370, Earth System Grid Federation, , doi:https://doi.org/10.22033/ESGF/CMIP6.8270, 2019f.

Bentsen, M., Oliviè, D. J. L., Seland, Ø., Toniazzo, T., Gjermundsen, A., Graff, L. S., Debernard, J. B., Gupta, A. K., He, Y., Kirkevåg, A., Schwinger, J., Tjiputra, J., Aas, K. S., Bethke, I., Fan, Y., Griesfeller, J., Grini, A., Guo, C., Ilicak, M., Karset, I. H. H., Landgren, O. A., Liakka, J., Moseid, K. O., Nummelin, A., Spensberger, C., Tang, H., Zhang, Z., Heinze, C., Iversen, T. and Schulz, M.: NCC NorESM2-MM model output prepared for CMIP6 ScenarioMIP ssp585, Earth System Grid Federation, , doi:https://doi.org/10.22033/ESGF/CMIP6.8321, 2019g.

Bethke, I., Wang, Y., Counillon, F., Kimmritz, M., Fransner, F., Samuelsen, A., Langehaug, H. R., Chiu, P.-G., Bentsen, M., Guo, C., Tjiputra, J., Kirkevåg, A., Oliviè, D. J. L., Seland, Ø., Fan, Y., Lawrence, P., Eldevik, T. and Keenlyside, N.: NCC NorCPM1 model output prepared for CMIP6 CMIP abrupt-4xCO2, Earth System Grid Federation, , doi:https://doi.org/10.22033/ESGF/CMIP6.10862, 2019a.

Bethke, I., Wang, Y., Counillon, F., Kimmritz, M., Fransner, F., Samuelsen, A., Langehaug, H. R., Chiu, P., Bentsen, M., Guo, C., Tjiputra, J., Kirkevåg, A., Oliviè, D. J. L., Seland, Ø., Fan, Y., Lawrence, P., Eldevik, T. and Keenlyside, N.: NCC NorCPM1 model output prepared for CMIP6 CMIP historical, Earth System Grid Federation, , doi:https://doi.org/10.22033/ESGF/CMIP6.10894, 2019b.

Bethke, I., Wang, Y., Counillon, F., Kimmritz, M., Fransner, F., Samuelsen, A., Langehaug, H. R., Chiu, P.-G., Bentsen, M., Guo, C., Tjiputra, J., Kirkevåg, A., Oliviè, D. J. L., Seland, Ø., Fan, Y., Lawrence, P., Eldevik, T. and Keenlyside, N.: NCC NorCPM1 model output prepared for CMIP6 CMIP piControl, Earth System Grid Federation, , doi:https://doi.org/10.22033/ESGF/CMIP6.10896, 2019c.

Bony, S., Colman, R., Kattsov, V. M., Allan, R. P., Bretherton, C. S., Dufresne, J. L., Hall, A., Hallegatte, S., Holland, M. M., Ingram, W., Randall, D. A., Soden, B. J., Tselioudis, G. and Webb, M. J.: How well do we understand and evaluate climate change feedback processes?, J. Clim., 19(15), 3445–3482, doi:10.1175/JCLI3819.1, 2006.

Boucher, O., Denvil, S., Caubel, A. and Foujols, M. A.: IPSL IPSL-CM6A-LR model output prepared for CMIP6 CMIP abrupt-4xCO2, Earth System Grid Federation, , doi:https://doi.org/10.22033/ESGF/CMIP6.5109, 2018a.

Boucher, O., Denvil, S., Caubel, A. and Foujols, M. A.: IPSL IPSL-CM6A-LR model output prepared for CMIP6 CMIP historical, Earth System Grid Federation, , doi:https://doi.org/10.22033/ESGF/CMIP6.5195, 2018b.

Boucher, O., Denvil, S., Caubel, A. and Foujols, M. A.: IPSL IPSL-CM6A-LR model output prepared for CMIP6 CMIP piControl, Earth System Grid Federation, , doi:https://doi.org/10.22033/ESGF/CMIP6.5251, 2018c.

Boucher, O., Denvil, S., Caubel, A. and Foujols, M. A.: IPSL IPSL-CM6a-LR model output prepared for CMIP6 ScenarioMIP ssp119, Earth System Grid Federation, , doi:https://doi.org/10.22033/ESGF/CMIP6.5261, 2019a.

Boucher, O., Denvil, S., Caubel, A. and Foujols, M. A.: IPSL IPSL-CM6A-LR model output prepared for CMIP6 ScenarioMIP ssp126, Earth System Grid Federation, , doi:https://doi.org/10.22033/ESGF/CMIP6.5262,

2019b.

Boucher, O., Denvil, S., Caubel, A. and Foujols, M. A.: IPSL IPSL-CM6A-LR model output prepared for CMIP6 ScenarioMIP ssp370, Earth System Grid Federation, , doi:https://doi.org/10.22033/ESGF/CMIP6.5265, 2019c.

Boucher, O., Denvil, S., Caubel, A. and Foujols, M. A.: IPSL IPSL-CM6A-LR model output prepared for CMIP6 ScenarioMIP ssp434, Earth System Grid Federation, , doi:https://doi.org/10.22033/ESGF/CMIP6.5267, 2019d.

Boucher, O., Denvil, S., Caubel, A. and Foujols, M. A.: IPSL IPSL-CM6A-LR model output prepared for CMIP6 ScenarioMIP ssp460, Earth System Grid Federation, , doi:https://doi.org/10.22033/ESGF/CMIP6.5268, 2019e.

Boucher, O., Denvil, S., Caubel, A. and Foujols, M. A.: IPSL IPSL-CM6A-LR model output prepared for CMIP6 ScenarioMIP ssp585, Earth System Grid Federation, , doi:https://doi.org/10.22033/ESGF/CMIP6.5271, 2019f.

Boucher, O., Denvil, S., Caubel, A. and Foujols, M. A.: PSL IPSL-CM6A-LR model output prepared for CMIP6 ScenarioMIP ssp245, Earth System Grid Federation, , doi:https://doi.org/10.22033/ESGF/CMIP6.5264, 2019g.

Byun, Y.-H.: NIMS-KMA UKESM1.0-LL model output prepared for CMIP6 CMIP historical, Earth System Grid Federation, , doi:https://doi.org/10.22033/ESGF/CMIP6.8379, 2020.

Byun, Y.-H., Lim, Y.-J., Sung, H. M., Kim, J., Sun, M. and Kim, B.-H.: NIMS-KMA KACE1.0-G model output prepared for CMIP6 CMIP historical, Earth System Grid Federation, , doi:https://doi.org/10.22033/ESGF/CMIP6.8378, 2019a.

Byun, Y.-H., Lim, Y.-J., Shim, S., Sung, H. M., Sun, M., Kim, J., Kim, B.-H., Lee, J.-H. and Moon, H.: NIMS-KMA KACE1.0-G model output prepared for CMIP6 ScenarioMIP ssp126, Earth System Grid Federation, , doi:https://doi.org/10.22033/ESGF/CMIP6.8432, 2019b.

Byun, Y.-H., Lim, Y.-J., Shim, S., Sung, H. M., Sun, M., Kim, J., Kim, B.-H., Lee, J.-H. and Moon, H.: NIMS-KMA KACE1.0-G model output prepared for CMIP6 ScenarioMIP ssp245, Earth System Grid Federation, , doi:https://doi.org/10.22033/ESGF/CMIP6.8435, 2019c.

Byun, Y.-H., Lim, Y.-J., Shim, S., Sung, H. M., Sun, M., Kim, J., Kim, B.-H., Lee, J.-H. and Moon, H.: NIMS-KMA KACE1.0-G model output prepared for CMIP6 ScenarioMIP ssp370, Earth System Grid Federation, , doi:https://doi.org/10.22033/ESGF/CMIP6.8437, 2019d.

Byun, Y.-H., Lim, Y.-J., Shim, S., Sung, H. M., Sun, M., Kim, J., Kim, B.-H., Lee, J.-H. and Moon, H.: NIMS-KMA KACE1.0-G model output prepared for CMIP6 ScenarioMIP ssp585, Earth System Grid Federation, , doi:https://doi.org/10.22033/ESGF/CMIP6.8456, 2019e.

Canty, T., Mascioli, N. R., Smarte, M. D. and Salawitch, R. J.: An empirical model of global climate – Part 1: A critical evaluation of volcanic cooling, Atmos. Chem. Phys., 13(8), 3997–4031, doi:10.5194/acp-13-3997-2013, 2013.

Cao, J.: NUIST NESMv3 model output prepared for CMIP6 ScenarioMIP ssp126, Earth System Grid Federation, , doi:https://doi.org/10.22033/ESGF/CMIP6.8780, 2019a.

Cao, J.: NUIST NESMv3 model output prepared for CMIP6 ScenarioMIP ssp245, Earth System Grid Federation, , doi:https://doi.org/10.22033/ESGF/CMIP6.8781, 2019b.

Cao, J.: NUIST NESMv3 model output prepared for CMIP6 ScenarioMIP ssp585, Earth System Grid Federation, , doi:https://doi.org/10.22033/ESGF/CMIP6.8790, 2019c.

Cao, J. and Wang, B.: NUIST NESMv3 model output prepared for CMIP6 CMIP historical, , doi:https://doi.org/10.22033/ESGF/CMIP6.8769, 2019.

Carton, J. A., Chepurin, G. A. and Chen, L.: SODA3: A New Ocean Climate Reanalysis, J. Clim., 31(17), 6967–6983, doi:10.1175/jcli-d-18-0149.1, 2018.

Chai, Z.: CAS CAS-ESM1.0 model output prepared for CMIP6 CMIP historical, Earth System Grid Federation, , doi:https://doi.org/10.22033/ESGF/CMIP6.3353, 2019.

Cheng, L., Trenberth, K. E., Fasullo, J., Boyer, T., Abraham, J. and Zhu, J.: Improved estimates of ocean heat content from 1960 to 2015, Sci. Adv., 3(3), 1–11, doi:10.1126/sciadv.1601545, 2017.

Danabasoglu, G.: NCAR CESM-WACCM model output prepared for CMIP6 ScenarioMIP ssp126, Earth System Grid Federation, , doi:https://doi.org/10.22033/ESGF/CMIP6.10100, 2019a.

Danabasoglu, G.: NCAR CESM2-FV2 model output prepared for CMIP6 CMIP historical, Earth System Grid Federation, , doi:https://doi.org/10.22033/ESGF/CMIP6.11297, 2019b.

Danabasoglu, G.: NCAR CESM2-FV2 model output prepared for CMIP6 CMIP piControl, Earth System Grid Federation, , doi:https://doi.org/10.22033/ESGF/CMIP6.11301, 2019c.

Danabasoglu, G.: NCAR CESM2-WACCM-FV2 model output prepared for CMIP6 CMIP historical, Earth System Grid Federation, , doi:https://doi.org/10.22033/ESGF/CMIP6.11298, 2019d.

Danabasoglu, G.: NCAR CESM2-WACCM-FV2 model output prepared for CMIP6 CMIP piControl, Earth System Grid Federation, , doi:https://doi.org/10.22033/ESGF/CMIP6.11302, 2019e.

Danabasoglu, G.: NCAR CESM2-WACCM model output prepared for CMIP6 CMIP abrupt-4xCO2, Earth System Grid Federation, , doi:https://doi.org/10.22033/ESGF/CMIP6.10039, 2019f.

Danabasoglu, G.: NCAR CESM2-WACCM model output prepared for CMIP6 CMIP historical, Earth System Grid Federation, , doi:https://doi.org/10.22033/ESGF/CMIP6.10071, 2019g.

Danabasoglu, G.: NCAR CESM2-WACCM model output prepared for CMIP6 CMIP piControl, Earth System Grid Federation, , doi:https://doi.org/10.22033/ESGF/CMIP6.10094, 2019h.

Danabasoglu, G.: NCAR CESM2-WACCM model output prepared for CMIP6 ScenarioMIP ssp245, Earth System Grid Federation, , doi:https://doi.org/10.22033/ESGF/CMIP6.10101, 2019i.

Danabasoglu, G.: NCAR CESM2-WACCM model output prepared for CMIP6 ScenarioMIP ssp370, Earth System Grid Federation, , doi:https://doi.org/10.22033/ESGF/CMIP6.10102, 2019j.

Danabasoglu, G.: NCAR CESM2-WACCM model output prepared for CMIP6 ScenarioMIP ssp585, Earth System Grid Federation, , doi:https://doi.org/10.22033/ESGF/CMIP6.10115, 2019k.

Danabasoglu, G.: NCAR CESM2 model output prepared for CMIP6 CMIP abrupt-4xCO2, Earth System Grid Federation, , doi:https://doi.org/10.22033/ESGF/CMIP6.7519, 2019l.

Danabasoglu, G.: NCAR CESM2 model output prepared for CMIP6 CMIP historical, Earth System Grid Federation, , doi:https://doi.org/10.22033/ESGF/CMIP6.7627, 2019m.

Danabasoglu, G.: NCAR CESM2 model output prepared for CMIP6 ScenarioMIP ssp126, Earth System Grid Federation, , doi:https://doi.org/10.22033/ESGF/CMIP6.7746, 2019n.

Danabasoglu, G.: NCAR CESM2 model output prepared for CMIP6 ScenarioMIP ssp245, Earth System Grid Federation, , doi:https://doi.org/10.22033/ESGF/CMIP6.7748, 2019o.

Danabasoglu, G.: NCAR CESM2 model output prepared for CMIP6 ScenarioMIP ssp370, Earth System Grid Federation, , doi:https://doi.org/10.22033/ESGF/CMIP6.7753, 2019p.

Danabasoglu, G.: NCAR CESM2 model output prepared for CMIP6 ScenarioMIP ssp585, Earth System Grid Federation, , doi:https://doi.org/10.22033/ESGF/CMIP6.7768, 2019q.

Danabasoglu, G.: CAR CESM2-WACCM-FV2 model output prepared for CMIP6 CMIP abrupt-4xCO2, Earth System Grid Federation, , doi:https://doi.org/10.22033/ESGF/CMIP6.11286, 2020a.

Danabasoglu, G.: NCAR CESM2-FV2 model output prepared for CMIP6 CMIP abrupt-4xCO2, Earth System Grid Federation, , doi:https://doi.org/10.22033/ESGF/CMIP6.11285, 2020b.

Danabasoglu, G., Lawrence, D., Lindsay, K., Lipscomb, W. and Strand, G.: NCAR CESM2 model output prepared for CMIP6 CMIP piControl, Earth System Grid Federation, , doi:https://doi.org/10.22033/ESGF/CMIP6.7733, 2019.

Dix, M., Bi, D., Dobrohotoff, P., Fiedler, R., Harman, I., Law, R., Mackallah, C., Marsland, S., O'Farrell, S., Rashid, H., Srbinovsky, J., Sullivan, A., Trenham, C., Vohralik, P., Watterson, I., Williams, G., Woodhouse, M., Bodman, R., Dias, F. B., Domingues, C., Hannah, N., Heerdegen, A., Savita, A., Wales, S., Allen, C., Druken, K., Evans, B., Richards, C., Ridzwan, S. M., Roberts, D., Smillie, J., Snow, K., Ward, M. and Yang, R.: CSIRO-ARCCSS ACCESS-CM2 model output prepared for CMIP6 CMIP abrupt-4xCO2, Earth System Grid Federation, , doi:https://doi.org/10.22033/ESGF/CMIP6.4237, 2019a.

Dix, M., Bi, D., Dobrohotoff, P., Fiedler, R., Harman, I., Law, R., Mackallah, C., Marsland, S., O'Farrell, S., Rashid, H., Srbinovsky, J., Sullivan, A., Trenham, C., Vohralik, P., Watterson, I., Williams, G., Woodhouse, M., Bodham, R., Dias, F. B., Domingues, C. M., Hannah, N., Heerdegen, A., Savita, A., Wales, S., Allen, C., Druken, K., Evans, B., Richards, C., Ridzwan, S. M., Robers, D., Smillie, J., Snow, K., Ward, M. and Yang, R.: CSIRO-ARCCSS ACCESS-CM2 model output prepared for CMIP6 CMIP historical, Earth System Grid Federation, , doi:https://doi.org/10.22033/ESGF/CMIP6.4271, 2019b.

Dix, M., Bi, D., Dobrohotoff, P., Fiedler, R., Harman, I., Law, R., Mackallah, C., Marsland, S., O'Farrell, S., Rashid, H., Srbinovsky, J., Sullivan, A., Trenham, C., Vohralik, P., Watterson, I., Williams, G., Woodhouse, M., Bodman, R., Dias, F. B., Domingues, C., Hannah, N., Heerdegen, A., Savita, A., Wales, S., Allen, C., Druken, K., Evans, B., Richards, C., Ridzwan, S. M., Roberts, D., Smillie, J., Snow, K., Ward, M. and Yang, R.: CSIRO-ARCCSS ACCESS-CM2 model output prepared for CMIP6 CMIP piControl, Earth System Grid Federation, , doi:https://doi.org/10.22033/ESGF/CMIP6.4311, 2019c.

Dix, M., Bi, D., Dobrohotoff, P., Fiedler, R., Harman, I., Law, R., Mackallah, C., Marsland, S., O'Farrell, S., Rashid, H., Srbinovsky, J., Sullivan, A., Trenham, C., Vohralik, P., Watterson, I., Williams, G., Woodhouse, M., Bodman, R., Dias, F. B., Domingues, C. M., Hannah, N., Heerdegen, A., Savita, A., Wales, S., Allen, C., Druken, K., Evans, B., Richards, C., Ridzwan, S. M., Roberts, D., Smillie, J., Snow, K., Ward, M. and Yang, R.: CSIRO-ARCCSS ACCESS-CM2 model output prepared for CMIP6 ScenarioMIP ssp126, Earth System Grid Federation, , doi:https://doi.org/10.22033/ESGF/CMIP6.4319, 2019d.

Dix, M., Bi, D., Dobrohotoff, P., Fiedler, R., Harman, I., Law, R., Mackallah, C., Marsland, S., O'Farrell, S., Rashid, H., Srbinovsky, J., Sullivan, A., Trenham, C., Vohralik, P., Watterson, I., Williams, G., Woodhouse, M., Bodman, R., Dias, F. B., Domingues, C., Hannah, N., Heerdegen, A., Savita, A., Wales, S., Allen, C., Druken, K., Evans, B., Richards, C., Ridzwan, S. M., Roberts, D., Smillie, J., Snow, K., Ward, M. and Yang, R.: CSIRO-ARCCSS ACCESS-CM2 model output prepared for CMIP6 ScenarioMIP ssp245, Earth System Grid Federation, , doi:https://doi.org/10.22033/ESGF/CMIP6.4321, 2019e.

Dix, M., Bi, D., Dobrohotoff, P., Fiedler, R., Harman, I., Law, R., Mackallah, C., Marsland, S., O'Farrell, S., Rashid,

H., Srbinovsky, J., Sullivan, A., Trenham, C., Vohralik, P., Watterson, I., Williams, G., Woodhouse, M., Bodman, R., Dias, F. B., Domingues, C., Hannah, N., Heerdegen, A., Savita, A., Wales, S., Allen, C., Druken, K., Evans, B., Richards, C., Ridzwan, S. M., Roberts, D., Smillie, J., Snow, K., Ward, M. and Yang, R.: CSIRO-ARCCSS ACCESS-CM2 model output prepared for CMIP6 ScenarioMIP ssp370, Earth System Grid Federation, , doi:https://doi.org/10.22033/ESGF/CMIP6.4323, 2019f.

Dix, M., Bi, D., Dobrohotoff, P., Fiedler, R., Harman, I., Law, R., Mackallah, C., Marsland, S., O'Farrell, S., Rashid, H., Srbinovsky, J., Sullivan, A., Trenham, C., Vohralik, P., Watterson, I., Williams, G., Woodhouse, M., Bodman, R., Dias, F. B., Domingues, C., Hannah, N., Heerdegen, A., Savita, A., Wales, S., Allen, C., Druken, K., Evans, B., Richards, C., Ridzwan, S. M., Roberts, D., Smillie, J., Snow, K., Ward, M. and Yang, R.: CSIRO-ARCCSS ACCESS-CM2 model output prepared for CMIP6 ScenarioMIP ssp585, Earth System Grid Federation, , doi:https://doi.org/10.22033/ESGF/CMIP6.4332, 2019g.

Douglass, D. H. and Knox, R. S.: Climate forcing by the volcanic eruption of Mount Pinatubo, Geophys. Res. Lett., 32(5), 1–5, doi:10.1029/2004GL022119, 2005.

EC-Earth Consortium (EC-Earth): EC-Earth-Consortium EC-Earth3-Veg model output prepared for CMIP6 CMIP, Earth System Grid Federation, , doi:https://doi.org/10.22033/ESGF/CMIP6.4706, 2019a.

EC-Earth Consortium (EC-Earth): EC-Earth-Consortium EC-Earth3-Veg model output prepared for CMIP6 CMIP abrupt-4xCO2, Earth System Grid Federation, , doi:https://doi.org/10.22033/ESGF/CMIP6.4524, 2019b.

EC-Earth Consortium (EC-Earth): EC-Earth-Consortium EC-Earth3-Veg model output prepared for CMIP6 CMIP piControl, Earth System Grid Federation, , doi:https://doi.org/10.22033/ESGF/CMIP6.4848, 2019c.

EC-Earth Consortium (EC-Earth): EC-Earth-Consortium EC-Earth3-Veg model output prepared for CMIP6 ScenarioMIP ssp119, Earth System Grid Federation, , doi:https://doi.org/10.22033/ESGF/CMIP6.4872, 2019d.

EC-Earth Consortium (EC-Earth): EC-Earth-Consortium EC-Earth3-Veg model output prepared for CMIP6 ScenarioMIP ssp126, Earth System Grid Federation, , doi:https://doi.org/10.22033/ESGF/CMIP6.4876, 2019e.

EC-Earth Consortium (EC-Earth): EC-Earth-Consortium EC-Earth3-Veg model output prepared for CMIP6 ScenarioMIP ssp245, Earth System Grid Federation, , doi:https://doi.org/10.22033/ESGF/CMIP6.4882, 2019f.

EC-Earth Consortium (EC-Earth): EC-Earth-Consortium EC-Earth3-Veg model output prepared for CMIP6 ScenarioMIP ssp370, Earth System Grid Federation, , doi:https://doi.org/10.22033/ESGF/CMIP6.4886, 2019g.

EC-Earth Consortium (EC-Earth): EC-Earth-Consortium EC-Earth3-Veg model output prepared for CMIP6 ScenarioMIP ssp585, Earth System Grid Federation, , doi:https://doi.org/10.22033/ESGF/CMIP6.4914, 2019h.

EC-Earth Consortium (EC-Earth): EC-Earth-Consortium EC-Earth3 model output prepared for CMIP6 CMIP abrupt-4xCO2, Earth System Grid Federation, , doi:https://doi.org/10.22033/ESGF/CMIP6.4518, 2019i.

EC-Earth Consortium (EC-Earth): EC-Earth-Consortium EC-Earth3 model output prepared for CMIP6 CMIP historical, Earth System Grid Federation, , doi:https://doi.org/10.22033/ESGF/CMIP6.4700, 2019j.

EC-Earth Consortium (EC-Earth): EC-Earth-Consortium EC-Earth3 model output prepared for CMIP6 CMIP piControl, Earth System Grid Federation, , doi:https://doi.org/10.22033/ESGF/CMIP6.4842, 2019k.

EC-Earth Consortium (EC-Earth): EC-Earth-Consortium EC-Earth3 model output prepared for CMIP6 ScenarioMIP

ssp126, Earth System Grid Federation, , doi:https://doi.org/10.22033/ESGF/CMIP6.4874, 2019l.

EC-Earth Consortium (EC-Earth): EC-Earth-Consortium EC-Earth3 model output prepared for CMIP6 ScenarioMIP ssp370, Earth System Grid Federation, , doi:https://doi.org/10.22033/ESGF/CMIP6.4884, 2019m.

Foster, G. and Rahmstorf, S.: Global temperature evolution 1979–2010, Environ. Res. Lett., 6(4), 044022, doi:10.1088/1748-9326/6/4/044022, 2011.

Friedlingstein, P., Meinshausen, M., Arora, V. K., Jones, C. D., Anav, A., Liddicoat, S. K. and Knutti, R.: Uncertainties in CMIP5 climate projections due to carbon cycle feedbacks, J. Clim., 27(2), 511–526, doi:10.1175/JCLI-D-12-00579.1, 2014.

Friedlingstein, P., Jones, M. W., Sullivan, M. O., Andrew, R. M., Hauck, J., Peters, G. P., Peters, W., Pongratz, J., Sitch, S., Quéré, C. Le, Bakker, D. C. E., Canadell, J. G., Ciais, P., Jackson, R. B., Anthoni, P., Barbero, L., Bastos, A., Bastrikov, V., Becker, M., Bopp, L., Buitenhuis, E., Chandra, N., Chevallier, F., Chini, L. P., Currie, K., Feely, R. A., Gehlen, M., Gilfillan, D., Gkritzalis, T., Goll, D. S., Gruber, N., Gutekunst, S., Harris, I., Haverd, V., Houghton, R. A., Hurtt, G., Ilyina, T., Jain, A. K., Joetzjer, E., Kaplan, J. O., Kato, E., Goldewijk, K. K., Korsbakken, J. I., Landschützer, P., Lauvset, S. K., Lefevre, N., Lenton, A., Lienert, S., Lombardozzi, D., Marland, G., McGuire, P. C., Melton, J. R., Metzl, N., Munro, D. R., Nabel, J. E. M. S., Nakaoka, S., Neill, C., Omar, A. M., Ono, T., Peregon, A., Pierrot, D., Poulter, B., Rehder, G., Resplandy, L., Robertson, E., Rodenbeck, C., Seferian, R., Schwinger, J., Smith, N., Tans, P. P., Tian, H., Tilbrook, B., Tubiello, F. N., Van Der Werf, G. R., Wiltshire, A. J. and Zaehle, S.: Global Carbon Budget 2019, Earth Syst. Sci. Data, (11), 1783–1838, 2019.

Good, P.: MOHC HadGEM3-GC31-LL model output prepared for CMIP6 ScenarioMIP ssp245, Earth System Grid Federation, , doi:https://doi.org/10.22033/ESGF/CMIP6.10851, 2019.

Good, P.: MOHC HadGEM3-GC31-LL model output prepared for CMIP6 ScenarioMIP ssp126, Earth System Grid Federation, , doi:https://doi.org/10.22033/ESGF/CMIP6.10849, 2020a.

Good, P.: MOHC HadGEM3-GC31-LL model output prepared for CMIP6 ScenarioMIP ssp585, Earth System Grid Federation, , doi:https://doi.org/10.22033/ESGF/CMIP6.10901, 2020b.

Good, P., Sellar, A., Tang, Y., Rumbold, S., Ellis, R., Kelley, D. and Kuhlbrodt, T.: MOHC UKESM1.0-LL model output prepared for CMIP6 ScenarioMIP ssp119, Earth System Grid Federation, , doi:https://doi.org/10.22033/ESGF/CMIP6.6329, 2019a.

Good, P., Sellar, A., Tang, Y., Rumbold, S., Ellis, R., Kelley, D. and Kuhlbrodt, T.: MOHC UKESM1.0-LL model output prepared for CMIP6 ScenarioMIP ssp126, Earth System Grid Federation, , doi:https://doi.org/10.22033/ESGF/CMIP6.6333, 2019b.

Good, P., Sellar, A., Tang, Y., Rumbold, S., Ellis, R., Kelley, D. and Kuhlbrodt, T.: MOHC UKESM1.0-LL model output prepared for CMIP6 ScenarioMIP ssp245, Earth System Grid Federation, , doi:https://doi.org/10.22033/ESGF/CMIP6.6339, 2019c.

Good, P., Sellar, A., Tang, Y., Rumbold, S., Ellis, R., Kelley, D. and Kuhlbrodt, T.: MOHC UKESM1.0-LL model output prepared for CMIP6 ScenarioMIP ssp370, Earth System Grid Federation, , doi:https://doi.org/10.22033/ESGF/CMIP6.6347, 2019d.

Good, P., Sellar, A., Tang, Y., Rumbold, S., Ellis, R., Kelley, D. and Kuhlbrodt, T.: MOHC UKESM1.0-LL model output prepared for CMIP6 ScenarioMIP ssp434, Earth System Grid Federation, , doi:https://doi.org/10.22033/ESGF/CMIP6.6389, 2019e.

Good, P., Sellar, A., Tang, Y., Rumbold, S., Ellis, R., Kelley, D. and Kuhlbrodt, T.: MOHC UKESM1.0-LL model output prepared for CMIP6 ScenarioMIP ssp585, Earth System Grid Federation, ,

doi:https://doi.org/10.22033/ESGF/CMIP6.6405, 2019f.

Gregory, J. M., Ingram, W. J., Palmer, M. A., Jones, G. S., Stott, P. A., Thorpe, R. B., Lowe, J. A., Johns, T. C. and Williams, K. D.: A new method for diagnosing radiative forcing and climate sensitivity, Geophys. Res. Lett., 31(3), 2–5, doi:10.1029/2003GL018747, 2004.

Guo, H., John, J. G., Blanton, C., McHugh, C., Nikonov, S., Radhakrishnan, A., Zadeh, N. T., Balaji, V., Durachta, J., Dupuis, C., Menzel, R., Robinson, T., Underwood, S., Vahlenkamp, H., Dunne, K. A., Gauthier, P. P., Ginoux, P., Griffies, S. M., Hallberg, R., Harrison, M., Hurlin, W., Malyshev, S., Naik, V., Paulot, F., Paynter, D. J., Ploshay, J., Schwarzkopf, D. M., Seman, C. J., Shao, A., Silvers, L., Wyman, B., Zeng, Y., Adcroft, A., Dunne, J. P., Held, I. M., Krasting, J. P., Horowitz, L. W., Milly, P. C. ., Shevliakova, E., Winton, M. and Zhao, M.: NOAA-GFDL GFDL-CM4 model output prepared for CMIP6 CMIP abrupt-4xCO2, Earth System Grid Federation, , doi:https://doi.org/10.22033/ESGF/CMIP6.8486, 2018a.

Guo, H., John, J. G., Blanton, C., McHugh, C., Nikonov, S., Radhakrishnan, A., Zadeh, N. T., Balaji, V., Durachta, J., Dupuis, C., Menzel, R., Robinson, T., Underwood, S., Vahlenkamp, H., Dunne, K. A., Gauthier, P. P., Ginoux, P., Griffies, S. M., Hallberg, R. W., Harrison, M., Hurlin, W., Malyshev, S., Naik, V., Paulot, F., Paynter, D. J., Ploshay, J., Schwarzkopf, D. M., Seman, C. J., Shao, A., Silvers, L. G., Wyman, B., Zeng, Y., Adcroft, A. J., Dunne, J. P., Held, I. M., Krasting, J. P., Horowitz, L. W., Milly, P. C. ., Shevliakova, E., Winton, M. and Zhao, M.: NOAA-GFDL GFDL-CM4 model output prepared for CMIP6 CMIP historical, Earth System Grid Federation, , doi:https://doi.org/10.22033/ESGF/CMIP6.8594, 2018b.

Guo, H., John, J. G., Blanton, C., McHugh, C., Nikonov, S., Radhakrishnan, A., Zadeh, N. T., Balaji, V., Durachta, J., Dupuis, C., Menzel, R., Robinson, T., Underwood, S., Vahlenkamp, H., Dunne, K. A., Gauthier, P. P., Ginoux, P., Griffies, S. M., Hallberg, R., Harrison, M., Hurlin, W., Malyshev, S., Naik, V., Paulot, F., Paynter, D. J., Ploshay, J., Rand, K., Schwarzkopf, D. M., Seman, C. J., Shao, A., Silvers, L., Wyman, B., Zeng, Y., Adcroft, A., Dunne, J. P., Held, I. M., Krasting, J. P., Horowitz, L. W., Milly, C., Shevliakova, E., Winton, M., Zhao, M., Yan, X. and Zhang, R.: NOAA-GFDL GFDL-CM4 model output prepared for CMIP6 ScenarioMIP ssp245, Earth System Grid Federation, , doi:https://doi.org/10.22033/ESGF/CMIP6.9263, 2018c.

Guo, H., John, J. G., Blanton, C., McHugh, C., Nikonov, S., Radhakrishnan, A., Zadeh, N. T., Balaji, V., Durachta, J., Dupuis, C., Menzel, R., Robinson, T., Underwood, S., Vahlenkamp, H., Dunne, K. A., Gauthier, P. P., Ginoux, P., Griffies, S. M., Hallberg, R., Harrison, M., Hurlin, W., Malyshev, S., Naik, V., Paulot, F., Paynter, D. J., Ploshay, J., Rand, K., Schwarzkopf, D. M., Seman, C. J., Shao, A., Silvers, L., Wyman, B., Zeng, Y., Adcroft, A., Dunne, J. P., Held, I. M., Krasting, J. P., Horowitz, L. W., Milly, C., Shevliakova, E., Winton, M., Zhao, M., Yan, X. and Zhang, R.: NOAA-GFDL GFDL-CM4 model output prepared for CMIP6 ScenarioMIP ssp585, Earth System Grid Federation, , doi:https://doi.org/10.22033/ESGF/CMIP6.9268, 2018d.

Guo, H., John, J. G., Blanton, C., McHugh, C., Nikonov, S., Radhakrishnan, A., Zadeh, N. T., Balaji, V., Durachta, J., Dupuis, C., Menzel, R., Robinson, T., Underwood, S., Vahlenkamp, H., Dunne, K. A., Gauthier, P. P., Ginoux, P., Griffies, S. M., Hallberg, R., Harrison, M., Hurlin, W., Malyshev, S., Naik, V., Paulot, F., Paynter, D. J., Ploshay, J., Schwarzkopf, D. M., Seman, C. J., Shao, A., Silvers, L., Wyman, B., Zeng, Y., Adcroft, A., Dunne, J. P., Held, I. M., Krasting, J. P., Horowitz, L. W., Milly, P. C. ., Shevliakova, E., Winton, M. and Zhao, M.: NOAA-GFDL GFDL-CM4 piControl model output, Earth System Grid Federation, , doi:https://doi.org/10.22033/ESGF/CMIP6.8666, 2018e.

Hajima, T., Abe, M., Arakawa, O., Suzuki, T., Komuro, Y., Ogura, T., Ogochi, K., Watanabe, M., Yamamoto, A., Tatebe, H., Noguchi, M. A., Ohgaito, R., Ito, A., Yamazaki, D., Ito, A., Takata, K., Watanabe, S., Kawamiya, M. and Tachiiri, K.: MIROC MIROC-ES2L model output prepared for CMIP6 CMIP historical, Earth System Grid Federation, , doi:https://doi.org/10.22033/ESGF/CMIP6.5602, 2019.

Hope, A. P., Canty, T. P., Salawitch, R. J., Tribett, W. R. and Bennett, B. F.: Forecasting Global Warming, in Paris Climate Agreement: Beacon of Hope, pp. 51–114, Springer Climate., 2017.

Huang, W.: THU CIESM model output prepared for CMIP6 CMIP historical, Earth System Grid Federation, , doi:https://doi.org/10.22033/ESGF/CMIP6.7789, 2019a.

Huang, W.: THU CIESM model output prepared for CMIP6 ScenarioMIP ssp126, Earth System Grid Federation, , doi:https://doi.org/10.22033/ESGF/CMIP6.8857, 2019b.

Huang, W.: THU CIESM model output prepared for CMIP6 ScenarioMIP ssp245, Earth System Grid Federation, , doi:https://doi.org/10.22033/ESGF/CMIP6.8858, 2020a.

Huang, W.: THU CIESM model output prepared for CMIP6 ScenarioMIP ssp585, Earth System Grid Federation, , doi:https://doi.org/10.22033/ESGF/CMIP6.8863, 2020b.

Ishii, M., Fukuda, Y., Hirahara, S., Yasui, S., Suzuki, T. and Sato, K.: Accuracy of Global Upper Ocean Heat Content Estimation Expected from Present Observational Data Sets, Sci. Online Lett. Atmos., 13(0), 163–167, doi:10.2151/sola.2017-030, 2017.

John, J. G., Blanton, C., McHugh, C., Nikonov, S., Radhakrishnan, A., Rand, K., Vahlenkamp, H., Zadeh, N. T., Gauthier, P. P., Ginoux, P., Harrison, M., Horowitz, L. W., Malyshev, S., Naik, V., Paynter, D. J., Ploshay, J., Silvers, L. G., Stock, C., Winton, M., Zeng, Y. and Dunne, J. P.: NOAA-GFDL GFDL-ESM4 model output prepared for CMIP6 ScenarioMIP ssp119, Earth System Grid Federation, , doi:https://doi.org/10.22033/ESGF/CMIP6.8683, 2018a.

John, J. G., Blanton, C., McHugh, C., Nikonov, S., Radhakrishnan, A., Rand, K., Vahlenkamp, H., Zadeh, N. T., Gauthier, P. P., Ginoux, P., Harrison, M., Horowitz, L. W., Malyshev, S., Naik, V., Paynter, D. J., Ploshay, J., Silvers, L. G., Stock, C., Winton, M., Zeng, Y. and Dunne, J. P.: NOAA-GFDL GFDL-ESM4 model output prepared for CMIP6 ScenarioMIP ssp126, Earth System Grid Federation, , doi:https://doi.org/10.22033/ESGF/CMIP6.8684, 2018b.

John, J. G., Blanton, C., McHugh, C., Radhakrishnan, A., Rand, K., Vahlenkamp, H., Wilson, C., Zadeh, N. T., Gauthier, P. P., Dunne, J. P., Dussin, R., Horowitz, L. W., Lin, P., Malyshev, S., Naik, V., Ploshay, J., Silvers, L., Stock, C., Winton, M. and Zeng, Y.: NOAA-GFDL GFDL-ESM4 model output prepared for CMIP6 ScenarioMIP ssp245, Earth System Grid Federation, , doi:https://doi.org/10.22033/ESGF/CMIP6.8686, 2018c.

John, J. G., Blanton, C., McHugh, C., Nikonov, S., Radhakrishnan, A., Rand, K., Vahlenkamp, H., Zadeh, N. T., Gauthier, P. P., Ginoux, P., Harrison, M., Horowitz, L. W., Malyshev, S., Naik, V., Paynter, D. J., Ploshay, J., Silvers, L., Stock, C., Winton, M., Zeng, Y. and Dunne, J. P.: NOAA-GFDL GFDL-ESM4 model output prepared for CMIP6 ScenarioMIP ssp370, Earth System Grid Federation, , doi:https://doi.org/10.22033/ESGF/CMIP6.8691, 2018d.

John, J. G., Blanton, C., McHugh, C., Nikonov, S., Radhakrishnan, A., Rand, K., Vahlenkamp, H., Zadeh, N. T., Gauthier, P. P., Ginoux, P., Harrison, M., Horowitz, L. W., Malyshev, S., Naik, V., Paynter, D. J., Ploshay, J., Silvers, L., Stock, C., Winton, M., Zeng, Y. and Dunne, J. P.: NOAA-GFDL GFDL-ESM4 model output prepared for CMIP6 ScenarioMIP ssp585, Earth System Grid Federation, , doi:https://doi.org/10.22033/ESGF/CMIP6.8706, 2018e.

Jungclaus, J. H., Bittner, M., Wieners, K.-H., Wachsmann, F., Schupfner, M., Legutke, S., Giorgetta, M., Reick, C., Gayler, V., Haak, H., de Vrese, P., Raddatz, T., Esch, M., Mauritsen, T., von Storch, J.-S., Behrens, J., Brovkin, V., Claussen, M., Crueger, T., Fast, I., Fiedler, S., Hagemann, S., Hohenegger, C., Jahns, T., Kloster, S., Kinne, S., Lasslop, G., Kornblueh, L., Marotzke, J., Matai, D., Meraner, K., Mikolajewicz, U., Modali, K., Muller, W., Nabel, J., Notz, D., Peters, K., Pincus, R., Pohlmann, H., Pongratz, J., Rast, S., Schmidt, H., Schnur, R., Schulzweida, U., Six, K., Stevens, B., Voigt, A. and Roeckner, E.: MPI-M MPI-ESM1.2-HR model output prepared for CMIP6 CMIP historical, Earth System Grid Federation, , doi:https://doi.org/10.22033/ESGF/CMIP6.6594, 2019.

Kavvada, A., Ruiz-Barradas, A. and Nigam, S.: AMO's structure and climate footprint in observations and IPCC AR5 climate simulations, Clim. Dyn., 41(5–6), 1345–1364, doi:10.1007/s00382-013-1712-1, 2013.

Kelley, M., Schmidt, G., Nazarenko, L., Bauer, S., Ruedy, R., Russell, G., Ackerman, A., Aleinov, I., Bauer, M., Bleck, R., Canuto, V., Cesana, G., Cheng, Y., Clune, T., Cook, B., Cruz, C., Del Genio, A., Elsaesser, G., Faluvegi, G., Kiang, N., Kim, D., Lacis, A., Leboissetier, A., LeGrande, A., Lo, K., Marshall, J., Matthews, E., McDermid, S., Mezuman, K., Miller, R., Murray, L., Oinas, V., Orbe, C., Pérez García-Pando, C., Perlwitz, J., Puma, M., Rind, D., Romanou, A., Shindell, D., Sun, S., Tausnev, N., Tsigaridis, K., Tselioudis, G., Weng, E., Wu, J. and Yao, M.: GISS-E2.1: Configurations and Climatology, J. Adv. Model. Earth Syst., 2018(Phase 6), doi:10.1029/2019MS002025, 2020.

Krasting, J. P., John, J. G., Blanton, C., McHugh, C., Nikonov, S., Radhakrishnan, A., Rand, K., Zadeh, N. T., Balaji, V., Durachta, J., Dupuis, C., Menzel, R., Robinson, T., Underwood, S., Vahlenkamp, H., Dunne, K. A., Gauthier, P. P., Ginoux, P., Griffies, S. M., Hallberg, R., Harrison, M., Hurlin, W., Malyshev, S., Naik, V., Paulot, F., Paynter, D. J., Ploshay, J., Schwarzkopf, D. M., Seman, C. J., Silvers, L., Wyman, B., Zeng, Y., Adcroft, A., Dunne, J. P., Guo, H., Held, I. M., Horowitz, L. W., Milly, P. C. ., Shevliakova, E., Stock, C., Winton, M. and Zhao, M.: NOAA-GFDL GFDL-ESM4 model output prepared for CMIP6 CMIP abrupt-4xCO2, Earth System Grid Federation, , doi:https://doi.org/10.22033/ESGF/CMIP6.8489, 2018a.

Krasting, J. P., John, J. G., Blanton, C., McHugh, C., Nikonov, S., Radhakrishnan, A., Rand, K., Zadeh, N. T., Balaji, V., Durachta, J., Dupuis, C., Menzel, R., Robinson, T., Underwood, S., Vahlenkamp, H., Dunne, K. A., Gauthier, P. P., Ginoux, P., Griffies, S. M., Hallberg, R. W., Harrison, M., Hurlin, W., Malyshev, S., Naik, V., Paulot, F., Paynter, D. J., Ploshay, J., Schwarzkopf, D. M., Seman, C. J., Silvers, L. G., Wyman, B., Zeng, Y., Adcroft, A. J., Dunne, J. P., Guo, H., Held, I. M., Horowitz, L. W., Milly, P. C. ., Shevliakova, E., Stock, C., Winton, M. and Zhao, M.: NOAA-GFDL GFDL-ESM4 model output prepared for CMIP6 CMIP historical, Earth System Grid Federation, , doi:https://doi.org/10.22033/ESGF/CMIP6.8597, 2018b.

Krasting, J. P., John, J. G., Blanton, C., McHugh, C., Nikonov, S., Radhakrishnan, A., Rand, K., Zadeh, N. T., Balaji, V., Durachta, J., Dupuis, C., Menzel, R., Robinson, T., Underwood, S., Vahlenkamp, H., Dunne, K. A., Gauthier, P. P., Ginoux, P., Griffies, S. M., Hallberg, R., Harrison, M., Hurlin, W., Malyshev, S., Naik, V., Paulot, F., Paynter, D. J., Ploshay, J., Schwarzkopf, D. M., Seman, C. J., Silvers, L., Wyman, B., Zeng, Y., Adcroft, A., Dunne, J. P., Guo, H., Held, I. M., Horowitz, L. W., Milly, P. C. ., Shevliakova, E., Stock, C., Winton, M. and Zhao, M.: NOAA-GFDL GFDL-ESM4 model output prepared for CMIP6 CMIP piControl, Earth System Grid Federation, , doi:https://doi.org/10.22033/ESGF/CMIP6.8669, 2018c.

Lean, J. L. and Rind, D. H.: How natural and anthropogenic influences alter global and regional surface temperatures: 1889 to 2006, Geophys. Res. Lett., 35(18), 1–6, doi:10.1029/2008GL034864, 2008.

Levitus, S., Antonov, J. I., Boyer, T. P., Baranova, O. K., Garcia, H. E., Locarnini, R. A., Mishonov, A. V., Reagan, J. R., Seidov, D., Yarosh, E. S. and Zweng, M. M.: World ocean heat content and thermosteric sea level change (0-2000m), 1955-2010, Geophys. Res. Lett., 39(10), 1–5, doi:10.1029/2012GL051106, 2012.

Li, L.: CAS FGOALS-g3 model output prepared for CMIP6 CMIP historical, Earth System Grid Federation, , doi:https://doi.org/10.22033/ESGF/CMIP6.3356, 2019a.

Li, L.: CAS FGOALS-g3 model output prepared for CMIP6 ScenarioMIP ssp126, Earth System Grid Federation, , doi:https://doi.org/10.22033/ESGF/CMIP6.3465, 2019b.

Li, L.: CAS FGOALS-g3 model output prepared for CMIP6 ScenarioMIP ssp245, Earth System Grid Federation, , doi:https://doi.org/10.22033/ESGF/CMIP6.3469, 2019c.

Li, L.: CAS FGOALS-g3 model output prepared for CMIP6 ScenarioMIP ssp370, Earth System Grid Federation, , doi:https://doi.org/10.22033/ESGF/CMIP6.3480, 2019d.

Li, L.: CAS FGOALS-g3 model output prepared for CMIP6 ScenarioMIP ssp585, Earth System Grid Federation, ,

doi:https://doi.org/10.22033/ESGF/CMIP6.3503, 2019e.

Meinshausen, M., Smith, S. J., Calvin, K., Daniel, J. S., Kainuma, M. L. T., Lamarque, J., Matsumoto, K., Montzka, S. A., Raper, S. C. B., Riahi, K., Thomson, A., Velders, G. J. M. and van Vuuren, D. P. P.: The RCP greenhouse gas concentrations and their extensions from 1765 to 2300, Clim. Change, 109(1), 213–241, doi:10.1007/s10584-011-0156-z, 2011.

Morice, C. P., Kennedy, J. J., Rayner, N. A. and Jones, P. D.: Quantifying uncertainties in global and regional temperature change using an ensemble of observational estimates: The HadCRUT4 data set, J. Geophys. Res. Atmos., 117(8), 1–22, doi:10.1029/2011JD017187, 2012.

Murphy, J. M., Booth, B. B. B., Boulton, C. A., Clark, R. T., Harris, G. R., Lowe, J. A. and Sexton, D. M. H.: Transient climate changes in a perturbed parameter ensemble of emissions-driven earth system model simulations, Clim. Dyn., 43(9–10), 2855–2885, doi:10.1007/s00382-014-2097-5, 2014.

Myhre, G., Shindell, D., Bréon, F.-M., Collins, W., Fuglestvedt, J., Huang, J., Koch, D., Lamarque, J.-F., Lee, D., Mendoza, B., Nakajima, T., Robock, A., Stephens, G., Takemura, T. and Zhang, H.: Anthropogenic and Natural Radiative Forcing, Clim. Chang. 2013 Phys. Sci. Basis. Contrib. Work. Gr. I to Fifth Assess. Rep. Intergov. Panel Clim. Chang., 659–740, doi:10.1017/ CBO9781107415324.018, 2013.

NASA Goddard Institute for Space Studies (NASA/GISS): NASA-GISS GISS-E2.1G model output prepared for CMIP6 CMIP abrupt-4xCO2, Earth System Grid Federation, , doi:https://doi.org/10.22033/ESGF/CMIP6.6976, 2018a.

NASA Goddard Institute for Space Studies (NASA/GISS): NASA-GISS GISS-E2.1G model output prepared for CMIP6 CMIP historical, Earth System Grid Federation, , doi:https://doi.org/10.22033/ESGF/CMIP6.7127, 2018b.

NASA Goddard Institute for Space Studies (NASA/GISS): NASA-GISS GISS-E2.1G model output prepared for CMIP6 CMIP piControl, Earth System Grid Federation, , doi:https://doi.org/10.22033/ESGF/CMIP6.7380, 2018c.

NASA Goddard Institute for Space Studies (NASA/GISS): NASA-GISS GISS-E2.1H model output prepared for CMIP6 CMIP piControl, Earth System Grid Federation, , doi:https://doi.org/10.22033/ESGF/CMIP6.7381, 2018d.

NASA Goddard Institute for Space Studies (NASA/GISS): NASA-GISS GISS-E2-2-G model output prepared for CMIP6 CMIP abrupt-4xCO2, Earth System Grid Federation, , doi:https://doi.org/10.22033/ESGF/CMIP6.6978, 2019a.

NASA Goddard Institute for Space Studies (NASA/GISS): NASA-GISS GISS-E2.1H model output prepared for CMIP6 CMIP abrupt-4xCO2, Earth System Grid Federation, , doi:https://doi.org/10.22033/ESGF/CMIP6.6977, 2019b.

NASA Goddard Institute for Space Studies (NASA/GISS): NASA-GISS GISS-E2.1H model output prepared for CMIP6 CMIP historical, Earth System Grid Federation, , doi:https://doi.org/10.22033/ESGF/CMIP6.7128, 2019c.

NASA Goddard Institute for Space Studies (NASA/GISS): NASA-GISS GISS-E2.1G model output prepared for CMIP6 ScenarioMIP ssp126, Earth System Grid Federation, , doi:https://doi.org/10.22033/ESGF/CMIP6.7410, 2020a.

NASA Goddard Institute for Space Studies (NASA/GISS): NASA-GISS GISS-E2.1G model output prepared for CMIP6 ScenarioMIP ssp245, Earth System Grid Federation, , doi:https://doi.org/10.22033/ESGF/CMIP6.7415, 2020b.

NASA Goddard Institute for Space Studies (NASA/GISS): NASA-GISS GISS-E2.1G model output prepared for CMIP6 ScenarioMIP ssp370, Earth System Grid Federation, , doi:https://doi.org/10.22033/ESGF/CMIP6.7426, 2020c.

NASA Goddard Institute for Space Studies (NASA/GISS): NASA-GISS GISS-E2.1G model output prepared for CMIP6 ScenarioMIP ssp585, Earth System Grid Federation, , doi:https://doi.org/10.22033/ESGF/CMIP6.7460, 2020d.

Neubauer, D., Ferrachat, S., Siegenthaler-Le Drian, C., Stoll, J., Folini, D. S., Tegen, I., Wieners, K.-H., Mauritsen, T., Stemmler, I., Barthel, S., Bey, I., Daskalakis, M., Heinold, B., Kokkola, H., Partridge, D., Rast, S., Schmidt, H., Schutgens, N., Stanelle, T., Stier, P., Watson-Parrs, D. and Lohmann, U.: HAMMOZ-Consortium MPI-ESM1.2-HAM model output prepared for CMIP6 CMIP6 historical, Earth System Grid Federation, , doi:https://doi.org/10.22033/ESGF/CMIP6.5016, 2019.

Nicholls, Z., Meinshausen, M., Lewis, J., Corradi, M. R., Dorheim, K., Gasser, T., Gieseke, R., Hope, A. P., Leach, N. J., McBride, L. A., Quilcaille, Y., Rogelj, J., Salawitch, R. J., Samset, B. H., Sandstad, M., Shiklomanov, A., Skeie, R. B., Smith, C. J., Smith, S. J., Su, X., Tsutsui, J., Vega-Westhoff, B. and Woodward, D.: Reduced Complexity Model Intercomparison Project Phase 2 : Synthesising Earth system knowledge for probabilistic climate projections, Earth's Futur., doi:https://doi.org/10.1002/essoar.10504793.1, 2020.

Park, S. and Shin, J.: SNU SAM0-UNICON model output prepared for CMIP6 CMIP abrupt-4xCO2, Earth System Grid Federation, , doi:https://doi.org/10.22033/ESGF/CMIP6.7783, 2019a.

Park, S. and Shin, J.: SNU SAM0-UNICON model output prepared for CMIP6 CMIP historical, Earth System Grid Federation, , doi:https://doi.org/10.22033/ESGF/CMIP6.7789, 2019b.

Park, S. and Shin, J.: SNU SAM0-UNICON model output prepared for CMIP6 CMIP piControl, Earth System Grid Federation, , doi:https://doi.org/10.22033/ESGF/CMIP6.7791, 2019c.

Ridley, J., Menary, M., Kuhlbrodt, T., Andrews, M. and Andrews, T.: MOHC HadGEM3-GC31-LL model output prepared for CMIP6 CMIP piControl, Earth System Grid Federation, , doi:https://doi.org/10.22033/ESGF/CMIP6.6294, 2018.

Ridley, J., Menary, M., Kuhlbrodt, T., Andrews, M. and Andrews, T.: MOHC HadGEM3-GC31-LL model output prepared for CMIP6 CMIP, Earth System Grid Federation, , doi:https://doi.org/10.22033/ESGF/CMIP6.6109, 2019a.

Ridley, J., Menary, M., Kuhlbrodt, T., Andrews, M. and Andrews, T.: MOHC HadGEM3-GC31-LL model output prepared for CMIP6 CMIP abrupt-4xCO2, Earth System Grid Federation, , doi:https://doi.org/10.22033/ESGF/CMIP6.5839, 2019b.

Ridley, J., Menary, M., Kuhlbrodt, T., Andrews, M. and Andrews, T.: MOHC HadGEM3-GC31-MM model output prepared for CMIP6 CMIP historical, Earth System Grid Federation, , doi:https://doi.org/10.22033/ESGF/CMIP6.6112, 2019c.

Rong, X.: CAMS CAMS_CSM1.0 model output preapred for CMIP6 CMIP historical, Earth System Grid Federation, , doi:https://doi.org/10.22033/ESGF/CMIP6.9754, 2019a.

Rong, X.: CAMS CAMS-CSM1.0 model output prepared for CMIP6 ScenarioMIP ssp119, Earth System Grid Federation, , doi:https://doi.org/10.22033/ESGF/CMIP6.11045, 2019b.

Rong, X.: CAMS CAMS-CSM1.0 model output prepared for CMIP6 ScenarioMIP ssp126, Earth System Grid Federation, , doi:https://doi.org/10.22033/ESGF/CMIP6.11046, 2019c.

Rong, X.: CAMS CAMS-CSM1.0 model output prepared for CMIP6 ScenarioMIP ssp245, Earth System Grid

Federation, , doi:https://doi.org/10.22033/ESGF/CMIP6.11047, 2019d.

Rong, X.: CAMS CAMS-CSM1.0 model output prepared for CMIP6 ScenarioMIP ssp370, Earth System Grid Federation, , doi:https://doi.org/10.22033/ESGF/CMIP6.11048, 2019e.

Rong, X.: CAMS CAMS-CSM1.0 model output prepared for CMIP6 ScenarioMIP ssp585, Earth System Grid Federation, , doi:https://doi.org/10.22033/ESGF/CMIP6.11052, 2019f.

Schupfner, M., Wieners, K.-H., Wachsmann, F., Steger, C., Bittner, M., Jungclaus, J., Früh, B., Pankatz, K., Giorgetta, M., Reick, C., Legutke, S., Esch, M., Gayler, V., Haak, H., de Vrese, P., Raddatz, T., Mauritsen, T., von Storch, J.-S., Behrens, J., Brovkin, V., Claussen, M., Crueger, T., Fast, I., Fiedler, S., Hagemann, S., Hohenegger, C., Jahns, T., Kloster, S., Kinne, S., Lasslop, G., Kornblueh, L., Marotzke, J., Matei, D., Meraner, K., Mikolajewicz, U., Modali, K., Müller, W., Nabel, J., Notz, D., Peters, K., Pincus, R., Pohlmann, H., Pongratz, J., Rast, S., Schmidt, H., Schnur, R., Schulzweida, U., Six, K., Stevens, B., Voigt, A. and Roeckner, E.: DKRZ MIP-ESM1.2-HR model output prepared for CMIP6 ScenarioMIP ssp126, Earth System Grid Federation, , doi:https://doi.org/10.22033/ESGF/CMIP6.4397, 2019a.

Schupfner, M., Wieners, K.-H., Wachsmann, F., Steger, C., Bittner, M., Jungclaus, J., Früh, B., Pankatz, K., Giorgetta, M., Reick, C., Legutke, S., Esch, M., Gayler, V., Haak, H., de Vrese, P., Raddatz, T., Mauritsen, T., von Storch, J.-S., Behrens, J., Brovkin, V., Claussen, M., Crueger, T., Fast, I., Fiedler, S., Hagemann, S., Hohenegger, C., Jahns, T., Kloster, S., Kinne, S., Lasslop, G., Kornblueh, L., Marotzke, J., Matei, D., Meraner, K., Mikolajewicz, U., Modali, K., Müller, W., Nabel, J., Notz, D., Peters, K., Pincus, R., Pohlmann, H., Pongratz, J., Rast, S., Schmidt, H., Schnur, R., Schulzweida, U., Six, K., Stevens, B., Voigt, A. and Roeckner, E.: DKRZ MPI-ESM1.2-HR model output prepared for CMIP6 ScenarioMIP ssp245, Earth System Grid Federation, , doi:https://doi.org/10.22033/ESGF/CMIP6.4398, 2019b.

Schupfner, M., Wieners, K.-H., Wachsmann, F., Steger, C., Bittner, M., Jungclaus, J., Früh, B., Pankatz, K., Giorgetta, M., Reick, C., Legutke, S., Esch, M., Gayler, V., Haak, H., de Vrese, P., Raddatz, T., Mauritsen, T., von Storch, J.-S., Behrens, J., Brovkin, V., Claussen, M., Crueger, T., Fast, I., Fiedler, S., Hagemann, S., Hohenegger, C., Jahns, T., Kloster, S., Kinne, S., Lasslop, G., Kornblueh, L., Marotzke, J., Matei, D., Meraner, K., Mikolajewicz, U., Modali, K., Müller, W., Nabel, J., Notz, D., Peters, K., Pincus, R., Pohlmann, H., Pongratz, J., Rast, S., Schmidt, H., Schnur, R., Schulzweida, U., Six, K., Stevens, B., Voigt, A. and Roeckner, E.: DKRZ MPI-ESM1.2-HR model output prepared for CMIP6 ScenarioMIP ssp370, Earth System Grid Federation, , doi:https://doi.org/10.22033/ESGF/CMIP6.4399, 2019c.

Schupfner, M., Wieners, K.-H., Wachsmann, F., Steger, C., Bittner, M., Jungclaus, J., Früh, B., Pankatz, K., Giorgetta, M., Reick, C., Legutke, S., Esch, M., Gayler, V., Haak, H., de Vrese, P., Raddatz, T., Mauritsen, T., von Storch, J.-S., Behrens, J., Brovkin, V., Claussen, M., Crueger, T., Fast, I., Fiedler, S., Hagemann, S., Hohenegger, C., Jahns, T., Kloster, S., Kinne, S., Lasslop, G., Kornblueh, L., Marotzke, J., Matei, D., Meraner, K., Mikolajewicz, U., Modali, K., Müller, W., Nabel, J., Notz, D., Peters, K., Pincus, R., Pohlmann, H., Pongratz, J., Rast, S., Schmidt, H., Schnur, R., Schulzweida, U., Six, K., Stevens, B., Voigt, A. and Roeckner, E.: DKRZ MPI-ESM1.2-HR model output prepared for CMIP6 ScenarioMIP ssp585, Earth System Grid Federation, , doi:https://doi.org/10.22033/ESGF/CMIP6.4403, 2019d.

Schwartz, S. E.: Determination of Earth's Transient and Equilibrium Climate Sensitivities from Observations Over the Twentieth Century: Strong Dependence on Assumed Forcing, Surv. Geophys., 33(3–4), 745–777, doi:10.1007/s10712-012-9180-4, 2012.

Seferian, R.: CNRM-CERFACS CNRM-ESM2-1 model output prepared for CMIP6 CMIP historical, Earth System Grid Federation, , doi:https://doi.org/10.22033/ESGF/CMIP6.4068, 2018.

Seland, Ø., Bentsen, M., Oliviè, D. J. L., Toniazzo, T., Gjermundsen, A., Graff, L. S., Debernard, J. B., Gupta, A. K., He, Y., Kirkevåg, A., Schwinger, J., Tjiputra, J., Aas, K. S., Bethke, I., Fan, Y., Griesfeller, J., Grini, A., Guo, C., Ilicak, M., Karset, I. H. H., Landgren, O. A., Liakka, J., Moseid, K. O., Nummelin, A., Spensberger, C., Tang, H., Zhang, Z., Heinze, C., Iversen, T. and Schulz, M.: NCC NorESM2-LM model output prepared

for CMIP6 CMIP abrupt-4xCO2, Earth System Grid Federation, , doi:https://doi.org/10.22033/ESGF/CMIP6.7836, 2019a.

Seland, Ø., Bentsen, M., Oliviè, D. J. L., Toniazzo, T., Gjermundsen, A., Graff, L. S., Debernard, J. B., Gupta, A. K., He, Y., Kirkevåg, A., Schwinger, J., Tjiputra, J., Aas, K. S., Bethke, I., Fan, Y., Griesfeller, J., Grini, A., Guo, C., Ilicak, M., Karset, I. H. H., Landgren, O. A., Liakka, J., Moseid, K. O., Nummelin, A., Spensberger, C., Tang, H., Zhang, Z., Heinze, C., Iversen, T. and Schulz, M.: NCC NorESM2-LM model output prepared for CMIP6 CMIP piControl, Earth System Grid Federation, , doi:https://doi.org/10.22033/ESGF/CMIP6.8217, 2019b.

Seland, Ø., Bentsen, M., Oliviè, D. J. L., Toniazzo, T., Gjermundsen, A., Graff, L. S., Debernard, J. B., Gupta, A. K., He, Y., Kirkevåg, A., Schwinger, J., Tjiputra, J., Aas, K. S., Bethke, I., Fan, Y., Griesfeller, J., Grini, A., Guo, C., Ilicak, M., Karset, I. H. H., Landgren, O. A., Liakka, J., Moseid, K. O., Nummelin, A., Spensberger, C., Tang, H., Zhang, Z., Heinze, C., Iversen, T. and Schulz, M.: NCC NorESM2-LM model output prepared for CMIP6 ScenarioMIP ssp126, Earth System Grid Federation, , doi:https://doi.org/10.22033/ESGF/CMIP6.8248, 2019c.

Seland, Ø., Bentsen, M., Oliviè, D. J. L., Toniazzo, T., Gjermundsen, A., Graff, L. S., Debernard, J. B., Gupta, A. K., He, Y., Kirkevåg, A., Schwinger, J., Tjiputra, J., Aas, K. S., Bethke, I., Fan, Y., Griesfeller, J., Grini, A., Guo, C., Ilicak, M., Karset, I. H. H., Landgren, O. A., Liakka, J., Moseid, K. O., Nummelin, A., Spensberger, C., Tang, H., Zhang, Z., Heinze, C., Iversen, T. and Schulz, M.: NCC NorESM2-LM model output prepared for CMIP6 ScenarioMIP ssp245, Earth System Grid Federation, , doi:https://doi.org/10.22033/ESGF/CMIP6.8253, 2019d.

Seland, Ø., Bentsen, M., Oliviè, D. J. L., Toniazzo, T., Gjermundsen, A., Graff, L. S., Debernard, J. B., Gupta, A. K., He, Y., Kirkevåg, A., Schwinger, J., Tjiputra, J., Aas, K. S., Bethke, I., Fan, Y., Griesfeller, J., Grini, A., Guo, C., Ilicak, M., Karset, I. H. H., Landgren, O. A., Liakka, J., Moseid, K. O., Nummelin, A., Spensberger, C., Tang, H., Zhang, Z., Heinze, C., Iversen, T. and Schulz, M.: NCC NorESM2-LM model output prepared for CMIP6 ScenarioMIP ssp370, Earth System Grid Federation, , doi:https://doi.org/10.22033/ESGF/CMIP6.8268, 2019e.

Seland, Ø., Bentsen, M., Oliviè, D. J. L., Toniazzo, T., Gjermundsen, A., Graff, L. S., Debernard, J. B., Gupta, A. K., He, Y., Kirkevåg, A., Schwinger, J., Tjiputra, J., Aas, K. S., Bethke, I., Fan, Y., Griesfeller, J., Grini, A., Guo, C., Ilicak, M., Karset, I. H. H., Landgren, O. A., Liakka, J., Moseid, K. O., Nummelin, A., Spensberger, C., Tang, H., Zhang, Z., Heinze, C., Iversen, T. and Schulz, M.: NCC NorESM2-LM model output prepared for CMIP6 ScenarioMIP ssp585, Earth System Grid Federation, , doi:https://doi.org/10.22033/ESGF/CMIP6.8319, 2019f.

Seland, Ø., Bentsen, M., Oliviè, D. J. L., Toniazzo, T., Gjermundsen, A., Graff, L. S., Debernard, J. B., Gupta, A. K., He, Y., Kirkevåg, A., Schwinger, J., Tjiputra, J., Aas, K. S., Bethke, I., Fan, Y., Griesfeller, J., Grini, A., Guo, C., Ilicak, M., Karset, I. H. H., Landgren, O. A., Liakka, J., Moseid, K. O., Nummelin, A., Spensberger, C., Tang, H., Zhang, Z., Heinze, C., Iversen, T. and Schulz, M.: NCC NorESM2-LM output prepared for CMIP6 CMIP historical, Earth System Grid Federation, , doi:https://doi.org/10.22033/ESGF/CMIP6.8036, 2019g.

Semmler, T., Danilov, S., Rackow, T., Sidorenko, D., Barbi, D., Hegewald, J., Sein, D., Wang, Q. and Jung, T.: AWI AWI-CM1.1MR model output prepared for CMIP6 CMIP historical, Earth System Grid Federation, , doi:https://doi.org/10.22033/ESGF/CMIP6.2686, 2018a.

Semmler, T., Danilov, S., Rackow, T., Sidorenko, D., Barbi, D., Hegewald, J., Pradhan, H. K., Sein, D., Wang, Q. and Jung, T.: AWI AWI-CM1.1MR model output prepared for CMIP6 ScenarioMIP ssp126, Earth System Grid Federation, , doi:https://doi.org/10.22033/ESGF/CMIP6.2796, 2018b.

Semmler, T., Danilov, S., Rackow, T., Sidorenko, D., Barbi, D., Hegewald, J., Pradhan, H. K., Sein, D., Wang, Q. and Jung, T.: AWI AWI-CM1.1MR model output prepared for CMIP6 ScenarioMIP ssp246, Earth System

Grid Federation, , doi:https://doi.org/10.22033/ESGF/CMIP6.2800, 2018c.

Semmler, T., Danilov, S., Rackow, T., Sidorenko, D., Barbi, D., Hegewald, J., Pradhan, H. K., Sein, D., Wang, Q. and Jung, T.: AWI AWI-CM1.1MR model output prepared for CMIP6 ScenarioMIP ssp370, Earth System Grid Federation, , doi:https://doi.org/10.22033/ESGF/CMIP6.2803, 2019a.

Semmler, T., Danilov, S., Rackow, T., Sidorenko, D., Barbi, D., Hegewald, J., Pradhan, H. K., Sein, D., Wang, Q. and Jung, T.: AWI AWI-CM1.1MR model output prepared for CMIP6 ScenarioMIP ssp585, Earth System Grid Federation, , doi:https://doi.org/10.22033/ESGF/CMIP6.2817, 2019b.

Shiogama, H., Abe, M. and Tatebe, H.: MIROC MIROC6 model output prepared for CMIP6 ScenarioMIP ssp119, Earth System Grid Federation, , doi:https://doi.org/10.22033/ESGF/CMIP6.5741, 2019a.

Shiogama, H., Abe, M. and Tatebe, H.: MIROC MIROC6 model output prepared for CMIP6 ScenarioMIP ssp126, Earth System Grid Federation, , doi:https://doi.org/10.22033/ESGF/CMIP6.5743, 2019b.

Shiogama, H., Abe, M. and Tatebe, H.: MIROC MIROC6 model output prepared for CMIP6 ScenarioMIP ssp245, Earth System Grid Federation, , doi:https://doi.org/10.22033/ESGF/CMIP6.5746, 2019c.

Shiogama, H., Abe, M. and Tatebe, H.: MIROC MIROC6 model output prepared for CMIP6 ScenarioMIP ssp370, Earth System Grid Federation, , doi:https://doi.org/10.22033/ESGF/CMIP6.5752, 2019d.

Shiogama, H., Abe, M. and Tatebe, H.: MIROC MIROC6 model output prepared for CMIP6 ScenarioMIP ssp434, Earth System Grid Federation, , doi:https://doi.org/10.22033/ESGF/CMIP6.5764, 2019e.

Shiogama, H., Abe, M. and Tatebe, H.: MIROC MIROC6 model output prepared for CMIP6 ScenarioMIP ssp460, Earth System Grid Federation, , doi:https://doi.org/10.22033/ESGF/CMIP6.5766, 2019f.

Shiogama, H., Abe, M. and Tatebe, H.: MIROC MIROC6 model output prepared for CMIP6 ScenarioMIP ssp585, Earth System Grid Federation, , doi:https://doi.org/10.22033/ESGF/CMIP6.5771, 2019g.

Song, Z., Qiao, F., Bao, Y., Shu, Q., Song, Y. and Yang, X.: FIO-QLNM FIO-ESM2.0 model output prepared for CMIP6 CMIP historical, Earth System Grid Federation, , doi:https://doi.org/10.22033/ESGF/CMIP6.9199, 2019a.

Song, Z., Qiao, F., Bao, Y., Shu, Q., Song, Y. and Yang, X.: FIO-QLNM FIO-ESM2.0 model output prepared for CMIP6 ScenarioMIP ssp126, Earth System Grid Federation, , doi:https://doi.org/10.22033/ESGF/CMIP6.9208, 2019b.

Song, Z., Qiao, F., Bao, Y., Shu, Q., Song, Y. and Yang, X.: FIO-QLNM FIO-ESM2.0 model output prepared for CMIP6 ScenarioMIP ssp245, Earth System Grid Federation, , doi:https://doi.org/10.22033/ESGF/CMIP6.9209, 2019c.

Song, Z., Qiao, F., Bao, Y., Shu, Q., Song, Y. and Yang, X.: FIO-QLNM FIO-ESM2.0 model output prepared for CMIP6 ScenarioMIP ssp585, Earth System Grid Federation, , doi:https://doi.org/10.22033/ESGF/CMIP6.9214, 2019d.

Steger, C., Schupfner, M., Wieners, K.-H., Wachsmann, F., Bittner, M., Jungclaus, J., Früh, B., Pankatz, K., Giorgetta, M., Reick, C., Legutke, S., Esch, M., Gayler, V., Haak, H., de Vrese, P., Raddatz, T., Mauritsen, T., von Storch, J.-S., Behrens, J., Brovkin, V., Claussen, M., Crueger, T., Fast, I., Fiedler, S., Hagemann, S., Hohenegger, C., Jahns, T., Kloster, S., Kinne, S., Lasslop, G., Kornblueh, L., Marotzke, J., Matei, D., Meraner, K., Mikolajewicz, U., Modali, K., Müller, W., Nabel, J., Notz, D., Peters, K., Pincus, R., Pohlmann, H., Pongratz, J., Rast, S., Schmidt, H., Schnur, R., Schulzweida, U., Ix, K., Stevens, B., Voigt, A. and Roeckner, E.: DWD MPI-ESM1.2-HR model output prepared for CMIP6 ScenarioMIP ssp585, Earth System Grid Federation, , doi:https://doi.org/10.22033/ESGF/CMIP6.4479, 2019.

Stouffer, R. J.: UA MCM-UA-1-0 model output prepared for CMIP6 CMIP abrupt-4xCO2, Earth System Grid Federation, , doi:https://doi.org/10.22033/ESGF/CMIP6.8882, 2019a.

Stouffer, R. J.: UA MCM-UA-1-0 model output prepared for CMIP6 CMIP historical, Earth System Grid Federation, , doi:https://doi.org/10.22033/ESGF/CMIP6.8888, 2019b.

Stouffer, R. J.: UA MCM-UA-1-0 model output prepared for CMIP6 CMIP piControl, Earth System Grid Federation, , doi:https://doi.org/10.22033/ESGF/CMIP6.8890, 2019c.

Stouffer, R. J.: UA MCM-UA-1-0 model output prepared for CMIP6 ScenarioMIP ssp245, Earth System Grid Federation, , doi:https://doi.org/10.22033/ESGF/CMIP6.13896, 2019d.

Stouffer, R. J.: UA MCM-UA-1-0 model output prepared for CMIP6 ScenarioMIP ssp370, Earth System Grid Federation, , doi:https://doi.org/10.22033/ESGF/CMIP6.13897, 2019e.

Stouffer, R. J.: UA MCM-UA-1-0 model output prepared for CMIP6 ScenarioMIP ssp585, Earth System Grid Federation, , doi:https://doi.org/10.22033/ESGF/CMIP6.13901, 2019f.

Stouffer, R. J.: UA MCM-UA-1.0 model output prepared for CMIP6 ScenarioMIP ssp126, Earth System Grid Federation, , doi:https://doi.org/10.22033/ESGF/CMIP6.13895, 2019g.

Swart, N. C., Jason, N. ., Kharin, V. V., Lazare, M., Scinocca, J. F., Gillett, N. P., Anstey, J., Arora, V. K., Christian, J. R., Jiao, Y., Lee, W. G., Majaess, F., Saenko, O. A., Seiler, C., Seinen, C., Shao, A., Solheim, L., von Salzen, K., Yang, D., Winter, B. and Sigmond, M.: CCCma CanESM5-CanOE model output prepared for CMIP6 CMIP, Earth System Grid Federation, , doi:https://doi.org/10.22033/ESGF/CMIP6.10260, 2019a.

Swart, N. C., Cole, J. N. S., Kharin, V. V., Lazare, M., Scinocca, J. F., Gillett, N. P., Anstey, J., Arora, V. K., Christian, J. R., Jiao, Y., Lee, W. G., Majaess, F., Saenko, O. A., Seiler, C., Seinen, C., Shao, A., Solheim, L., von Salzen, K., Yang, D., Winter, B. and Sigmond, M.: CCCma CaneSM5-CanOE model output prepared for CMIP6 ScenarioMIP ssp126, Earth System Grid Federation, , doi:https://doi.org/10.22033/ESGF/CMIP6.10269, 2019b.

Swart, N. C., Cole, J. N. S., Kharin, V. V., Lazare, M., Scinocca, J. F., Gillett, N. P., Anstey, J., Arora, V., Christian, J. R., Jiao, Y., Lee, W. G., Majaess, F., Saenko, O. A., Seiler, C., Seinen, C., Shao, A., Solheim, L., von Salzen, K., Yang, D., Winter, B. and Sigmond, M.: CCCma CanESM5-CanOE model output prepared for CMIP6 ScenarioMIP ssp245, Earth System Grid Federation, , doi:https://doi.org/10.22033/ESGF/CMIP6.10270, 2019c.

Swart, N. C., Cole, J. N. S., Kharin, V. V., Lazare, M., Scinocca, J. F., Gillett, N. P., Anstey, J., Arora, V., Christian, J. R., Jiao, Y., Lee, W. G., Majaess, F., Saenko, O. A., Seiler, C., Seinen, C., Shao, A., Solheim, L., von Salzen, K., Yang, D., Winter, B. and Sigmond, M.: CCCma CanESM5-CanOE model output prepared for CMIP6 ScenarioMIP ssp370, Earth System Grid Federation, , doi:https://doi.org/10.22033/ESGF/CMIP6.10271, 2019d.

Swart, N. C., Cole, J. N. S., Kharin, V. V., Lazare, M., Scinocca, J. F., Gillett, N. P., Anstey, J., Arora, V., Christian, J. R., Jiao, Y., Lee, W. G., Majaess, F., Saenko, O. A., Seiler, C., Seinen, C., Shao, A., Solheim, L., von Salzen, K., Yang, D., Winter, B. and Sigmond, M.: CCCma CanESM5-CanOE model output prepared for CMIP6 ScenarioMIP ssp585, Earth System Grid Federation, , doi:https://doi.org/10.22033/ESGF/CMIP6.10276, 2019e.

Swart, N. C., Cole, J. N. S., Kharin, V. V., Lazare, M., Scinocca, J. F., Gillett, N. P., Anstey, J., Arora, V., Christian, J. R., Jiao, Y., Lee, W. G., Majaess, F., Saenko, O. A., Seiler, C., Seinen, C., Shao, A., Solheim, L., von Salzen, K., Yang, D., Winter, B. and Sigmond, M.: CCCma CanESM5 model output prepared for CMIP6 CMIP abrupt-4xCO2, Earth System Grid Federation, , doi:https://doi.org/10.22033/ESGF/CMIP6.3532, 2019f.

Swart, N. C., Cole, J. N. S., Kharin, V. V., Lazare, M., Scinocca, J. F., Gillett, N. P., Anstey, J., Arora, V. K., Christian, J. R., Jiao, Y., Lee, W. G., Majaess, F., Saenko, O. A., Seiler, C., Seinen, C., Shao, A., Solheim, L., von Salzen, K., Yang, D., Winter, B. and Sigmond, M.: CCCma CanESM5 model output prepared for CMIP6 CMIP historical, Earth System Grid Federation, , doi:https://doi.org/10.22033/ESGF/CMIP6.3610, 2019g.

Swart, N. C., Cole, J. N. S., Kharin, V. V., Lazare, M., Scinocca, J. F., Gillett, N. P., Anstey, J., Arora, V., Christian, J. R., Jiao, Y., Lee, W. G., Majaess, F., Saenko, O. A., Seiler, C., Seinen, C., Shao, A., Solheim, L., von Salzen, K., Yang, D., Winter, B. and Sigmond, M.: CCCma CanESM5 model output prepared for CMIP6 CMIP piControl, Earth System Grid Federation, , doi:https://doi.org/10.22033/ESGF/CMIP6.3673, 2019h.

Swart, N. C., Cole, J. N. S., Kharin, V. V., Lazare, M., Scinocca, J. F., Gillett, N. P., Anstey, J., Arora, V. K., Christian, J. R., Jiao, Y., Lee, W. G., Majaess, F., Saenko, O. A., Seiler, C., Seinen, C., Shao, A., Solheim, L., von Salzen, K., Yang, D., Winter, B. and Sigmond, M.: CCCma CanESM5 model output prepared for CMIP6 ScenarioMIP ssp119, Earth System Grid Federation, , doi:https://doi.org/10.22033/ESGF/CMIP6.3682, 2019i.

Swart, N. C., Cole, J. N. S., Jason, N. ., Kharin, V. V., Lazare, M., Scinocca, J. F., Gillett, N. P., Anstey, J., Arora, V. K., Christian, J. R., Jiao, Y., Lee, W. G., Majaess, F., Saenko, O. A., Seiler, C., Seinen, C., Shao, A., Solheim, L., von Salzen, K., Yang, D., Winter, B. and Sigmond, M.: CCCma CanESM5 model output prepared for CMIP6 ScenarioMIP ssp126, Earth System Grid Federation, , doi:https://doi.org/10.22033/ESGF/CMIP6.3683, 2019j.

Swart, N. C., Cole, J. N. S., Kharin, V. V., Lazare, M., Scinocca, J. F., Gillett, N. P., Anstey, J., Arora, V., Christian, J. R., Jiao, Y., Lee, W. G., Majaess, F., Saenko, O. A., Seiler, C., Seinen, C., Shao, A., Solheim, L., von Salzen, K., Yang, D., Winter, B. and Sigmond, M.: CCCma CanESM5 model output prepared for CMIP6 ScenarioMIP ssp245, Earth System Grid Federation, , doi:https://doi.org/10.22033/ESGF/CMIP6.3685, 2019k.

Swart, N. C., Cole, J. N. S., Kharin, V. V., Lazare, M., Scinocca, J. F., Gillett, N. P., Anstey, J., Arora, V., Christian, J. R., Jiao, Y., Lee, W. G., Majaess, F., Saenko, O. A., Seiler, C., Seinen, C., Shao, A., Solheim, L., von Salzen, K., Yang, D., Winter, B. and Sigmond, M.: CCCma CanESM5 model output prepared for CMIP6 ScenarioMIP ssp370, Earth System Grid Federation, , doi:https://doi.org/10.22033/ESGF/CMIP6.3690, 2019l.

Swart, N. C., Cole, J. N. S., Kharin, V. V., Lazare, M., Scinocca, J. F., Gillett, N. P., Anstey, J., Arora, V., Christian, J. R., Jiao, Y., Lee, W. G., Majaess, F., Saenko, O. A., Seiler, C., Seinen, C., Shao, A., Solheim, L., von Salzen, K., Yang, D., Winter, B. and Sigmond, M.: CCCma CanESM5 model output prepared for CMIP6 ScenarioMIP ssp434, Earth System Grid Federation, , doi:https://doi.org/10.22033/ESGF/CMIP6.3692, 2019m.

Swart, N. C., Cole, J. N. S., Kharin, V. V., Lazare, M., Scinocca, J. F., Gillett, N. P., Anstey, J., Arora, V., Christian, J. R., Jiao, Y., Lee, W. G., Majaess, F., Saenko, O. A., Seiler, C., Seinen, C., Shao, A., Solheim, L., von Salzen, K., Yang, D., Winter, B. and Sigmond, M.: CCCma CanESM5 model output prepared for CMIP6 ScenarioMIP ssp460, Earth System Grid Federation, , doi:https://doi.org/10.22033/ESGF/CMIP6.3693, 2019n.

Swart, N. C., Cole, J. N. S., Kharin, V. V., Lazare, M., Scinocca, J. F., Gillett, N. P., Anstey, J., Arora, V., Christian, J. R., Jiao, Y., Lee, W. G., Majaess, F., Saenko, O. A., Seiler, C., Seinen, C., Shao, A., Solheim, L., von Salzen, K., Yang, D., Winter, B. and Sigmond, M.: CCCma CanESM5 model output prepared for CMIP6 ScenarioMIP ssp585, Earth System Grid Federation, , doi:https://doi.org/10.22033/ESGF/CMIP6.3696, 2019o.

Tachiiri, K., Abe, M., Hajima, T., Arakawa, O., Suzuki, T., Komuro, Y., Ogochi, K., Watanabe, M., Yamamoto, A., Tatebe, H., Noguchi, M. A., Ohgaito, R., Ito, A., Yamazaki, D., Ito, A., Takata, K., Watanabe, S. and

Kawamiya, M.: MIROC MIROC-ES2L model output prepared for CMIP6 ScenarioMIP ssp119, Earth System Grid Federation, , doi:https://doi.org/10.22033/ESGF/CMIP6.5740, 2019a.

Tachiiri, K., Abe, M., Hajima, T., Arakawa, O., Suzuki, T., Komuro, Y., Ogochi, K., Watanabe, M., Yamamoto, A., Tatebe, H., Noguchi, M. A., Ohgaito, R., Ito, A., Yamazaki, D., Ito, A., Takata, K., Watanabe, S. and Kawamiya, M.: MIROC MIROC-ES2L model output prepared for CMIP6 ScenarioMIP ssp126, , doi:https://doi.org/10.22033/ESGF/CMIP6.5742, 2019b.

Tachiiri, K., Abe, M., Hajima, T., Arakawa, O., Suzuki, T., Komuro, Y., Ogochi, K., Watanabe, M., Yamamoto, A., Tatebe, H., Noguchi, M. A., Ohgaito, R., Ito, A., Yamazaki, D., Ito, A., Takata, K., Watanabe, S. and Kawamiya, M.: MIROC MIROC-ES2L model output prepared for CMIP6 ScenarioMIP ssp245, Earth System Grid Federation, , doi:https://doi.org/10.22033/ESGF/CMIP6.5745, 2019c.

Tachiiri, K., Abe, M., Hajima, T., Arakawa, O., Suzuki, T., Komuro, Y., Ogochi, K., Watanabe, M., Yamamoto, A., Tatebe, H., Noguchi, M. A., Ohgaito, R., Ito, A., Yamazaki, D., Ito, A., Takata, K., Watanabe, S. and Kawamiya, M.: MIROC MIROC-ES2L model output prepared for CMIP6 ScenarioMIP ssp370, Earth System Grid Federation, , doi:https://doi.org/10.22033/ESGF/CMIP6.5751, 2019d.

Tachiiri, K., Abe, M., Hajima, T., Arakawa, O., Suzuki, T., Komuro, Y., Ogochi, K., Watanabe, M., Yamamoto, A., Tatebe, H., Noguchi, M. A., Ohgaito, R., Ito, A., Yamazaki, D., Ito, A., Takata, K., Watanabe, S. and Kawamiya, M.: MIROC MIROC-ES2L model output prepared for CMIP6 ScenarioMIP ssp585, Earth System Grid Federation, , doi:https://doi.org/10.22033/ESGF/CMIP6.5770, 2019e.

Tang, Y., Rumbold, S., Ellis, R., Kelley, D., Mulcahy, J., Sellar, A., Walton, J. and Jones, C.: MOHC UKESM1.0-LL model output prepared for CMIP6 CMIP abrupt-4xCO2, Earth System Grid Federation, , doi:https://doi.org/10.22033/ESGF/CMIP6.5843, 2019a.

Tang, Y., Rumbold, S., Ellis, R., Kelley, D., Mulcahy, J., Sellar, A., Walton, J. and Jones, C.: MOHC UKESM1.0-LL model output prepared for CMIP6 CMIP piControl, Earth System Grid Federation, , doi:https://doi.org/10.22033/ESGF/CMIP6.6298, 2019b.

Tang, Y., Rumbold, S., Ellis, R., Kelley, D., Mulcahy, J., Sellar, A., Walton, J. and Jones, C.: MOHC UKESM1.0LL model output prepared for CMIP6 CMIP historical, Earth System Grid Federation, , doi:https://doi.org/10.22033/ESGF/CMIP6.6113, 2019c.

Tatebe, H. and Watanabe, M.: MIROC MIROC6 model output prepared for CMIP6 CMIP abrupt-4xCO2, Earth System Grid Federation, , doi:https://doi.org/10.22033/ESGF/CMIP6.5411, 2018a.

Tatebe, H. and Watanabe, M.: MIROC MIROC6 model output prepared for CMIP6 CMIP historical, Earth System Grid Federation, , doi:https://doi.org/10.22033/ESGF/CMIP6.5603, 2018b.

Tatebe, H. and Watanabe, M.: MIROC MIROC6 model output prepared for CMIP6 CMIP piControl, Earth System Grid Federation, , doi:https://doi.org/10.22033/ESGF/CMIP6.5711, 2018c.

Thompson, D. W. J., Wallace, J. M., Jones, P. D. and Kennedy, J. J.: Identifying signatures of natural climate variability in time series of global-mean surface temperature: Methodology and insights, J. Clim., 22(22), 6120–6141, doi:10.1175/2009JCLI3089.1, 2009.

Tokarska, K. B., Stolpe, M. B., Sippel, S., Fischer, E. M., Smith, C. J., Lehner, F. and Knutti, R.: Past warming trend constrains future warming in CMIP6 models, Sci. Adv., 6(12), 1–13, doi:10.1126/sciadv.aaz9549, 2020.

Voldoire, A.: CMIP6 simulations of the CNRM-CERFACS based on CNRM-CM6-1 model for CMIP experiment historical, Earth System Grid Federation, , doi:https://doi.org/10.22033/ESGF/CMIP6.4066, 2018.

Voldoire, A.: CNRM-CERFACS CNRM-CM6-1-HR model output prepared for CMIP6 ScenarioMIP ssp245, Earth

System Grid Federation, , doi:https://doi.org/10.22033/ESGF/CMIP6.4190, 2019a.

Voldoire, A.: CNRM-CERFACS CNRM-CM6-1-HR model output prepared for CMIP6 ScenarioMIP ssp585, Earth System Grid Federation, , doi:https://doi.org/10.22033/ESGF/CMIP6.4225, 2019b.

Voldoire, A.: CNRM-CERFACS CNRM-CM6-1 model output prepared for CMIP6 ScenarioMIP for ssp245, Earth System Grid Federation, , doi:https://doi.org/10.22033/ESGF/CMIP6.4189, 2019c.

Voldoire, A.: CNRM-CERFACS CNRM-CM6-1 model output prepared for CMIP6 ScenarioMIP ssp126, Earth System Grid Federation, , doi:https://doi.org/10.22033/ESGF/CMIP6.4184, 2019d.

Voldoire, A.: CNRM-CERFACS CNRM-CM6-1 model output prepared for CMIP6 ScenarioMIP ssp370, Earth System Grid Federation, , doi:https://doi.org/10.22033/ESGF/CMIP6.4197, 2019e.

Voldoire, A.: CNRM-CERFACS CNRM-CM6-1 model output prepared for CMIP6 ScenarioMIP ssp585, Earth System Grid Federation, , doi:https://doi.org/10.22033/ESGF/CMIP6.4224, 2019f.

Voldoire, A.: CNRM-CERFACS CNRM-ESM2-1 model output prepared for CMIP6 ScenarioMIP ssp119, Earth System Grid Federation, , doi:https://doi.org/10.22033/ESGF/CMIP6.4182, 2019g.

Voldoire, A.: CNRM-CERFACS CNRM-ESM2-1 model output prepared for CMIP6 ScenarioMIP ssp126, Earth System Grid Federation, , doi:https://doi.org/10.22033/ESGF/CMIP6.4186, 2019h.

Voldoire, A.: CNRM-CERFACS CNRM-ESM2-1 model output prepared for CMIP6 ScenarioMIP ssp245, Earth System Grid Federation, , doi:https://doi.org/10.22033/ESGF/CMIP6.4191, 2019i.

Voldoire, A.: CNRM-CERFACS CNRM-ESM2-1 model output prepared for CMIP6 ScenarioMIP ssp370, Earth System Grid Federation, , doi:https://doi.org/10.22033/ESGF/CMIP6.4199, 2019j.

Voldoire, A.: CNRM-CERFACS CNRM-ESM2-1 model output prepared for CMIP6 ScenarioMIP ssp434, Earth System Grid Federation, , doi:https://doi.org/10.22033/ESGF/CMIP6.4213, 2019k.

Voldoire, A.: CNRM-CERFACS CNRM-ESM2-1 model output prepared for CMIP6 ScenarioMIP ssp460, Earth System Grid Federation, , doi:https://doi.org/10.22033/ESGF/CMIP6.4217, 2019l.

Voldoire, A.: CNRM-CERFACS CNRM-CM6-1-HR model output prepared for CMIP6 ScenarioMIP ssp126, Earth System Grid Federation, , doi:https://doi.org/10.22033/ESGF/CMIP6.4185, 2020a.

Voldoire, A.: CNRM-CERFACS CNRM-CM6-1-HR model output prepared for CMIP6 ScenarioMIP ssp370, Earth System Grid Federation, , doi:https://doi.org/10.22033/ESGF/CMIP6.4198, 2020b.

Volodin, E., Mortikov, E., Gritsun, A., Lykossov, V., Galin, V., Diansky, N., Gusev, A., Kostrykin, S., Iakovlev, N., Shestakova, A. and Emelina, S.: INM INM-CM4-8 model output prepared for CMIP6 CMIP abrupt-4xCO2, Earth System Grid Federation, , doi:https://doi.org/10.22033/ESGF/CMIP6.4931, 2019a.

Volodin, E., Mortikov, E., Gritsun, A., Lykossov, V., Galin, V., Diansky, N., Gusev, A., Kostrykin, S., Iakovlev, N., Shestakova, A. and Emelina, S.: INM INM-CM4-8 model output prepared for CMIP6 CMIP historical, Earth System Grid Federation, , doi:https://doi.org/10.22033/ESGF/CMIP6.5069, 2019b.

Volodin, E., Mortikov, E., Gritsun, A., Lykossov, V., Galin, V., Diansky, N., Gusev, A., Kostrykin, S., Iakovlev, N., Shestakova, A. and Emelina, S.: INM INM-CM4-8 model output prepared for CMIP6 CMIP piControl, Earth System Grid Federation, , doi:https://doi.org/10.22033/ESGF/CMIP6.5080, 2019c.

Volodin, E., Mortikov, E., Gritsun, A., Lykossov, V., Galin, V., Diansky, N., Gusev, A., Kostrykin, S., Iakovlev, N., Shestakova, A. and Emelina, S.: INM INM-CM4-8 model output prepared for CMIP6 ScenarioMIP ssp126,

Earth System Grid Federation, , doi:https://doi.org/10.22033/ESGF/CMIP6.12325, 2019d.

Volodin, E., Mortikov, E., Gritsun, A., Lykossov, V., Galin, V., Diansky, N., Gusev, A., Kostrykin, S., Iakovlev, N., Shestakova, A. and Emelina, S.: INM INM-CM4-8 model output prepared for CMIP6 ScenarioMIP ssp245, Earth System Grid Federation, , doi:https://doi.org/10.22033/ESGF/CMIP6.12327, 2019e.

Volodin, E., Mortikov, E., Gritsun, A., Lykossov, V., Galin, V., Diansky, N., Gusev, A., Kostrykin, S., Iakovlev, N., Shestakova, A. and Emelina, S.: INM INM-CM4-8 model output prepared for CMIP6 ScenarioMIP ssp370, Earth System Grid Federation, , doi:https://doi.org/10.22033/ESGF/CMIP6.12329, 2019f.

Volodin, E., Mortikov, E., Gritsun, A., Lykossov, V., Galin, V., Diansky, N., Gusev, A., Kostrykin, S., Iakovlev, N., Shestakova, A. and Emelina, S.: INM INM-CM4-8 model output prepared for CMIP6 ScenarioMIP ssp585, Earth System Grid Federation, , doi:https://doi.org/10.22033/ESGF/CMIP6.12337, 2019g.

Volodin, E., Mortikov, E., Gritsun, A., Lykossov, V., Galin, V., Diansky, N., Gusev, A., Kostrykin, S., Iakovlev, N., Shestakova, A. and Emelina, S.: INM INM-CM5-0 model output prepared for CMIP6 CMIP historical, Earth System Grid Federation, , doi:https://doi.org/10.22033/ESGF/CMIP6.5070, 2019h.

Volodin, E., Mortikov, E., Gritsun, A., Lykossov, V., Galin, V., Diansky, N., Gusev, A., Kostrykin, S., Iakovlev, N., Shestakova, A. and Emelina, S.: INM INM-CM5-0 model output prepared for CMIP6 ScenarioMIP ssp126, Earth System Grid Federation, , doi:https://doi.org/10.22033/ESGF/CMIP6.12326, 2019i.

Volodin, E., Mortikov, E., Gritsun, A., Lykossov, V., Galin, V., Diansky, N., Gusev, A., Kostrykin, S., Iakovlev, N., Shestakova, A. and Emelina, S.: INM INM-CM5-0 model output prepared for CMIP6 ScenarioMIP ssp245, Earth System Grid Federation, , doi:https://doi.org/10.22033/ESGF/CMIP6.12328, 2019j.

Volodin, E., Mortikov, E., Gritsun, A., Lykossov, V., Galin, V., Diansky, N., Gusev, A., Kostrykin, S., Iakovlev, N., Shestakova, A. and Emelina, S.: INM INM-CM5-0 model output prepared for CMIP6 ScenarioMIP ssp370, Earth System Grid Federation, , doi:https://doi.org/10.22033/ESGF/CMIP6.12330, 2019k.

Volodin, E., Mortikov, E., Gritsun, A., Lykossov, V., Galin, V., Diansky, N., Gusev, A., Kostrykin, S., Iakovlev, N., Shestakova, A. and Emelina, S.: INM INM-CM5-0 model output prepared for CMIP6 ScenarioMIP ssp585, Earth System Grid Federation, , doi:https://doi.org/10.22033/ESGF/CMIP6.12338, 2019l.

Volodin, E., Mortikov, E., Gritsun, A., Lykossov, V., Galin, V., Diansky, N., Gusev, A., Kostrykin, S., Iakovlev, N., Shestakova, A. and Emelina, S.: NM INM-CM5-0 model output prepared for CMIP6 CMIP abrupt-4xCO2, Earth System Grid Federation, , doi:https://doi.org/10.22033/ESGF/CMIP6.4932, 2019m.

Volodin, E., Mortikov, E., Gritsun, A., Lykossov, V., Galin, V., Diansky, N., Gusev, A., Kostrykin, S., Iakovlev, N., Shestakova, A. and Emelina, S.: NM INM-CM5-0 model output prepared for CMIP6 CMIP piControl, Earth System Grid Federation, , doi:https://doi.org/10.22033/ESGF/CMIP6.5081, 2019n.

Wieners, K.-H., Giorgetta, M., Jungclaus, J. H., Reick, C., Esch, M., Bittner, M., Legutke, S., Schupfner, M., Wachsmann, F., Gayler, V., Haak, H., de Vrese, P., Raddatz, T., Mauritsen, T., von Storch, J.-S., Behrens, J., Brovkin, V., Claussen, M., Crueger, T., Fast, I., Fiedler, S., Hagemann, S., Hohenegger, C., Jahns, T., Kloster, S., Kinne, S., Lasslop, G., Kornblueh, L., Marotzke, J., Matei, D., Meraner, K., Mikolajewicz, U., Modali, K., Muller, W., Nabel, J. E. M. S., Notz, D., Peters, K., Pincus, R., Pohlmann, H., Pongratz, J., Rast, S., Schmidt, H., Schnur, R., Schulzweida, U., Six, K., Stevens, B., Voigt, A. and Roeckner, E.: MPI-M MPI-ESM1.2-LR model output prepared for CMIP6 CMIP historical, Earth System Grid Federation, , doi:https://doi.org/10.22033/ESGF/CMIP6.6595, 2019a.

Wieners, K.-H., Giorgetta, M., Jungclaus, J., Reick, C., Esch, M., Bittner, M., Gayler, V., Haak, H., de Vrese, P., Raddatz, T., Mauritsen, T., von Storch, J.-S., Behrens, J., Brovkin, V., Claussen, M., Crueger, T., Fast, I., Fiedler, S., Hagemann, S., Hohenegger, C., Jahns, T., Kloster, S., Kinne, S., Lasslop, G., Kornblueh, L., Marotzke, J., Matei, D., Meraner, K., Mikolajewicz, U., Modali, K., Müller, W., Nabel, J., Notz, D., Peters,

K., Pincus, R., Pohlmann, H., Pongratz, J., Rast, S., Schmidt, H., Schnur, R., Schulzweida, U., Six, K., Stevens, B., Voigt, A. and Roeckner, E.: MPI-M MPI-ESM1.2-LR model output prepared for CMIP6 ScenarioMIP ssp126, Earth System Grid Federation, , doi:https://doi.org/10.22033/ESGF/CMIP6.6690, 2019b.

Wieners, K.-H., Giorgetta, M., Jungclaus, J., Reick, C., Esch, M., Bittner, M., Gayler, V., Haak, H., de Vrese, P., Raddatz, T., Mauritsen, T., von Storch, J.-S., Behrens, J., Brovkin, V., Claussen, M., Crueger, T., Fast, I., Fiedler, S., Hagemann, S., Hohenegger, C., Jahns, T., Kloster, S., Kinne, S., Lasslop, G., Kornblueh, L., Marotzke, J., Matei, D., Meraner, K., Mikolajewicz, U., Modali, K., Müller, W., Nabel, J., Notz, D., Peters, K., Pincus, R., Pohlmann, H., Pongratz, J., Rast, S., Schmidt, H., Schnur, R., Schulzweida, U., Six, K., Stevens, B., Voigt, A. and Roeckner, E.: MPI-M MPI-ESM1.2-LR model output prepared for CMIP6 ScenarioMIP ssp245, Earth System Grid Federation, , doi:https://doi.org/10.22033/ESGF/CMIP6.6693, 2019c.

Wieners, K.-H., Giorgetta, M., Jungclaus, J., Reick, C., Esch, M., Bittner, M., Gayler, V., Haak, H., de Vrese, P., Raddatz, T., Mauritsen, T., von Storch, J.-S., Behrens, J., Brovkin, V., Claussen, M., Crueger, T., Fast, I., Fiedler, S., Hagemann, S., Hohenegger, C., Jahns, T., Kloster, S., Kinne, S., Lasslop, G., Kornblueh, L., Marotzke, J., Matei, D., Meraner, K., Mikolajewicz, U., Modali, K., Müller, W., Nabel, J., Notz, D., Peters, K., Pincus, R., Pohlmann, H., Pongratz, J., Rast, S., Schmidt, H., Schnur, R., Schulzweida, U., Six, K., Stevens, B., Voigt, A. and Roeckner, E.: MPI-M MPI-ESM1.2-LR model output prepared for CMIP6 ScenarioMIP ssp370, Earth System Grid Federation, , doi:https://doi.org/10.22033/ESGF/CMIP6.6695, 2019d.

Wieners, K.-H., Giorgetta, M., Jungclaus, J., Reick, C., Esch, M., Bittner, M., Gayler, V., Haak, H., de Vrese, P., Raddatz, T., Mauritsen, T., von Storch, J.-S., Behrens, J., Brovkin, V., Claussen, M., Crueger, T., Fast, I., Fiedler, S., Hagemann, S., Hohenegger, C., Jahns, T., Kloster, S., Kinne, S., Lasslop, G., Kornblueh, L., Marotzke, J., Matei, D., Meraner, K., Mikolajewicz, U., Modali, K., Müller, W., Nabel, J., Notz, D., Peters, K., Pincus, R., Pohlmann, H., Pongratz, J., Rast, S., Schmidt, H., Schnur, R., Schulzweida, U., Six, K., Stevens, B., Voigt, A. and Roeckner, E.: MPI-M MPI-ESM1.2-LR model output prepared for CMIP6 ScenarioMIP ssp585, Earth System Grid Federation, , doi:https://doi.org/10.22033/ESGF/CMIP6.6705, 2019e.

Wu, T., Chu, M., Dong, M., Fang, Y., Jie, W., Li, J., Li, W., Liu, Q., Shi, X., Xin, X., Yan, J., Zhang, F., Zhang, J., Zhang, L. and Zhang, Y.: BCC BCC-CSM2MR model output prepared for CMIP6 CMIP abrupt-4xCO2, Earth System Grid Federation, , doi:https://doi.org/10.22033/ESGF/CMIP6.2845, 2018a.

Wu, T., Chu, M., Dong, M., Fang, Y., Jie, W., Li, J., Li, W., Liu, Q., Shi, X., Xin, X., Yan, J., Zhang, F., Zhang, J., Zhang, L. and Zhang, Y.: BCC BCC-CSM2MR model output prepared for CMIP6 CMIP historical, Earth System Grid Federation, , doi:https://doi.org/10.22033/ESGF/CMIP6.2948, 2018b.

Wu, T., Chu, M., Dong, M., Fang, Y., Jie, W., Li, J., Li, W., Liu, Q., Shi, X., Xin, X., Yan, J., Zhang, F., Zhang, J., Zhang, L. and Zhang, Y.: BCC BCC-CSM2MR model output prepared for CMIP6 CMIP piControl, Earth System Grid Federation, , doi:https://doi.org/10.22033/ESGF/CMIP6.3016, 2018c.

Xin, X., Wu, T., Shi, X., Zhang, F., Li, J., Chu, M., Liu, Q., Yan, J., Ma, Q. and Wei, M.: BCC BCC-CSM2MR model output prepared for CMIP6 ScenarioMIP ssp126, Earth System Grid Federation, , doi:https://doi.org/10.22033/ESGF/CMIP6.3028, 2019a.

Xin, X., Wu, T., Shi, X., Zhang, F., Li, J., Chu, M., Liu, Q., Yan, J., Ma, Q. and Wei, M.: BCC BCC-CSM2MR model output prepared for CMIP6 ScenarioMIP ssp245, Earth System Grid Federation, , doi:https://doi.org/10.22033/ESGF/CMIP6.3030, 2019b.

Xin, X., Wu, T., Shi, X., Zhang, F., Li, J., Chu, M., Liu, Q., Yan, J., Ma, Q. and Wei, M.: BCC BCC-CSM2MR model output prepared for CMIP6 ScenarioMIP ssp370, Earth System Grid Federation, , doi:https://doi.org/10.22033/ESGF/CMIP6.3035, 2019c.

Xin, X., Wu, T., Shi, X., Zhang, F., Li, J., Chu, M., Liu, Q., Yan, J., Ma, Q. and Wei, M.: BCC BCC-CSM2MR model output prepared for CMIP6 ScenarioMIP ssp585, Earth System Grid Federation, , doi:https://doi.org/10.22033/ESGF/CMIP6.3050, 2019d.

YU, Y.: CAS FGOALS-f3-L model output prepared for CMIP6 CMIP historical, Earth System Grid Federation, , doi:https://doi.org/10.22033/ESGF/CMIP6.3355, 2019a.

YU, Y.: CAS FGOALS-f3-L model output prepared for CMIP6 ScenarioMIP ssp126, Earth System Grid Federation, , doi:https://doi.org/10.22033/ESGF/CMIP6.3464, 2019b.

YU, Y.: CAS FGOALS-f3-L model output prepared for CMIP6 ScenarioMIP ssp245, Earth System Grid Federation, , doi:https://doi.org/10.22033/ESGF/CMIP6.3468, 2019c.

YU, Y.: CAS FGOALS-f3-L model output prepared for CMIP6 ScenarioMIP ssp370, Earth System Grid Federation, , doi:https://doi.org/10.22033/ESGF/CMIP6.3479, 2019d.

YU, Y.: CAS FGOALS-f3-L model output prepared for CMIP6 ScenarioMIP ssp585, Earth System Grid Federation, , doi:https://doi.org/10.22033/ESGF/CMIP6.3502, 2019e.

Yukimoto, S., Koshiro, T., Kawai, H., Oshima, N., Yoshida, K., Urakawa, S., Tsujino, H., Deushi, M., Tanaka, T., Hosaka, M., Yoshimura, H., Shindo, E., Mizuta, R., Ishii, M., Obata, A. and Adachi, Y.: MRI MRI-ESM2.0 model output prepared for CMIP6 CMIP historical, Earth System Grid Federation, , doi:https://doi.org/10.22033/ESGF/CMIP6.6842, 2019a.

Yukimoto, S., Koshiro, T., Kawai, H., Oshima, N., Yoshida, K., Urakawa, S., Tsujino, H., Deushi, M., Tanaka, T., Hosaka, M., Yoshimura, H., Shindo, E., Mizuta, R., Ishii, M., Obata, A. and Adachi, Y.: MRI MRI-ESM2.0 model output prepared for CMIP6 ScenarioMIP ssp119, Earth System Grid Federation, , doi:https://doi.org/10.22033/ESGF/CMIP6.6908, 2019b.

Yukimoto, S., Koshiro, T., Kawai, H., Oshima, N., Yoshida, K., Urakawa, S., Tsujino, H., Deushi, M., Tanaka, T., Hosaka, M., Yoshimura, H., Shindo, E., Mizuta, R., Ishii, M., Obata, A. and Adachi, Y.: MRI MRI-ESM2.0 model output prepared for CMIP6 ScenarioMIP ssp126, Earth System Grid Federation, , doi:https://doi.org/10.22033/ESGF/CMIP6.6909, 2019c.

Yukimoto, S., Koshiro, T., Kawai, H., Oshima, N., Yoshida, K., Urakawa, S., Tsujino, H., Deushi, M., Tanaka, T., Hosaka, M., Yoshimura, H., Shindo, E., Mizuta, R., Ishii, M., Obata, A. and Adachi, Y.: MRI MRI-ESM2.0 model output prepared for CMIP6 ScenarioMIP ssp245, Earth System Grid Federation, , doi:https://doi.org/10.22033/ESGF/CMIP6.6910, 2019d.

Yukimoto, S., Koshiro, T., Kawai, H., Oshima, N., Yoshida, K., Urakawa, S., Tsujino, H., Deushi, M., Tanaka, T., Hosaka, M., Yoshimura, H., Shindo, E., Mizuta, R., Ishii, M., Obata, A. and Adachi, Y.: MRI MRI-ESM2.0 model output prepared for CMIP6 ScenarioMIP ssp370, Earth System Grid Federation, , doi:https://doi.org/10.22033/ESGF/CMIP6.6915, 2019e.

Yukimoto, S., Koshiro, T., Kawai, H., Oshima, N., Yoshida, K., Urakawa, S., Tsujino, H., Deushi, M., Tanaka, T., Hosaka, M., Yoshimura, H., Shindo, E., Mizuta, R., Ishii, M., Obata, A. and Adachi, Y.: MRI MRI-ESM2.0 model output prepared for CMIP6 ScenarioMIP ssp434, Earth System Grid Federation, , doi:https://doi.org/10.22033/ESGF/CMIP6.6925, 2019f.

Yukimoto, S., Koshiro, T., Kawai, H., Oshima, N., Yoshida, K., Urakawa, S., Tsujino, H., Deushi, M., Tanaka, T., Hosaka, M., Yoshimura, H., Shindo, E., Mizuta, R., Ishii, M., Obata, A. and Adachi, Y.: MRI MRI-ESM2.0 model output prepared for CMIP6 ScenarioMIP ssp460, Earth System Grid Federation, , doi:https://doi.org/10.22033/ESGF/CMIP6.6926, 2019g.

Yukimoto, S., Koshiro, T., Kawai, H., Oshima, N., Yoshida, K., Urakawa, S., Tsujino, H., Deushi, M., Tanaka, T.,

Hosaka, M., Yoshimura, H., Shindo, E., Mizuta, R., Ishii, M., Obata, A. and Adachi, Y.: MRI MRI-ESM2.0 model output prepared for CMIP6 ScenarioMIP ssp585, Earth System Grid Federation, , doi:https://doi.org/10.22033/ESGF/CMIP6.6929, 2019h.

Zhang, J., Wu, T., Shi, X., Zhang, F., Li, J., Chu, M., Liu, Q., Yan, J., Ma, Q. and Wei, M.: BCC BCC-ESM1 model output prepared for CMIP6 CMIP historical, Earth System Grid Federation, , doi:https://doi.org/10.22033/ESGF/CMIP6.2949, 2018a.

Zhang, J., Wu, T., Shi, X., Zhang, F., Li, J., Chu, M., Liu, Q., Yan, J., Ma, Q. and Wei, M.: BCC BCC-ESM1 model output prepared for CMIP6 CMIP piControl, Earth System Grid Federation, , doi:https://doi.org/10.22033/ESGF/CMIP6.3017, 2018b.

Zhang, J., Wu, T., Shi, X., Zhang, F., Li, J., Chu, M., Liu, Q., Yan, J., Ma, Q. and Wei, M.: BCC BCC-ESM1 model output prepared for CMIP6 CMIP abrupt-4xCO2, Earth System Grid Federation, , doi:https://doi.org/10.22033/ESGF/CMIP6.2846, 2019.

Ziehn, T., Chamberlain, M., Lenton, A., Law, R., Bodman, R., Dix, M., Wang, Y., Dobrohotoff, P., Srbinovsky, J., Stevens, L., Vohralik, P., Mackallah, C., Sullivan, A., O'Farrell, S. and Druken, K.: CSIRO ACCESS-ESM1.5 model output prepared for CMIP6 CMIP abrupt-4xCO2, Earth System Grid Federation, , doi:https://doi.org/10.22033/ESGF/CMIP6.4238, 2019a.

Ziehn, T., Chamberlain, M., Lenton, A., Law, R., Bodman, R., Dix, M., Wang, Y., Dobrohotoff, P., Srbinovsky, J., Stevens, L., Vohralik, P., Mackallah, C., Sullivan, A., O'Farrell, S. and Druken, K.: CSIRO ACCESS-ESM1.5 model output prepared for CMIP6 CMIP historical, Earth System Grid Federation, , doi:https://doi.org/10.22033/ESGF/CMIP6.4272, 2019b.

Ziehn, T., Chamberlain, M., Lenton, A., Law, R., Bodman, R., Dix, M., Wang, Y., Dobrohotoff, P., Srbinovsky, J., Stevens, L., Vohralik, P., Mackallah, C., Sullivan, A., O'Farrell, S. and Druken, K.: CSIRO ACCESS-ESM1.5 model output prepared for CMIP6 CMIP piControl, Earth System Grid Federation, , doi:https://doi.org/10.22033/ESGF/CMIP6.4312, 2019c.

Ziehn, T., Chamberlain, M., Lenton, A., Law, R., Bodman, R., Dix, M., Wang, Y., Dobrohotoff, P., Srbinovsky, J., Stevens, L., Vohralik, P., Mackallah, C., Sullivan, A., O'Farrell, S. and Druken, K.: CSIRO ACCESS-ESM1.5 model output prepared for CMIP6 ScenarioMIP ssp126, Earth System Grid Federation, , doi:https://doi.org/10.22033/ESGF/CMIP6.4320, 2019d.

Ziehn, T., Chamberlain, M., Lenton, A., Law, R., Bodman, R., Dix, M., Wang, Y., Dobrohotoff, P., Srbinovsky, J., Stevens, L., Vohralik, P., Mackallah, C., Sullivan, A., O'Farrell, S. and Druken, K.: CSIRO ACCESS-ESM1.5 model output prepared for CMIP6 ScenarioMIP ssp245, Earth System Grid Federation, , doi:https://doi.org/10.22033/ESGF/CMIP6.4322, 2019e.

Ziehn, T., Chamberlain, M., Lenton, A., Law, R., Bodman, R., Dix, M., Wang, Y., Dobrohotoff, P., Srbinovsky, J., Stevens, L., Vohralik, P., Mackallah, C., Sullivan, A., O'Farrell, S. and Druken, K.: CSIRO ACCESS-ESM1.5 model output prepared for CMIP6 ScenarioMIP ssp370, Earth System Grid Federation, , doi:https://doi.org/10.22033/ESGF/CMIP6.4324, 2019f.

Ziehn, T., Chamberlain, M., Lenton, A., Law, R., Bodman, R., Dix, M., Wang, Y., Dobrohotoff, P., Srbinovsky, J., Stevens, L., Vohralik, P., Mackallah, C., Sullivan, A., O'Farrell, S. and Druken, K.: CSIRO ACCESS-ESM1.5 model output prepared for CMIP6 ScenarioMIP ssp585, Earth System Grid Federation, , doi:https://doi.org/10.22033/ESGF/CMIP6.4333, 2019g.